Influence of electron dynamics and electromagnetic effects on zonal flow pattern formation and the interplay with microturbulence in fusion plasmas

Von der Universität Bayreuth
zur Erlangung des Grades eines
Doktors der Naturwissenschaften (Dr. rer. nat.)
genehmigte Abhandlung

von

Florian Rath
aus Würzburg

1. Gutachter: Prof. Dr. Arthur G. Peeters
2. Gutachter: Assoc. Prof. Dr. Ben F. McMillan

Tag der Einreichung: 18.01.2023
Tag des Kolloquiums: 09.05.2023

Betreut durch Prof. Dr. Arthur G. Peeters

Acknowledgments

First of all, I would like to express my greatest gratitude to my supervisor Arthur Peeters. I would like to thank him for his guidance and his enduring support throughout the process of this thesis. The research presented in thesis benefitted from the many insightful discussions we had.

I would like to thank Arne Weikl for his helpfulness in many situations in and outside academia. In addition, I would like to thank him for granting me access to his simulation data and for proofreading one of the publications. I would like to thank Rico Buchholz for the time we shared the office and for always being helpful. I thank Stefan Großhauser for his effort in developing diagnostics, which made this thesis possible. Finally, I would like to thank Lukas Krönert, Felix Seiferling and Pierluigi Migliano for the time we spent, while working in plasma physics.

Outside academia, I would like to express my gratitude to my parents, my brother and Anita Freundorfer for their encouragement and support during the course of this thesis.

Abstract

Influence of electron dynamics and electromagnetic effects on zonal flow pattern formation and the interplay with microturbulence in fusion plasmas

The realization of the thermonuclear fusion requires a sufficiently good confinement of a hot fusion plasma. The tokamak concept, studied in this thesis, uses magnetic fields to achieve confinement. Turbulent losses of particles and energy, partially caused by turbulence on spatial scales comparable to the ion Larmor radius —so-called microturbulence —, constitute one of the main limitations of confinement. Future fusion experiments on reactor relevant scales are predicted to operate close to marginal stability of microturbulence, —a regime that is often accompanied by zonal flow structure formation. Here, zonal flows refer to a form of radially sheared plasma rotation that does not contribute to turbulent losses. On the contrary, they have a positive influence on confinement through their ability to suppress microturbulence. The interplay of zonal flow structure formation and microturbulence is therefore assumed to be relevant for future fusion reactors.

In this thesis the interplay of microturbulence and zonal flow pattern formation is investigated by means of gyrokinetic simulations performed with the Eulerian gyrokinetic code GKW. In the gyrokinetic framework the Maxwell-Vlasov system is solved, exploiting the time scale separation between the fast gyro-motion and the relatively slow turbulent dynamics. Gyrokinetic simulations represent the state of the art numerical description of fusion plasmas. This thesis focuses on the influence of electron dynamics and electromagnetic effects on zonal flow pattern formation, both extensions of the existing literature about zonal flow structure formation. Hence, this thesis aims to contribute to a more comprehensive understanding of the interplay of zonal flow structure formation and microturbulence. First, zonal flow pattern formation in electrostatic near marginal turbulence with inclusion of electron dynamics is studied using director field methods. It is shown that the dominant fine scale features in the $E \times B$ shearing rate, structures that are driven by the so-called self-interaction mechanism, do hardly contribute to the

zonal flow shear induced tilt of turbulent structures. Instead, zonal flow pattern formation on mesoscales, also known as the $E \times B$ staircase pattern, is diagnosed by demonstrating its role for shear deformation of turbulent structures. Furthermore, the modifications of staircase patterns by electron dynamics are discussed.
Second, electromagnetic microturbulence is investigated with the focus on high β turbulence runaways, i. e., the lack of turbulence saturation above a critical β_{c}. Temporally persistent mesoscale zonal flow patterns, developing on long time scales, are shown to mitigate high β turbulence runaways. These patterns, therefore, allow for the access of an improved β-regime, i. e., $\beta > \beta_{\mathrm{c}}$. Various aspects of those mesoscale zonal flow dominated improved states are investigated such as (i) the stability constraints with respect to the mesoscale zonal flow level for the triggering of turbulence runaways, (ii) the influence of mesoscale zonal flows on magnetic stochasticity, and (iii) the transfer processes connected to the drive and damping of mesoscale zonal flows.
Third, the self-interaction mechanism, i. e., the nonlinear interaction of a parallel to the magnetic field strongly elongated mode with itself, is studied by means of nonlinear energy transfer methods. The self-interaction mechanism is a phenomenon that occurs especially in descriptions including electron dynamics. It is known to be responsible for the generation of fine scale features in the $E \times B$ shearing rate. In this thesis this mechanism is shown to have only a small (of the order of a few percent) direct influence on the processes governing nonlinear saturation of ion temperature gradient driven microturbulence for plasma core parameters. Furthermore, the contribution of self-interaction driven zonal fine scale structures to the zonal flow mediated nonlinear transfer is also small (of the order of a few percent), corroborating the outcome of the director field analysis.
Fourth, the influence of modified (by electron dynamics) staircase states on the stability properties close to marginality is investigated. Various unstable Eigenmodes are identified that are absent in the primary instability spectrum, i. e., without the presence of modified staircase states. These Eigenmodes localize to disparate scales connected to the modified staircase structures and require a finite electron background temperature gradient drive. Hence, electron dynamics and electron temperature gradient drive both modify the stability properties close to marginality. Their consideration may be required for a proper description of near marginal microturbulence.

Zusammenfassung

Influence of electron dynamics and electromagnetic effects on zonal flow pattern formation and the interplay with microturbulence in fusion plasmas

Die Realisierung der thermonuklearen Fusion erfordert einen ausreichend guten Einschluss eines heißen Fusionsplasmas. Das Tokamak Konzept, welches Gegenstand dieser Arbeit ist, nutzt Magnetfelder, um das Plasma einzuschließen. Turbulente Verluste von Teilchen und Energie, zum Teil verursacht durch Turbulenz auf räumlichen Skalen vergleichbar mit dem Larmor Radius —sogenannte Mikroturbulenz —, stellt eine der Haupteinschränkungen des Plasmaeinschlusses dar. Zukünftige Fusionsexperimente auf reaktorrelevanten Größenskalen werden voraussichtlich nahe marginaler Stabilität von Mikroturbulenz operieren, —ein Regime, das oft von Strukturbildung zonaler $E \times B$ Strömungen (zonal flows) geprägt ist. Dabei bezeichnen zonale $E \times B$ Strömungen eine bestimmte Form von radial verscherter Plasmarotation, welche nicht zu den turbulenten Verlusten beiträgt. Ganz im Gegenteil, durch ihre Fähigkeit Mikroturbulenz zu unterdrücken, wirken sich zonale $E \times B$ Strömungen positiv auf den Plasmaeinschluss aus. Das Zusammenspiel von Strukturbildung zonaler $E \times B$ Strömungen und Mitroturbulenz birgt daher eine Relevanz für zukünftige Fusionsreaktoren.
Diese Arbeit untersucht das Zusammenspiel von Strukturbildung zonaler $E \times B$ Strömungen und Mitroturbulenz anhand von gyrokinetischen Simulationen, die mit dem Euler'schen gyrokinetischen code GKW durchgeführt werden. Der gyrokinetsiche Ansatz löst das Maxwell-Vlasov System unter Ausnutzen der Zeitskalentrennung der schnellen Gyrationsbewegung und der relativ dazu langsamen turbulenten Dynamik. Gyrokinetische Simulationen stellen den state-of-the-art Ansatz zur numerischen Beschreibung von Fusionsplasmen dar. Der Fokus dieser Arbeit liegt auf dem Einfluss von Elektronendynamik und elektromagnetischen Effekten auf Strukturbildung zonaler $E \times B$ Strömungen, beides Erweiterungen der dazu existierenden Literatur. Damit trägt diese Arbeit zu einem umfassenderen Verständnis des Zusammenspiels von Strukturbildung zonaler $E \times B$ Strömungen und Miktroturbulenz bei.

Als erstes wird Strukturbildung zonaler $E \times B$ Strömungen in elektrostatischer marginaler Turbulenz unter Berücksichtigung von Elektronendynamik und mit Hilfe von Direktorfeldmethoden untersucht. Es wird gezeigt, dass dominante Feinskalenstrukturen in der $E \times B$ Scherrate, welche durch die sogenannte Selbstinteraktion getrieben werden, kaum zur durch zonaler $E \times B$ Strömungen induzierten Deformation von turbulenten Strukturen beitragen. Stattdessen wird Strukturbildung zonaler $E \times B$ Strömungen auf Mesoskalen, auch bekannt als $E \times B$ Treppenmuster ($E \times B$ staircase pattern), anhand ihrer Rolle für die Scherdeformation von turbulenten Strukturen diagnostiziert. Weiterhin werden die Modifizierungen dieser $E \times B$ Treppenstrukturen durch Elektronendynamik diskutiert.
Als zweites wird elektromagnetische Miktroturbulenz untersucht. Dabei liegt der Fokus auf sogenannte turbulente Ausreißer im Bereich hoher nomierter Plasmadrücke β (high β turbulence runwaways), —eine Form von transienter turbulenter Dynamik oberhalb eines kritischen β_{c}, welche keine Sättigung des Turbulenzlevels aufweist. Es wird gezeigt, dass zeitlich persistente zonale $E \times B$ Strömungen auf Mesoskalen, welche sich auf langen Zeitskalen entwickeln, diese turbulenten Ausreißer unterdrücken. Dadurch erlauben diese Strukturen den Zugang zu einem β-Regime mit verbesserten Einschluss, also einem Regime mit $\beta > \beta_{\mathrm{c}}$. Verschiedene Aspekte dieser durch zonalen $E \times B$ Strömungen dominierten günstigen Zustände werden untersucht, wie zum Beispiel (i) die Stabiltätsbedingungen an das Level der zonalen $E \times B$ Strömungen für das Auslösen von turbulenten Ausreißern, (ii) der Einfluss von zonalen $E \times B$ Strömungen auf magnetische Stochastizität, und (iii) Transferprozesse verknüpft mit dem Treiben und Dämpfen von zonalen $E \times B$ Strömungen.
Als drittes wird die Selbstinteraktion, also die nichtlineare Wechselwirkung von parallel zum Magnetfeld stark elongierten Moden mit sich selbst, mit Hilfe von nichtlinearen Energietransfermethoden studiert. Die Selbstinteraktion ist ein Phänomen, das vor allem in Beschreibungen mit Berücksichtigung von Elektronendynamik auftritt. Dabei ist dieser Mechanismus für die Entstehung von Feinskalenstrukturen in der $E \times B$ Scherrate verantwortlich. In dieser Arbeit wird gezeigt, dass die Selbstinteraktion lediglich einen kleinen (auf Größenordnung einiger weniger Prozent) direkten Einfluss auf die Prozesse hat, welche die nichtlineare Sättigung von ionentemperaturgetriebener Mikroturbulenz bestimmen. Weiterhin wird gezeigt, dass der Beitrag von selbwechselwirkungsgetriebenen Feinskalenstrukturen zum durch zonale $E \times B$ Strömungen mediierten nichtlinearen Transfer ebenfalls klein (auf Größenordnung einiger weniger Prozent) ist. Dieses Ergebnis stützt die Aussage der oben aufgeführten Direktorfeldanalyse.
Als viertes wird der Einfluss von (durch Elektronendynamik) modifizierten $E \times B$ Treppenstrukturen auf die Stabilitätseigenschaften nahe marginaler Stabilität untersucht. Verschiedene instabile Eigenmoden können identifizert werden, welche im primären Instabilitätsspektrum, also in Abwesenheit von modifizerten $E \times B$ Treppenstrukturen, nicht vorhanden sind. Diese Eigenmoden sind bezüglich

unterschiedlicher Skalen lokalisiert, welche direkt mit der modifzierten $E \times B$ Treppenstrukturen verknüpft werden können, und erfordern einen endlichen Elektronentemperaturgradienten. Da sowohl Elektronendynamik als auch endliche Elektronentemperaturgradienten die Stabilitätseigenschaften in der Nähe von marginaler Stabilität beeinflussen, ist eine Berücksichtigung dieser Effekte für eine angemessene Beschreibung von marginaler Mikroturbulenz notwendig.

Declaration

The author declares that the material presented in this thesis is his own work, unless explicitly stated otherwise. Parts of this thesis have been published in a peer reviewed journal. Chapters 6 and 7 are based on

> F. Rath, A. G. Peeters, and A. Weikl, *Analysis of zonal flow pattern formation and the modification of staircase states by electron dynamics in gyrokinetic near marginal turbulence*, Phys. Plasmas **28**, 072305 (2021)

and

> F. Rath, and A. G. Peeters, *Transport hysteresis in electromagnetic microturbulence caused by mesoscale zonal flow pattern-induced mitigation of high β turbulence runaways*, Phys. Plasma **29**, 042305 (2022),

respectively.
Part of the simulation raw data presented in chapter 6 have been produced and made available by Arne Weikl. More specifically, the gyrokinetic simulation dataset G_2 of Ref. [1] has both been extended in time and included in the postprocessing analysis of chapter 6.

Contents

Chapter 1

Motivation 1: Thermonuclear fusion

The growing world population, global warming and current geopolitical tensions highlight the need for future reliable and climate-neutral energy sources. Nuclear fusion is a promising candidate due to the existence of a vast abundance of the required fuel and due to the absence of climate-damaging products. In the underlying process two light nuclei fuse and thereby release energy in accordance to the mass defect and the mass-energy equivalence. In order to allow for the nuclei to fuse, the mutual repulsion associated with their positive charge has to be overcome. A promising way to provide the necessary energy is to heat the fuel to sufficiently high temperatures, referred to as *thermonuclear fusion*.
Since fusion reactions require the reactants to collide, the fusion cross section σ provides a measure of the probability of such reactions. Fig. 1.1 depicts cross sections for various fusion reactions involving deuterium (D), tritium (T) and helium-3 (^{3}He). At low temperatures the cross section is small, since the Coulomb barrier prevents the reactants to approach sufficiently close for the nuclear strong force to dominate. Due to the combined effect of an increasing relative velocity with increasing temperature and quantum tunnelling, the cross section exhibits a maximum at a certain temperature. A comparison of different fusion reactions involving deuterium (see Fig. 1.1) shows that the the D-T reaction has the largest maximum cross section at the smallest temperature; —it is, therefore, the most promising reaction for the realization of thermonuclear fusion. From Fig. 1.1 it is also clear that fusion relevant collision energies are of the order of $10^1 - 10^2$ keV. The ionization energy of hydrogen is 13.6 eV and, therefore, the fuel is completely ionized, i. e., the fuel is in the *plasma state*.
In the D-T reaction the nuclei of deuterium (D) and tritium (T) fuse and an alpha particle, i. e., a helium (He) nucleus, and a neutron (n) is produced according to

$$ {}_1\mathrm{D}^2 \; + {}_1\mathrm{T}^3 \; \rightarrow \; {}_2\mathrm{He}^4 + \; {}_0\mathrm{n}^1. \tag{1.1} $$

This reaction releases an energy of $\mathcal{E} = 17.59$ MeV, of which one fifth is carried by the helium nucleus and the remainder by the neutron.

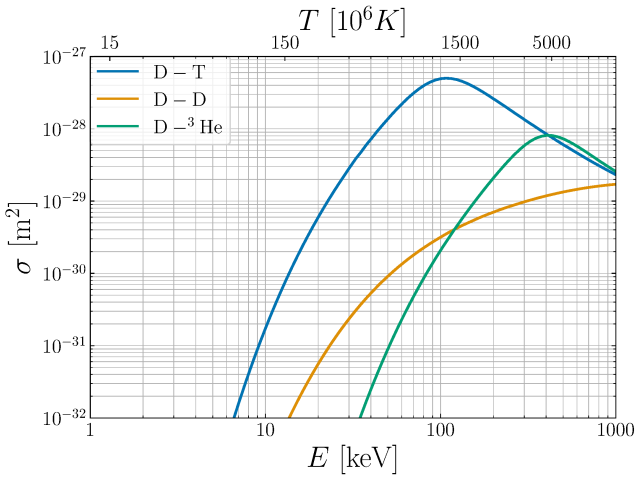

Figure 1.1: Fusion cross section σ as function of the collision energy E (bottom axis), i. e., the kinetic energy of the lighter reactant in a frame of reference in which the heavier reactant is at rest, as well as the temperature $T = E/k_\mathrm{B}$ (top axis) for three fusion reactions involving deuterium. The data has been retrieved from the International Atomic Energy Agency database [2].

For the D-T reaction the thermonuclear power is maximized for $n_D = n_T = n/2$ [3], with $n = n_D + n_T$, and therefore the fusion power density reads

$$p_\mathrm{fus} = \frac{1}{4} n^2 \langle \sigma v \rangle \mathcal{E}. \tag{1.2}$$

Here, $\langle \sigma v \rangle$ is the *reactivity*, defined by

$$\langle \sigma v \rangle = \int_0^\infty \sigma(v) v f(v)\, \mathrm{d}v \tag{1.3}$$

where v is the relative velocity of the reactants and $f(v)$ is the distribution of relative velocities [4].[1] Since the neutrons leave the plasma without interaction the energy $\mathcal{E}_\alpha$ carried by the α-particles remains to heat the plasma. The total α-particle heating is

$$P_\alpha = \frac{1}{4} \overline{n^2 \langle \sigma v \rangle} \mathcal{E}_\alpha V, \tag{1.4}$$

where the overbar denotes a volume average.
In a reactor a continuous loss of energy from the plasma occurs and the rate of energy loss

$$P_\mathrm{L} = \frac{W}{\tau_E} \tag{1.5}$$

is typically expressed through the total plasma energy $W = 3\overline{nT}V$ [3] and the energy confinement time τ_E. A stationary plasma requires the energy loss to be

[1] In this calculation the plasma particles are assumed to obey a Maxwellian distribution [4].

balanced by the α-particle heating and external heating P_{H} as expressed by the power balance

$$P_{\mathrm{H}} + P_{\alpha} = P_{\mathrm{L}}. \tag{1.6}$$

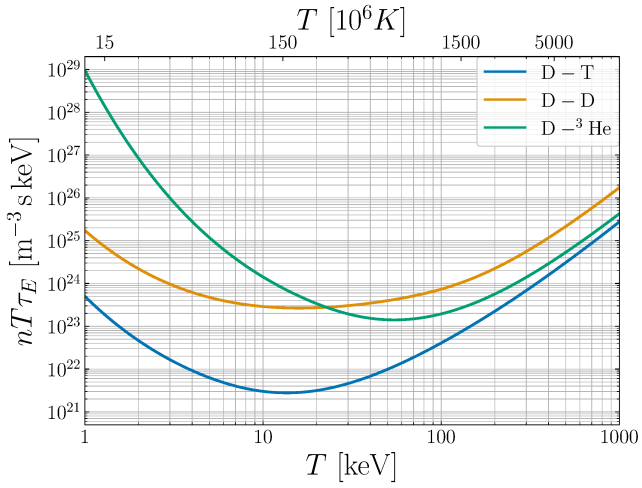

Figure 1.2: Triple product $nT\tau_E$ as function of the temperature for three fusion reactions of the deuterium cycle. The data has been retrieved from the International Atomic Energy Agency database [2].

When the plasma is heated to fusion relevant conditions, α-particle heating constitutes an increasing fraction of the total heating. Provided the plasma is sufficiently well confined, at a certain point, the energy losses may be entirely balanced by α-particle heating. This situation is called *ignition* and fusion reactions then proceeds in a self-sustained manner.
Assuming, for simplicity, profiles of constant density and temperature, the power balance equation (1.6) leads to the condition

$$nT\tau_E > \frac{12}{\langle\sigma v\rangle}\frac{T^2}{\mathcal{E}_{\alpha}} \tag{1.7}$$

for ignition, where the right-hand side is a function of the temperature only. The quantity $nT\tau_E$ is the so-called *triple product* and is shown in Fig. 1.2 for the three deuterium fusion reactions. In case of the D-T reaction it has a minimum at $T \approx 13$ keV ($T \approx 150 \times 10^6$ K).
The triple product is a convenient measure for ignition conditions, since it identifies the requirements on typical plasma parameters like density and temperature as well as the confinement quality. As expressed by inequality (1.7), a critical aspect of the feasibility of thermonuclear fusion is the confinement of the hot plasma. In the tokamak device, the configuration investigated in this thesis, the plasma is confined by strong magnetic fields. Turbulent transport constitutes one of the main limitations of confinement in a tokamak and the understanding of

the processes underlying (micro-) turbulence is, therefore, subject of extensive research. One aspect of microturbulence is the generation of patterns in the plasma rotation, also referred to as zonal flows, which favor confinement. The interplay of microturbulence and zonal flow pattern formation is the main subject of this thesis.

Chapter 2

Plasma physics background and magnetic confinement in a tokamak

At fusion relevant temperatures of 150×10^6 K, the fuel is fully ionized and is, therefore, in the plasma state. This chapter introduces plasma physics concepts and the magnetic confinement of a plasma in a tokamak device.

2.1 Charged particle motion in the presence of magnetic and electric fields

In magnetic confinement devices, such as the tokamak, the charged plasma particles experience magnetic and electric fields. The solution of the equation of motion, considering the associated forces, results in a distinct particle motion that will be introduced in this section. This section is based on Ref. [3] and for more details the reader is referred to this reference.

2.1.1 Gyro-motion

In a homogeneous ambient[1] magnetic field, plasma particles with a velocity component perpendicular to the magnetic field $v_{\perp,\mathrm{sp}}$ execute a circular motion in the plane perpendicular to the magnetic field due to the Lorentz force. For a plasma particle with charge q_{sp} and mass m_{sp}, the circulation frequency, also referred to

[1]Here, *ambient* or *equilibrium* magnetic field refers to the static part of the magnetic field in a tokamak device that is generated both by external coils and by toroidal plasma currents either induced externally or driven self-consistently by the plasma dynamics. By contrast, the *perturbed* of *fluctuating* magnetic field is the time dependent part of the magnetic field resulting from the turbulent plasma dynamics. It satisfies the gyrokinetic ordering 3.2.

as *cyclotron frequency*, is defined by

$$\omega_{\mathrm{c,sp}} = \frac{|q_{\mathrm{sp}}|B}{m_{\mathrm{sp}}}, \tag{2.1}$$

where B is the magnetic field strength. The radius of the circular motion, the so-called *Larmor radius*, is given by

$$\rho_{\mathrm{sp}} = \frac{m_{\mathrm{sp}} v_{\perp,\mathrm{sp}}}{|q_{\mathrm{sp}}|B}, \tag{2.2}$$

and its center is usually referred to as *gyro-center*. Since the Lorentz force depends on the sign of the particle's charge, the circulation direction of electrons and ions is opposed.
Due to coulomb collisions the plasma is thermalized and the species velocity distribution can be approximately described by a Maxwell-Boltzmann distribution.[2] A typical velocity is then the species thermal velocity

$$v_{\mathrm{th,sp}} = \sqrt{\frac{2T_{\mathrm{sp}}}{m_{\mathrm{sp}}}}, \tag{2.3}$$

where m_{sp} denotes the species mass and T_{sp} is the species temperature. Based on the thermal velocity it, is convenient to introduce a *thermal Larmor radius*

$$\rho_{\mathrm{th,sp}} = \frac{m_{\mathrm{sp}} v_{\mathrm{th,sp}}}{|q_{\mathrm{sp}}|B}. \tag{2.4}$$

Under reactor conditions the thermal Larmor radius of ions is of the order of a few millimeters, while for electrons it is smaller by two orders of magnitude (see appendix E).

2.1.2 Particle motion parallel to the magnetic field

Free parallel streaming: While the motion perpendicular to a homogeneous magnetic field is restricted by the Lorentz force, due to the absence of parallel forces, particles can stream freely parallel to a homogeneous magnetic field, also referred to as *parallel streaming* throughout this thesis. The velocity connected to this parallel motion is of the order of the thermal velocity $v_{\mathrm{th,sp}}$. Since electrons are significantly lighter than ions, the parallel streaming of the electrons is much larger compared to ions.[3]

[2] In the course of the thesis the Maxwell-Boltzmann distribution will mostly referred to as *Maxwellian*.

[3] Assuming same ion and electron temperature, in a deuterium plasma the ratio of the thermal velocities is $v_{\mathrm{th,e}}/v_{\mathrm{th,i}} \approx 60$.

Parallel acceleration due to an electric field: An electric field with a component parallel to the magnetic field $E_\parallel$ accelerates a plasma particle through the force

$$F_{\parallel,E} = q_{\rm sp} E_\parallel. \tag{2.5}$$

The parallel electric field may depend both on the position along the field line and on time. The parallel motion, then, follows from the solution of the equation of motion [3].

Parallel acceleration due to a parallel gradient of the magnetic field: When the magnetic field is inhomogeneous and when its gradient ∇B has a component parallel to the magnetic field $\nabla_\parallel B \equiv (\mathbf{B}/B)\cdot\nabla B$, a plasma particle experiences the force

$$F_{\parallel,\nabla_\parallel B} = -\frac{m_{\rm sp} v_\perp^2}{2B}\nabla_\parallel B. \tag{2.6}$$

The force incorporates the *magnetic moment*

$$\mu = \frac{m_{\rm sp} v_\perp^2}{2B}. \tag{2.7}$$

In a slowly varying magnetic field the magnetic moment is an adiabatic invariant, i. e., it is a constant of motion.[4] When a particle moves into a region with increasing magnetic field, it can be reflected due to the force $F_{\parallel,\nabla_\parallel B}$. This effect is called the mirror effect and the associated force is called the mirror force.

2.1.3 Gyro-center drifts

In the presence of an inhomogeneous equilibrium magnetic field or perturbed magnetic as well as (time dependent) electric fields the gyro-center undergoes various slow drift motions perpendicular to the ambient magnetic field. Here, the property *slow* means that the drifts are slow compared to the thermal velocity.[5]

$E\times B$-drift: If a homogeneous electric field with a component perpendicular to the magnetic field is present, the action of the Coulomb force leads to a drift of the gyro-center with a velocity

$$\mathbf{v}_E = \frac{\mathbf{E}\times\mathbf{B}}{B^2} \tag{2.8}$$

[4]Here, *slowly varying* refers to temporal variations that are slow compared to the inverse cyclotron frequency $\omega_{\rm c,sp}^{-1}$ and spatial variations that are large compared to the Larmor radius $\rho_{\rm sp}$ [3].

[5]In tokamak devices the equilibrium fields vary on length scales larger then the ion Larmor radius $\rho_{\rm i}$ and on time scales slow compared to the inverse ion cyclotron frequency $\omega_{\rm c,i}^{-1}$. Furthermore, fluctuations are smaller compared to the equilibrium field by a small parameter $\epsilon_g \ll 1$. The gyro-center drifts then satisfy the ordering $\mathbf{v}_d \sim \epsilon_g v_{\rm th,sp}$.

called the $E \times B$-drift, where $\mathbf{E}$ denotes the electric field. Since both the circulation direction of the gyromotion and the Coulomb force depend on the sign of the particle's charge, the direction of the $E \times B$-drift is equal for ions and electrons.

∇B-drift: When the magnetic field is inhomogeneous, i. e., when it exhibits a finite gradient ∇B, gyro-centers undergo the so-called ∇B-*drift*

$$\mathbf{v}_{\nabla B} = \frac{m_{\mathrm{sp}} v_{\perp,\mathrm{sp}}^2}{2 q_{\mathrm{sp}}} \frac{\mathbf{B} \times \nabla B}{B^3}. \tag{2.9}$$

The form given in Eq. (2.9) requires the gradient of the magnetic field to vary on scales that are large compared to the Larmor radius. This condition is usually well satisfied for tokamak devices, as the magnetic field varies on scales of the machine size. The ∇B-drift depends on the particle charge and, therefore, its direction differs among ions and electrons.

Curvature drift: Due to the centrifugal force acting on a particle in a curved magnetic field, the gyro-center experience the *curvature drift*

$$\mathbf{v}_C = \frac{m_{\mathrm{sp}} v_{\parallel}^2}{q_{\mathrm{sp}}} \frac{\mathbf{B} \times \kappa}{B^2}. \tag{2.10}$$

The curvature can be written as

$$\kappa = -(\mathbf{b} \cdot \nabla)\mathbf{b} = -\mathbf{b} \times \left(\nabla \times \frac{\mathbf{B}}{B} \right) = \mu_0 \frac{\mathbf{J} \times \mathbf{B}}{B^2} + \frac{\nabla B}{B} = \mu_0 \frac{\nabla p}{B^2} + \frac{\nabla B}{B}, \tag{2.11}$$

where Amperè's law and the force balance $\mathbf{J} \times \mathbf{B} = \nabla p$ for the equilibrium [3] has been used.
If the ratio of the plasma pressure and the magnetic field pressure is small, the pressure gradient correction can be neglected and the curvature drift reduces to

$$\mathbf{v}_C = \frac{m_{\mathrm{sp}} v_{\parallel,\mathrm{sp}}^2}{q_{\mathrm{sp}}} \frac{\mathbf{B} \times \nabla B}{B^3}. \tag{2.12}$$

In this form the ∇B- and curvature drift can be treated similarly.

Polarization drift: When an electric field perpendicular to the magnetic field varies temporally the particle's gyro-center undergoes the drift

$$\mathbf{v}_P = \frac{1}{\omega_{\mathrm{c,sp}} B} \frac{\partial \mathbf{E}_{\perp}}{\partial t}. \tag{2.13}$$

The direction of this drift depends on the species charge and results in a polarization current. Therefore, it is referred to as *polarization drift*.

Parallel motion along perturbed magnetic field lines: The parallel streaming along a perturbed magnetic field $\delta\mathbf{B} = \nabla \times A_\parallel \mathbf{b} \approx \mathbf{b} \times \nabla A_\parallel$ results in the gyro-center drift

$$\mathbf{v}_{\delta B} = -\frac{\mathbf{b} \times \nabla v_\parallel A_\parallel}{B}, \tag{2.14}$$

where $A_\parallel$ is component of the perturbed vector potential parallel to the equilibrium magnetic field.

2.2 Magnetic confinement in the tokamak

This section introduces the magnetic confinement of a plasma in a toroidal device called the *tokamak* (see Fig. 2.1 for a sketch). The basic properties and geometric parameters are discussed.
A tokamak device applies strong magnetic fields to confine the hot plasma. As outlined in Sec. 2.1 a magnetic field constraints the perpendicular particle motion to a superposition of the gyromotion and slow perpendicular gyrocenter drifts. The Larmor radius is typically much smaller than the device size, such that particle and energy loss is associated to the slow gyrocenter drifts.
To avoid particle losses at the end of field lines, the magnetic field of a tokamak has a torus shape. In such a geometry the magnetic field lines lie on closed nested surfaces with constant magnetic flux, so-called *flux-surfaces*.
In order to balance the plasma pressure and for stability reasons [3, 5] the magnetic field must have both a toroidal and a poloidal component. The toroidal component of the magnetic field is the principal component and is imposed by external coils. A toroidal plasma current, either driven by changing the magnetic field of a central solenoid or self-consistently by the plasma through the bootstrap effect [6, 7, 8], provides the poloidal component. The poloidal component of the confining magnetic field is typically ten times smaller than the toroidal one [3] and the superposition results in field lines following helical trajectories. A schematic illustration of this configuration is shown in Fig. 2.1. A parameter that characterizes the quality of confinement is the so-called *plasma beta* [3]

$$\beta = \frac{nT}{\mu_0 B^2/2}, \tag{2.15}$$

which compares the thermal plasma pressure nT (n and T are the plasma density and temperature, respectively) with the ambient magnetic field pressure $\mu_0 B^2/2$ (μ_0 and B are the permeability of free space and the magnetic field strength, respectively). In a tokamak reactor the plasma beta is typically of the order of a few percent.[6]

[6]For an ITER core deuterium plasma (see appendix E) one finds $\beta \approx 0.019$.

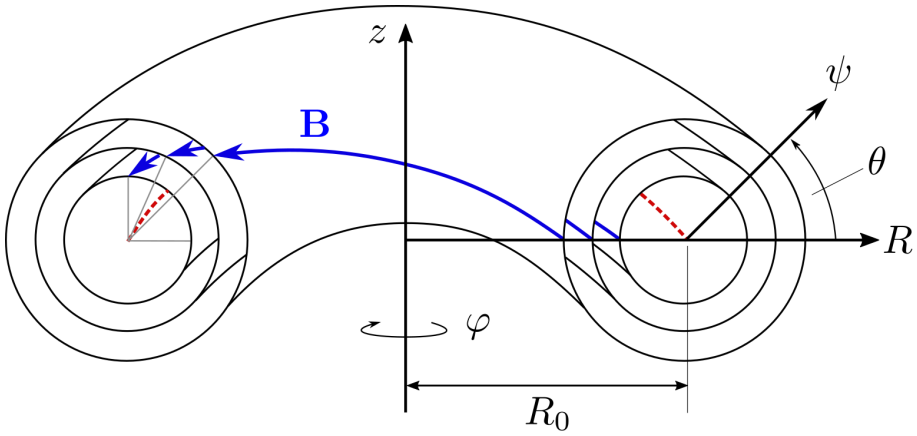

Figure 2.1: Sketch of circular shaped nested flux-surfaces of a tokamak in toroidal coordinates (ψ, φ, θ) and reference cylindrical coordinates $(z, -\varphi, R)$. Helical magnetic field lines are depicted by blue arrows and the magnetic axis is shown by the red dashed line.

In theoretical studies of the plasma core, as presented in this thesis, the flux-surfaces are often considered to be circular concentric.[7] The coordinate ψ, that labels the flux-surfaces, then can be chosen the minor radial coordinate r. Below, geometric parameters characterizing such a toroidal magnetic equilibrium are introduced.
It is useful to define the *inverse aspect ratio* of a flux-surface by [3]

$$\epsilon = \frac{r}{R_0}, \tag{2.16}$$

where R_0 is the major radius of the tokamak.
Additionally, the *safety-factor* q of a field line denotes the number of toroidal turns a field line executes per poloidal turn. It is defined by [3]

$$q = \frac{1}{2\pi} \oint \frac{1}{R} \frac{B_\varphi}{B_\theta} \, \mathrm{d}s, \tag{2.17}$$

where B_φ and B_θ specifies the toroidal and poloidal field, respectively, and the integral is carried out over one poloidal turn around the flux-surface. The safety factor plays a significant role in determining the stability against magneto hydrodynamic instabilities.
While on a fixed flux-surface each field line has the same safety factor, its value changes with the minor radial coordinate. The radial variation of the safety factor is quantified by the *magnetic shear* [5]

$$\hat{s} = \frac{r}{q} \frac{\partial q}{\partial r}. \tag{2.18}$$

[7] This approximation is valid for flux-surfaces with small minor radial coordinate r compared to the major radius R_0 and for small β.

These geometric parameters are used in Sec. 4.2.4 to define the geometry of the fluxtube simulation domain.
The magnitude of magnetic field in a tokamak decreases with the coordinate R away from the central axis of symmetry (z-axis in Fig. 2.1). For circular concentric flux-surfaces the magnitude $B = B_0 R_0/R$, with B_0 being the strength of the magnetic field on the magnetic axis, obeys [9]

$$B = \frac{B_0}{1 + \epsilon \cos\theta}, \tag{2.19}$$

where $R = R_0 + r\cos\theta$ and the inverse aspect ratio ϵ [Eq. (2.16)] have been used. On a given flux-surface the inboard side ($\theta = \pm\pi$) is the location where the magnitude of the magnetic field is largest. It is also referred to as the *high field side*. Conversely, the outboard side ($\theta = 0$) is the location with the smallest magnetic field and is referred to as the *low field side*.
The inhomogeneous magnetic field of a tokamak and the conservation of the magnetic moment μ [Eq. (2.7)] as well as the kinetic energy $(m_{\mathrm{sp}}/2)(v_\parallel^2 + v_\perp^2)$ give rise to particle trapping on the outboard side. When a particle moves along a field line from the low field side towards the high field side, its perpendicular velocity increases while its parallel velocity decreases due to the above conservation properties. Physically, it is the mirror force introduced in Sec. 2.1 that causes the deceleration parallel to the magnetic field.
If the parallel velocity of a particle is small enough, it is decelerated to zero before the particle reaches the high field side. This leads to a bounce motion of certain particles, so-called *trapped particles*, on the outboard side of the tokamak. Particles that reach and pass the high field side, in turn, are called *passing particles*.
The trapping condition can be derived from the conservation properties and reads

$$\mu B(\theta = \pm\pi) = \frac{1}{2} m_{\mathrm{sp}} v_{\parallel,L}^2 + \mu B(\theta = 0), \tag{2.20}$$

where $B(\theta = \pm\pi)$ and $B(\theta = 0)$ denote the magnetic field on the high and low field side, respectively. In the case of circular concentric flux-surfaces the trapping condition can be re-formulated using the expression (2.19). For particles to be trapped the velocities have to satisfy

$$v_\perp^2 > \left(\frac{1-\epsilon}{2\epsilon}\right) v_\parallel^2. \tag{2.21}$$

Having established charged particle motion and the tokamak, the next sections will focus on collective phenomena in a tokamak plasma such as microturbulence and zonal flows.

2.3 Microturbulence caused by the ion temperature gradient driven instability

The electromagnetic forces acting in a tokamak plasma give rise to a variety of collective phenomena. One example are *microinstabilities*, i. e., instabilities on spatial scales of the Larmor radius and frequencies much smaller than the cyclotron frequency, that are driven by density and temperature gradients present in tokamak devices. Turbulence caused by microinstabilities is considered the main reason for the loss of particles, energy and momentum from a tokamak plasma [10, 11, 12]. As such, microturbulence is the main reason for the degradation of confinement and, thereby, limits the confinement time.
Among multiple microinstabilities, the ion temperature gradient (ITG) driven instability [13, 14, 15] is assumed to dominate in the core of tokamak reactors. Turbulence caused by the ITG driven instability is subject of this thesis and, therefore, this section briefly (and qualitatively) reviews the underlying mechanisms.

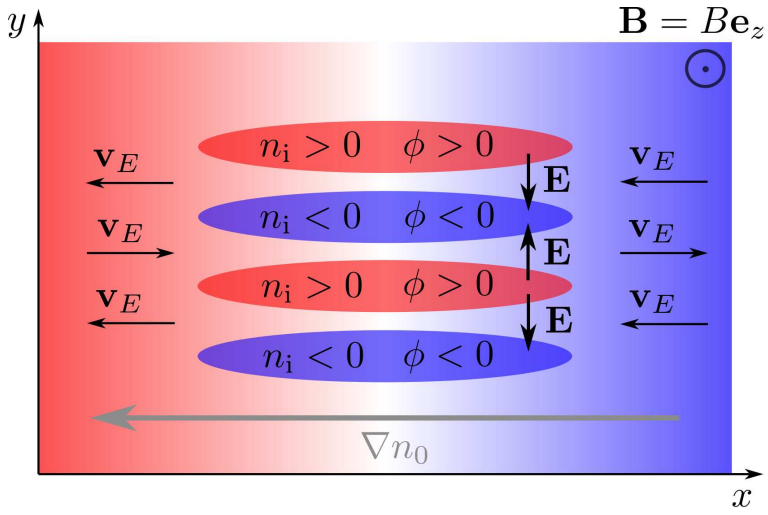

Figure 2.2: Sketch of a drift wave: Due to the adiabatic electron response [Eq. (2.26)] an ion density perturbation ($n_\mathrm{i} \gtrless 0$) causes an in phase potential perturbation ($\phi \gtrless 0$). The connected electric field $\mathbf{E}$ (vertical black arrows) results in an $E \times B$-drift $\mathbf{v}_E$ (horizontal black arrows) that is aligned with the density gradient ∇n_0 (horizontal gray arrow). The $E \times B$-drift brings denser plasma into regions above the positive density perturbation $n_\mathrm{i} > 0$ and less dense plasma into regions above the negative density perturbations $n_\mathrm{i} < 0$, causing the drift wave to propagate in the positive y-direction.

2.3.1 The drift wave

The ITG driven instability is of the drift wave type and it is convenient to introduces the basic mechanisms behind drift waves first. For a more detailed discussion the reader is referred to Ref. [12].
Drift waves are low frequency waves, since they evolve on time scales much larger than the cyclotron frequency $\omega \ll \omega_{c,\mathrm{sp}}$. This property motivates the consideration of the slow guiding-center drifts (see Sec. 2.1.3). A simple description of a drift wave can be obtained within an ion fluid model with the adiabatic electron approximation [16, 17] as detailed out below.
In what follows a small test volume is considered with the radial coordinate x, the binormal coordinate y, the parallel coordinate z and a homogeneous magnetic field $\mathbf{B} = B\hat{\mathbf{e}}_z$ (see Fig. 2.2). The plasma shall be non-uniform in the radial direction and a radial density gradient $\nabla n_0 = -n_0\hat{\mathbf{e}}_x/L_n$ is assumed, with the density gradient length L_n and the equilibrium density n_0. A density perturbation with wave vector $\mathbf{k} = k_y\hat{\mathbf{e}}_y$ is assumed (cells in Fig. 2.2) and is written in the plane wave form

$$n_\mathrm{i} \propto \exp[\mathrm{i}(k_y y - \omega t)], \tag{2.22}$$

with $n_i \ll n_0$. Note that $\hat{\mathbf{e}}_x$, $\hat{\mathbf{e}}_y$ and $\hat{\mathbf{e}}_z$ denote unit vectors in the three spatial direction. Furthermore, $k_y\rho_{\mathrm{th,i}} \ll 1$ is assumed, to be able to neglect finite Larmor radius effects (see Sec. 3.5 for a description of finite Larmor radius effects).
Due to their small mass (compared to ions) electrons move rapidly along the field lines and thereby re-establish quasi-neutrality $n_\mathrm{i} = n_\mathrm{e}$. As a result the electron pressure is modified and then reads

$$p_\mathrm{e} = (n_{0,\mathrm{e}} + n_\mathrm{e})T_{0,\mathrm{e}}, \tag{2.23}$$

where the background electron temperature $T_{0,\mathrm{e}}$ is assumed to be uniform.
With the simplifying assumptions of an isotropic plasma and neglecting friction the parallel electron force balance may be written as

$$m_\mathrm{e}(n_{0,\mathrm{e}} + n_\mathrm{e})\frac{\mathrm{d}v_{\parallel,\mathrm{e}}}{\mathrm{d}t} = -\frac{\partial p_\mathrm{e}}{\partial z} + e(n_{0,\mathrm{e}} + n_\mathrm{e})\frac{\partial \phi}{\partial z}. \tag{2.24}$$

Since electrons respond quasi-instantaneously, the inertia term on the left-hand side can be neglected. As a consequence, the electron pressure needs to be balanced by a parallel electric field. Neglecting second order terms in the perturbations, the force balance is

$$T_{0,\mathrm{e}}\frac{\partial n_\mathrm{e}}{\partial z} = e n_{0,\mathrm{e}}\frac{\partial \phi}{\partial z}. \tag{2.25}$$

The above equation can be integrated to obtain the so-called adiabatic electron response

$$\frac{n_\mathrm{e}}{n_{0,\mathrm{e}}} = \frac{e\phi}{T_{0,\mathrm{e}}}. \tag{2.26}$$

According to the adiabatic electron response an ion density perturbation causes an in phase potential perturbation due to quasi-neutrality and electrons establishing parallel force balance.
The ion density perturbation (2.22), hence, results in an $E \times B$-drift of the ions given by $\mathbf{v}_E = -(\mathrm{i}k_y\phi/B)\hat{\mathbf{e}}_x$ (black horizontal arrows in Fig. 2.2). The evolution of the perturbed ion density due to this $E \times B$-drift is described by the linearized ion continuity equation

$$\frac{\partial n_\mathrm{i}}{\partial t} = -\mathbf{v}_E \cdot \nabla n_{0,\mathrm{i}}. \tag{2.27}$$

Noting that the direction of the $E \times B$-drift is parallel to the background density gradient and using quasi-neutrality together with the adiabatic electron response one obtains the dispersion relation of the drift wave

$$\omega = \frac{k_y T_{0,\mathrm{e}}}{eBL_n}. \tag{2.28}$$

The frequency of the drift wave is purely real, such that the perturbation propagates in the y-direction with the velocity $v_\mathrm{ph} = \omega/k_y$, but does not grow or decay in time.[8] The phase velocity is equivalent to the so-called electron diamagnetic velocity and the drift wave, therefore, propagates in the electron diamagnetic direction (positive y-direction in Fig. 2.2). A conceptual sketch of the drift wave mechanism is depicted in Fig. 2.2.
In the toroidal geometry of a tokamak the ∇B- and curvature drifts cause a coupling between temperature and density perturbations. The presence of an (sufficiently large) ion temperature gradient can then lead to the ITG driven instability, which is discussed in the next section.

2.3.2 The toroidal ion temperature gradient driven instability

The toroidal ITG driven instability occurs in the presence of a sufficiently large ion temperature gradient and is driven by the so-called bad curvature on the outboard side of a tokamak (where the gradient of the magnetic field ∇B and the temperature ∇T_0 are aligned). In this section the underlying mechanism of this instability is described on the basis of Refs. [18, 17, 16] and Fig. 2.3. The electrostatic limit is considered, in that perturbations in the electrostatic potential are included, while magnetic field perturbations are neglected (this is equivalent to the limit $\beta \to 0$, see Sec. 4.3.2).
A perturbation in the ion temperature T_i with $k_x \ll k_y$ is considered (red and blue

[8] The classical drift wave is driven unstable by collisions and is, therefore, more important in the edge of a tokamak device.

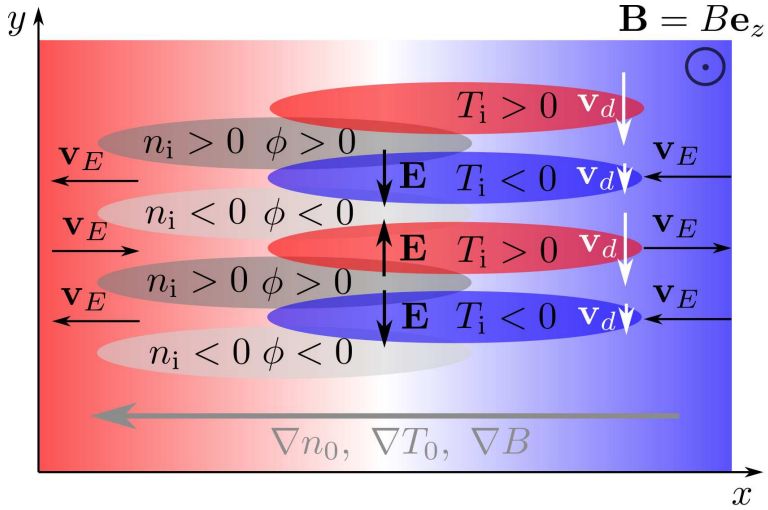

Figure 2.3: Sketch of the toroidal ion temperature gradient driven instability on the outboard low field side of the tokamak: An ion temperature perturbation ($T_\mathrm{i} \gtrless 0$, blue and red cells) causes a modulation of the curvature and ∇B-drift $\mathbf{v}_d$ (white arrows). This originates in a compression of the plasma ($n_\mathrm{i} \gtrless 0$, gray cells) that relates to a potential perturbation ($\phi \gtrless 0$) due to the adiabatic electron response. The resulting $E \times B$-drift $\mathbf{v}_E$ (horizontal black arrows) is aligned with the temperature gradient ∇T_0 (horizontal gray arrow) and brings hot plasma into hot regions of the perturbation ($n_\mathrm{i} > 0$, red cells) and cooler plasma into cold regions of the perturbation ($n_\mathrm{i} < 0$, blue cells), reinforcing the process.

cells in Fig. 2.3), which shall be located on the outboard low field side. Since the combination of the curvature and ∇B-drift is velocity dependent $\mathbf{v}_d \propto (v_\parallel^2 + v_\perp^2/2)$, its magnitude is modulated across the temperature perturbation (white arrows in Fig. 2.3). This pattern in the drift motion has a finite divergence and, therefore, leads to a compression of the plasma. The resulting density perturbation (gray cells in Fig. 2.3) is $\pi/2$ out of phase compared with the temperature perturbation. Assuming an adiabatic electron response [Eq. (2.26)], an in phase potential perturbation relates to the density perturbation. The resulting $E \times B$-drift (horizontal black arrows in Fig. 2.3) brings cool plasma into regions with negative temperature perturbation ($T_\mathrm{i} < 0$) and hot plasma into regions with positive temperature perturbation ($T_\mathrm{i} > 0$), thereby reinforcing the temperature perturbation. This final step closes a feedback loop and, hence, causes the perturbation to grow in time.

While on the outboard side of the tokamak this mechanism causes the perturbation to grow, on the inboard side the opposing ∇B and ∇T_0 results in the perturbation to decay. The former region is, therefore, said to have bad curvature and the instability is localized there. In contrast to the drift wave, the ITG driven mode propagates in the ion diamagnetic direction (negative y-direction in

Fig. 2.3), since the ∇B-drift dominates the compression [16, 17].
Linear studies within fluid models (similar to Sec. 2.3.1) or more sophisticated gyrokinetic models (chapter 3) find a critical temperature gradient above which instability occurs (see left panel of Fig. 2.4). In this thesis this critical threshold is referred to as *linear threshold*. Furthermore, compliant with its classification as microinstability, the growth rate of the ITG driven instability typically peaks at perpendicular wave vectors of $k_\perp \rho_{\mathrm{th,i}} \sim 0.4 - 0.5$ (see right panel of Fig. 2.4). For $k_\perp \rho_{\mathrm{th,i}} \gtrsim 1$ so-called finite (ion) Larmor radius effects (see also Sec. 3.5) reduce the growth rate of the ITG driven instability and other instabilities like the trapped electron mode may occur.
As discussed above, ITG driven Eigenmodes are typically localized at the low field side of the tokamak. The high mobility of passing electrons, however, leads to an extension of the mode structure along the field lines covering multiple poloidal turns. This phenomenon is known as *giant tails* [19] and is the basis for the self-interaction mechanism [1], which is investigated in greater detail in chapter 8.
With increasing plasma β the Eigenmodes of the ITG driven instability acquire an electromagnetic character through the coupling to shear Alfvén waves [20]. Beside the electrostatic potential, Eigenmodes then exhibit an perturbed magnetic field component as well. In addition, the coupling to shear Alfvén waves causes the growth rate to decrease with β [20, 21]. Electromagnetic microturbulence is subject of chapter 7.

Beside the ITG driven instability, the trapped electron mode (TEM) is considered to contribute to the turbulent transport in a tokamak plasma. In the cases considered in this thesis, however, the TEM occurs as a subdominant instability (see for example the right panel of Fig. 2.3) and is, therefore, of minor interest. For details about the TEM the reader is referred to Refs. [17, 16].
When the plasma is unstable against microinstabilities a turbulent state may arise, hereafter referred to as *microturbulence*. Central to the development of a saturated turbulent state is the nonlinear interaction of the Eigenmodes driven by microinstabilities (nonlinear processes responsible for saturation of microturbulence are studied in greater detail within a nonlinear transfer analysis in chapter 8), which, in ITG driven microturbulence, is mainly caused by turbulence driven zonal flows [22] (see Sec. 2.4 for an introduction to zonal flows). The resulting perturbations, composed of Eigenmode remnants and nonlinearly generated vortices (see Fig. 6.6 of chapter 6), cause turbulent transport of particles, energy and momentum through advection by the $E \times B$-drift for example. Moreover, close to marginality microturbulence and zonal flows often self-organize into patterns [23, 24, 25]. Turbulent transport is then mediated by avalanches, i. e., radial ballistically propagating events, which are closely correlated with zonal flow shear zones [26, 27].

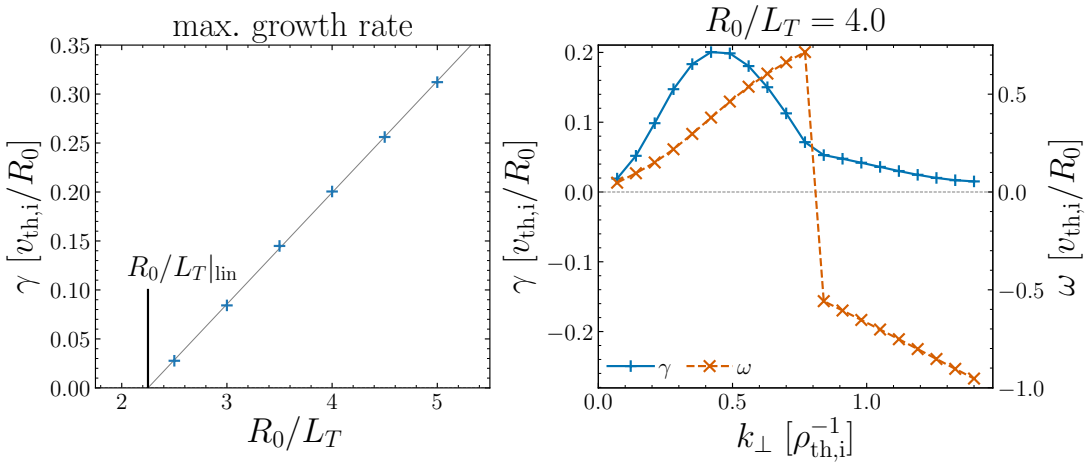

Figure 2.4: Linear gyrokinetic study of the ITG driven instability considering the electrostatic limit, circular concentric flux-surfaces, CYCLONE base case parameters and electron dynamics. Left: Growth rate γ (blue +-symbols) of the dominantly growing ITG driven Eigenmode as function of the normalized inverse background temperature gradient length R_0/L_T as well as a linear fit (gray solid line). Above a linear threshold $R_0/L_T|_{\mathrm{lin}} \approx 2.25$ the ITG driven instability is unstable. Right: Growth rate γ (blue +-symbols) and frequency ω (orange $\times$-symbols) as function of the perpendicular wave vector $k_\perp$ for the same plasma parameters but fixed $R_0/L_T = 4.0$. The ITG driven instability dominates in the regime $0 < k_\perp \rho_{\mathrm{th,i}} \lesssim 0.8$, while the TEM dominates at $k_\perp \rho_{\mathrm{th,i}} > 0.8$ in this case.

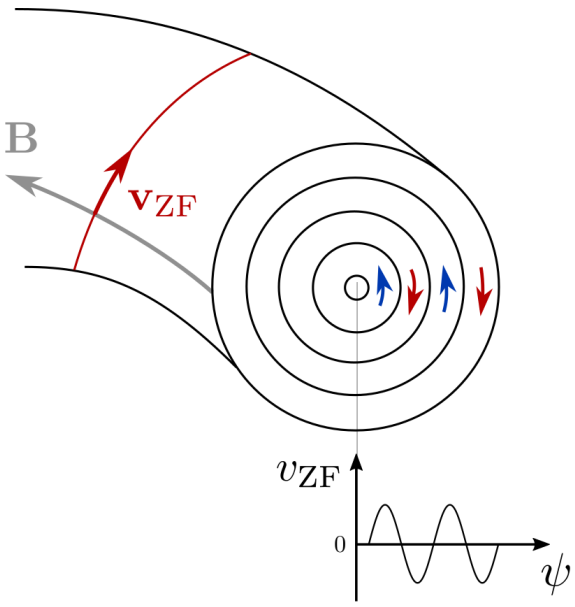

Figure 2.5: Illustration of zonal flows: Zonal flows are $E \times B$-flows connected to the part of the electrostatic potential that is constant on flux-surfaces. The related plasma motion $\mathbf{v}_{\mathrm{ZF}}$ is tangential to flux-surfaces. The rotation velocity v_{ZF} of zonal flows exhibits an alternating pattern with the flux-surface label ψ and velocity shear is, therefore, inherent to such flows.

2.4 Zonal flows

In the tokamak plasma context zonal flows are referred to as $E \times B$-flows [Eq. (2.8)] connected to the electrostatic potential that is constant on flux-surfaces [28]. The latter is also denoted by the zonal potential $\langle\phi\rangle$; a nomenclature that is adopted in this thesis. Since the zonal potential varies across flux-surfaces only, zonal flows are tangential to flux-surfaces as illustrated in Fig. 2.5. As a result, zonal flows do not contribute to the turbulent transport across flux-surfaces usually connected to $E \times B$-motion. This property renders zonal flows harmless in view of confinement degradation.
In addition, zonal flows are $E \times B$-flows connected with a radially alternating zonal potential. Therefore, their rotation velocity v_{ZF} alternates with the flux-surface label ψ as depicted schematically in Fig. 2.5. This differential rotation necessarily introduces a velocity shear, i. e., a radial variation of the zonal flow velocity, and therefore allows for the shear deformation of turbulent structures. Zonal flow shearing is considered to play a significant role in the saturation and even suppression of turbulence [29]. In this sense, zonal flows are considered beneficial for confinement.
When the radial scale of the zonal potential is large compared to the Larmor radius, the zonal flow velocity can be defined by

$$\mathbf{v}_{\mathrm{ZF}} = \frac{\mathbf{b} \times \nabla\langle\phi\rangle}{B}. \tag{2.29}$$

The inhomogeneous magnetic field of a tokamak causes a finite divergence $\nabla \cdot \mathbf{v}_{\mathrm{ZF}} \neq 0$. On time scales larger than the inverse sound frequency a flow parallel to the magnetic field $\mathbf{u}_{\parallel}$ emerges to establish incompressibility $\nabla \cdot (\mathbf{v}_{\mathrm{ZF}} + \mathbf{u}_{\parallel}) = 0$ [30]. In addition, trapped particles undergo a toroidal precession [31] coupling the zonal flow to a parallel flow. As a result, zonal flows in a tokamak plasma are always accompanied by secondary flows parallel to the magnetic field.

2.4.1 Generation of zonal flows

Zonal flows are linearly stable, but are considered to be driven nonlinearly through turbulent Reynolds stresses [32]. In drift wave type turbulence zonal flow generation is based on modulational [33, 34, 35, 36, 37, 33] or equivalently secondary instabilities [15, 38, 39, 40, 41]. This section briefly reviews the basic zonal flow generation mechanism within the modified Hasegawa Mima equation (mHME) [42, 43], which emerges as a 2D limit of the gyrokinetic equation in the cold ion and adiabatic electron approximation [44, 43, 10].
The mHME is one of the simplest two-dimensional fluid models allowing for electrostatic drift wave turbulence and nonlinear dynamics associated with the $E \times B$-nonlinearity. It describes the plasma dynamics in the doubly periodic

x-y-plane (x and y are the radial and bi-normal direction respectively) perpendicular to a static and homogeneous magnetic field $\mathbf{B}$ and in the presence of an equilibrium density gradient. Its dimensionless form reads [39, 40]

$$\frac{\mathrm{d}}{\mathrm{d}t}\left(\phi - \langle\phi\rangle - \nabla^2\phi - x\right) = 0, \tag{2.30}$$

which describes the conservation of the generalized potential vorticity $\phi - \langle\phi\rangle - \nabla^2\phi - x$. Here, the electrostatic potential averaged over the y-direction

$$\langle\phi\rangle(x) = \frac{1}{L_y}\int_{-L_y/2}^{L_y/2} \mathrm{d}y\ \phi \tag{2.31}$$

(L_y is the bi-normal extend of the considered domain) constitutes the two-dimensional equivalent of the flux-surface averaged or zonal potential in a tokamak. It is then customary to define the turbulent potential by

$$\tilde{\phi} = \phi - \langle\phi\rangle. \tag{2.32}$$

The total time derivative is defined as

$$\frac{\mathrm{d}}{\mathrm{d}t} = \frac{\partial}{\partial t} + [\phi, \ldots], \tag{2.33}$$

with the Possion bracket given by

$$[G, H] = \frac{\partial G}{\partial x}\frac{\partial H}{\partial y} - \frac{\partial G}{\partial y}\frac{\partial H}{\partial x}. \tag{2.34}$$

Eq. (2.33) represents the advective derivative with the $E \times B$-velocity

$$\mathbf{v}_E = (v_{Ex}, v_{Ey}) = \left(-\frac{\partial\phi}{\partial y},\ \frac{\partial\phi}{\partial x}\right) \tag{2.35}$$

being the advecting velocity.
An evolution equation for the zonal flow $v_{\mathrm{ZF}} = \partial_x\langle\phi\rangle$ can be obtained by averaging Eq. (2.30) over the $y-$direction and taking the derivative with respect to the radial coordinate. After some algebra one obtains

$$\frac{\partial v_{\mathrm{ZF}}}{\partial t} = \frac{\partial}{\partial x}\left\langle\frac{\partial\tilde{\phi}}{\partial x}\frac{\partial\tilde{\phi}}{\partial y}\right\rangle = -\frac{\partial\Pi}{\partial x}, \tag{2.36}$$

where $\Pi \equiv \langle\tilde{v}_{Ex}\tilde{v}_{Ey}\rangle$ is the Reynolds stress.

Although the instantaneous value of the Reynolds stress may exhibit strong positive and negative samples during the turbulent state, without a symmetry breaking mechanism the ensemble averaged stress is zero. A finite zonal flow shear induced tilt of turbulent structures, in turn, breaks the symmetry and causes a

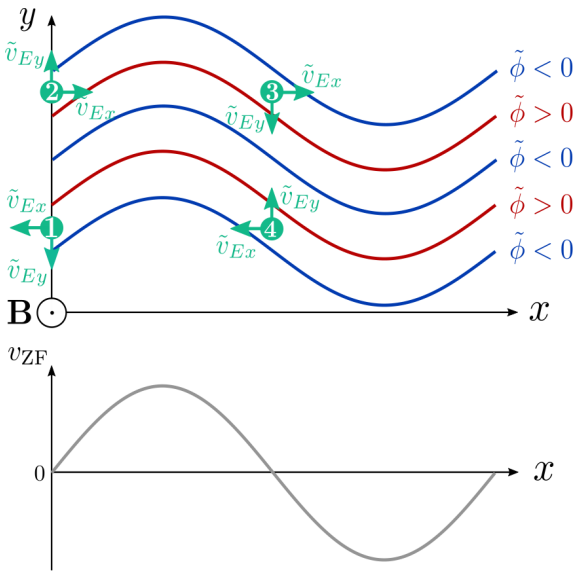

Figure 2.6: Zonal flow induced symmetry breaking: The radial velocity shear connect to the radially varying zonal flow v_{ZF} (bottom) causes a deformation of turbulent structures as illustrated by the radial modulation of drift wave iso-contour lines in the x-y-plane perpendicular to the ambient magnetic field $\mathbf{B}$ (top). Due to the broken symmetry the radial transport of bi-normal momentum $\tilde{v}_{Ex}\tilde{v}_{Ey}$ exhibits positive values at ① as well as ② and negative values at ③ as well as ④.

finite averaged Reynolds stress [31, 45]. This process is depicted schematically in Fig. 2.6 on the basis of a zonal flow modulated drift wave. Due to the broken symmetry the radial transport of bi-normal momentum $\tilde{v}_{Ex}\tilde{v}_{Ey}$ exhibits positive values at positions ① as well as ② and negative values at ③ as well as ④. The resulting divergence of the Reynolds stress acts to reinforce the zonal flow. This process is at the basis of the modulational instability.
A more quantitative, albeit greatly simplified, description of the modulational instability can be obtained within a four wave truncation [34, 36, 37, 46, 40] of the modes involved in the underlying nonlinear processes. The electrostatic potential is decomposed into Fourier modes

$$\phi(x,y,t) = \sum_{\mathbf{k}} \hat{\phi}_{\mathbf{k}}(t) \times \exp[\mathrm{i}(k_x x + k_y y)] \tag{2.37}$$

with the perpendicular wave vector $\mathbf{k} = (k_x, k_y)$, which allows to express the mHME in Fourier space

$$(\alpha_{\mathbf{k}} + k^2)\dot{\phi}_{\mathbf{k}} + ik_y\phi_{\mathbf{k}} = \sum_{\mathbf{k}_1+\mathbf{k}_2=\mathbf{k}} [\hat{\mathbf{z}} \cdot (\mathbf{k}_1 \times \mathbf{k}_2)(\beta_{\mathbf{k}} + k_2^2)]\phi_{\mathbf{k}_1}\phi_{\mathbf{k}_2}, \tag{2.38}$$

with the dot denoting a partial derivative with respect to time. The coefficients $\alpha_{\mathbf{k}}$ and $\beta_{\mathbf{k}}$ are connected to the adiabatic electron response [43] and are defined by

$$\alpha_{\mathbf{k}} \equiv \begin{cases} 0, & \text{if } k_y = 0 \\ 1, & \text{otherwise} \end{cases} \tag{2.39}$$

and

$$\beta_{\mathbf{k}} \equiv \begin{cases} 0, & \text{if } k_{2y} = 0 \\ 1, & \text{otherwise.} \end{cases} \tag{2.40}$$

The right-hand side of Eq. (2.38) describes three wave interactions mediated by the $E \times B$-nonlinearity. The concept of three wave or triad interactions, satisfying the wave vector addition rule $\mathbf{k}_1 + \mathbf{k}_2 = \mathbf{k}$, is generic to quadratic nonlinearities and applies analogously to the gyrokinetic equation presented in Sec. 3.4. Therefore, many of the concepts discussed in this section apply similarly to the nonlinear dynamics emerging from the gyrokinetic model (and will occur similarly in chapter 8).
The four-wave truncation investigates the evolution of a turbulent pump mode $\hat{\phi}_q$ with $\mathbf{k} = (0, q)$ and a zonal mode $\hat{\phi}_0$ with $\mathbf{k} = (p, 0)$ coupled nonlinearly through sideband modes $\hat{\phi}_\pm$ with $\mathbf{k} = (p, \pm q)$. Thereby, the pump drift wave is considered a constant drive and the ordering $\hat{\phi}_q \sim \mathcal{O}(1) \gg \hat{\phi}_0, \hat{\phi}_+, \hat{\phi}_-$ is adopted. The coupled set of equations describing the time evolution of the considered modes can be deduced from Eq. (2.38) and is given by [40]

$$\dot{\hat{\phi}}_q + \mathrm{i}\Omega_q \hat{\phi}_q = 0 \tag{2.41}$$

$$\dot{\hat{\phi}}_0 = -qp(\hat{\phi}_q \hat{\phi}_- - \hat{\phi}_q^* \hat{\phi}_+) \tag{2.42}$$

$$\dot{\hat{\phi}}_+ + \mathrm{i}\Omega_+ \hat{\phi}_+ = \frac{qp(1+q^2-p^2)}{1+q^2+p^2} \hat{\phi}_q \hat{\phi}_0 \tag{2.43}$$

$$\dot{\hat{\phi}}_- + \mathrm{i}\Omega_- \hat{\phi}_+ = -\frac{qp(1+q^2-p^2)}{1+q^2+p^2} \hat{\phi}_q^* \hat{\phi}_0. \tag{2.44}$$

The above set of equations contains the drift frequencies of the pump wave and the sideband modes defined by $\Omega_q = q/(1+q^2)$ and $\Omega_\pm = \pm q/(1+q^2+p^2)$, respectively.
From Eq. (2.41)-(2.44) a third order differential equation for the time evolution of $\hat{\phi}_0$ can be obtained. The Ansatz $\hat{\phi}_0 = A_0 \exp(\mathrm{i}\gamma_0 t)$ then yields the instability growth rate [40]

$$\gamma_0 = \sqrt{\frac{2q^2p^2(1+q^2-p^2)}{1+q^2+p^2} |\hat{\phi}_q|^2 - \Delta\Omega^2}, \tag{2.45}$$

with the frequency mismatch $\Delta\Omega = \Omega_q - \Omega_+$. In the high amplitude limit $|\hat{\phi}_q|^2 \gg 1$ zonal growth is limited to wave vectors $0 < p^2 < 1 + q^2$. At small pump wave amplitudes the frequency mismatch $\Delta\Omega$ between the interacting pump and sideband modes reduce the efficiency of the nonlinear interaction.
The mechanism underlying the modulational instability may be understood as follows: The velocity shear of a seed zonal flow modulates the pump drift wave as depicted schematically in Fig. 2.6. This modulation is equivalent to the nonlinear generation of sideband modes through the three wave interaction of the pump wave and the zonal flow as described by Eqs. (2.43) and (2.44). The radial modulation of the pump wave causes a Reynolds stress that acts to increase the seed zonal flow closing the feedback loop. Note that the Reynolds stress is given by the products $qp\hat{\phi}_q\hat{\phi}_-$ and $qp\hat{\phi}_q^*\hat{\phi}_+$ on the right-hand side of Eq. (2.42). As a

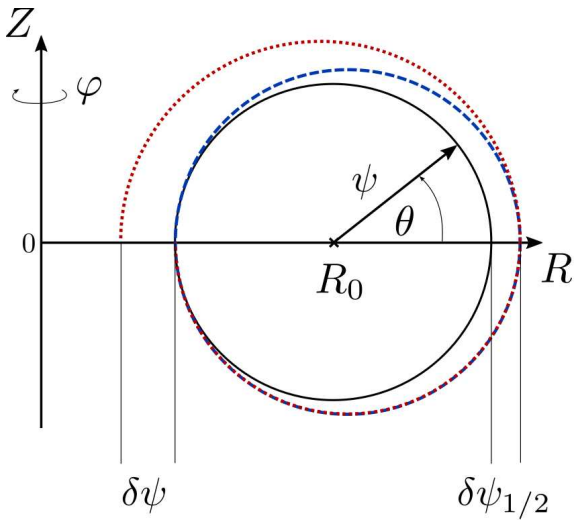

Figure 2.7: Projection of perturbed magnetic field lines followed for one poloidal turn onto the poloidal plane: A flux-surface preserving field line (blue dashed) returns to its original flux-surface (black solid circle) after one poloidal turn, while a flux-surface breaking field line (red dotted) exhibit a radial displacement $\delta\psi$. The latter causes magnetic stochasticity.

consequence, the modulation instability directly relates to the shear deformation of turbulent structures.
The physics behind the generation of zonal flows introduced above is greatly simplified and modifications due to pressure fluctuations [47], toroidal geometry [34], electromagnetic effects [48] or energetic particles [49, 50] enter a more elaborated description. Furthermore, in chapter 7 it is demonstrated that in toroidal geometry zonal flows can be driven through the coupling to parallel flow sidebands.

2.4.2 Damping of zonal flows

Zonal flows may be subject to various damping mechanism such as collisions [51, 52, 53], tertiary instabilities [54], turbulent parallel viscous stresses [30] and toroidal momentum transport [55], geodesic transfer [56, 45] and radial charge loss associated with magnetic stochasticity [57, 58]. Saturation of zonal flows then occurs, when the driving Reynolds stress is balanced by the combined effect of damping mechanisms.
Due to its relevance for this thesis (chapter 7) the damping of zonal flows through magnetic stochasticity is outlined below. Magnetic perturbations associated with microturbulence can destroy the intactness of magnetic flux-surfaces [57]. More in detail, perturbed magnetic field lines that depart from their original flux-surface after one poloidal turn allow for a radial displacement of particles streaming along such field lines (see Fig. 2.7). This radial transport process is also referred to as *magnetic flutter*. The radial electric field connected to zonal flows may accelerate electrons along such flux-surface breaking field lines, causing a radial charge current density that reduces the radial electric field and, thereby, damps the zonal flow.
Since electrons respond much faster along (perturbed) field lines than ions an

electrons-only calculation is invoked [58], while the ions are assumed at rest. The electron response parallel to the perturbed magnetic field $\delta\mathbf{B}$ and in the presence of a radial electric field $E_\psi = -\nabla\langle\phi\rangle$ can be estimated by

$$m_\mathrm{e}\frac{\Delta v_\parallel}{\Delta t} \sim e\frac{\delta\mathbf{B}}{B_0}\cdot\nabla\langle\phi\rangle = -e\frac{\delta B_\psi}{B_0}E_\psi. \tag{2.46}$$

Provided the perturbed field line is flux-surface breaking, the velocity increment $\Delta v_\parallel$ resulting from the acceleration by the radial electric field can be estimated by assuming that Δt is determined by the electron thermal velocity $v_\mathrm{th,e}$ and the length of the perturbed field line l_m[9], and reads

$$\Delta v_\parallel = -\frac{e l_m}{v_\mathrm{th,e} m_\mathrm{e}}\frac{\delta B_\psi}{B_0}E_\psi. \tag{2.47}$$

Since ions are assumed to rest, this electron motion leads to a radial current density

$$\delta J_\psi = -e n_\mathrm{e}\Delta v_\parallel\left(\frac{\delta B_\psi}{B_0}\right) = \frac{e^2 n_\mathrm{e} l_m}{v_\mathrm{th,e} m_\mathrm{e}}\left(\frac{\delta B_\psi}{B_0}\right)^2 E_\psi, \tag{2.48}$$

and, considering surface charge continuity and Poisson equation [58], to an associated decay of the radial electric field $\partial_t E_\psi \propto -\delta J_\psi$. In the case of flux-surface preserving magnetic perturbations the acceleration of electrons during the first poloidal half-turn is canceled by a deceleration during the second half-turn, as δB_ψ changes sign, and zonal flow damping does not occur.
The above discussed physics picture of zonal flow damping due to magnetic stochasticity is greatly simplified. More sophisticated studies [58, 59, 60], taking into account the full kinetic response of zonal flows to magnetic perturbations, however, confirm zonal flow damping due to flux-surface breaking magnetic perturbations.
Under certain circumstances the damping associated with magnetic stochasticity may inhibiting the development of zonal flows. The consequence are turbulence runaways [21, 61, 60], i. e., a transient growth of turbulence to indeterminate levels, since zonal flows as the main regulation mechanism of microturbulence driven by the ITG [22] are disabled. Turbulence runaways and the influence of magnetic perturbations on zonal flows are subject of chapter 7.

2.4.3 Influence of zonal flows on microturbulence

Zonal flows have a stabilizing effect on turbulence driven by microinstabilities [62, 29]. They play a dominant role in the nonlinear saturation of ion temperature gradient driven turbulence [22, 63, 64, 65, 66] and may even suppress

[9] An estimate of the length of a perturbed field line followed for one poloidal turn may be provided by the connection length $l_m \sim qR$.

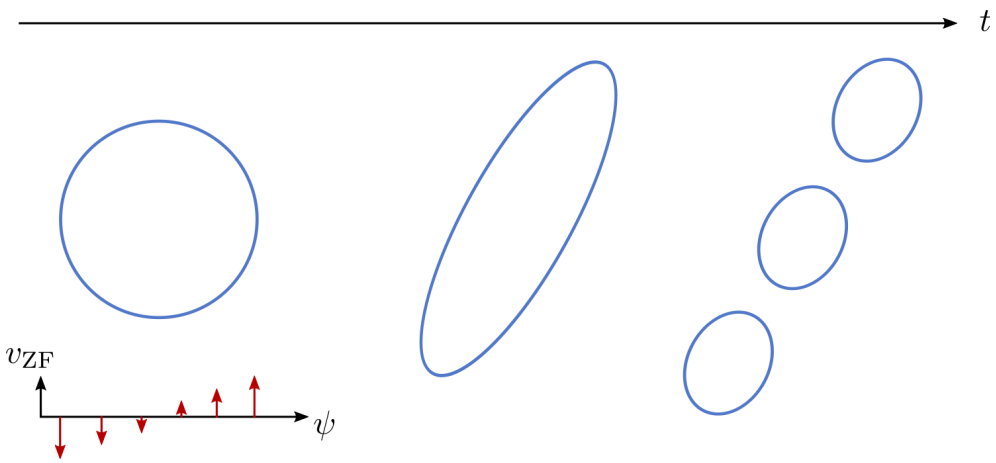

Figure 2.8: Zonal flow shear decorrelation: A turbulent vortex (blue) that is subject to a homogeneously sheared flow (red arrows) gets deformed over time until it breaks up into smaller vortices.

microturbulence [29, 67]. As such, the nonlinear generation of zonal flows leads to an upshift of the critical temperature gradient for the development of ion temperature gradient driven turbulence known as the Dimits shift [67]. This section introduces basic concepts connected to shear stabilization and nonlinear mode coupling related to zonal flows.

The stabilization of turbulence stems from their shearing action and, therefore, is also referred to as *shear stabilization*. Early works on this topic describe shear stabilization as a decorrelation process [29, 68, 28], which is depicted schematically in the case of a homogeneously sheared flow $\mathbf{v}_s = \alpha\psi$ ($\alpha > 0$) in Fig. 2.8. A turbulent eddy that is subject to this shear flow gets deformed over time. It is tilted and stretched until it breaks up into smaller eddies with reduced radial correlation length. Turbulent transport is reduced in the latter case [68] compared to the initial state.

Sufficiently strong zonal flows can also suppress turbulence completely through shear stabilization. Ref. [69] introduces an empirical rule for shear stabilization $\omega_{\mathrm{ExB}} \sim \gamma$ based on the so-called $E \times B$ shearing rate

$$\omega_{\mathrm{ExB}} = \frac{1}{B}\frac{\partial^2\langle\phi\rangle}{\partial\psi^2} \tag{2.49}$$

and the growth rate γ of the most unstable ITG driven mode and is referred to as the *Waltz rule*. According to this rule turbulence is suppressed when the $E \times B$-shearing rate exceeds the dominant linear growth rate of the underlying microinstability. Gyrokinetic studies of ITG driven turbulence support this simple rule [70, 71, 25].

Zonal flow shearing can also be described by a mode coupling process [72, 73] in analogy to sideband generation within the modulational instability framework

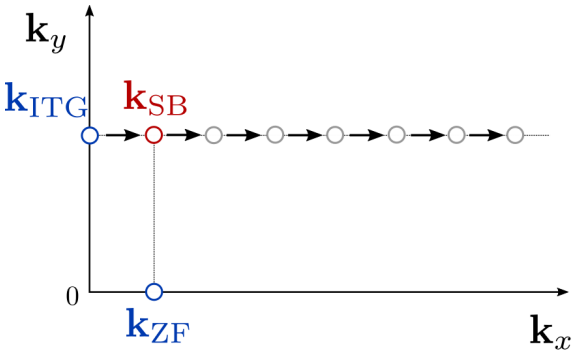

Figure 2.9: Zonal flow shearing as a nonlinear mode coupling process: A zonal flow $\mathbf{k}_{\mathrm{ZF}}$ couples to an ITG driven mode $\mathbf{k}_{\mathrm{ITG}}$ and produces a sideband mode $\mathbf{k}_{\mathrm{SB}} = \mathbf{k}_{\mathrm{ZF}} + \mathbf{k}_{\mathrm{ITG}}$. Successively, energy is transferred to the large radial wave vector regime.

(see Sec. 2.4.1). For simplicity, modes are defined as Fourier modes of the electrostatic potential ϕ on a doubly periodic domain perpendicular to the magnetic field with perpendicular wave vector $\mathbf{k} = (k_y,\ k_x)$. The coupling of a zonal mode $\hat{\phi}_{\mathrm{ZF}}$ with $\mathbf{k}_{\mathrm{ZF}} = (0, k_{\mathrm{ZF}})$ and an ITG driven mode $\hat{\phi}_{\mathrm{ITG}}$ with $\mathbf{k}_{\mathrm{ITG}} = (k_y, 0)$ through the quadratic $E \times B$-nonlinearity produces a sideband mode $\hat{\phi}_{\mathrm{SB}}$ with $\mathbf{k}_{\mathrm{SB}} = (k_y, k_{\mathrm{ZF}})$ in agreement with the wave vector addition rule $\mathbf{k}_{\mathrm{SB}} = \mathbf{k}_Z + \mathbf{k}_{\mathrm{ITG}}$. This process is illustrated in Fig. 2.9. Sophisticated nonlinear energy transfer studies [22, 66] show that the zonal flow acts as a mediator for the nonlinear transfer of energy from the unstable ITG mode to the sideband mode. Zonal flows, therefore, introduce an anisotropic transfer of energy to modes with increasing radial wave vector k_x. Energy dissipation is enhanced for large radial wave vectors, such that zonal flow shearing contributes to establish an energy balance and thereby a statistically stationary state.
Recent studies focusing on the effect of stable Eigenmodes on ITG driven turbulence [74, 75, 63, 66] revealed that a significant fraction of energy is transferred to stable Eigenmodes through the above discussed zonal flow shearing process. Therein, zonal flow mediated transfer is found to dominate the nonlinear processes leading to the nonlinear saturation of ITG driven turbulence. These studies confirm the importance of zonal flows for the regulation of ion temperature gradient driven turbulence on the basis of mode coupling processes.

2.4.4 Zonal flow pattern formation

Close to marginal stability zonal flows and microturbulence often self-organize into patterns [23, 24, 25, 76, 77]. Such patterns, also known as $E \times B$-staircases [23], exhibit the following properties: (i) They occur on a *radial mesoscale* of the order of $10^1\ \rho_{\mathrm{th,i}}$, i. e., a scale larger than the Larmor radius but smaller than the machine size. (ii) The structures are *quasi-stationary*, in that the radial position varies on a time scale much longer than typical turbulent times scales. (iii) They exhibit a *typical amplitude* in terms of the $E \times B$-shearing rate of the order of $10^{-1}\ v_{\mathrm{th,i}}/R_0$. (iv) Turbulent transport occurs through *avalanches*, whose propagation direction is strongly linked to the local $E \times B$-shearing rate.

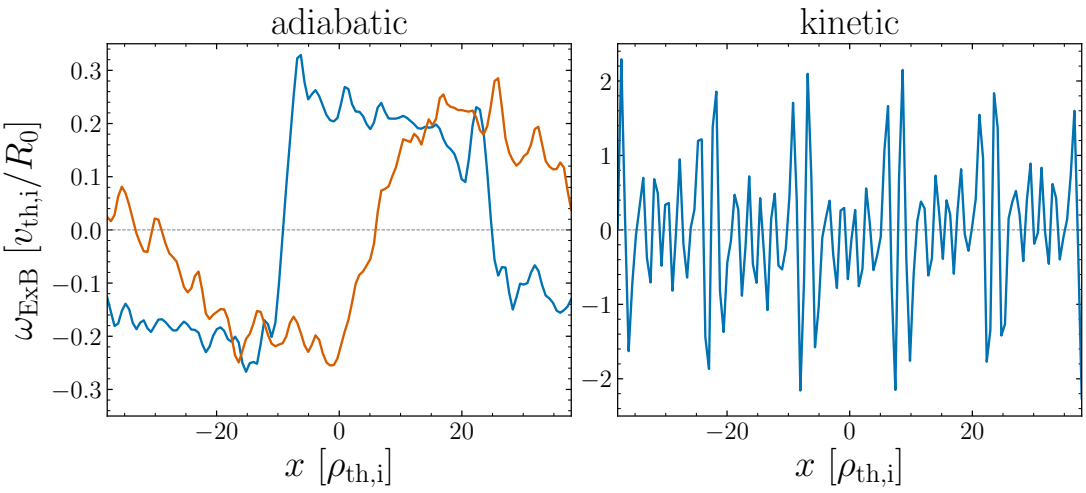

Figure 2.10: Pattern formation in the radial profile of the $E \times B$ shearing rate: Shown are temporally averaged radial profiles of the $E \times B$ shearing rate in near marginal ion temperature gradient driven turbulence with adiabatic electrons (left) and kinetic electrons (right). In the adiabatic case two variants of the mesoscale $E \times B$ staircase pattern known as fully- (blue) and partially-developed (red) staircase do occur. Mesoscale pattern formation is absent in the case of kinetic electrons. Instead, dominant radial fine scale features can be observed with an order of magnitude increased amplitude (note the difference in the axis range).

Experimental evidence of mesoscale pattern formation has been reported in several tokamak devices such as JET [78], Tore Supra [79], HL-2A [80], KSTAR [81] and DIII-D [82] including the observation of stationary mesoscale structures in the radial electric field and organization of turbulence in form of avalanches on similar mesoscales. Those observations point towards a potential importance of mesoscale pattern formation for the turbulence dynamics and energy confinement in tokamak fusion devices.
The $E \times B$-staircase pattern is robustly reproduced in gyrokinetic studies that apply the adiabatic electron closure [23, 24, 25, 76, 77]. The left panel of Fig. 2.10 shows the two variants known as fully- (blue) and partially-developed (red) staircase emerging in ITG driven turbulence with the adiabatic electron approximation [25]. The latter type allows for turbulence mediated by avalanches. Avalanches are triggered at the zero crossing with a flattened flank (close to the inner radial edge of the simulation domain) and propagate radially outwards (inwards) through regions with negative (positive) shearing rate consistent with other gyrokinetic turbulence studies [26, 27]. The fully-developed type leads to almost completely quenched turbulence. Its development results in a discontinuous step in the dependency of the turbulent fluxes on the temperature gradient,

also referred to as finite heat flux threshold [25, 77]. The mesoscale character and the typical amplitude is clearly apparent in Fig. 2.10.
By contrast, gyrokinetic studies that consider electrons as kinetic species report of dominant radial fine scale structures in the $E \times B$-shearing rate [83, 1, 84, 85, 86]. Such structures organize on radial scales of the Larmor radius $\sim \rho_{\mathrm{th,i}}$ and exhibit amplitudes (in terms of the shearing rate) of the order of $\sim 10^0 \; v_{\mathrm{th,i}}/R_0$. An exemplary case is shown in the right panel of Fig. 2.10. In Ref. [1] the fine scale structures have been demonstrated to be driven by the nonlinear self-interaction of parallel to the magnetic field elongated turbulent modes. In the aforementioned reference mesoscale structures have been recovered only in specific parameter regimes with weakened self-interaction. These findings led to the speculation that the development of mesoscale staircase structures may be inhibited by the presence of the dominant fine scale features.

Chapter 3

Gyrokinetic theory

The dynamics of a plasma may be completely described by the Newton-Maxwell system. However, the large number of ions and electrons of $\sim 10^{20}\ m^{-3}$ in a fusion plasma [11] renders this approach infeasible, even on todays most powerful supercomputers. Instead, a statistical approach is pursued and, through averaging over the fast gyro-motion, is provided by the gyrokinetic approach [87, 44, 88]. This chapter gives an introduction to the gyrokinetic framework. For further details the reader is referred to the review articles [10, 11, 89, 90].

3.1 Vlasov-Maxwell system

In kinetic theory the plasma is described by a particle density distribution function $F_{V,\mathrm{sp}}(\mathbf{x}, \mathbf{v}, t)$ [91] on the six-dimensional phase space $(\mathbf{x}, \mathbf{v})$, with $\mathbf{x}$ and $\mathbf{v}$ being the particle's position and velocity, respectively. Short range two particle interactions may be described by a collision operator $C[F'_{V,\mathrm{sp}}, F_{V,\mathrm{sp}}]$. However, since the collision frequency is typically much smaller than the characteristic frequencies connected to microturbulence [11] a collisionless model is often considered. This simplification is adopted also in this thesis. In this case the evolution of the one particle distribution function is governed by the Vlasov equation

$$\frac{\partial F_{V,\mathrm{sp}}}{\partial t} + \frac{\mathrm{d}\mathbf{x}}{\mathrm{d}t} \cdot \frac{\partial F_{V,\mathrm{sp}}}{\partial \mathbf{x}} + \frac{\mathrm{d}\mathbf{v}}{\mathrm{d}t} \cdot \frac{\partial F_{V,\mathrm{sp}}}{\partial \mathbf{x}} = 0. \tag{3.1}$$

In a magnetized plasma the time derivative of both the particle position $\mathbf{x}$ and velocity $\mathbf{v}$ are determined by electromagnetic fields and can be obtained from the appropriate single particle Hamiltonian or Lagrangian [11].
To obtain a closed system, the electric and magnetic fields have to be obtained self-consistently through Maxwell's equations. This is achieved by taking velocity moments of the distribution function to express the particle density n_{sp} and

current density $j_{\rm sp}$ through

$$n_{\rm sp} = \int \mathrm{d}^3 v \; F_{V,\rm sp} \tag{3.2}$$

$$j_{\rm sp} = q_{\rm sp} \int \mathrm{d}^3 v \; v F_{V,\rm sp}, \tag{3.3}$$

which are then substituted into Maxwell's equations

$$\nabla \times \mathbf{E} = -\frac{\partial \mathbf{B}}{\partial t} \tag{3.4}$$

$$\nabla \cdot \mathbf{E} = \frac{1}{\epsilon_0} \sum_{\rm sp} q_{\rm sp} n_{\rm sp} \tag{3.5}$$

$$\nabla \times \mathbf{B} = \mu_0 \left(\sum_{\rm sp} j_{\rm sp} + \epsilon_0 \frac{\partial \mathbf{E}}{\partial t} \right) \tag{3.6}$$

$$\nabla \cdot \mathbf{B} = 0. \tag{3.7}$$

Eq. (3.1) and Eqs. (3.4)-(3.7) constitute the Valsov-Maxwell system that is at the basis of the gyrokinetic model.

3.2 Gyrokinetic ordering

The plasma dynamics in tokamak devices is characterized by a large variety of spatio-temporal scales. This scale separation is exploited by the gyrokinetic ordering described in this section.
Due to the strong external magnetic field, the time scale of the fast gyro-motion is much shorter than the time scale connected with turbulent dynamics. For the ratio of the turbulence characteristic frequency ω and the ion cyclotron frequency $\omega_{c,\rm i}$ typical parameters yield $\omega/\omega_{c,\rm i} \sim 10^{-3}$ [10, 90].[1]
Furthermore, the perpendicular length scales associated with microturbulence is of the order of the ion thermal Larmor radius $k_\perp^{-1} \sim \rho_{\rm th,i}$, where $k_\perp = |\mathbf{k} \times \mathbf{b}|$ defines the perpendicular component of wave vector $\mathbf{k}$ of turbulent perturbations and $\mathbf{b}$ is the unit vector parallel to the ambient magnetic field. With a few millimeters the ion thermal Larmor radius $\rho_{\rm th,i}$, in turn, is significantly smaller than the scales on which the equilibrium density n_0 varies. The latter can be expressed through the gradient length $L_n = |\nabla \ln n_0|^{-1}$ and compares with the machine size of the order of a few meters. This scale separation is quantified by the normalized Larmor radius $\rho_* = \rho_{\rm th,i}/R_0$, where R_0 is the major radius of the tokamak, which is of the order of $\rho_* = 10^{-3} - 10^{-4}$.[2]

[1] Alternatively, considering that the turbulence dynamics occurs on the transit time $\tau = v_{\rm th,i}/R_0$, one finds $\tau\omega_{c,\rm i} = m_{\rm i} v_{\rm th,i}/(eBR_0) = \rho_{\rm th,i}/R_0 = \rho_* \ll 1$.

[2] ASDEX Upgrade: $\rho_* \approx 3.0 \times 10^{-3}$, ITER: $\rho_* \approx 7.2 \times 10^{-4}$ (see appendix E)

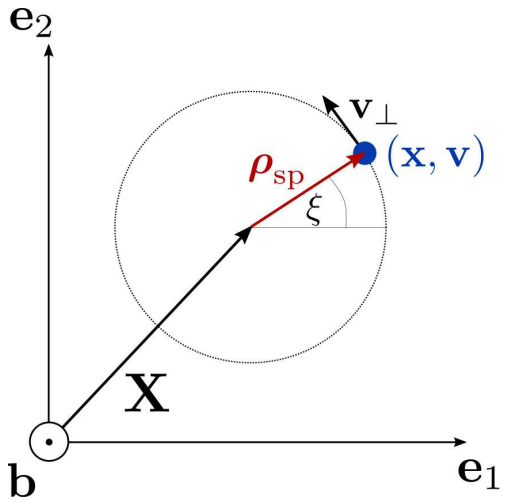

Figure 3.1: Transformation to guiding-center phase space $(\mathbf{X}, v_\parallel, \mu, \xi)$: The particle dynamics is expressed through the position of the guiding-center $\mathbf{X} = \mathbf{x} - \boldsymbol{\rho}_{\mathrm{sp}}$ with the Larmor radius vector $\boldsymbol{\rho}_{\mathrm{sp}}$, the magnetic moment $\mu = m_{\mathrm{sp}} v_\perp^2/(2B)$ with $v_\perp = |\mathbf{v} \times \mathbf{b}|$, the parallel velocity $v_\parallel = \mathbf{v} \cdot \mathbf{b}$ and the gyro-phase angle ξ.

Another typical scale relates to the high mobility of particles along the field lines that causes turbulent perturbations to be significantly extended parallel to the magnetic field. The parallel length scale of turbulent fluctuations $k_\parallel^{-1}$, with $k_\parallel = \mathbf{b} \cdot \mathbf{k}$, is, therefore, of the order of the machine size.
In addition, a clear separation of magnitudes connected to equilibrium and fluctuating quantities does occur. Experimental measurements of core plasmas show that the relative fluctuation amplitude of both density perturbations $\delta n/n_0$ and magnetic field fluctuations $\delta B/B_0$, where B_0 is the magnitude of the equilibrium magnetic field, is of the order of $\sim 10^{-4}$ [10].
Consequently, the ordering [11]

$$\frac{\omega}{\omega_{c,\mathrm{i}}} \sim \frac{k_\parallel}{k_\perp} \sim \frac{\rho_{\mathrm{th,i}}}{L_n} \sim \frac{\delta n}{n_0} \sim \frac{\delta B}{B_0} \sim \frac{v_d}{v_{\mathrm{th,i}}} \sim \epsilon_g \tag{3.8}$$

with $\epsilon_g \ll 1$ applies to the typical dynamics of a fusion core plasma. This ordering, also referred to as the *gyrokinetic ordering*, allows for the development of a reduced set of dynamical equations as outlined below.

3.3 Guiding- and gyrocenter transformation

The gyrokinetic ordering [Eq. (3.8)] motivates the elimination of the fast gyromotion from the Vlasov-Maxwell system since it is dynamically not relevant for the description of low frequency microturbulence. In early gyrokinetic theory this has been realized by averaging the Vlasov equation over the gyro-orbit, also referred to as gyro-averaging. In modern gyrokinetic theory phase-space transformation based on the Hamiltonian or Lagrangian formalism and the Lie perturbation theory [92, 93] and an asymptotic expansion in the smallness parameter ϵ_g is applied, which retains symmetry and conservation properties of the physical

system.
Starting from the conventional particle phase space $(\mathbf{x}, \mathbf{v})$, in a first transformation —the guiding-center transformation [94] —the particle motion is described in guiding-center phase space $(\mathbf{X}, \mu, v_\parallel, \xi)$. As sketched in Fig. 3.1 the particles position is expressed through the guiding-center position $\mathbf{X} = \mathbf{x} - \boldsymbol{\rho}_{\mathrm{sp}}$ with the Larmor radius vector $\boldsymbol{\rho}_{\mathrm{sp}}$ and the gyro-phase angle ξ, taking into account circular gyro-orbits[3]. The particle's velocity is decomposed into a component parallel to the ambient magnetic field $v_\parallel = \mathbf{b}\cdot\mathbf{v}$ and a perpendicular component $v_\perp = |\mathbf{v}\times\mathbf{b}|$. The latter relates to the magnetic moment $\mu = m_{\mathrm{sp}} v_\perp^2/(2B)$, which is an approximate adiabatic invariant in guiding-center phase space and in the considered low frequency limit [11].
A second transformation —the gyro-center transformation [44] —is then constructed such that the gyro-phase dependence is eliminated from the Hamiltonian or Lagrangian in lowest order of ϵ_g [10]. This transformation also deals with gyro-phase dependent perturbations in the electromagnetic fields that particles experience on the gyro-orbit. It is, therefore, suitable for the description of microturbulence that introduces fluctuations on spatial scales of the order of the Larmor radius. The gyro-phase dependent part of fluctuations is absorbed in the gauge freedom of the transformation [17] and, hence, enters the description when transforming between gyro- and guiding-center phase space. In the lowest order gyro-center phase space $(\overline{\mathbf{X}}, \overline{v}_\parallel, \overline{\mu}, \overline{\xi})$ the magnetic moment $\overline{\mu}$ is an exact invariant leaving the gyro-phase $\overline{\xi}$ an ignorable viarable [11].
The guiding- and gyro-center transformations allow to formulate a reduced kinetic equation —the *gyrokinetic equation* —that makes numerical studies of microturbulence feasible because of two reasons: (i) The fast gyro-motion is removed from the problem enabling the use of a much larger time step to resolve the dynamics relevant for low frequency microturbulence. (ii) The equations are independent of the gyro-phase angle, which reduces the dimensionality of the problem from six to five dimensions. In the subsequent sections the five-dimensional gyro-center phase space is denoted by $(\mathbf{X}, v_\parallel, \mu)$, omitting the overlines for simplicity.

3.4 Gyrokinetic equation

Based on the Vlasov equation [E. (3.1)], the gyrokinetic ordering (Sec. 3.2) and the guiding- and gyro-center transform (Sec. 3.3) an equation for the time evolution of the *gyro-center distribution function* $F_{\mathrm{sp}}(\mathbf{X}, v_\parallel, \mu, t)$ of a given species 'sp'

[3]The gyro-orbits are, in general, not circular due to spatial variations in the magnetic field and perpendicular velocity. Circular orbits emerge at lowest order in an expansion in the small parameter ϵ_g based on the gyrokinetic ordering [90].

can be formulated [17]

$$\frac{\partial F_{\mathrm{sp}}}{\partial t} + \frac{\partial \mathbf{X}}{\partial t} \cdot \frac{\partial F_{\mathrm{sp}}}{\partial \mathbf{X}} + \frac{\partial v_{\parallel}}{\partial t} \cdot \frac{\partial F_{\mathrm{sp}}}{\partial v_{\parallel}} = 0. \tag{3.9}$$

Eq. (3.9) is called the *gyrokinetic equation*.
Below, the gyrokinetic equation is discussed for the case of a non-rotating plasma and in the presence of electromagnetic perturbations. For the purpose of this thesis it is sufficient to consider perpendicular (to the background magnetic field) magnetic perturbations only. This simplification is valid for small β [17, 10], which applies to this thesis.[4] Extensions of the gyrokinetic equation due to plasma rotation and parallel magnetic perturbations can be found in Refs. [95] and [17], respectively.
Since the magnetic moment is an exact invariant of motion in gyro-center phase space, i. e., $\partial_t \mu = 0$, its time derivative is absent in Eq. (3.9). The remaining equations of motion can be obtained from the Lagrangian in gyro-center phase space and read [17]

$$\frac{\partial \mathbf{X}}{\partial t} = v_{\parallel}\mathbf{b} + \mathbf{v}_D + \mathbf{v}_{\chi} \tag{3.10}$$

$$\frac{\partial v_{\parallel}}{\partial t} = \frac{\mathrm{d}\mathbf{X}}{\mathrm{d}t} \cdot [q_{\mathrm{sp}}\mathbf{E} - \mu \nabla B]. \tag{3.11}$$

Eq. (3.10) describes the motion of gyro-centers in the presence of electromagnetic fields. It consists of the motion parallel to the ambient magnetic field $v_{\parallel}\mathbf{b}$, the gyro-center drift due to the inhomogeneous ambient magnetic field

$$\mathbf{v}_D = \frac{1}{q_{\mathrm{sp}}}\left[\frac{m_{\mathrm{sp}} v_{\parallel}^2}{B} + \mu\right]\frac{\mathbf{B} \times \nabla B}{B^2} + \frac{m_{\mathrm{sp}} v_{\parallel}^2}{2 q_{\mathrm{sp}} B}\beta' \mathbf{b} \times \nabla \psi \tag{3.12}$$

and

$$\mathbf{v}_{\chi} = \frac{\mathbf{b} \times \nabla \chi}{B} \tag{3.13}$$

with the modified potential

$$\chi = \langle \phi \rangle_{\mathrm{ga,sp}} - v_{\parallel} \langle A_{\parallel} \rangle_{\mathrm{ga,sp}}. \tag{3.14}$$

The drift $\mathbf{v}_{\chi}$ is a combination of the $E \times B$-drift

$$\mathbf{v}_E = \frac{\mathbf{b} \times \nabla \langle \phi \rangle_{\mathrm{ga,sp}}}{B} \tag{3.15}$$

[4] For the perturbed magnetic field the ordering $|\delta \mathbf{B}_{\perp}|/B_0 \sim \epsilon_g$ and $|\delta B_{\parallel}|/B_0 \sim \beta \epsilon_g$ applies [17, 10]. In this thesis $\beta \sim 1$ % and parallel magnetic field perturbations can therefore be neglected compared to perpendicular perturbations.

and the parallel motion along perturbed magnetic field lines

$$\mathbf{v}_{\delta B} = -\frac{\mathbf{b} \times \nabla v_{\parallel} \langle A_{\parallel} \rangle_{\mathrm{ga,sp}}}{B}, \tag{3.16}$$

arising from perturbations in the electrostatic potential ϕ and the parallel component of the magnetic vector potential $A_{\parallel}$. The operator $\langle ... \rangle_{\mathrm{ga,sp}}$ denotes a gyro-average (see Sec. 3.5).
The first term on the right-hand side of Eq. (3.12) is the combination of the ∇B-drift and the curvature drift, while the second term is the correction to the curvature drift due to the modification of the equilibrium magnetic field in the presence of a normalized plasma pressure gradient

$$\beta' = \frac{2\mu_0}{B^2} \frac{\partial p}{\partial \psi}. \tag{3.17}$$

In the above equations ψ is a radial coordinate (flux-surface label).
Eq. (3.11) describes the parallel acceleration of gyro-centers due to electromagnetic fields with

$$\mathbf{E} = -\nabla \langle \phi \rangle_{\mathrm{ga,sp}} - \frac{\partial \langle A_{\parallel} \rangle_{\mathrm{ga,sp}}}{\partial t} \mathbf{b} \tag{3.18}$$

being the gyro-averaged perturbed electric field.

3.5 Gyro-average

One consequence of the dynamical reduction introduced through the gyro-center transformation is the occurrence of the gyro-averaged fields $\langle \phi(\mathbf{x}) \rangle_{\mathrm{ga,sp}}$ and $\langle A_{\parallel}(\mathbf{x}) \rangle_{\mathrm{ga,sp}}$ entering the drift $\mathbf{v}_{\chi}$ and the perturbed electric field $\mathbf{E}$. During the (slow) dynamics described by the gyrokinetic equation, the gyro-centers experience effective electromagnetic fields. The latter relate to the sampling of the electromagnetic fields on the gyro-orbit during the course of the (fast) gyromotion. Here, the terms *slow* and *fast* are based on the gyrokinetic ordering $\omega/\omega_{c,\mathrm{i}} \ll 1$.
The gyro-average is the spatial average over an orbit $\mathbf{x} = \mathbf{X} + \boldsymbol{\rho}_{\mathrm{sp}}(\xi)$ defined by a full cycle of the gyro-phase $\xi \in [0, 2\pi]$ at fixed gyro-center position $\mathbf{X}$ (dotted circle in Fig. 3.1). Using the Fourier space representation of a quantity

$$G(\mathbf{x}) = \int \hat{G}(\mathbf{k}) \mathrm{e}^{\mathrm{i}\mathbf{k}\cdot\mathbf{x}} \, \mathrm{d}\mathbf{k} \tag{3.19}$$

it reads [17]

$$\langle G(\mathbf{x})\rangle_{\mathrm{ga,sp}} = \langle G(\mathbf{X}+\boldsymbol{\rho}_{\mathrm{sp}})\rangle_{\mathrm{ga,sp}} = \langle \int \hat{G}(\mathbf{k})\mathrm{e}^{\mathrm{i}\mathbf{k}\cdot(\mathbf{X}+\boldsymbol{\rho}_{\mathrm{sp}})}\ \mathrm{d}\mathbf{k}\rangle_{\mathrm{ga,sp}} \tag{3.20}$$

$$= \frac{1}{2\pi}\int_0^{2\pi}\int \hat{G}(\mathbf{k})\mathrm{e}^{\mathrm{i}\mathbf{k}\cdot(\mathbf{X}+\boldsymbol{\rho}_{\mathrm{sp}})}\ \mathrm{d}\mathbf{k}\ \mathrm{d}\xi \tag{3.21}$$

$$= \int \hat{G}(\mathbf{k})\mathrm{e}^{\mathrm{i}\mathbf{k}\cdot\mathbf{X}}\underbrace{\frac{1}{2\pi}\int_0^{2\pi}\mathrm{e}^{\mathrm{i}k_\perp\rho_{\mathrm{sp}}\cos(\xi)}\ \mathrm{d}\xi}_{J_0(\rho_{\mathrm{sp}}k_\perp)}\ \mathrm{d}\mathbf{k} \tag{3.22}$$

$$= \int J_0(\rho_{\mathrm{sp}}k_\perp)\hat{G}(\mathbf{k})\mathrm{e}^{\mathrm{i}\mathbf{k}\cdot\mathbf{X}}\ \mathrm{d}\mathbf{k} = J_0(\lambda_{\mathrm{sp}})G(\mathbf{X}), \tag{3.23}$$

where J_0 is the zeroth order Bessel function of the first kind, $k_\perp$ is the component of the wave vector $\mathbf{k}$ perpendicular to the ambient magnetic field and $\lambda_{\mathrm{sp}} = \mathrm{i}\rho_{\mathrm{sp}}\nabla_\perp$ with $\nabla_\perp$ being the component of the gradient perpendicular to the ambient magnetic field. Motivated by the calculation above, the Bessel function J_0 is sometimes referred to as gyro-average operator.
When the electromagnetic field varies on spatial scales of the Larmor radius, the gyro-average results in a reduction of the field's amplitude commonly referred to as *finite Larmor radius (FLR) effects* [89]. Fields that vary rapidly with $\mathbf{x}$ are effectively smoothed in gyro-center phase space $\mathbf{X}$ after gyro-averaging. This effect influences the turbulence - zonal flow interplay, when zonal structures occur on scales comparable to the Larmor radius as shown in chapter 6 of this thesis.

3.6 Gyrokinetic field equations

A closed set of equations requires to relate the electromagnetic fields to the distribution function. This is achieved by expressing the charge and current densities, entering the Maxwell's equations, through the gyro-center distribution function. The resulting gyrokinetic field equations are presented in this section which is based on Ref. [96].
In a plasma a small relative displacement in the ion and electron particle density causes a strong electric field and an associated high frequency oscillation with the plasma frequency $\omega_p = [e^2 n_0/(\epsilon_0 m_{\mathrm{e}})]^{1/2}$ [97]. Furthermore, on spatial scales larger than the Debye length $\lambda_D = [\epsilon_0 T_{\mathrm{e}}/(n_{\mathrm{e}}e^2)]^{1/2}$ electric fields caused by the charged particles are shielded [97]. On time scales long compared to the inverse plasma frequency and spatial scales larger than the Debye length a plasma can be considered quasi-neutral. The Gauss law [Eq. (3.5)] is then replaced by the quasi-neutrality condition [17]

$$\sum_{\mathrm{sp}} q_{\mathrm{sp}} n_{\mathrm{sp}}(\mathbf{x}) = 0, \tag{3.24}$$

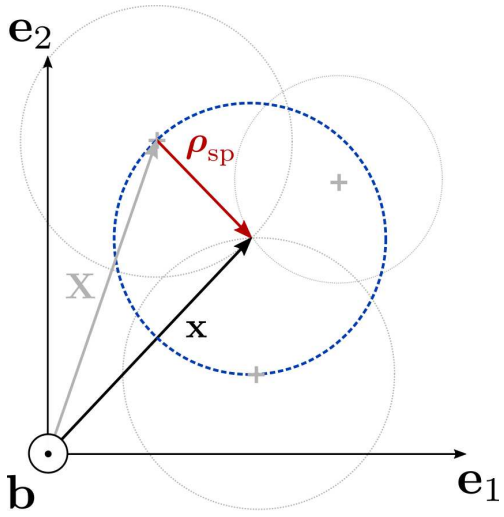

Figure 3.2: Connection between density of particles and density of guiding-centers: Gyro-orbits with different guiding-center $\mathbf{X}$ (gray +-symbols) can cross in $\mathbf{x}$, such that the respective gyrating particles add to the particle density $n_{\mathrm{sp}}(\mathbf{x})$ there. For a fixed Larmor radius $\rho_{\mathrm{sp}} = |\boldsymbol{\rho}_{\mathrm{sp}}|$ (red) the particle density at $\mathbf{x}$ is obtained by collecting the contributions of all guiding-centers on a circle with radius ρ_{sp} centered at $\mathbf{x}$ (blue dashed).

where $n_{\mathrm{sp}}(\mathbf{x})$ is the species particle density in particle space $\mathbf{x}$.

The particle density is a velocity moment of the Vlasov distribution function $F_{V,\mathrm{sp}}(\mathbf{x}, \mathbf{v})$ in particle phase space [Eq. (3.2)]. However, the solution of the gyrokinetic equation provides one with the gyro-center distribution function $F_{\mathrm{sp}}(\mathbf{X}, v_\parallel, \mu)$ in gyro-center phase space. As a consequence, the Vlasov distribution function in Eq. (3.2) has to be expressed through the gyro-center distribution function making use of the guiding- and gyro-center transforms. This is realized by first transforming the Valsov distribution function $F_{V,\mathrm{sp}}$ to guiding-center phase space and then expressing the resulting guiding-center distribution function $F_{\mathrm{gc,sp}}$ through the gyro-center distribution function F_{sp}. Within Lie perturbation theory the latter step is performed through the action of the so-called pull-back operator T [17] and reads

$$F_{\mathrm{gc,sp}} = TF_{\mathrm{sp}} = F_{\mathrm{sp}} + (T-1)F_{\mathrm{sp}} = F_{\mathrm{sp}} + PF_{\mathrm{sp}}, \tag{3.25}$$

where $P = T - 1$. Applying the above steps to Eq. (3.2) yields

$$n_{\mathrm{sp}}(\mathbf{x}) = \frac{B}{m_{\mathrm{sp}}} \int \delta[\mathbf{X} + \boldsymbol{\rho}_{\mathrm{sp}}(\xi) - \mathbf{x}] F_{\mathrm{gc,sp}}(\mathbf{X}, v_\parallel, \mu)\ \mathrm{d}\mathbf{X}\mathrm{d}v_\parallel\mathrm{d}\mu\mathrm{d}\xi \tag{3.26}$$

$$= \frac{B}{m_{\mathrm{sp}}} \int \delta[\mathbf{X} + \boldsymbol{\rho}_{\mathrm{sp}}(\xi) - \mathbf{x}] \Big[F_{\mathrm{sp}}(\mathbf{X}, v_\parallel, \mu) + PF_{\mathrm{sp}}(\mathbf{X}, v_\parallel, \mu) \Big]\ \mathrm{d}\mathbf{X}\mathrm{d}v_\parallel\mathrm{d}\mu\mathrm{d}\xi \tag{3.27}$$

$$\equiv \overline{n}_{\mathrm{sp}}(\mathbf{x}) + n_{\mathrm{sp},P}(\mathbf{x}). \tag{3.28}$$

The delta-function $\delta[\mathbf{X}+\boldsymbol{\rho}_{\mathrm{sp}}(\xi)-\mathbf{x}]$ enters due to the transformation from particle to gyro-center phase space. Physically, it expresses that gyro-orbits with different guiding-center $\mathbf{X}$ can cross in $\mathbf{x}$, such that the respective gyrating particles add to the particle density there (see Fig. 3.2). The prefactor B/m_{sp} represents the velocity space Jacobian in guiding-center phase space.

The first term on the right-hand side of expression (3.28) is the contribution of the gyro-center density at $\mathbf{x}$ defined by

$$\overline{n}_{\mathrm{sp}}(\mathbf{x}) = \frac{2\pi B}{m_{\mathrm{sp}}} \int J_0(\lambda_{\mathrm{sp}}) F_{\mathrm{sp}}(\mathbf{x}, v_\parallel, \mu)\ \mathrm{d}v_\parallel \mathrm{d}\mu. \tag{3.29}$$

Analogously to the argumentation above $\overline{n}_{\mathrm{sp}}(\mathbf{x})$ collects the contributions of the gyro-center distribution function for all gyro-centers $\mathbf{X}$ on a circle with radius ρ_{sp} centered at $\mathbf{x}$ (blue dashed circle in Fig. 3.2). This operation is equivalent to a gyro-average over the orbit $\mathbf{X} = \mathbf{x} - \boldsymbol{\rho}_{\mathrm{sp}}(\xi)$ with fixed $\mathbf{x}$ and introduces the Bessel function J_0 in Eq. (3.29). In chapter 6 these FLR effects are shown to influence the ability of small scale zonal structures in shear-stabilizing microturbulence.
The second term on the right-hand side of expression (3.28) is the contribution of the variations on the gyro-orbit to the particle density at $\mathbf{x}$. It describes the polarization effects of the fluctuating fields on the gyro-orbit [10]. In the δf-approximation (see Sec. 4.1) the polarization density relates to the electrostatic potential through [17]

$$n_{\mathrm{sp},P}(\mathbf{x}) = \frac{q_{\mathrm{sp}} n_{0,\mathrm{sp}}}{T_{\mathrm{sp}}} [\Gamma_0(b_{\mathrm{sp}}) - 1] \phi(\mathbf{x}), \tag{3.30}$$

where $n_{0,\mathrm{sp}}$ is a background density, T_{sp} is a background temperature and $\Gamma_0(b_{\mathrm{sp}}) = I_0(b_{\mathrm{sp}}) e^{-b_{\mathrm{sp}}}$ with the modified Bessel function of the first kind I_0 and $b_{\mathrm{sp}} = -\rho_{\mathrm{th,sp}}^2 \nabla_\perp^2$ with the thermal Larmor radius $\rho_{\mathrm{th,sp}} = m_{\mathrm{sp}} v_{\mathrm{th,sp}} / (q_{\mathrm{sp}} B_0)$. The electrostatic potential, hence, enters the quasi-neutrality condition due to polarization effects, which describe the difference between the real particle density and the gyro-center density.
In this thesis perturbations in the perpendicular component of the magnetic field $\delta \mathbf{B}_\perp = \nabla \times \mathbf{A}_\parallel = \nabla \times \mathbf{b} A_\parallel$ are considered exclusively. Due to the low frequency phenomena under consideration, the displacement current can be neglected [11]. Using the Coulomb gauge $\nabla \cdot \mathbf{A} = 0$, the parallel component of Ampère's law [Eq. (3.6)]

$$\nabla^2 \mathbf{A}_\parallel = \mu \mathbf{j}_\parallel \tag{3.31}$$

then relates the parallel component of the vector potential to the particles current density

$$\mathbf{j}_\parallel = \mathbf{b} \sum_{\mathrm{sp}} j_{\parallel,\mathrm{sp}}. \tag{3.32}$$

The latter can be expressed as a velocity moment of the Vlasov particle distribution function [Eq. (3.3)].
Again the species current densities have to be expressed through the gyrocenter distribution function making use of the pull-back operator. The species current density can be formulated by [17]

$$j_{\parallel,\mathrm{sp}}(\mathbf{x}) = q_{\mathrm{sp}} \frac{B}{m_{\mathrm{sp}}} \int v_\parallel J_0(\lambda_{\mathrm{sp}}) F_{\mathrm{sp}}(\mathbf{x}, v_\parallel, \mu)\ \mathrm{d}v_\parallel \mathrm{d}\mu. \tag{3.33}$$

The gyrokinetic equation [Eq. (3.9)], the quasi-neutrality condition [Eq. (3.24)] and the parallel component of Ampère's law [Eq. (3.31)] constitute the gyrokinetic Vlasov-Maxwell system. This set of governing equations is suitable for the study of low frequency phenomena and is exploited in this thesis to investigate the interplay of zonal flows and microturbulence in tokamak plasmas.

Chapter 4

Gyrokinetic practice

This section introduces concepts that are required to bring the gyrokinetic Valsov-Maxwell equation into a form that is suitable for numerical simulations. The material presented in this section is based on the documentation [98] of the gyrokinetic solver Gyrokinetic Workshop (GKW) [95].

4.1 The δf-approximation and the local limit

All simulations presented in this thesis apply two approximations known as the δf-approximation and the local limit. These approximations further simplify the governing equations and, thereby, reduce the computational costs. In GKW the normalize Larmor radius $\rho_* = \rho_{\mathrm{th,i}}/R_0$ is considered as basic expansion parameter in both approximations.
The *δf-approximation* is based on the amplitude separation between fluctuations and equilibrium as expressed by the gyrokinetic ordering [Eq. (3.8)]. In the δf-approximation the gyro-center distribution function is split into a constant in time equilibrium $F_{0,\mathrm{sp}}$ and a fluctuation perturbed part f_{sp} according to

$$F_{\mathrm{sp}} = F_{0,\mathrm{sp}} + f_{\mathrm{sp}}, \tag{4.1}$$

with the ordering

$$f_{\mathrm{sp}} \sim \rho_* F_{0,\mathrm{sp}}. \tag{4.2}$$

Variations of the perturbed distribution function perpendicular to the ambient magnetic field are considered to be of the order of the Larmor radius, while the background changes on scales of the system size. Hence, the ordering

$$\nabla_\perp f_{\mathrm{sp}} \sim \nabla_\perp F_{0,\mathrm{sp}}. \tag{4.3}$$

applies. Finally, the ordering

$$\frac{\partial f_{\mathrm{sp}}}{\partial v_\parallel} = \rho_* \frac{\partial F_{0,\mathrm{sp}}}{\partial v_\parallel} \tag{4.4}$$

is adopted, which removes the so-called velocity nonlinearity from the gyrokinetic equation in first order of ρ_*.[1] Although strict energy conservation is lost, this simplification does not introduce noticeable effects on microturbulence over a wide range of ρ_* as shown in the gyrokinetic study of Ref. [99].
The δf-approximation is suitable for global and local descriptions. In the former case the equilibrium distribution function $F_{0,\mathrm{sp}}$ includes the profile variation over the plasma minor radius and, hence, is a function of the radial coordinate ψ, while in the latter case it is taken to be constant in the radial direction. It is the local approach that is applied in this thesis and is, therefore, discussed below.
The *local limit* exploits the spatial scale separation of equilibrium and perturbations. In this limit the perpendicular length scale of the perturbations, which is of the order of the Larmor radius $\rho_{\mathrm{th,i}}$, is assumed to be much smaller than the equilibrium length scale, which is of the order of the device size R_0. Hence, it assumes $\rho_* \ll 1$ and is, therefore, compliant with the gyrokinetic ordering.
The local limit implies that all equilibrium and geometry quantities can be taken constant over the radial extent of the simulation volume, given the latter covers only a thin radial extent compared to the scale of the equilibrium profile variation. This applies to the equilibrium density $n_{0,\mathrm{sp}}$ and temperature $T_{0,\mathrm{sp}}$, and therefore to $F_{0,\mathrm{sp}}$, but also to the perpendicular gradient $\nabla_\perp F_{0,\mathrm{sp}}$ entering the gyrokinetic equation through the advection by $\mathbf{v}_\chi$ [see Eq. (3.9)].
Also the ambient magnetic field geometry varies on the scale of the device size rather than the Larmor radius. The equilibrium magnetic field and any geometric factors, entering the gyro-center drifts [Eq. (3.10)] for example, are therefore assumed to be constant in the radial direction as well. Due to the toroidal symmetry of the tokamak, all equilibrium quantities are also constant in the toroidal direction. The dependency of the equilibrium magnetic field on the poloidal angle, however, is retrained in general.

4.2 Geometry

In this section basic concepts associated with the geometry are introduced. First, a coordinate system is discussed in which the background magnetic field lines are straight with one coordinate being aligned to the field. Then the coordinates are given explicitly for two analytical magnetic field equilibria. Finally, the considered plasma volume is constraint to a flux-tube allowing for the introduction of the spectral representation.

[1] The velocity nonlinearity is the combination of the electromagnetic fields and the velocity space derivative of the distribution function [combination of the third term on the left-hand side of Eq. (3.9) and parts of Eq. (3.11)].

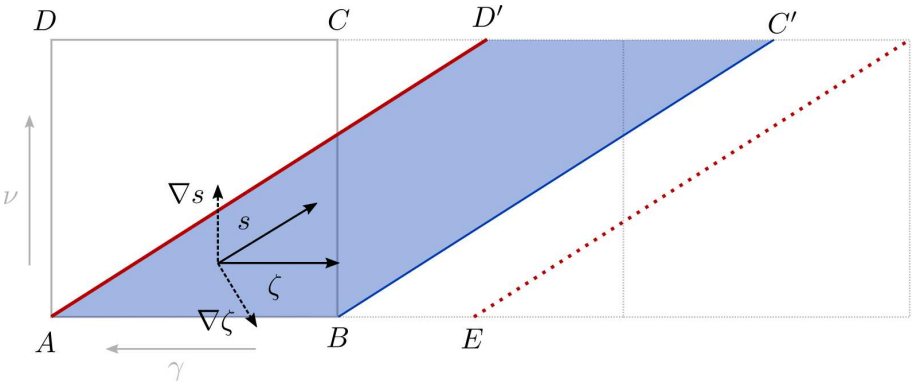

Figure 4.1: Coordinate transformation from intermediate (ψ, ν, γ) to field-aligned (ψ, ζ, s) coordinates sketched for a flux-surface with safety factor $q = 1.5$. In both coordinate systems the field line (red solid) is straight. A flux-surface in the intermediate coordinate system is given by the rectangle $ABCD$ (gray dotted rectangles depict periodic copies by successive toroidal mappings $\gamma \to \gamma - 1$). In the field-aligned coordinates the flux-surface is mapped (one-to-one and onto) onto the parallelogram $ABC'D'$ (blue area). Solid arrows are tangential to coordinate curves and point into the direction of an increasing coordinate, while dashed arrows depict coordinate gradients.

4.2.1 Straight field-aligned Hamada coordinates

As discussed within the gyrokinetic ordering (Sec. 3.2) the spatial structures connected to microturbulence are highly anisotropic with respect to the ambient magnetic field. While microturbulence varies rapidly perpendicular to the magnetic field, its parallel scale is of the order of the device size. For an efficient discretization of the spatial grid it is therefore advantageous to align one coordinate with the field. The number of grid points in the field-aligned coordinate can then be chosen much smaller than the number of grid points perpendicular to it, thereby saving computational resources. GKW applies field-aligned Hamada coordinates [100]. The transformation from basic toroidal coordinates (ψ, θ, φ) to field-aligned Hamada coordinates (ψ, ζ, s) is achieved through intermediate straight field line coordinates (ψ, ν, γ), as outlined below.
Starting point is the orthogonal coordinate system (ψ, θ, φ), with ψ the radial coordinate, $-\pi \leq \theta \leq \pi$ the poloidal angle and $-\pi \leq \varphi \leq \pi$ the toroidal angle. Here, 'radial' means that the coordinate gradient $\nabla\psi$ is orthogonal to the flux-surfaces and, hence, $\mathbf{B} \cdot \nabla\psi = 0$. In this coordinates a toroidally symmetric but otherwise arbitrarily shaped equilibrium magnetic field can be written as

$$\mathbf{B} = s_B R B_\mathrm{t} \nabla\varphi + s_j \nabla\varphi \times \nabla\Psi, \tag{4.5}$$

where $B_\mathrm{t} > 0$ is the toroidal magnetic field strength, R is the major radius and Ψ is the poloidal magnetic flux. The parameters $s_B \equiv \mathrm{sign}(\mathbf{B} \cdot \nabla\varphi)$ and

$s_j \equiv \text{sign}(\mathbf{j} \cdot \nabla\varphi)$ define the sign of the equilibrium magnetic field and current density with respect to the toroidal direction.
In a first transformation the field lines are made straight. The poloidal angle is transformed by

$$\nu = \int_0^\theta \frac{\mathrm{d}\theta'}{\nabla\theta' \cdot \mathbf{B}} \Big/ \oint \frac{\mathrm{d}\theta'}{\nabla\theta' \cdot \mathbf{B}}, \tag{4.6}$$

and the toroidal angle by

$$\gamma = \frac{\varphi}{2\pi} + \frac{RB_\mathrm{t}}{2\pi} \int_0^\theta \frac{\mathrm{d}\theta'}{\nabla\theta' \cdot \mathbf{B}} \left[\oint \frac{\mathrm{d}s}{R^2} - \frac{1}{R^2} \right]. \tag{4.7}$$

In the new coordinate system the safety factor is defined by

$$q = \oint \frac{\mathbf{B} \cdot \nabla\gamma}{\mathbf{B} \cdot \nabla\nu} \mathrm{d}\nu. \tag{4.8}$$

Fig. 4.1 depicts a full flux surface ($ABCD$, gray solid rectangle) in the intermediate coordinate system (ψ, ν, γ) and two toroidal periodic copies (gray dotted rectangles). A field line with $q = 1.5$ (red line) and the coordinate curves[2] (parallel to gray arrows) are shown as well
A second coordinate transformation

$$s = \nu \tag{4.9}$$

$$\zeta = q\nu - \gamma \tag{4.10}$$

aligns one coordinate with the field. At fixed ζ, the position along the field line is then specified by s, which will also be referred to as the parallel coordinate. The above transformations ensure that $\mathbf{B} \cdot \nabla\zeta = 0$ and the coordinate ζ, therefore, labels field lines on a given flux-surface. As shown in Fig. 4.1 a flux-surface in the intermediate coordinate system ($ABCD$) is mapped (one-to-one and onto) to a parallelogram ($ABC'D'$) by this transformation. The so defined coordinates $-1/2 \leq \zeta \leq 1/2$ and $-1/2 \leq s \leq 1/2$ are dimensionless, while the coordinate ψ has the dimension of a spatial length.
A tokamak is periodic both in the toroidal as well as poloidal direction, which is now discussed on the basis of Fig. 4.1. Poloidal periodicity holds between the points $A \leftrightarrow D$, $B \leftrightarrow C$ and $E \leftrightarrow D'$, for example. Toroidal periodicity applies between the points $A \leftrightarrow B$, $D \leftrightarrow C$ and $D' \leftrightarrow C'$. In field aligned Hamada coordinates the poloidal and toroidal periodicity constraints on a full flux-surface can be formulated for an arbitrary function $f(\psi, \zeta, s)$ by [101]

$$f(\psi, \zeta, s \pm 1) = f(\psi, \zeta \pm q, s) \tag{4.11}$$

$$f(\psi, \zeta \pm 1, s) = f(\psi, \zeta, s). \tag{4.12}$$

[2]Coordinate curves follow from the variation of one coordinate (label of arrows in Fig. 4.1) while holding the other coordinates fixed.

The poloidal periodicity constraint [Eq. (4.11)] is applied at point D' with respect to point A and causes a toroidal displacement DD' (or equivalently AE) equals q. It expresses the fact that s is an extended angle, moving poloidally but following the field line at the same time. The toroidal periodicity constraint [Eq. (4.12)] is trivially applied at B with respect to A, for example.
The periodicity in ζ allows to define a Fourier decomposition

$$f(\psi, \zeta, s) = \sum_l \hat{f}_l(\psi, s) \mathrm{e}^{2\pi i l \zeta}, \tag{4.13}$$

where l is an integer mode number and $\hat{f}_l(\psi, s)$ is a complex Fourier coefficient. From the poloidal periodicity constraint a condition for the Fourier coefficient

$$\hat{f}_l(\psi, s \pm 1) = \hat{f}_l(\psi, s) \mathrm{e}^{\pm 2\pi i l q} \tag{4.14}$$

can be derived. A displacement of $\Delta s = \pm 1$, hence, induces a phase shift depending on l and q. Only when lq is an integer, i. e., when q is rational, the s domain is periodic and the flux-surface is called resonant for the mode with wave number l. A general structure of the Fourier coefficients allowed on a full flux-surface and in field-aligned Hamada coordinates is given by [101]

$$\hat{f}_l(\psi, s) = \sum_m \hat{f}_{lm}(\psi) \mathrm{e}^{2\pi \mathrm{i}(lq + m - m_0)s} \tag{4.15}$$

and adds an arbitrary number of periodic modes on $s \in [0, 1]$. The wave number $m_0 = \mathrm{NINT}(lq)$ is the nearest integer to lq and defines the longest wavelength satisfying the periodicity constraint for a given l.
Eqs. (4.13) and (4.15) define the discrete set of allowed wavelengths on a full toroidal flux-surface in straight field-aligned Hamada coordinates. This formulation is globally consistent, since the safety factor q is allowed to be an arbitrary function of ψ.[3] A truncation of the number of modes due to the consideration of a reduced flux-tube domain is discussed in Sec. 4.2.4.

4.2.2 Circular geometry

Although in GKW it is possible to use experimental MHD equilibria obtained from an interface with the CHEASE MHD code [102], it is common to work with simple analytical equilibria. One basic model assumes circular concentric flux-surfaces [9] (see Fig. 4.2). The assumption of circular concentric flux-surfaces is valid for a small inverse aspect ratio ϵ and normalized plasma pressure β, which

[3] The formulation of the flux-tube model (see Sec. 4.2.4) is based on Eqs. (4.13) and (4.15). In the context of a flux-tube *global consistency* also refers to the fact that a flux-tube can describe the whole flux-surface without limitations, provided enough toroidal modes are retained.

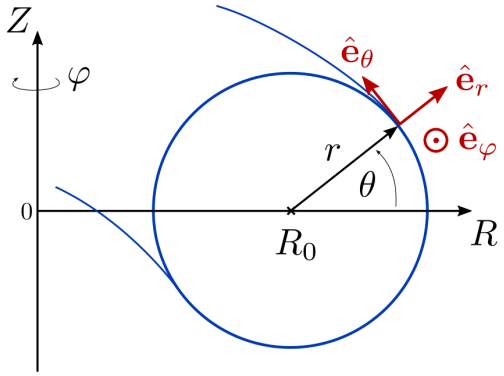

Figure 4.2: Circular concentric flux-surface (blue) centered at $R = R_0$ and $Z = 0$ in the coordinate system (r, θ, φ). The unit vectors $\hat{\mathbf{e}}_r$, $\hat{\mathbf{e}}_\theta$ and $\hat{\mathbf{e}}_\varphi$ form a local orthogonal base.

allows to neglect the Shafranov shift.[4] This simple equilibrium is applied also in this thesis, where it is referred to as *circular geometry*.
In this geometry model the flux-surfaces are parametrized by (see Fig. 4.2)

$$R = R_0 + r\cos\theta \tag{4.16}$$

$$Z = r\sin\theta \tag{4.17}$$

and the coordinate gradients relate to the unit vectors through

$$\nabla r = \hat{\mathbf{e}}_r \qquad \nabla\theta = \frac{1}{\epsilon R_0}\hat{\mathbf{e}}_\theta \qquad \nabla\varphi = \frac{1}{R}\hat{\mathbf{e}}_\varphi. \tag{4.18}$$

Furthermore, the radial derivative of the poloidal flux is given by

$$\frac{\partial\Psi}{\partial r} = \frac{rB_0}{\overline{q}}, \tag{4.19}$$

with

$$\overline{q} = s_B s_j \sqrt{1-\epsilon^2}\, q \tag{4.20}$$

and

$$\epsilon = \frac{r}{R_0}. \tag{4.21}$$

The expressions above uniquely determine the equilibrium magnetic field [Eq. (4.5)], which allows to derive the field-aligned Hamada coordinates [95]:

$$\psi = r \tag{4.22}$$

$$\zeta = -\frac{\varphi}{2\pi} + s_B s_j \frac{|q|}{\pi}\arctan\left[\sqrt{\frac{1-\epsilon}{1+\epsilon}}\tan\left(\frac{\theta}{2}\right)\right] \tag{4.23}$$

$$s = \frac{1}{2\pi}[\theta + \epsilon\cos\theta]. \tag{4.24}$$

The above coordinates describe exact circular concentric flux-surfaces, in that all orders of ϵ are kept in their definition. Further simplifications of this geometry type through the neglect of finite ϵ contributions are discussed in the next section.

[4] The Shafranov shift is the radial shift of the centers of consecutive flux-surfaces due to the presence of a radial pressure gradient [3]. Here, it is considered to be of the order of ϵ^2 and the approximation of the physcis is, therefore, valid up to order ϵ.

4.2.3 s-α geometry

The circular geometry introduced in Sec. 4.2.2 can be further simplified in the limit of an infinitely small inverse aspect ratio $\epsilon \ll 1$ by retaining only the lowest order terms of an expansion in ϵ. This leads to the simplified $s - \alpha$ model [103], where s and α relate to the magnetic shear and the pressure gradient, respectively. In this thesis, the Shafranov shift is neglected by setting the pressure gradient parameter $\alpha = -q_0^2 R_0 \beta'$ to zero [9].
The field-aligned Hamada coordinates follow from the expansion of Eq. (4.22)-(4.24) and read [95]

$$\psi = r \tag{4.25}$$

$$\zeta = \frac{s_B s_j}{2\pi}[|q|\theta - \varphi] \tag{4.26}$$

$$s = \frac{\theta}{2\pi}. \tag{4.27}$$

In order to retain trapping effects, finite inverse aspect ratio terms are kept in the definition of the magnitude of the magnetic field

$$B = \frac{B_0}{1 + \epsilon \cos\theta}, \tag{4.28}$$

that introduce the poloidal variation of the magnetic field. Although the simplified $s - \alpha$ model is inconsistent in the ϵ ordering of individual terms [9], it is applied in this thesis for comparability with previous studies [21].

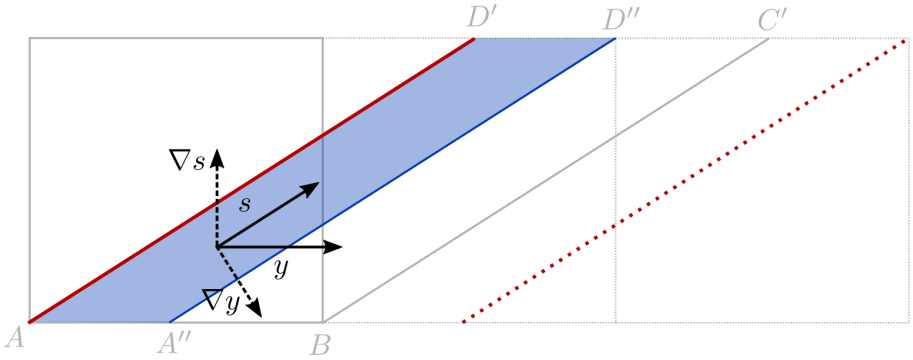

Figure 4.3: Truncation of the full flux-surface ($ABC'D'$) to a reduced flux-tube domain ($AA''D''D'$) with truncation number $l_0 = 2$. The flux-tube follows a reference field line (red solid line). Gray rectangles depict toroidal copies of full flux-surfaces in (ψ, ν, γ) coordinates (compare Fig. 4.1).

4.2.4 The flux-tube

The flux-tube represents a minimum plasma volume sufficient for the description of microturbulence. Here, it is defined as a domain with a perpendicular extent

sufficiently large compared with the perpendicular correlation length connected to microturbulence[5] and a parallel extent of the machine size, following a reference field line around the torus [104]. In straight field-aligned Hamada coordinates the reference field line is uniquely defined by the pair of coordinates (ψ_0, ζ_0).
The flux-tube model is closely related to the local limit (see Sec. 4.1). The local limit implies that geometry quantities are constant over the radial extent of the simulation volume. Constant values are defined at the position of the reference field line, such as the safety-factor $q(\psi_0) \equiv q_0$ and the inverse aspect ratio $\epsilon(\psi_0) \equiv \epsilon_0$. An exception is the radial variation of the safety factor[6], which is taken into account through a Taylor expansion up to first order in ρ_*

$$q(\psi) = q_0 + \frac{\partial q}{\partial \psi}\Big|_{\psi_0} (\psi - \psi_0) + \mathcal{O}(\rho_*^2), \tag{4.29}$$

with

$$\frac{\partial q}{\partial \psi}\Big|_{\psi_0} = \frac{q_0 \hat{s}_0}{\epsilon_0 R_0} \tag{4.30}$$

defining the magnetic shear $\hat{s}_0$, which is considered constant as well. In the local limit the safety factor, hence, varies linearly with the radial coordinate. The radial variation of the safety-factor causes a twist of the flux-tube domain (see Fig. 4.4).
Any numerical treatment requires the specification of boundary conditions. In the local limit the turbulence becomes homogeneous in the perpendicular direction, which demands periodicity in the spatial directions ψ and ζ. The twist of the flux-tube domain renders the boundary condition parallel to the magnetic field non-trivial, which is further elaborated on below.
A flux-tube is equivalent to a thinning of the set of allowed wave numbers on the full surface $l \in [\pm 1, \pm 2, ...]$ to $l \in [\pm l_0, \pm 2l_0, ...]$ with a truncation wave number $l_0 \gg 1$. In contrast to the full surface domain size $\zeta \in [0, 1]$ the extent of the flux-tube is reduced to $\zeta \in [0, l_0^{-1}]$ (see Fig. 4.3). On the reduced domain a function f can be Fourier decomposed by

$$f(\psi, \zeta, s) = \sum_{l'} \hat{f}_{l'}(\psi, s) \mathrm{e}^{\mathrm{i}2\pi l' l_0 (\zeta - \zeta_0)} \tag{4.31}$$

with l' an integer mode number. A full flux-surface description is then recovered for $l_0 = 1$.
Furthermore, it is convenient to define local coordinates

$$x - x_0 = \psi - \psi_0 \tag{4.32}$$

$$y - y_0 = R_0 \cdot (\zeta - \zeta_0) \tag{4.33}$$

[5]Since the scale connected to microturbulence is of the order of the Larmor radius $\rho_{\mathrm{th,i}}$, a typical perpendicular domain size, hence, is of the order of $10^1 - 10^2\ \rho_{\mathrm{th,i}}$.

[6]This is a consequence of Eq. (4.14) where q and l appear together, with the latter scaling as ρ_*^{-1}.

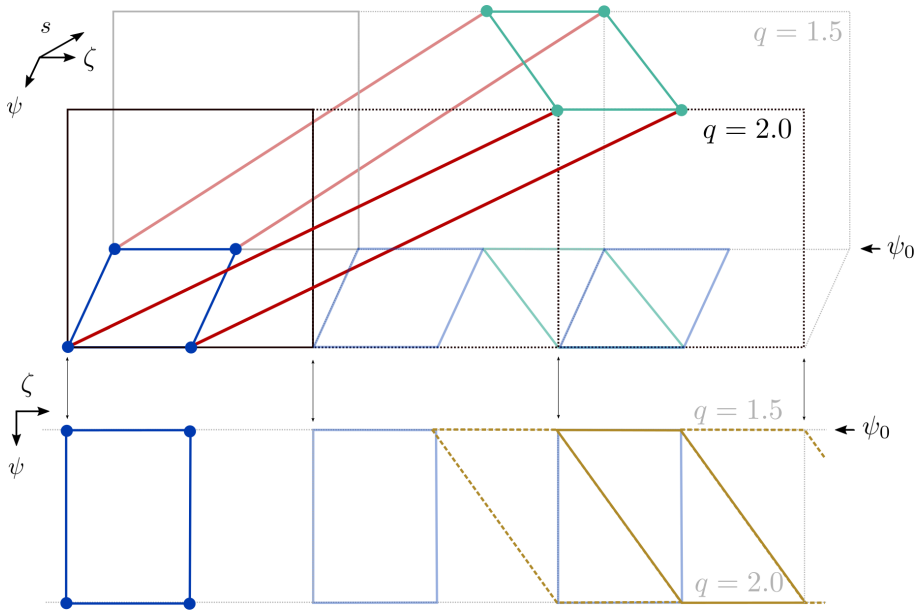

Figure 4.4: Top: Twist of the flux-tube domain due to sheared ambient magnetic field. Two radially displaced surfaces with $q = 1.5$ and $q = 2.0$ are shown. A rectangle cross section (blue dots connected by blue lines) deforms to a parallelogram (turquoise dots connected by lines) during a displacement $\Delta s = 1$ along the field lines (red lines). Light blue rectangles depict physically periodic toroidal copies of the initial cross section. The light turquoise parallelogram depict the physically periodic poloidal copy of the deformed cross section. Toroidal copies of full flux-surfaces in the coordinates (ψ, ν, γ) are indicated by black and gray rectangles (compare Fig. 4.1). Bottom: Mapping of the deformed cross section onto the initial cross section by periodic extension (gold dashed) according to the shifted parallel boundary conditions in a flux-tube.

and the local wave vector

$$k_y = \frac{2\pi l' l_0}{R_0}. \tag{4.34}$$

Both x and y then have the dimension of a spatial length and the box sizes L_x and L_y will be chosen of the order of several 10^1 $\rho_{\mathrm{th,i}}$ throughout this thesis. Furthermore, $x_0 = L_x/2$ and $y_0 = L_y/2$ defining the center (reference field line) of the flux-tube.
Applying a Fourier decomposition in the radial direction as well, the representation of a spatial function in the local coordinates $f(x, y, s)$ becomes

$$f(x, y, s) = \sum_{k_x, k_y} \hat{f}(k_x, k_y, s) \mathrm{e}^{\mathrm{i}[k_x \cdot (x - x_0) + k_y \cdot (y - y_0)]}. \tag{4.35}$$

The above Fourier decomposition is applied to all perturbed quantities in GKW such as the perturbed distribution function f_{sp}, the electrostatic potential ϕ and

the magnetic vector potential $A_\parallel$. This approach is referred to as the *spectral representation*.
Using the spectral representation [Eq. (4.35)] and the expansion of q [Eq. (4.29)], in the local limit the ploidal periodicity constraint [Eq. (4.14)] can be formulated by

$$\sum_{k_x,k_y} \hat{f}(k_x,k_y,s\pm 1)\mathrm{e}^{\mathrm{i}[k_x\cdot(x-x_0)+k_y\cdot(y-y_0)]}$$
$$= \sum_{k_x,k_y} \hat{f}(k_x,k_y,s)\mathrm{e}^{\mathrm{i}k_y\cdot(y-y_0)\pm\mathrm{i}k_y(q_0\hat{s}_0/\epsilon_0)\cdot(x-x_0)+\mathrm{i}k_x\cdot(x-x_0)} \times \mathrm{e}^{\pm\mathrm{i}2\pi l' l_0 q_0}. \tag{4.36}$$

For an integer $l_0 q_0$ the exponential factor $\exp(\pm 2\pi \mathrm{i} l' l_0 q_0) = 1$. In this case $q_0 = n/l_0$, with n an integer, is rational on the reference flux-surface and the truncation mode l_0 is said to be resonant there. This applies also to full flux-surface descriptions ($l_0 = 1$), provided q_0 is an integer. Due to $l_0 \gg 1$ in the flux-tube limit, it is usually assumed that $l_0 q_0$ can be made an integer by very small corrections to the safety-factor [95]. The safety factor q_0 is then quasi-rational and the truncation mode l_0 is quasi-resonant on the reference flux-surface.
To proceed, the periodicity constraint (4.36) can then be recast into a condition for the Fourier coefficients at the parallel domain boundary $s = \pm 1/2$ of the flux-tube

$$\hat{f}(k_x,k_y,\pm 1/2) = \hat{f}(k_x \pm \Delta k_x, k_y, \mp 1/2), \tag{4.37}$$

with the radial wave vector shift defined by

$$\Delta k_x = k_y \frac{q_0 \hat{s}_0}{\epsilon_0}. \tag{4.38}$$

The expression above is called the *shifted periodic boundary condition* and is commonly applied in local flux-tube simulations.
A visualization of the shifted periodic parallel boundary conditions is given in Fig. 4.4 in the coordinates (ψ, ζ, s). Due to the sheared ambient magnetic field a rectangular cross section deforms into a parallelogram, when following the field lines for one poloidal turn $\Delta s = 1$. Toroidal periodicity is indicated by the light blue copies while poloidal periodicity is depicted by the light turquoise copy. The overlap of the rightmost light blue rectangle and the light turquoise parallelogram clearly brings out the points that are physically equal in the double periodic tokamak.
If only a part of the flux-surface is considered ($l_0 \neq 1$), there is no full (or even any) overlap and consequently in a flux-tube the poloidal periodicity constraint has to be modelled appropriately. First, the assumption of q_0 being quasi-resonant amounts for shifting the deformed cross section such that side at ψ_0 is aligned with the initial rectangle (solid gold). Second, periodic boundary conditions in ζ then allow to extend the domain periodically (dashed gold) and to map out the

entire cross section. This mapping in position space is equivalent to the radial wave vector shift in Fourier space as expressed through Eqs. (4.37) and (4.38). Form Eq. (4.36) it is also seen that the poloidal periodicity constraint is equivalent to a radially dependent phase shift $\exp[\mathrm{i}\Delta\varphi(x)]$ with $\Delta\varphi(x) = \Delta k_x \cdot (x - x_0)$. A wave is defined to be resonant, if $\Delta\varphi = 2\pi n$, with n an integer (including zero). Clearly, all allowed waves in the simulation domain are resonant at $x = x_0$. At the reference surface the simulation domain, hence, is strictly periodic in s. This is a direct consequence of q_0 being quasi-rational and the truncation mode l_0 (and all higher order harmonics $l' > 1$) being quasi-resonant there. The location $x = x_0$ is therefore referred to as lowest order rational or resonant layer (LORL). Due to the radially varying safety factor there may exist multiple resonant layers (RL) per mode in the simulation domain with the radial spacing

$$\Delta x_{\mathrm{RL}}(l') = \frac{2\pi}{k_y(l')} \frac{\epsilon_0}{q_0 \hat{s}_0} = \frac{R_0}{l' l_0} \frac{\epsilon_0}{q_0 \hat{s}_0} \tag{4.39}$$

depending on the mode's wave number l'. The positions $x_{\mathrm{LORL}} = x_0 + n \cdot \Delta x_{\mathrm{RL}}(l' = 1)$, with n an integer, represent locations of high symmetry, since all allowed waves are resonant there. At x_{LORL} the simulation domain, again, is strictly periodic in the coordinate s.

4.2.5 Spatial grid setup

Having established the basic concept of the local flux-tube approach in Sec. 4.2.4, this section will be more specific about the discretization of the spatial grid required for a numerical simulation. A length scale is ascribed to the simulation domain and its relation to the truncation wave number l_0 is discussed within the local limit.

It is common to restrict the field-aligned coordinate to the interval $-1/2 < s < 1/2$ representing one poloidal turn. Here, $s = 0$ defines the low field side and $s = \pm 1/2$ the high field side. This is a convenient choice since it leads to a full flux-surface description, if $l_0 = 1$, and since it does not introduce unphysical modes which would be present for multiple poloidal turns [101].

Next, the wave vector grid in x and y is to be discussed. A discrete set of wave vectors may be defined through an odd number of wave vectors N_k and a minimum wave vector $k_{\min} = k_{\max}/[(N_k - 1)/2]$ by $k_i = i \cdot k_{\min}$ with the integer $-(N_k - 1)/2 \leq i \leq (N_k - 1)/2$ and $k_{\max}$ the maximum resolved wave vector. The reality of any physical quantity f demands $\hat{f}(k_x, k_y, s) = \hat{f}^*(-k_x, -k_y, s)$, where the asterik denotes the complex conjugate. The complete information of f is therefore retained on the half grid $0 \leq k_y \leq k_{y,\max}$ and $-k_{x,\max} \leq k_x \leq k_{x,\max}$. In this thesis the number of the former modes is denoted by N_{k_θ}, while the number of the latter modes is referred to as N_{k_x}. The full set of wave vectors then is defined by $k_y = i_y k_{y,\min}$ with the integer $0 \leq i_y \leq (N_{k_\theta} - 1)$ and $k_x = i_x k_{x,\min}$ with the

integer $-(N_{k_x}-1)/2 \leq i_x \leq (N_{k_x}-1)/2$.
In order to introduce a length scale into the system, the maximum resolved wave vector $k_{y,\max}$ is specified in units of the Larmor radius $\rho_{\mathrm{th,i}}$. Considering a wave with $k_x = 0$ the perpendicular gradient

$$\nabla y \frac{\partial f}{\partial y} = \sum_{k_y} \mathrm{i} \nabla y k_y \hat{f}(k_y, k_x, s) \mathrm{e}^{\mathrm{i}k_y \cdot (y - y_0)} \equiv \sum_{k_y} \mathrm{i}\mathbf{k} \hat{f}(k_y, k_x, s) \mathrm{e}^{\mathrm{i}k_y \cdot (y - y_0)} \tag{4.40}$$

may be used to assign

$$(k_{\theta,\max}\rho_{\mathrm{th,i}})^2 = g^{yy}|_{s=0} (k_{y,\max}\rho_{\mathrm{th,i}})^2, \tag{4.41}$$

where $g^{yy}|_{s=0} = \nabla y \cdot \nabla y|_{s=0}$ is the y-y-component of the metric tensor at $s = 0$. The right-hand side of Eq. (4.41) is the squared magnitude of the wave vector of a perpendicular mode at the low field side normalized by $\rho_{\mathrm{th,i}}$. It is sometimes referred to as the poloidal wave vector k_θ. In GKW $k_{\theta,\max}\rho_{\mathrm{th,i}}$ and N_{k_θ} are input parameters which determine the k_y-grid setup entirely. Once the grid is defined the box size $L_y = 2\pi/k_{y,\min} = 2\pi(N_{k_\theta} - 1)/k_{y,\max}$ is determined.
Based on the shifted parallel boundary condition [Eq. (4.37)] a convenient choice of the minimum radial wave vector is

$$k_{x,\min} = \frac{k_{y,\min}}{i_{\mathrm{k}}} \frac{q_0 \hat{s}_0}{\epsilon_0}, \tag{4.42}$$

where i_{k} is a positive integer. The equation above expresses that the wave length $2\pi/\Delta k_x$ connected to the radial wave vector shift Δk_x needs to be an integer fraction of the radial box size $L_x = 2\pi/k_{x,\min}$. For $k_{y,\min}$ the former wavelength is equivalent to Δx_{RL} as defined in Eq. (4.39). The input parameter i_{k}, therefore, defines the number of lowest order resonant layers in the simulation domain. In a turbulence simulation the parameter i_{k} is contraint by the requirement of the numerics to resolve turbulent eddies that tend to form circular structures, i. e., $k_{x,\min} \sim k_{y,\min}$. For the CYCLONE base case parameters (see Sec. 4.4), considered throughout this thesis, the condition $k_{x,\min} \sim k_{y,\min}$ then demands $i_{\mathrm{k}} \in [5,\ 6]$.
A normalized Lamor radius can be assigned to the simulated surface through equating Eq. (4.34) and $k_y = l' k_{y,\max}/(N_{k_\theta} - 1)$ to obtain

$$\rho_* = \frac{k_{\theta,\max}\rho_{\mathrm{th,i}}}{2\pi\sqrt{g^{yy}|_{s=0}}} \frac{1}{l_0(N_{k_\theta} - 1)} \approx \frac{(k_{\theta,\max}\rho_{\mathrm{th,i}})\epsilon_0}{q_0} \frac{1}{l_0(N_{k_\theta} - 1)} \tag{4.43}$$

In the latter step the large aspect ratio limit $\sqrt{g^{yy}|_{s=0}} \approx q_0/(2\pi\epsilon_0)$ is adopted. For typical simulation parameters $(k_{\theta,\max}\rho_{\mathrm{th,i}}, N_{k_\theta}, \epsilon_0, q_0) = (1.4, 21, 0.19, 1.4)$ compliant to most of the simulations presented in this thesis and for a full flux-surface description $l_0 = 1$ one finds $\rho_* \approx 1.0 \times 10^{-2}$.[7] For the local model to describe a

[7] In the case of exact circular concentric flux-surfaces and the given standard parameters $\rho_* \approx 2.7 \times 10^{-2}$.

full surface compliant to present day tokamaks [$\rho_* \sim \mathcal{O}(10^{-3})$] a ten-fold increase of N_{k_θ} at fixed $k_{\theta,\max}\rho_{\mathrm{th,i}}$ would be required. This is equivalent to an increase of the box size L_y by an order of magnitude.

4.3 Gyrokinetic Workshop (GKW)

The flux-tube version of the Eulerian gyrokinetic code GKW [95], applied in this thesis, solves the gyrokinetic equation in the δf-approximation and in flux-tube geometry. This section summarizes the equations implemented in GKW and in the form used throughout this work. Finally, the diagnostics applied in the body of this work are briefly discussed.

4.3.1 Gyrokinetic equation

The gyrokinetic equation implemented in the flux-tube version of GKW is obtained by applying the δf-approximation and retaining only first order terms in ρ_*. This procedure provides an evolution equation for the perturbed distribution function.
In the present work the equilibrium distribution function is chosen to be a maxwellian

$$F_{0,\mathrm{sp}} = F_{\mathrm{M,sp}} = \frac{n_{0,\mathrm{sp}}}{(2\pi T_{0,\mathrm{sp}}/m_{\mathrm{sp}})^{3/2}} \exp\left(-\frac{m_{\mathrm{sp}} v_\parallel^2/2 + \mu B}{T_{0,\mathrm{sp}}}\right), \tag{4.44}$$

with $n_{0,\mathrm{sp}}$ and $T_{0,\mathrm{sp}}$ denoting the species equilibrium density and temperature, respectively, and B is the equilibrium magnetic field. Modifications of the equilibrium distribution by fast particles [105] or neoclassical effects [106] are not considered.
Since the term on the right-hand side of the gyrokinetic equation [Eq. (3.9)] containing the time derivative of the parallel vector potential[8] is numerically difficult to handel, a modified perturbed gyrocenter distribution function

$$g_{\mathrm{sp}} = f_{\mathrm{sp}} + \frac{Z_{\mathrm{sp}} e v_\parallel}{T_{0,\mathrm{sp}}} \langle A_\parallel \rangle_{\mathrm{ga,sp}} F_{\mathrm{M,sp}} \tag{4.45}$$

is defined, where Z_{sp} is the (signed) species charge number, e is the elementary charge, $A_\parallel$ is the parallel component of the perturbed vector potential and $\langle ... \rangle_{\mathrm{ga,sp}}$ denotes the gyro-average.
The evolution equation for the modified perturbed distribution function in first

[8] The time derivative of the parallel vector potential enters through the equation of motion $\partial_t v_\parallel$ [Eq. (3.11)] together with the expression for the gyro-averaged perturbed electric field $\mathbf{E}$ [Eq. (3.18)].

order of ρ_* then reads [95]

$$\frac{\partial g_{\mathrm{sp}}}{\partial t} + (v_\parallel \mathbf{b} + \mathbf{v}_D) \cdot \nabla f_{\mathrm{sp}} + (\mathbf{v}_E + \mathbf{v}_{\delta B}) \cdot \nabla g_{\mathrm{sp}} - \frac{\mu \mathbf{b} \cdot \nabla B}{m_{\mathrm{sp}}} \frac{\partial f_{\mathrm{sp}}}{\partial v_\parallel} = S_{\mathrm{sp}} + D_{\mathrm{sp}} \tag{4.46}$$

with the source term

$$S_{\mathrm{sp}} = -(\mathbf{v}_E + \mathbf{v}_{\delta B}) \cdot \nabla_p F_{\mathrm{M,sp}} - \frac{F_{\mathrm{M,sp}}}{T_{0,\mathrm{sp}}} (v_\parallel \mathbf{b} + \mathbf{v}_D) \cdot Z_{\mathrm{sp}} e \nabla \langle \phi \rangle_{\mathrm{ga,sp}}. \tag{4.47}$$

The inverse radial density and temperature gradient lengths $L_{n,\mathrm{sp}}^{-1} = -\partial_\psi \ln(n_{0,\mathrm{sp}})$ and $L_{T,\mathrm{sp}}^{-1} = -\partial_\psi \ln(T_{0,\mathrm{sp}})$ enter the source term through

$$\nabla_p F_{\mathrm{M,sp}} = -\nabla\psi \left[\frac{1}{L_{n,\mathrm{sp}}} + \left(\frac{m_{\mathrm{sp}} v_\parallel^2/2 + \mu B}{T_{0,\mathrm{sp}}} - \frac{3}{2} \right) \frac{1}{L_{T,\mathrm{sp}}} \right] F_{\mathrm{M,sp}}. \tag{4.48}$$

Energy injection and hence instability drive is provided by the above term. Due to the periodic boundary conditions in the radial direction the radially averaged gradients cannot change in time, i. e., they are fixed in time. Therefore, this formalism is also referred to as the *gradient-driven* approach. In GKW the inverse gradient lengths can be specified as input parameters and allow to control the level of instability and consequently the turbulence level.
In GKW both the parallel derivatives $\mathbf{b} \cdot \nabla$ and the parallel velocity derivative $\partial_{v_\parallel}$ are approximated by finite differences. Numerical stability, therefore, requires numerical dissipation which is incorporated into D_{sp} [11]. Details about the dissipation operator D_{sp} can be found in appendix B. In a collisionless description, as pursued in this thesis, numerical dissipation also provides the energy sink that balances energy injection by the background gradients [107].
The product of $\mathbf{v}_E$ and $\mathbf{v}_{\delta B}$ with ∇g_{sp} represent the only nonlinearities of Eq. (4.46) and are referred to as the $E \times B$- and magnetic flutter nonlinearity, respectively. These terms can be switched off and a simulation is then called a *linear simulation*, while calculations which retain the nonlinearities are referred to as *nonlinear simulations*.

4.3.2 Gyrokinetic field equations

The gyrokinetic field equations implemented in GKW are formulated in terms of the modified perturbed distribution function g_{sp} based on the Lie-perturbation technique described in Sec. 3.6.
In the δf-approximation and the local limit, the gyrokinetic Poisson equation reads

$$\sum_{\mathrm{sp}} Z_{\mathrm{sp}} e \left[\frac{2\pi B}{m_{\mathrm{sp}}} \int \mathrm{d}v_\parallel \int \mathrm{d}\mu \; J_0(\lambda_{\mathrm{sp}}) g_{\mathrm{sp}} + \frac{Z_{\mathrm{sp}} e n_{0,\mathrm{sp}}}{T_{0,\mathrm{sp}}} [\Gamma_0(b_{\mathrm{sp}}) - 1] \phi \right] = 0, \tag{4.49}$$

with the Bessel functions J_0 and Γ_0 as well as their arguments being discussed in Sec. 3.6. The above Poisson equation is linear in the perturbed distribution function g_{sp} and the perturbed electrostatic potential ϕ, since the background distribution function $F_{\mathrm{M,sp}}$ has been considered in the pull-back operator from gyro- to guiding-center phase space only [96].
The gyrokinetic Ampère's law for the parallel component of the perturbed vector potential is given by

$$\left[\nabla_\perp^2 + \mu_0 \sum_{\mathrm{sp}} \frac{Z_{\mathrm{sp}}^2 e^2 n_{0,\mathrm{sp}}}{m_{\mathrm{sp}}} \Gamma_0(b_{\mathrm{sp}})\right] A_\parallel = \mu_0 \sum_{\mathrm{sp}} Z_{\mathrm{sp}} e \frac{2\pi B}{m_{\mathrm{sp}}} \int \mathrm{d}v_\parallel \int \mathrm{d}\mu \; v_\parallel J_0(\lambda_{\mathrm{sp}}) g_{\mathrm{sp}}. \tag{4.50}$$

When the equation above is written in normalized form (see Sec. 4.3.4 for the details about the normalization)

$$\left[\nabla_{\perp,\mathrm{N}}^2 + \beta \sum_{\mathrm{sp}} \frac{Z_{\mathrm{sp}}^2 n_{\mathrm{R,sp}}}{m_{\mathrm{R,sp}}} \Gamma_0(b_{\mathrm{sp}})\right] A_{\parallel,\mathrm{N}} = \tag{4.51}$$

$$\beta \sum_{\mathrm{sp}} Z_{\mathrm{sp}} \frac{2\pi B_{\mathrm{N}}}{m_{\mathrm{R,sp}}} \int \mathrm{d}v_{\parallel,\mathrm{N}} \int \mathrm{d}\mu_{\mathrm{N}} \; v_{\parallel,\mathrm{N}} J_0(\lambda_{\mathrm{sp}}) g_{\mathrm{sp,N}}, \tag{4.52}$$

the normalized plasma pressure

$$\beta = \frac{n_0 T_0}{B_0^2/(2\mu_0)} \tag{4.53}$$

enters. In the case of a finite β, the perturbed gyro-center current density on the right-hand side of Eq. (4.52) couples to the parallel component of the perturbed vector potential. The quantity β can be specified as input parameter in GKW.
A simulation is called *electromagnetic*, if $\beta \neq 0$ and, hence, if perturbations in $A_\parallel$ are introduced. Otherwise a simulation is referred to as *electrostatic* with perturbations in the electrostatic potential then contribute to the electromagnetic field exclusively. The strength of electromagnetic effects increases with β, which is typically of the order of ~ 1 % in a tokamak device [10, 11].

4.3.3 Spectral representation and semi-spectral approach

Throughout this thesis the spectral version of GKW is employed. In the spectral version all perturbed quantities are Fourier decomposed in the coordinates x and

y. The perturbed distribution function, for example, reads

$$f_{\mathrm{sp}}(x,y,s) = \sum_{k_x} \hat{f}_{\mathbf{k}}(k_x, k_y = 0, s) \tag{4.54}$$

$$+ \sum_{k_y>0} \sum_{k_x} \Big\{ \hat{f}_{\mathbf{k}}(k_x,k_y,s) \times \exp[\mathrm{i}k_x \cdot (x-x_0) + \mathrm{i}k_y \cdot (y-y_0)] \tag{4.55}$$

$$+ \hat{f}^*_{\mathbf{k}}(k_x,k_y,s) \times \exp[-\mathrm{i}k_x \cdot (x-x_0) - \mathrm{i}k_y \cdot (y-y_0) \Big\}, \tag{4.56}$$

where the asterik denotes the complex conjugate. Since the distribution function is a real quantity the Fourier coefficients satisfy $\hat{f}_{-\mathbf{k}}(-k_x,-k_y,s) = \hat{f}^*_{\mathbf{k}}(k_x,k_y,s)$. Consequently some Fourier coefficients are redundant and in the code the evolution of modes with $k_y \geq 0$ is calculated exclusively, while both positive and negative k_x are kept. The wave vector grid setup as well as the boundary conditions are described in Sec. 4.2.5 and Sec. 4.2.4, respectively.
The spectral approach is beneficiary for numerical computations since spatial derivatives in x and y become multiplicative operations

$$\frac{\partial}{\partial x^\alpha} \rightarrow \mathrm{i}k_\alpha, \tag{4.57}$$

where $x^\alpha \in [x,y]$ and $k_\alpha \in [k_x,k_y]$. Furthermore, in Fourier space the gyroaverage is equivalent to a multiplication with the Bessel function (see Sec. 3.5), rather than a nonlocal spatial average over the Larmor orbit as it would be in position space. A summary of the governing equations in the spectral representation is given in appendix B
The evaluation of the quadratic nonlinearity of the gyrokinetic equation in Fourier space, however, is inefficient. Instead, the nonlinearity is evaluated according to $\mathcal{T}(\mathcal{T}^{-1}(\hat{A})\mathcal{T}^{-1}(\hat{B}))$, where $\hat{A}$ and $\hat{B}$ are the Fourier coefficients of the products entering the $E \times B$- and magnetic flutter nonlinearity [see Eq. (4.46)] and $\mathcal{T}$ as well as $\mathcal{T}^{-1}$ denote a direct and inverse Fourier transform, respectively. This procedure is known as the *semi-spectral approach*.

4.3.4 Normalizations

The set of governing equations (4.46), (4.49) and (4.50) is given in dimensional form. In the code, however, they are implemented in dimensionless form. This section summarizes the normalization convention applied throughout this thesis.

First a set of reference quantities is defined:

$$\rho_{\mathrm{th},0} : \text{reference thermal Lamor radius} \tag{4.58}$$
$$v_{\mathrm{th},0} : \text{reference thermal velocity} \tag{4.59}$$
$$m_0 : \text{reference mass} \tag{4.60}$$
$$n_0 : \text{reference density} \tag{4.61}$$
$$T_0 : \text{reference temperature} \tag{4.62}$$
$$B_0 : \text{reference magetic field strength} \tag{4.63}$$
$$R_0 : \text{reference major radius} \tag{4.64}$$

Some of the reference quantities are related through

$$T_0 = \frac{1}{2} m_0 v_{\mathrm{th},0}^2 \qquad \rho_{\mathrm{th},0} = \frac{m_0 v_{\mathrm{th},0}}{e B_0} \qquad \beta = \frac{n_0 T_0}{B_0^2/(2\mu_0)}. \tag{4.65}$$

The latter represents a constraint on the reference quantities in electromagnetic simulations, when the normalized plasma pressure β is specified.
Equilibrium quantities are normalized according to

$$T_{0,\mathrm{sp}} = T_{\mathrm{R,sp}} T_0 \qquad m_{\mathrm{sp}} = m_{\mathrm{R,sp}} m_0 \qquad n_{0,\mathrm{sp}} = n_{\mathrm{R,sp}} n_0 \qquad v_{\mathrm{th,sp}} = v_{\mathrm{R,sp}} v_{\mathrm{th},0}, \tag{4.66}$$

with the index 'R' referring to normalized background quantities with species dependence. The perturbed fields are normalized by

$$\phi = \rho_* \frac{T_0}{e} \phi_{\mathrm{N}} \qquad A_\parallel = B_0 R_0 \rho_*^2 A_{\parallel,\mathrm{N}}, \tag{4.67}$$

where the index 'N' denotes normalized quantities. The parameters time t, equilibrium magnetic field strength B and major radius R are normalized by

$$t = R_0 t_{\mathrm{N}} / v_{\mathrm{th},0} \qquad B = B_0 B_{\mathrm{N}} \qquad R = R_0 R_{\mathrm{N}}. \tag{4.68}$$

The distribution functions are normalized by

$$f_{\mathrm{sp}} = \rho_* \frac{n_{0,\mathrm{sp}}}{v_{\mathrm{th,sp}}^3} f_{\mathrm{sp,N}} \qquad F_{\mathrm{M,sp}} = \frac{n_{0,\mathrm{sp}}}{v_{\mathrm{th,sp}}^3} F_{\mathrm{M,sp,N}}. \tag{4.69}$$

The background gradient lengths are normalized by

$$\frac{1}{L_{n,\mathrm{sp,N}}} = \frac{R_0}{L_{n,\mathrm{sp}}} \qquad \frac{1}{L_{T,\mathrm{sp,N}}} = \frac{R_0}{L_{T,\mathrm{sp}}} \tag{4.70}$$

The spatial coordinates are normalized with the reference Larmor radius

$$\psi = \psi_{\mathrm{N}} / \rho_{\mathrm{th},0} \qquad x = x_{\mathrm{N}} / \rho_{\mathrm{th},0} \qquad y = y_{\mathrm{N}} / \rho_{\mathrm{th},0} \tag{4.71}$$

and the velocity space coordinates are normalized by

$$v_\parallel = v_{\mathrm{th,sp}} v_{\parallel,\mathrm{N}} \qquad \mu = \frac{m_{\mathrm{sp}} v_{\mathrm{th,sp}}^2}{B_0} \mu_{\mathrm{N}}. \tag{4.72}$$

Throughout this work $T_{\mathrm{R,i}} = m_{\mathrm{R,i}} = n_{\mathrm{R,i}} = 1$ and hence $\rho_{\mathrm{th},0} = \rho_{\mathrm{th,i}}$ as well as $v_{\mathrm{th},0} = v_{\mathrm{th,i}}$. The latter (ion-) quantity is therefore always chosen to specify the units in the body of this thesis.

4.3.5 Diagnostics

The solution of the gyrokinetic Valsov-Maxwell system provides one with the trajectory of the perturbed distribution function $f_{\mathrm{sp}}(x, y, s, v_{\parallel}, \mu, t)$ in five-dimensional gyrocenter phase space and the fields $\phi(x, y, s, t)$ as well as $A_{\parallel}(x, y, s, t)$ in three-dimensional position space. In order to allow for physical interpretations of the outcome of a numerical simulation the above quantities have to be further processed. This is done by *diagnostics*.
One of the main focus of this thesis is the development and application of diagnostics that allow for a proper interpretation of the interplay of zonal flows and microturbulence. Several diagnostics have been developed and the reader is referred to the respective chapters for a more detailed description.
In chapter 6 director field diagnostics (see Refs. [108, 27] for more details) are applied in postprocessing to obtain a direct measure of the zonal flow shear induced tilt of turbulent structures.
In chapter 7 a field line tracing diagnostic[9] (see Refs. [57, 59] for more details) is applied in postprocessing to identify the influence of mesoscale zonal flow patterns on magnetic stochasticity. Note, that the original version of the field line tracing diagnostic has not been implemented by the author. The authors work covered debugging and testing of this diagnostic.
Both in chapter 7 and 8 a zonal flow intensity evolution diagnostic[10] is applied that has been implemented in GKW by the author to be able to study zonal flow driving and damping mechanisms. A description of this diagnostic is available in the GKW documentation [98].
In chapter 8 energetics and nonlinear transfer diagnostics[11] (see Refs. [72, 99, 73, 110, 74, 111, 22, 63, 64, 65, 66, 112] for more details) are applied to obtain a direct measure of the role of the self-interaction mechanism and the resulting zonal fine scale structures for the nonlinear saturation of ion temperature gradient driven turbulence. Note, that the original version of these diagnostics has not been implemented by the author. The authors work covered an extension of the diagnostics suitable for the study of electromagnetic turbulence as well as debugging and testing. A description of these diagnostics has been added to the GKW documentation [98].

[9] The octave code `FL_Tracing.m` can be found on the gkw git repository [109] in the directory `/octave`.

[10] This diagnostic is implemented in the Fortran module file `diagnos_zonal_evo.f90`, which can be found in the gkw git repository [109] in the directory `/src`

[11] These diagnostics are implemented in the Fortran module files `diagnos_energy_evo.f90` and `diagnos_nonlin_transfer.f90`, which can be found in the gkw git repository [109] in the directory `/src`

4.3.6 Background $E \times B$-shear flow

In chapter 6 a sheared background $E \times B$ shear flow is applied through the wave vector re-mapping method [103]. This section briefly introduces the underlying concepts.
A sheared equilibrium $E \times B$ flow

$$\mathbf{v}_s(x) = \frac{\mathbf{b} \times \nabla \overline{\Phi}}{B} \tag{4.73}$$

is assumed, where $\overline{\Phi}(x)$ is the perturbed electrostatic potential connected to this flow, such that the background $E \times B$ shearing rate

$$\gamma_E = \frac{1}{B_0} \frac{\partial^2 \overline{\Phi}}{\partial x^2} = \text{const.} \tag{4.74}$$

is constant. Eq. (4.74) requires $\mathbf{v}_s$ to vary linearly with the coordinates x.
The background $E \times B$ flow contributes to the gyrokinetic equation in form of an additional convective term for the distribution function

$$\frac{\partial \hat{g}_{\text{sp}}}{\partial t} \stackrel{+}{=} -\mathbf{v}_s \cdot \nabla g_{\text{sp}} = -\overline{\gamma}_E x \frac{\partial g_{\text{sp}}}{\partial y}, \tag{4.75}$$

where

$$\overline{\gamma}_E = \frac{\nabla x \times \nabla y}{B} \frac{\partial^2 \overline{\Phi}}{\partial x^2} = \gamma_E \frac{\nabla x \times \nabla y}{B_{\text{N}}}. \tag{4.76}$$

In the coordinates that move with the flow $\mathbf{v}_s$

$$x' = x \tag{4.77}$$
$$y' = y - x \overline{\gamma}_E t \tag{4.78}$$

the radial wave vector becomes time dependent [95]

$$k'_y = k_y \tag{4.79}$$
$$k'_x = k_x - k_y \overline{\gamma}_E t. \tag{4.80}$$

In a gyrokinetic code, the time dependent wave vector would require the re-evaluation of the linear terms and the Bessel functions at every time-step, which would be computationally expensive. Instead, in GKW the solution $\hat{g}_{\text{sp}}(k_x, k_y, s)$ is re-mapped between the fixed wave vectors of the original wave vector grid. In practice for $\overline{\gamma}_E > 0$ the re-mapping

$$\hat{g}_{\text{sp}}(k_x, k_y, s) \rightarrow \hat{g}_{\text{sp}}(k_x - \delta k_x, k_y, s) \tag{4.81}$$

is applied, when the inequality

$$\text{NINT}(k_y \overline{\gamma}_E t / \delta k_x) > i_r(k_y) \tag{4.82}$$

is satisfied, where NINT is a function that returns the nearest integer, δk_x is the radial wave vector grid spacing and i_r is an integer counting the number of times the solution has been remapped during the time t. The re-mapping is applied for each k_y independently.

4.4 CYCLONE base case

Given the large parameter space a tokamak plasma provides, it is useful to define some form of reference parameter set. The CYCLONE base case (CBC) parameters defined in Ref. [67] represent such a set that is widely used in the microturbulence community for the study of a typical tokamak core plasma.
CBC parameters are local parameters taken from a DIII-D high-confinement shot (shot#81499) [113] at $t = 4000$ ms and minor radius $r = 0.5a$, where a is the minor radius of the last closed flux-surface. Equal ion and electron temperature $T_\mathrm{i} = T_\mathrm{e}$ and equal ion and electron density $n_\mathrm{i} = n_\mathrm{e}$ are assumed. The normalized inverse ion temperature gradient length is $R/L_{T\mathrm{i}} = 6.92$, where R is the major radius, and the ratio of the ion density to temperature gradient length is $\eta_\mathrm{i} \equiv L_n/L_T = 3.114$. The geometry parameters are fixed by the safety factor $q = 1.4$, the inverse aspect ratio $\epsilon \equiv r/R = 0.18$ and the magnetic shear $\hat{s} \equiv (r/q)dq/dr = 0.776 - 0.796$.
In the original work [67] further simplifying assumptions were made, such as the consideration of electrostatic fluctuations, the adiabatic electron closure and a single ion species. In the present thesis CBC parameters serve as base case for any parameter study, while two of the simplifying assumptions are relaxed in that electrons are treated as a kinetic species and electromagnetic fluctuations are included. The former modification requires a specification of the normalized electron inverse temperature and density gradient lengths which are set to $R/L_{T\mathrm{e}} = R/L_{T\mathrm{i}}$ and $\eta_\mathrm{e} = \eta_\mathrm{i}$. Electromagnetic fluctuations are included through the choice of a finite β.

Chapter 5

Motivation 2: Interplay of microturbulence and zonal flow patterns —Why considering electron dynamics and electromagnetic effects?

This chapter motivates the work presented in the body of this thesis by asking the question: Why should one consider the impact of electron dynamics and electromagnetic effects on the interplay of microturbulence and zonal flow patterns? First, zonal flow pattern formation, a phenomenon often observed in near marginal turbulence, can be considered relevant for future fusion reactors, since they are likely to operate close to marginality [114, 115]. Second, the inclusion of electron dynamics and electromagnetic effects represents a crucial step towards a realistic description of the interplay of microturbulence and zonal flow patterns. Below, the authors intentions and aims behind the chapters 6 - 9 are outlined.

Chapter 6: *Analysis of zonal flow pattern formation and the modification of staircase states by electron dynamics in gyrokinetic near marginal turbulence*

Chapter 6 is based on the author's wish to improve the understanding of the apparent discrepancy between adiabatic and kinetic electron studies concerning zonal flow pattern formation in near marginal turbulence (i. e., difference in spatial scale and amplitude of 'zonal flow' patterns; see also Sec. 2.4.4). This chapter approaches this issue by means of a different (and somewhat unconventional) view on zonal flows based on the direct measurement of the

zonal flow induced tilt of turbulent structures through director field methods, instead of the often considered $E \times B$ shearing rate. In addition, the need for resolving long-term dynamics, often observed close to marginality in connection with mesoscale zonal flow pattern formation, is addressed. This chapter aims to improve the understanding of near marginal microturbulence;—a regime that is expected to be relevant for future reactors [114, 115].

Chapter 7: *Transport hysteresis in electromagnetic microturbulence caused by mesoscale zonal flow pattern induced mitigation of high β turbulence runaways*

Most of the research on near marginal microturbulence and mesoscale zonal flow pattern formation considers the electrostatic limit.[1] To the best knowledge of the author an investigation of electromagnetic microturbulence with the focus on mesoscale zonal flow pattern formation has not been addressed so far and, therefore, is subject of chapter 7. This chapter builds on the authors experience with mesoscale ZF pattern formation and long-term dynamics (Refs. [24, 25, 77] and especially chapter 6) and addresses the questions: Given that magnetic flutter may deplete zonal flows ([58, 60, 59], and Sec. 2.4.2), does mesoscale zonal flow pattern formation occur in near marginal electromagnetic microturbulence (it turns out that it does)? What consequence does mesoscale ZF pattern formation have on turbulence runaways and magnetic stochasticity (both being inherently electromagnetic effects)? These questions are approached through gyrokinetic long-term simulations complemented by diagnostics suitable for the study of magnetic stochasticity and zonal flow drive and damping processes. This chapter envisages to improve the understanding of (near marginal) electromagnetic microturbulence and, hence, may be relevant to future steady state tokamak scenarios [116, 117].

Chapter 8: *Energetics and nonlinear transfer analysis of the self-interaction mechanism in local gyrokinetic fluxtube simulations of ion temperature gradient driven turbulence*

The author's main intention of chapter 8 was a confirmation of the outcome of the director field study[2] by means of a well accepted additional nonlinear

[1] This has multiple reasons: (i) In a tokamak plasma β is typically small and, hence, electromagnetic effects are often neglected. (ii) Inclusion of electromagnetic effects compels the inclusion of electron dynamics which is computationally expensive; especially due to the occurrence of long-term dynamics in near marignal turbulence. (iii) The accessible β-range is limited due to the occurrence of turbulence runaways, which complicates the study of electromagnetic microturbulence.

[2] As one of the main results of chapter 6, self-interaction driven zonal fine scale structures are shown to hardly contribute to the zonal flow induced tilt of turbulent structures. Chapter 8

energy transfer study. With an energetics and nonlinear transfer diagnostic at hand one is capable to study nonlinear saturation processes, which motivated the author to investigate the self-interaction mechanism[3], and its role for nonlinear saturation, more in detail. This chapter aims to contribute to the current debate on the role of self-correlations in local fluxtube simulations [104, 85], with the focus being on the self-interaction parallel to the magnetic field.

Chapter 9: *Stability analysis of toroidally symmetric secondary modified staircase equilibria.*

The analysis presented in chapter 9 is motivated by the difference in the near marginal flux-gradient relation among adiabatic and kinetic electron studies.[4] The (dynamical) relevance of zonal flow patterns in near marginal turbulence and the tertiary instiability formalism [54][5] motivated the author to investigate the influence of such patterns on the stability properties. Here, the focus lies on the role of patterns directly related to electron dynamics as well as the role of electron instabilities. This chapter aims to improve the understanding of the role of electron dynamics and electron temperature gradient drive for turbulence generating instabilities close to marginality.

supports this statement by showing that self-interaction driven zonal structures do hardly contribute to the zonal flow mediated nonlinear transfer of generalized energy.

[3]The self-interaction mechanism is considered to affect studies that include electron dynamics in particular, since passing electrons lead to a significant extent of Eigenmodes along the magnetic field [19].

[4]Adiabatic electron studies show a discontinuous flux-gradient relation due to the formation of fully-developed staircase structures [24, 25], while kinetic electron studies find a smooth transition to turbulence [1] (and chapter 6).

[5]The tertiary instability formalism states that zonal structures (i. e., structures driven through secondary instabilities) may drive tertiary instabilities beside the primary instabilities driven by the background density and temperature gradients.

Chapter 6

Analysis of zonal flow pattern formation and the modification of staircase states by electron dynamics in gyrokinetic near marginal turbulence

This chapter is based on the publication [118].

6.1 Introduction

A rich body of literature demonstrates the significance of radially sheared zonal flows (ZFs), i. e., toroidally symmetric plasma flows due to the $E \times B$-drift, for both the nonlinear saturation [119, 120, 22, 65] as well as the nonlinear stabilization [62, 29, 69, 67] of microturbulence in tokamak plasmas. The underlying process is mediated by the $E \times B$ nonlinearity and can be understood either as resulting from the deformation or equivalently tilting of turbulent structures through the advection by the sheared ZFs [29, 121, 68], or as a ZF mediated spectral transfer of energy to larger radial wave vectors [120, 22, 65]. As a consequence of ZF shearing turbulent structures exhibit an anisotropy or equivalently a tilt in position space; an property robustly observed in experiments [122, 123, 124] and simulations [68, 119].
A metric that characterizes the strength of this shearing process is the $E \times B$ shearing rate ω_{ExB}, i. e., the radial derivative of the advecting ZF velocity [121, 125]. Shear stabilization of microturbulence is then often expressed in form of the empirical Waltz rule $\omega_{\mathrm{ExB}} \sim \gamma$ [69, 125], where γ denotes the maximum linear growth rate of the underlying microinstabilities. Gyrokinetic studies sup-

port this condition [70, 71].
Since the nonlinear threshold for turbulence generation is directly related to shear stabilization [67], the stabilization rule $\omega_{\mathrm{ExB}} \sim \gamma$ suggests the shearing rate connected to ZFs close to marginality being of the order of typical growth rates. Indeed, the more recently discovered mesoscale ZF states in near margnial turbulence, also known as $E \times B$ staircases [23], exhibit amplitudes in terms of the $E \times B$ shearing rate satisfying the stabilization criterion remarkably well [25, 24]. The development of mesoscale staircase states is a robust phenomenon close to marginality when electrons are treated adiabatically [23, 25, 24, 76, 77]. By contrast, recent gyrokinetic studies that include electron dynamics report the development of dominant radial fine scale zonal structures [83, 126, 1]. Not only is the radial scale of such structures one order of magnitude smaller than the mesoscale of $E \times B$ staircases, also their $E \times B$ shearing rate is found to be one order of magnitude larger than typical growth rates [1]. Although the shearing rate connected to fine scale features exceeds typical growth rates significantly, turbulence is not quenched by such ZF structures. Most notably, in contrast to the adiabatic electron case, $E \times B$-staircase structures cannot be identified in the radial profile of ω_{ExB} for Cyclone Base Case (CBC) parameters [67] when kinetic electrons are included. Specific parameter choices, i. e., an increased magnetic shear compared to CBC parameters, have been necessary for the re-occurrence of $E \times B$ staircase structures also in kinetic electron models [1].
The above observations and discrepancies lead to the following questions: Do zonal fine scale structures prevent the development of mesoscale staircase structures? Why do fine scale features not result in shear stabilization although they over-satisfy the stabilization rule? Questions which will be addressed to in this work.
This work continues on from the work presented in Ref. [1] which uses the $E \times B$ shearing rate ω_{ExB} for the characterization of ZF pattern formation. Here, however, director field techniques [108] are applied to study zonal flow structure formation; a technique that has found application in the microturbulence context in Ref. [27]. This method is based on the ZF induced tilting of turbulent structures and, therefore, represents a more direct way of quantifying the ZF shearing compared to the $E \times B$ shearing rate. The focus lies on the detection of mesoscale ZF signatures and a comparison with fine scale structures. The remainder is organized as follows: In Sec. 6.2 the simulation set-up and the director field technique is described. The numerical results are presented in Sec. 6.3, consisting of an investigation of mesocscale zonal potential signatures in Sec. 6.3.1, the director field analysis in Sec. 6.3.2 and a study of the interplay of staircase states (detected in Sec. 6.3.2) with background $E \times B$ shear flows and turbulent heat transport in Sec. 6.3.3. Concluding remarks are given in Sec. 6.4.

6.2 Numerical set-up and diagnostics

6.2.1 Gyrokinetic simulation set-up

Nonlinear gradient-driven gyrokinetic simulations performed with the flux-tube version of GKW [95] under the δf-approximation are investigated. The plasma parameters are those of the CYCLONE base case (see Sec. 4.4). No plasma rotation and no collisions are considered. Both a single ion species (deuterium) and electrons are treated as separate kinetic species with an electron to ion mass $m_\mathrm{e}/m_\mathrm{i} = 2.72 \times 10^{-4}$. A small normalized pressure $\beta = 3 \times 10^{-4}$ is applied to include shear Alfvén wave physics. This allows for larger time steps and reduces the numerical cost. Furthermore, an ad-hoc circular geometry (see Sec. 4.2.2) is chosen. The numerical set-up, i. e., grid resolution, boundary conditions and numerical dissipation, is identical to the set G_1^circ summarized in Tab. 7.1 of chapter 7.

6.2.2 Director field diagnostic

In this work the orientation of tilted turbulent structures is measured by means of the director field [108]. This technique has already been applied to gyrokinetic turbulence in order to detect zonal flow shear zones [27]. Furthermore, measurements of eddy tilting in connection with sheared $E \times B$ flows also find application in various machines such as DIII-D [122], Tore Supra [79], MAST [123] and ASDEX Upgrade [124].
The director field of a two dimensional field $G(x, y)$ is defined by

$$k_G = \varphi(\overline{k}_G/|\overline{k}_G|), \tag{6.1}$$

where

$$\overline{k}_G = \left(\frac{\partial G}{\partial y}\right)^2 - \left(\frac{\partial G}{\partial x}\right)^2 - 2\mathrm{i}\frac{\partial G}{\partial y}\frac{\partial G}{\partial x} \tag{6.2}$$

and φ is the angle of the complex number $\overline{k}_G/|\overline{k}_G| = A\exp(\mathrm{i}\varphi)$ with $A, \varphi \in \mathbb{R}$. The director field maps the local orientation of structures in the morphology of G onto an angle with $k_G \in [-\pi, +\pi]$. It is reasonable to define turbulent structures in a 2D field $G(x, y)$ as structures formed by contour lines. The local tilting angle Θ of a turbulent structure may then be defined through the angle formed by the x-axis and the tangent to the contour line. This allows for a descriptive interpretation of the director field in terms of the tilting angle by noting the relation $\Theta = k_G/2$ with $\Theta \in [-\pi/2, +\pi/2]$. The validity of the tilting angle on the half circle mirrors the invariance of the orientation under rotation by π.
In this work the director field of the turbulent part of the electrostatic potential

$$\tilde{\phi} = \phi(x, y, s \approx 0) - \frac{1}{L_y}\int_{-L_y/2}^{L_y/2} \mathrm{d}y\ \phi(x, y, s \approx 0), \tag{6.3}$$

normalized by $\rho_* T_0/e$ ($\rho_* = \rho_{\mathrm{th,i}}/R_0$ is the normalized Larmor radius, $\rho_{\mathrm{th,i}}$ is the ion thermal Larmor radius and T_0 is the background temperature) and taken at the low field side (LFS) $s \approx 0$ is investigated (unless stated otherwise). The characterization of turbulent eddies through structures in $\tilde{\phi}$ at the LFS is justified by both the $E \times B$-drift being approximately tangential to contours in $\tilde{\phi}$ [45] and the turbulence intensity peaking at the LFS. Since the zonal $E \times B$ flow, and equivalently its shearing rate, is constant in y per definition, the director field is always averaged over y which is denoted by $K_G = \langle k_G \rangle_y$.

6.3 Numerical results

6.3.1 Investigation of mesoscale zonal potential signatures

In this section an investigation of mesoscale zonal potential signatures in turbulent states close to marginality is presented. The mesoscale is defined by the radial scale of the box size $L_x = 76.27\ \rho_{\mathrm{th,i}}$ and therefore relates to the zonal flow mode number $n_{\mathrm{ZF}} = 1$ (the zonal flow wave vector is $k_{\mathrm{ZF}} = 2\pi n_{\mathrm{ZF}}/L_x$).

Temporal longterm evolution

Although the turbulent ion heat flux $Q_{\mathrm{es,i}}$ typically saturates nonlinearly within an initial time period of a few 10^2 transit times $R_0/v_{\mathrm{th,i}}$, a transition to quasi-stationary stages with reduced flux [e. g. the time inteval $t \in [2250, 3900]\ R_0/v_{\mathrm{th,i}}$ for $R_0/L_T = 4.0$ (blue) in the top panel of Fig. 6.1] occurs at late times for cases close to marginality. Here, the species heat flux is defined by

$$Q_{\mathrm{es,sp}} = \int \mathrm{d}^3 v\ \frac{1}{2} m_{\mathrm{sp}} v^2 (\mathbf{v}_{\mathrm{E}} \cdot \nabla x)\ f_{\mathrm{sp}}, \tag{6.4}$$

where m_{sp} is the species mass, $\nabla x \cdot \mathbf{v}_{\mathrm{E}}$ is the radial component of he $E \times B$ drift and the flux being normalized by $\rho_*^2 n_0 T_0 v_{\mathrm{th,i}}^2$ with the background density n_0. The heat flux during both the periods with high and reduced turbulence level is mediated by avalanches (see also Sec. 6.3.3). The time scales connected to both the point of transition as well as the duration of the quasi-stationary stage can be large, i. e., up to several $10^3\ R_0/v_{\mathrm{th,i}}$, introducing a temporal long-term behavior.

The transition in $Q_{\mathrm{es,i}}$ is correlated with a temporal long term evolution of the mesoscale zonal potential component. The saturation of the shear in the $n_{\mathrm{ZF}} = 1$ zonal mode to its maximum value agrees with the transition in the turbulent level (see mid panel of Fig. 6.1). Here, the $E \times B$ shear rate is defined through [21, 24, 1]

$$\omega_{\mathrm{ExB}} = \frac{1}{2} \frac{\partial^2 \langle \phi \rangle}{\partial x^2} \tag{6.5}$$

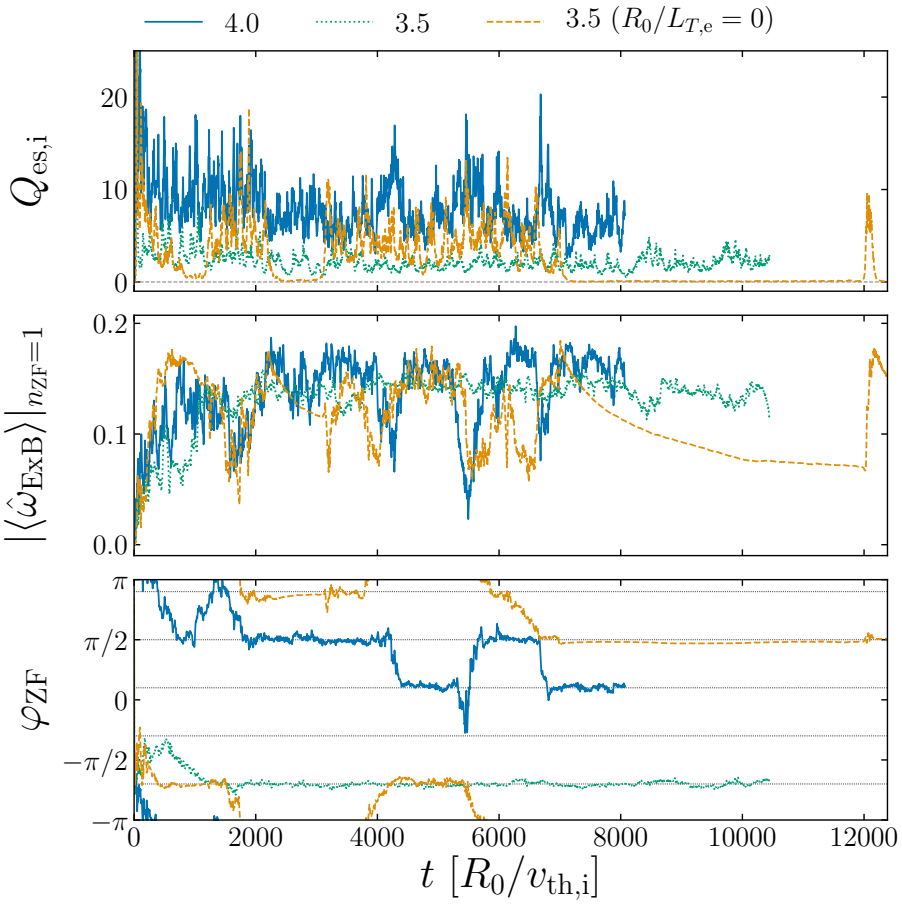

Figure 6.1: Time trace of the volume averaged ion electrostatic heat flux $Q_{es,i}$ (top), the shear carried by the $n_{ZF} = 1$ zonal mode $|\langle\hat{\omega}_{ExB}\rangle|_{n_{ZF}=1}$ in terms of $v_{th,i}/R_0$ (mid) and its radial phase φ_{ZF} in terms of radiants (bottom) for cases with $R_0/L_{T,i} = R_0/L_{T,e} = 4.0$ (blue, solid), $R_0/L_{T,i} = R_0/L_{T,e} = 3.5$ (green, dotted) and $R_0/L_{T,i} = 3.5$ and $R_0/L_{T,e} = 0$ (orange, dashed). Mind the periodicity of φ_{ZF} on $[-\pi, \pi]$.

where the zonal electrostatic potential is estimated by

$$\langle\phi\rangle = \frac{1}{L_y}\int_{-L_y/2}^{L_y/2} \mathrm{d}y\ \phi(x, y, s \approx 0). \tag{6.6}$$

Note that only normalized quantities enter the definitions above. The mesoscale shear $|\langle\hat{\omega}_{ExB}\rangle|_{n_{ZF}=1}$ is defined by the Fourier coefficient connected to the zonal flow wave vector $k_{ZF} = 2\pi n_{ZF}/L_x$ with $n_{ZF} = 1$ and is obtained by a radial Fourier transform of the zonal flow shearing rate. Estimated times scales on which the $n_{ZF} = 1$ zonal mode saturates to its quasi-stationary maximum value vary between several $10^2 - 10^3\ R_0/v_{th,i}$ and show no systematic dependence on R_0/L_T.

R_0/L_T	ΔT_1	ΔT_2	$Q_{\mathrm{es,i}}\vert_{\Delta T_1}$	$Q_{\mathrm{es,i}}\vert_{\Delta T_2}$
4.0	$225 - 1800$	$2250 - 3900$	9.48	6.80
3.5	$75 - 2025$	$3825 - 6979.5$	3.09	1.93

Table 6.1: Temporally and volume averaged ion electrostatic heat flux $Q_{\mathrm{es,i}}$ (in terms of $\rho_*^2 n_0 T_0 v_{\mathrm{th,i}}^2$) during high turbulent states ΔT_1 and reduced turbulent states ΔT_2 after the transition (both time intervals in terms of $R_0/v_{\mathrm{th,i}}$) for two cases which exhibit clearly separated turbulent periods.

The observed long-term behavior requires a long time integration to accurately describe the turbulent transport levels, since a reduction of $28 - 37$ % can occur as summarized in Tab. 6.1. The existence of this long term behavior is not always appreciated in literature.
A similar temporal long term behavior close to the nonlinear threshold is typically observed in studies that apply the adiabatic electron closure. In those cases a staircase state develops, quenching the turbulence after considerable time scales up to $10^3 - 10^4$ $R_0/v_{\mathrm{th,i}}$. The result is a non-monotonic dependence of the heat flux on R_0/L_T, referred to as the finite heat flux threshold [25], which expresses the inability of the local gradient-driven approach (with adiabatic electrons) to correctly access near marginal turbulence. It is therefore justified to ask whether (i) the present simulations are temporally converged and (ii) the local gradient-driven approach is appropriate to access near marginal turbulence.
In the present simulations with kinetic electrons and CBC parameters a transition from finite turbulence to suppressed states similar to Ref. [25] has not been observed. As reported in the aforementioned reference the onset of this transition is parameter dependent and occurs at earlier times with reduction of R_0/L_T. Although the case with $R_0/L_T = 3.5$ has been run up to 10000 $R_0/v_{\mathrm{th,i}}$ (see green dotted data in Fig. 6.1) no significant time evolution of both the turbulence and mesoscale shear level can be observed in the long time limit. The present simulations are, hence, considered temporally converged.
The flux-gradient relation (see Fig. 6.4) shows a smooth transition to turbulence, demonstrating that the local gradient-driven approach with kinetic electrons is able to access near marginal turbulence with arbitrary heat flux levels (at least for the plasma parameters compliant to the data shown). Indeed, the inclusion of electron physics results in a different overall turbulence regime. In order to elucidate this statement further a case with $R_0/L_{T,\mathrm{i}} = 3.5$ but $R_0/L_{T,\mathrm{e}} = 0$ has been investigated (see orange dashed data in Fig. 6.1). This case features turbulence - mesoscale zonal flow dynamics similar to gradient-driven simulations with the adiabatic electron approximation just below the finite heat flux threshold [25]; —transitions between extended phases with finite intermittent turbulence and suppressed states are clearly visible. This outcome indicates that the ability of the local gradient-driven approach (with kinetic electrons and CBC paramet-

ers) in accessing arbitrary near marginal turbulent states is related to electron instabilities that are not included into an adiabatic electron description. Due to this outcome the local gradient-driven approach with kinetic electrons is valued an appropriate (and computationally feasible) approach to access near marginal turbulence.

Radial lock-in of mesoscale structures

The long-term evolution of the mesoscale zonal potential mode exhibit a concomitant reduction in its radial variability. Here, the radial orientation is diagnosed through the use of the radial phase φ_{ZF} defined by

$$\hat{\omega}_{\mathrm{ExB}}(k_{\mathrm{ZF}}) = \hat{\omega}^{A}_{\mathrm{ExB}}(k_{\mathrm{ZF}}) \exp[\mathrm{i}\varphi_{\mathrm{ZF}}(k_{\mathrm{ZF}})], \tag{6.7}$$

with $\hat{\omega}^{A}_{\mathrm{ExB}}, \varphi_{\mathrm{ZF}} \in \mathbb{R}$ and $\hat{\omega}_{\mathrm{ExB}}$ being the complex Fourier coefficient of the $E \times B$ shear [Eq. (6.5)] connected to the ZF mode with wave vector k_{ZF}. A striking

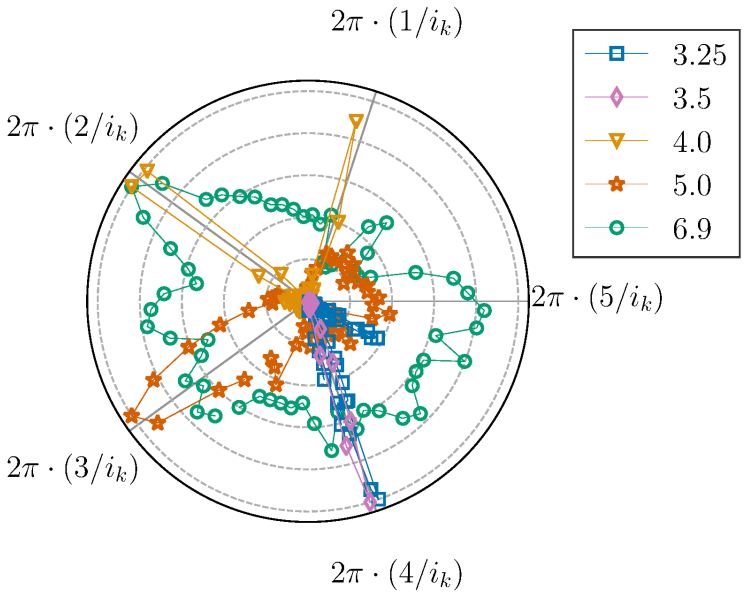

Figure 6.2: Distribution of the radial phase φ_{ZF} of the $n_{\mathrm{ZF}} = 1$ mode in the $E \times B$ shear [Eq. (6.7)] with respect to its domain of validity $\varphi_{\mathrm{ZF}} \in [0, 2\pi[$ (full circle) during the stationary state for various realizations of R_0/L_T. The five ($i_{\mathrm{k}} = 5$) radial grey rays depict the orientations to which the $n_{\mathrm{ZF}} = 1$ zonal mode locks in (compare bottom panel of Fig. 6.1). The individual distributions are normalized to the respective maximum.

observation is the lock-in of the longest wavelength zonal mode at distinct radial locations. This mode keeps its radial orientation for long time periods as indicated by the restriction of φ_{ZF} to specific values highlighted by horizontal dotted

lines in the bottom panel of Fig. 6.1. Extended phases with lock-in behavior are dispersed by intermittent phases with increased turbulent level, reduced mesoscale zonal potential level and elevated radial variability. The latter allow for the radial migration of the mesoscale zonal potential component pattern among different lock-in positions.
This outcome holds for a wider range in R_0/L_T as shown by the temporal distribution of the radial phase PDF(φ_{ZF}) normalized to the maximum of the respective distribution (see Fig. 6.2). An i_{k}-fold symmetry is found, where $i_{\mathrm{k}} = 5$ specifies the number of lowest order rational layers (LORLs) in the simulation domain. LORLs are radial locations with high symmetry, in that all k_y-modes project onto itself when connected over the radial boundary leading to strict parallel periodicity, and are determined by the geometry of the confining magnetic field. The radial lock-in behavior, therefore, demonstrates an interplay of mesoscale zonal potential structures with lowest order rational surfaces. Furthermore, the radial variability increases with R_0/L_T. While the radial orientation in cases with $R_0/L_T \in [3.25, 3.5, 4.0]$ is strongly tied to LORLs, the radial phase distribution indicates an increased mobility around LORLs for $R_0/L_T = 5.0$ and an almost random phase distribution at $R_0/L_T = 6.9$.

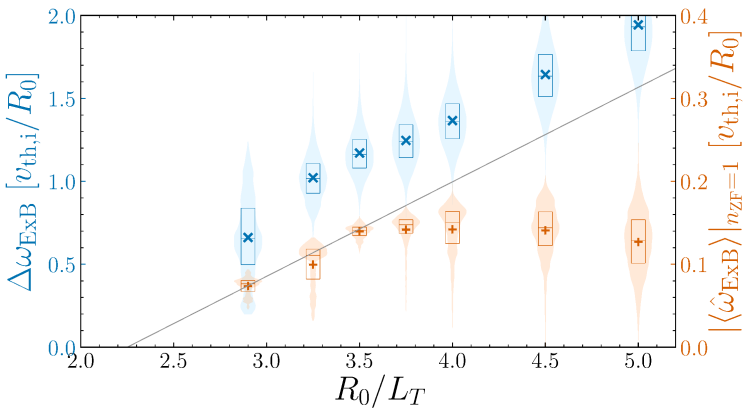

Figure 6.3: Temporally averaged spike intensity in the $E \times B$ shearing rate $\Delta\omega_{\mathrm{ExB}}$ (blue '×', left axis) and shear carried by the mesoscale $n_{\mathrm{ZF}} = 1$ zonal flow mode $|\langle\hat{\omega}_{\mathrm{ExB}}\rangle|_{n_{\mathrm{ZF}}=1}$ (red '+', right axis) against R_0/L_T. Shaded regions represent the temporal distribution and boxes indicate the upper and lower quartiles. The growth rate of the most unstable mode is depicted by a thin grey line (with respect to right axis).

Spatial scale dependence of the $E \times B$ shear

Here, a quantitative analysis of the $E \times B$ shearing rate connected to meso- and fine scale zonal structures is provided. The shear carried by the mesoscale zonal potential component $|\langle\hat{\omega}_{\mathrm{ExB}}\rangle|_{n_{\mathrm{ZF}}=1}$ (red '+' in Fig. 6.3) is a further characteristic of the above mentioned late quasi-stationary states. In general, the mesoscale shear level is of the order of $10^{-1}\ v_{\mathrm{th,i}}/R_0$ and, hence, agrees with typical values of the growth rate as well as staircase amplitudes [24, 25]. A striking observation is the linear increase in the interval $R_0/L_T = 2.9-3.5$ following the rule $\omega_{\mathrm{ExB}} \sim \gamma$. For inverse temperature gradient lengths around $R_0/L_T = 3.5$ the mesoscale ZF level is limited to an amplitude of $\omega_{\mathrm{ExB}} \approx 0.15\ v_{\mathrm{th,i}}/R_0$. Narrow quartiles indicate the temporal persistence of this typical mesoscale level, which is confirmed by the time traces in Fig. 6.1. Further increase of R_0/L_T results in a slight decrease of the averaged mesoscale ZF level. And although the temporal distribution is somewhat broadened the upper and lower quartiles show that 75 % of the time the ZF state still resides at amplitudes of $\hat{\omega}_{\mathrm{ExB}} \sim 0.1 - 0.15\ v_{\mathrm{th,i}}/R_0$. In Ref. [77] similar observations have been made in connection to $E \times B$ staircase states.
The above discussed characteristics of the mesoscales have to be contrasted to the shear carried by fine scale features (blue 'x' in Fig. 6.3) that significantly exceeds the shear carried by the mesoscale component. Here, an estimate of the amplitude of fine scale features is provided by the spike intensity

$$\Delta\omega_{\mathrm{ExB}} = \frac{1}{N_{\mathrm{spikes}}} \sum_{i=1}^{N_{\mathrm{spikes}}} |\omega_{\mathrm{ExB}}(x_i)|, \tag{6.8}$$

where $\omega_{\mathrm{ExB}}(x_i)$ is the shearing rate taken at the radial position of a spike x_i and N_{spikes} denotes the number of spikes in the radial profile of ω_{ExB} at a fixed point of time. A spike is defined by a local extremum in the radial profile of ω_{ExB} (blue profiles in Fig. 6.6). In contrast to the averaged mesoscale shear, the averaged spike intensity increases monotonically with R_0/L_T.
Both the large spike intensity and the linear increase is in contradiction with the obtained turbulent level (see Fig. 6.4) when the Waltz stabilization rule $\gamma \sim \omega_{\mathrm{ExB}}$ is considered. The dependence of the shear carried by mesoscale zonal potential structures, however, appears to be consistent with the increase of the turbulent level for $R_0/L_T > 3.5$. This suggests that the fine scale features in ω_{ExB} are less relevant for the shear stabilization of turbulence.

6.3.2 Director field analysis

In this section the director field diagnostic introduced in Sec. 6.2.2 is applied in order to investigate ZF pattern formation through the shear induced tilting of turbulent structures.

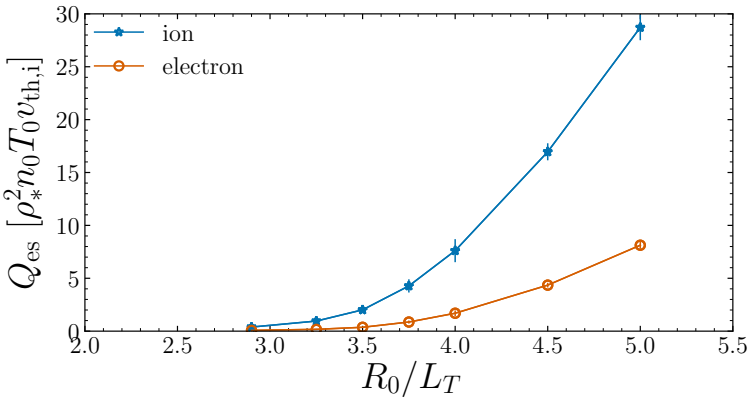

Figure 6.4: Time and volume averaged electrostatic heat flux Q_{es} of ions (blue) and electrons (red) against the background inverse temperature gradient length.

Director field in the presence of a homogeneously sheared background $E \times B$ flow

Before the director field method is applied to turbulence generated radially periodic ZFs, here, the connection between the $E \times B$ flow shearing rate and the director field is established using a constant (both in time and space) sheared background $E \times B$ flow. In GKW the background shear is implemented using the wave vector remapping method of Ref. [103] that has been benchmarked in Ref. [71] (see Sec. 4.3.6 for a description of the background $E \times B$ shear flow). The strength of the shear flow is controlled by the constant shearing rate γ_E.
Without external sources of shear as well as persistent ZFs symmetry properties of the gyrokinetic equation require the turbulent structures at the LFS ($s = 0$) to be radially symmetric in a statistically sense [123]. As a consequence, the ensemble averaged local orientation of turbulent structures and, hence, the director field have to vanish. However, even in the presence of periodic ZFs the director field can be made to vanish when averaging over the radial direction, since negative and positive shear zones cancel. Eddies that experience an $E \times B$ shear being constant over the simulation domain, in turn, exhibit a preferential tilt. The radially averaged director field $\langle K_\phi \rangle_x$ ($\langle ... \rangle_x$ denotes a radial average) is then finite and is, therefore, measured in the analysis below.
Due to the even number of grid points along the field line ($N_s = 32$) and the finite magnetic shear $\hat{s}$ of the chosen numerical parameters the 2D slice of the potential $\tilde{\phi}(x, y, s \approx 0)$ used in the director field diagnostic is slightly off the LFS. This results in a small radially constant positive tilt of turbulent eddies due to the alignment of turbulent modes along the sheared magnetic field [15]. It has been verified that an odd number of s-grid points, and consequently the positioning of the potential slice at $s = 0$, removes this offset. In order to mitigate this effect, the radially averaged director field at arbitrary background shear $\langle K_\phi \rangle_x$

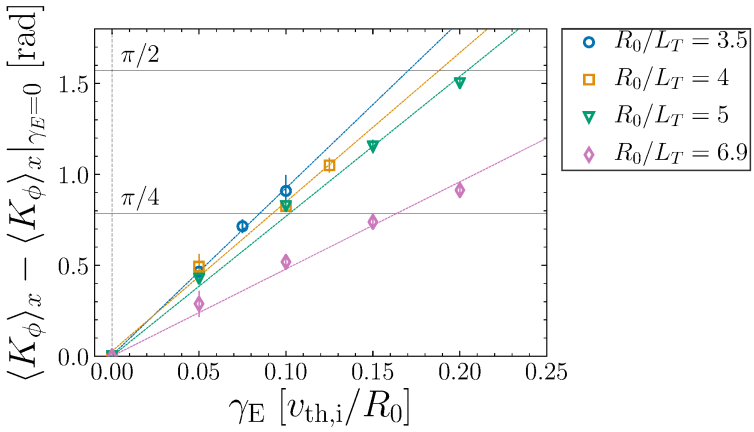

Figure 6.5: Temporally and radially averaged corrected director field $\langle K_\phi \rangle_x - \langle K_\phi \rangle_x|_{\gamma_E=0}$ against the background $E \times B$ shearing rate γ_E for various values of the inverse background temperature gradient length. Only stationary turbulent states are depicted and dashed lines represent fits of the model Eq. (6.9).

is corrected by the radially averaged director field at zero shear $\langle K_\phi \rangle_x|_{\gamma_E=0}$, i. e., $\langle K_\phi \rangle_x - \langle K_\phi \rangle_x|_{\gamma_E=0}$, at fixed value of R_0/L_T. It has been ensured that the radially averaged director field at finite background shear is always significantly larger than the radially averaged director field at zero shear (the latter is summarized in Tab. 6.2).
Since already a small level of background shear is known to result in complete stabilization in the linear regime [125, 127], late nonlinearly saturated states without background shear are used as initial conditions for realizations with finite background shear. This procedure is required to access stationary turbulent states at finite background shear. Furthermore, only cases with well defined, i. e., non-quenched, turbulence are considered, since it will be evident below that the director field depends on the turbulent level.
In general, the averaged director field and, hence, the level of eddy tilt increases with the background shear (see Fig. 6.5) as expected [123]. The sign sensitivity has been ensured through a sample point with $R_0/L_T = 6.9$ and $\gamma_E = -0.1$ (not shown) which results in a negative averaged director field. Fig. 6.5 makes clear that the mapping between the shearing rate γ_E and the director field $\langle K_\phi \rangle_x$ is not unique. An increase of R_0/L_T and therefore the turbulence level (see also Fig. 6.12) at same level of background shear results in a reduction of the averaged director field and equivalently the averaged tilt of eddies. This observation is partly interpreted as a reduction of the eddy life time, i. e., the time during which turbulent structures can be tilted by the sheared $E \times B$ flow, with increasing turbulence level [123]. Furthermore, the velocity shear connected to turbulent structures itself, i. e., turbulent mixing, might compete the background $E \times B$ shear with increasing turbulence strength and thereby lead to an isotropization

R_0/L_T	3.5	4.0	5.0	6.9
$\langle K_\phi \rangle_x|_{\gamma_\mathrm{E}=0}$ [rad]	0.009	0.047	0.055	0.118
α_cal [rad $\cdot\, R_0/v_\mathrm{th,i}$]	9.25	8.21	7.70	4.80

Table 6.2: Radially and time averaged director field without background shear $\langle K_\phi \rangle_x|_{\gamma_\mathrm{E}=0}$ and fit parameter α_cal of the linear model Eq. (6.9) corresponding to individual R_0/L_T-realizations in Fig. 6.5.

as the $E \times B$ nonlinearity tend to produce isotropic eddies [45]. It is noted, however, that this dependency poses no problem for the director field analysis of turbulence generated zonal flows in the subsequent sections, since a fixed value of R_0/L_T ensures a roughly constant turbulence level during the stationary state (see top panel of Fig. 6.3).
Given the complex interplay of sheared ZFs and turbulence, the development of a general model describing the averaged director field response on the $E \times B$ shearing rate is not further investigated here. Motivated by the outcome shown in Fig. 6.5 and for simplicity a linear dependence

$$K_\phi = \alpha_\mathrm{cal} \gamma_\mathrm{E} \tag{6.9}$$

is adopted with the constant α_cal having the unit rad $\cdot\, R_0/v_\mathrm{th,i}$. The linear model applies satisfactory well (dashed lines in Fig. 6.5) within the considered range of γ_E and provides a proxy for the conversion of the averaged director field into an $E \times B$ shearing rate. The corresponding fit parameter α_cal is summarized in Tab. 6.2.
To conclude, this numerical experiment demonstrates that the level of eddy tilt ($\sim K_\phi$) provides information about the zonal flow induced shear ($\sim \gamma_\mathrm{E}$). This motivates the application of director field techniques for the investigation of the shearing action provided by turbulence generated sheared zonal flows below.

Director field analysis of turbulence generated radially periodic zonal flows

In this section the director field method is applied to investigate the deformation of turbulent structures induced by self-consistently generated radially periodic ZFs. None of the simulations presented here and in the remainder of Sec. 6.3.2 apply background $E \times B$ shear, such that the considered sheared ZFs evolve self-consistently, i. e., with back-reaction to the turbulence. In order to separate the deformation induced by radially periodic ZFs from the constant tilt due to the alignment along the sheared background magnetic field (see also Sec. 6.3.2), the radially averaged director field $\langle K_G \rangle_x$ is always subtracted from the total director

field K_G in the remainder of Sec. 6.3.2. The focus lies on the role of fine- and mesoscale ZFs for the shear induced tilting.
The case selection in this analysis is representative for three distinct regimes with respect to mesoscale $n_{\mathrm{ZF}} = 1$ structure development in ω_{ExB} (see Fig. 6.3) as well as turbulent transport level (see Fig. 6.4): Case (A) with $R_0/L_T = 3.25$ lies in the regime with linearly increasing shear in the mesoscale ZF and exhibits a small turbulence level. Case (B) with $R_0/L_T = 4.0$ represents the transition to a linearly and more strongly increasing heat flux and is situated in the regime with saturated mesoscale ZF shear. Case (C) with $R_0/L_T = 6.9$ is a strong turbulent reference case with highly variable mesoscale ZF (see Fig. 6.2) at a level of $\langle|\langle\hat{\omega}_{\mathrm{ExB}}\rangle|_{n_{\mathrm{ZF}}=1}\rangle_t = 0.11\ v_{\mathrm{th,i}}/R_0$ and high turbulent level $\langle\langle Q_{\mathrm{es}}\rangle_\psi\rangle_t = 74.33\ \rho_*^2 n_0 T_0 v_{\mathrm{th,i}}$.
Evidence of fine scale features in the radial profiles of K_ϕ can only be observed in case (A) (red profile in top left panel of Fig. 6.6). The level of fine scale features in the director field, however, does not reflect the respective structures in ω_{ExB} (blue profile). While the profile of the shearing rate ω_{ExB} is clearly dominated by fine scale features, it is the $n_{\mathrm{ZF}} = 1$ mesoscale variation that prevails over the fine scale features in the director field. The actual shearing action, i. e., the ability of tilting turbulent structures, of spikes in ω_{ExB}, hence, appears to be significantly reduced. This observation is in agreement with structures in the spatial morphology of the turbulent electrostatic potential $\tilde{\phi}$ (bottom left panel of Fig. 6.6). Therein, the tilting by fine scale features is only faintly visible by radially periodic vertically coherent zig-zag structures (see bottom left panel of Fig. 6.6).
In cases with increasing turbulent level, i. e., case (B) and (C), the fine scale signatures in the director field disappear (mid and right top panels of Fig. 6.6). This stands in contrast to the increase of the spike intensity in the shearing rate ω_{ExB} (see also $\Delta\omega_{\mathrm{ExB}}$ in Fig. 6.3) and is therefore conjectured to be directly related to the increasing turbulence level. Note that both the turbulence correlation length and the scale on which turbulence spreading acts is of the order of several Larmor radii [128]. The zonal flow shear induced tilting on scales of the spike structures is therefore in particular susceptible to turbulent mixing. The above observation is confirmed by the absence of vertically aligned zig-zag structures and the appearance of small scale and more irregular eddies for $R_0/L_T = 4.0$ and $R_0/L_T = 6.9$ (mid and right bottom panels of Fig. 6.6). To conclude, despite the large amplitude ($\sim 1\ v_{\mathrm{th,i}}/R_0$) of fine scale features in ω_{ExB} their contribution to shear deformation of turbulent structures is marginal in the cases considered here.
A striking observation is the development of mesoscale pattern in the director field (top panels of Fig. 6.6), occurring on two distinct disparate scales:
(i) Close to LORLs (vertical black dotted lines) the radial profile of K_ϕ features corrugations. Radial intervals with $\partial_x K_\phi < 0$ are always centered at LORLs introducing an i_{k}-fold mesoscale pattern in K_ϕ.

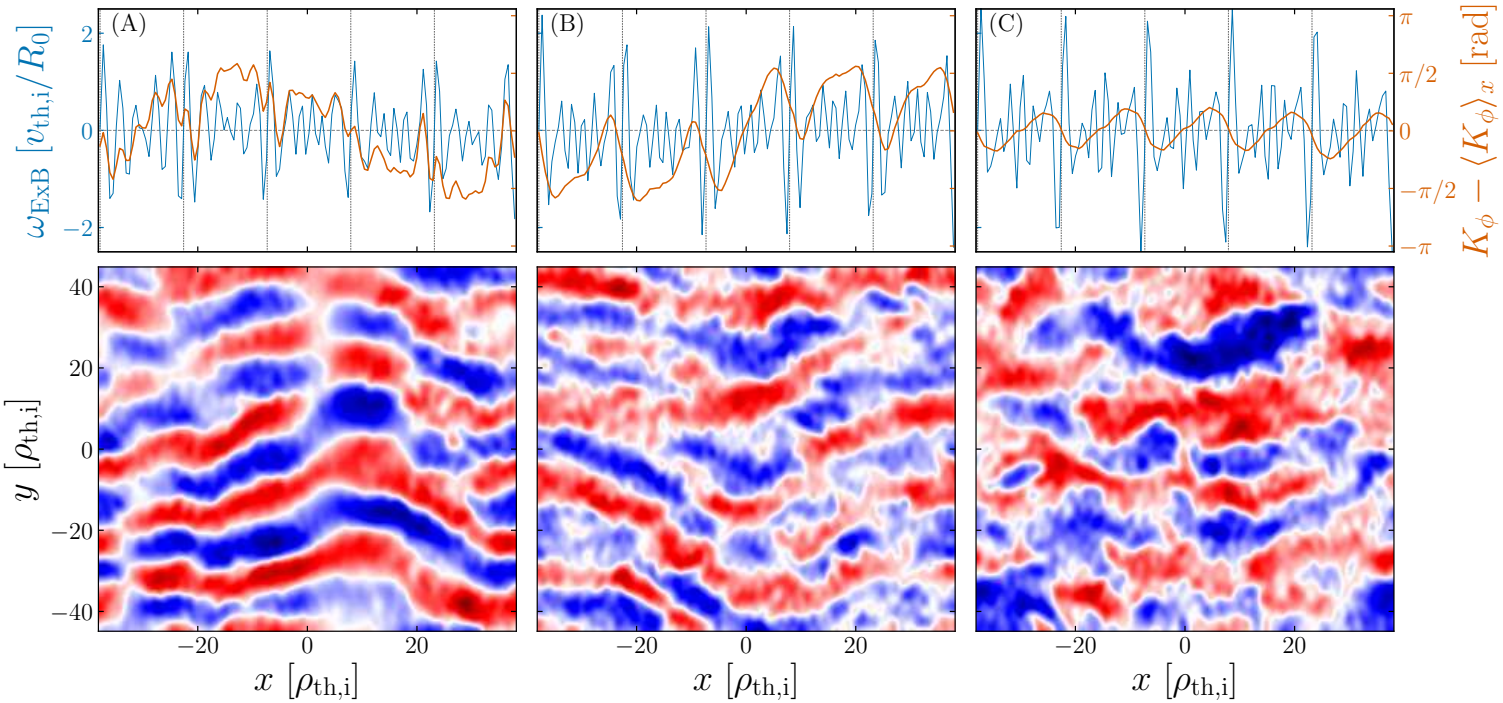

Figure 6.6: Top panels: Radial profiles of the temporally averaged shearing rate ω_{ExB} (blue, left vertical axis) and the director field $K_\phi - \langle K_\phi \rangle_x$ (red, right vertical axis) for cases (A), (B) and (C) described in the text. Vertical black dotted lines indicate LORLs. Bottom panels: Snapshots of the turbulent part of the electrostatic potential $\tilde{\phi}$ in the x-y-plane at the LFS. The data is taken from the same time intervals used for time averaging of the respective radial profile in the top panels. Bicubic interpolation is applied to enhance the visibility of structures on grid scale. The potential is normalized to its maximum value and the color scale ranges linearly $\in [-1.05, +1.05] \rightarrow [\mathrm{blue}, \mathrm{red}]$.

It has been verified that this period length changes accordingly with varying i_{k}. In case (B) the corrugations result in zero crossings and reduced averaged deformation in the vicinity of LORLs. In the strong turbulent reference case (C) signatures of the $n_{\mathrm{ZF}} = 1$ mesoscale ZF average out due to its quasi-random phase distribution (see Fig. 6.2), leaving signatures of the corrugations visible in form of bipolar shear layers centered at LORLs. These spatially fixed corrugations feature amplitudes of $K_\phi \sim \pi/4$ that can be related to a shearing rate of $\gamma_{\mathrm{E}} \sim 0.15\ v_{\mathrm{th,i}}/R_0$ (see Fig. 6.5). The formation of zonal flow corrugations emerging at low order rational surfaces has been reported in Ref. [129] and is distinct from the fine scale features in ω_{ExB} that are not restricted to LORLs [1]. (ii) The subset of cases with radial lock-in of the mesoscale zonal mode, i. e., $R_0/L_T \in [3.25, 3.5, 3.75, 4.0]$, exhibits a $n_{\mathrm{ZF}} = 1$ mesoscale variation in the director field when averaging over a locked-in phase. The spatial morphology of turbulent structures confirms the significance of this mesoscale structure in the ZF induced tilting (left and mid bottom panels of Fig. 6.6). The zero crossing of the $n_{\mathrm{ZF}} = 1$ modulation satisfying $K_\phi < 0 \rightarrow K_\phi > 0$ with increasing radial coordinate is always centered in between two LORLs, while the opposite zero crossing always coincides with a LORL. It has been verified that this behavior translates to even values of i_k. As a result, an uneven number of LORLs allows for an even radial symmetry of the structure in K_ϕ. This restriction on the mesoscale pattern is a manifestation of the interplay of the $n_{\mathrm{ZF}} = 1$ ZF component with LOLRs as observed in Sec. 6.3.1. In case (B) the director field exhibits intervals with finite and almost constant eddy tilt in between the corrugations, indicating a finite shearing rate there. The overall shape resembles a fully-developed staircase [25, 77] (this nomenclature follows the aforementioned references and denotes the staircase state emerging in gradient-driven simulations with adiabatic electrons just below the non-monotonic finite heat flux threshold) with the modification of $i_{\mathrm{k}} - 1$ additional corrugations close to LORLs. Since the development of the corrugations in the present study requires electron dynamics the overall structure will be referred to as a modified staircase state hereafter. Structures of this type occur for $R_0/L_T \in [3.5, 3.75, 4.5, 5.0]$ as well (a case with $R_0/L_T = 3.5$ is shown in the top left panel of Fig. 6.7). In the latter two cases the spatial persistence is significantly reduced, which is consistent with a higher radial variability of the largest scale zonal flow mode (see Fig. 6.2). The amplitudes of modified staircases of $K_\phi \sim \pi/2$ can be roughly related to shearing rates of $\gamma_{\mathrm{E}} \sim 0.15 - 0.2\ v_{\mathrm{th,i}}/R_0$ through extrapolation of $K_\phi(\gamma_{\mathrm{E}})$ obtained in the director field calibration (Fig. 6.5). It is, therefore, comparable to the shear carried by the mesoscale component of zonal potential (see Fig. 6.3).
The above observations are somewhat surprising and deserve further clarifications. Especially the following questions are raised: (i) Why do the fine scale features in ω_{ExB} hardly contribute to the tilting of turbulent structures? (ii) Can the modified staircase pattern in the director field, and especially the corrugations, be related to physically meaningful perturbations in the distribution

function? (iii) Do modified staircase share similarities with their adiabatic counterpart? Questions that will be addressed to in the next sections.

Role of finite Larmor radius effects for the shearing action of fine scale structures in the shearing rate ω_{ExB}

A fundamental aspect of the gyrokinetic framework is the dynamical reduction through the average over the fast gyro-motion. The so introduced gyro-average (GA) appears at various places as for example in form of the gyro-averaged potential entering the $E \times B$ nonlinearity of the gyrokinetic equation, or the gyro-averaged distribution function entering the integral part of the Poisson equation [95]. While the gyro-average can be neglected on scales significantly larger than the Larmor radius, it is relevant on scales comparable to it and introduces so-called finite Larmor radius (FLR) effects. The shearing of turbulent structures by zonal $E \times B$ flow is mediated by the $E \times B$ nonlinearity and due to the small radial scale of the spike structures of a few Larmor radii (see Fig. 6.6), their shearing action might be susceptible to FLR effects in particular.

In order to test if FLR effects mitigate the shearing through small scale features in ω_{ExB}, the gyrokinetic as well as the Poisson equation are manipulated in two steps. First, the gyro-average is neglected in the $E \times B$ nonlinearity in case it acts on the $k_y = 0$ mode of the electrostatic potential. This is realized by the modification

$$J_0 \hat{\phi}|_{k_y=0} \rightarrow \hat{\phi}|_{k_y=0}, \tag{6.10}$$

with J_0 being the zeroth order Bessel function and $\hat{\phi}$ being the Fourier transformed electrostatic potential.

A well saturated base case with $R_0/L_T = 3.5$ is used as initial condition for the cases considered below. The base case is restarted both with and without the GA in the $E \times B$ nonlinearity and the influence on the deformation of turbulent structures in the electrostatic potential $\tilde{\phi}$ and the ion gyro-center density $\delta\tilde{n}_{\mathrm{i}} = \delta n_{\mathrm{i}} - \langle \delta n_{\mathrm{i}} \rangle$, with

$$\delta n_{\mathrm{sp}} = \int \mathrm{d}^3 v \; f_{\mathrm{sp}} \tag{6.11}$$

is characterized by the respective temporally averaged director field (top panels of Fig. 6.7). Clear fine scale features can be observed in the director field of the ion gyro-center density when the GA is removed (blue) in contrast to the unmodified reference case (red). The spike intensity in the shearing rate ω_{ExB} is not found to be influenced by this modification. This demonstrates that FLR effects mitigate the shearing action of fine scale structures in the shearing rate ω_{ExB} efficiently by filtering fine scale features in the zonal electrostatic potential.

Although the removal of the GA in the $E \times B$ nonlinearity has profound influences on the ion gyro-center density, its influence on the deformation of turbulent structures in the electrostatic potential is found to be less pronounced (top left

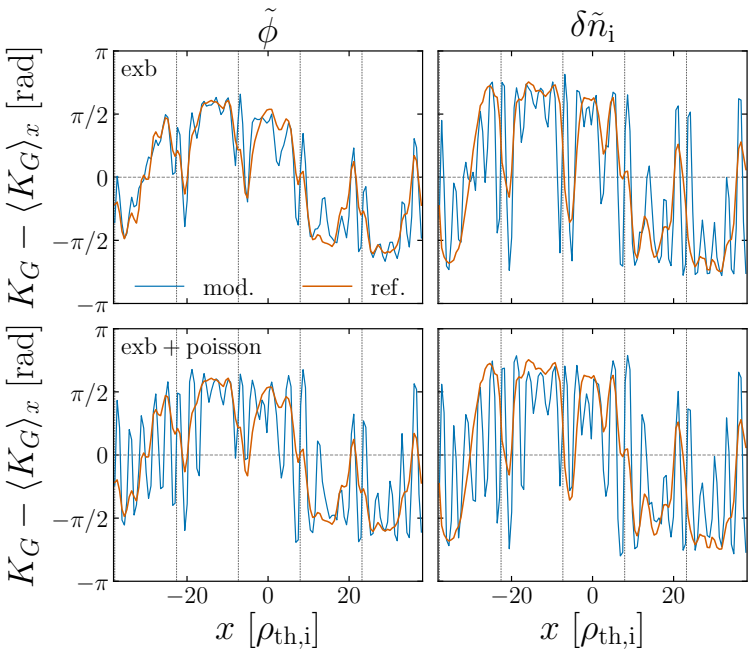

Figure 6.7: Radial profiles of the temporally averaged director field $K_G - \langle K_G \rangle_x$ of the electrostatic potential $G = \tilde{\phi}$ (left panels), the ion gyro-center density $G = \delta\tilde{n}_\mathrm{i}$ (right panels). Shown are an unmodified reference case (red) and cases without GA in the $E \times B$ nonlinearity (blue top panels) as well as without GA in both the $E \times B$ nonlinearity as well as the integral part of the Poisson equation (blue bottom panels). All cases have $R_0/L_T = 3.5$ and vertical black dotted lines indicate LORLs.

panel). The above outcome is confirmed by the spatial morphology of turbulent structures in the electrostatic potential and gyro-center density (top panels of Fig. 6.8). Now, clear vertically coherent small scale deformations are visible in the turbulent gyro-center density field (right), while being considerably fainter in the electrostatic potential (left).
The discrepancy relates to polarization effects entering the gyrokinetic Poisson equation due to the pull-back transformation from gyro-center to particle phase space [11]. This involves a further GA in the integral part of Poisson equation [95] and, hence, introduces a second smoothing of small scale features, now however of the turbulent structures itself. In order to clarify the above effect, the GA in the integral part of the Poisson equation is neglected when acting on turbulent $k_y \neq 0$ modes of the distribution function. This second manipulation is realized by the substitution

$$\int J_0 \hat{g}|_{k_y \neq 0} \, \mathrm{d}\mu \mathrm{d}v_\parallel \rightarrow \int \hat{g}|_{k_y \neq 0} \, \mathrm{d}\mu \mathrm{d}v_\parallel \tag{6.12}$$

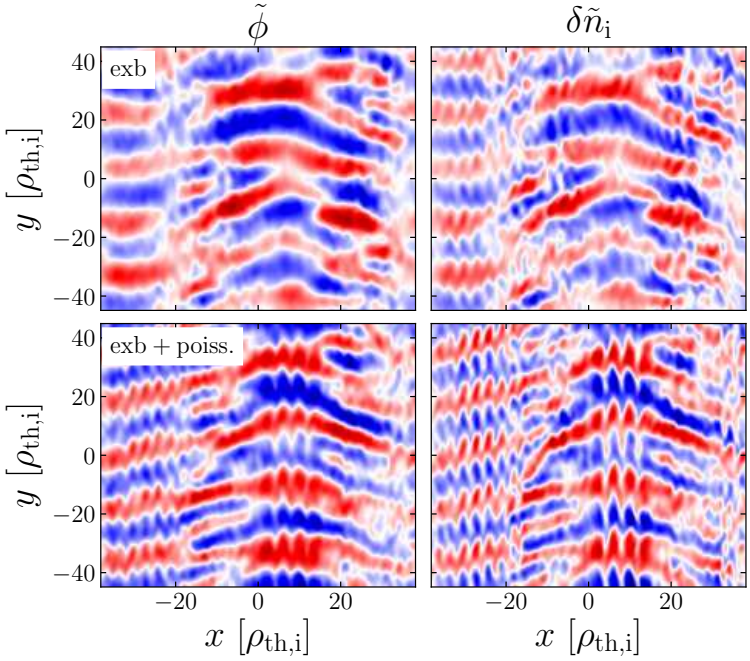

Figure 6.8: Turbulent part of the electrostatic potential $\tilde{\phi}$ (left) and the ion gyro-center density (right) in the x-y-plane with the gyro-average removed in the $E \times B$ nonlinearity (top) and both the $E \times B$ nonlinearity as well as the integral part of the Poisson equation (bottom). All cases have $R_0/L_T = 3.5$. Bicubic interpolation is applied to enhance the visibility of structures on grid scale. Both quantities are normalized to the maximum value and the color scale ranges linearly $\in [-1.05, +1.05] \rightarrow [\mathrm{blue}, \mathrm{red}]$.

in the integral part of Poisson equation (see Eq. (73) of Ref. [95]). As a result similar profiles of K_ϕ and $K_{\delta n_\mathrm{i}}$ are obtained with K_ϕ now exhibiting spike features as well (bottom panels of Fig. 6.8). It is noted, that the structures in K_ϕ do not show the same strong spikes as occurring in ω_ExB around LORLs (see top panels of Fig. 6.6). This fact is attributed to the extreme values of the shear at these points for which the validity of the linear model anticipated in Sec. 6.3.2 cannot be guaranteed. Clear signatures of sheared fine scale structures are now visible also in the spatial morphology of $\tilde{\phi}$ (bottom panel of Fig. 6.8). This numerical experiment, hence, demonstrates a significant reduction of the shearing action connected to fine scale structures in ω_ExB due to FLR effects.
While the role of FLR effects for the deformation of turbulent structures has been considered before, now its influence on shear stabilization [62, 29, 69] is investigated. Fig. 6.9 shows time traces of the ion and electron electrostatic heat flux for the same cases discussed above. Both manipulations of the gyrokinetic set of equations result in a reduction of the turbulent transport level. In the case without the GA in both the zonal $E \times B$ nonlinearity as well as the integral part of

Poisson equation an extended phase with almost zero heat flux is observed. The

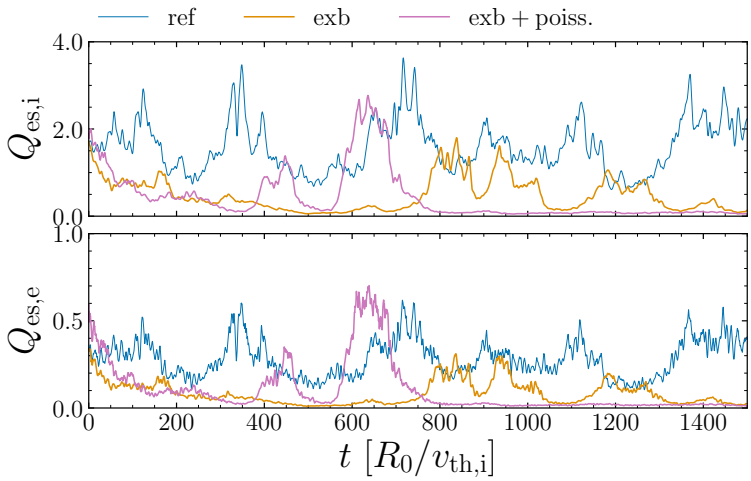

Figure 6.9: Time traces of the ion- (top) and electron (bottom) electrostatic heat flux $Q_{\mathrm{es,sp}}$ (in units of $\rho_*^2 n_0 T_0 v_{\mathrm{th,i}}^2$) for the unmodified reference case (blue), a case without GA in the zonal $E \times B$ nonlinearity (orange) and a case without GA both in the zonal $E \times B$-nonliniarity as well as the integral part of the Poisson equation (violet). All cases have $R_0/L_T = 3.5$.

spike features in the shearing rate ω_{ExB}, therefore, have the potential to stabilize turbulence through decorrelation. In practice, FLR effects on ion Larmor radius scales render this potential ineffective.

Connection of zonal flow corrugations to perpendicular ion pressure corrugations

In this section the corrugations in the director field close to LORLs (see Fig. 6.6) are related to perpendicular ion pressure corrugations making use of both the parallel electron and the radial ion force balance. Below, only toroidally constant quantities, i. e., $k_y = 0$ components, are considered.
Neglecting the electron inertia term and the gyroviscous pressure tensor the parallel electron force balance in lowest order of ρ_* can be formulated by (see appendix A)

$$0 = \nabla_\parallel \phi - [\mathcal{K}_\parallel(p_{\parallel,\mathrm{e}}, p_{\perp,\mathrm{e}}) + \nabla_\parallel p_{\parallel,\mathrm{e}}], \tag{6.13}$$

where $\nabla_\parallel = \mathbf{b} \cdot \nabla$ is the gradient along the magnetic field, $\mathcal{K}_\parallel$ expresses magnetic curvature effects entering through the divergence of the gyrotropic pressure tensor and $p_{\parallel,\mathrm{e}}$ as well as $p_{\perp,\mathrm{e}}$ are the parallel and perpendicular electron pressure

respectively given by moments of the gyro-center distribution function

$$p_{\parallel,\mathrm{sp}} = \int \mathrm{d}^3 v \; m_{\mathrm{sp}} v_\parallel^2 f_{\mathrm{sp}} \tag{6.14}$$

$$p_{\perp,\mathrm{sp}} = \int \mathrm{d}^3 v \; B\mu f_{\mathrm{sp}}, \tag{6.15}$$

where $\mu = m_{\mathrm{sp}} v_\perp^2 / 2B$ is the magnetic moment. Eq. (6.13) can be shown to apply well to the modified staircase states (see Fig. A.1 in appendix A). Given profiles of $p_{\parallel,\mathrm{e}}$ and $p_{\perp,\mathrm{e}}$ determine the parallel dependence of the electrostatic potential through Eq. (6.13). Curvature effects entering through $\mathcal{K}_\parallel$ have similar magnitude compared to the parallel pressure and parallel electric field term (see Fig. A.1) and, therefore, might introduce a variation of the electrostatic potential along s. The amplitude of the pressure and curvature terms, however, is small enough to introduce only a small relative variation of the electrostatic potential along s of

$$\Delta\phi = \frac{\max_s(\delta\phi) - \min_s(\delta\phi)}{\max_x(\langle\phi\rangle)} \sim 3 - 4 \; \%, \tag{6.16}$$

in the case of a modified staircase, where $\delta\phi = \phi - \langle\phi\rangle$ defines the s-varying part of ϕ and $\max_\alpha / \min_\alpha$ denotes maximum/minimum with respect to α. The electrostatic potential can, therefore, be considered constant on a flux surface in good approximation. And as a consequence, ZF structures deduced from the director field diagnostic at the LFS represent the zonal $E \times B$-flow on the whole flux surface. The solution of the parallel electron force balance $\phi(x,s) = \delta\phi(x,s) + C$ determines the electrostatic potential up to a constant C with respect to s and, hence, leaves the zonal part of the electrostatic potential $C = \langle\phi\rangle$ undetermined.

The zonal potential is related to plasma rotation and pressure through the radial ion force balance, which has found application in gyrokinetic studies [130, 129, 131]. In the local limit ($\rho_* \to 0$) the flux surface averaged form can be written (see appendix A)

$$0 = \nabla_x \langle\phi\rangle + [\nabla_x \langle p_{\perp,\mathrm{i}}\rangle + \langle(\nabla \cdot \mathbf{\Pi}_{\mathrm{i}})_x\rangle] - \langle(2\mathbf{u}_{\mathrm{i}} \times \mathbf{B})_x\rangle, \tag{6.17}$$

where $\nabla_x = \partial_x$ is the radial gradient, $\mathbf{u}_{\mathrm{i}}$ is the perturbed ion velocity and $(\nabla \cdot \mathbf{\Pi}_{\mathrm{i}})_x$ is the radial component of the divergence of the ion gyroviscous pressure tensor. The radial gradient of the ion perpendicular pressure exhibits a distinct corrugated structure [see the exemplary cases with $R_0/L_T = 3.75$ (left panels) and $R_0/L_T = 6.9$ (right panels) in Fig. 6.10], with the radial location of the corrugations correlating with LORLs (vertical dotted lines) similar to Refs. [132, 129]. A variation along s is apparent, manifesting itself in positive radial corrugations at the LFS (orange dashed line in the mid panels) and negative mesoscale corrugations when averaging over the flux surface (blue solid line). This observation

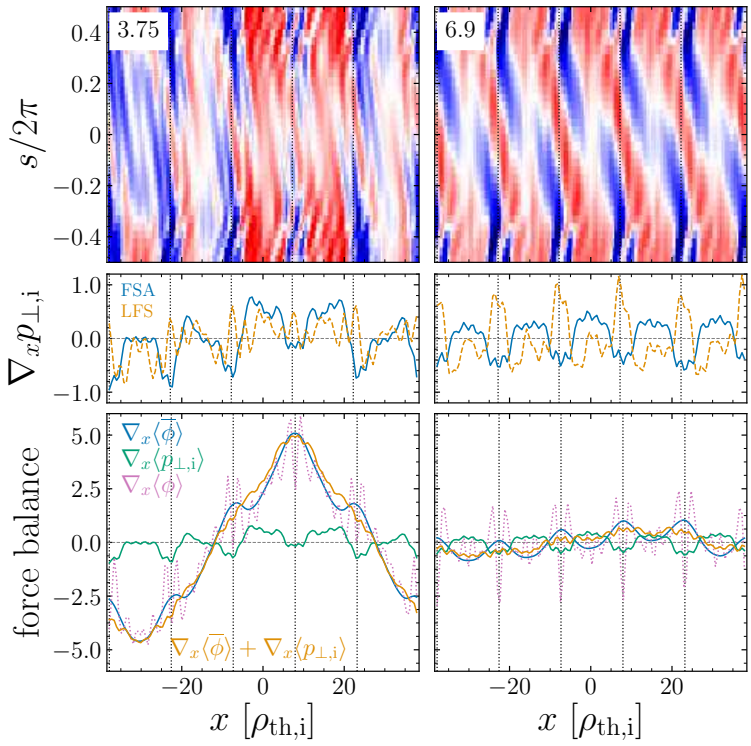

Figure 6.10: Top panels: Radial gradient of the ion perpendicular pressure $\nabla_x p_{\perp,\mathrm{i}}$ ($k_y = 0$ component) in the x-s-plane. The data is normalized to its maximum value and the color scale ranges linearly $\in [-1.05, +1.05] \rightarrow$ [blue, red]. Mid panels: Radial profiles of the same quantity averaged over the flux surface (FSA) and at the low field side (LFS). Bottom panels: Flux-surface and time averaged radial profiles of $\nabla_x\langle\overline{\phi}\rangle$ (blue), $\nabla_x\langle p_{\perp,\mathrm{i}}\rangle$ (green), $\nabla_x\langle\phi\rangle$ (violet dotted) and $\nabla_x\langle\overline{\phi}\rangle + \nabla_x\langle p_{\perp,\mathrm{i}}\rangle$ (orange). The left panels represent a modified staircase state at $R_0/L_T = 3.75$ and the right panels the strong turbulence reference case at $R_0/L_T = 6.9$.

might relate to the perpendicular pressure component of Rosenbluth-Hinton residuals with reduced radial scale showing a similar poloidal variation [131], or to the ballooning nature of the underlying ITG turbulence [15]. A further characteristic of the pressure corrugations is the radial asymmetry in the case of $R_0/L_T = 3.75$ and the more symmetric appearance in the strong turbulent case with $R_0/L_T = 6.9$ with respect LORLs.
Now, individual terms of the radial force balance [Eq. (6.17)] are evaluated for the cases depicted in Fig. 6.10. The $\nabla_x\langle\phi\rangle$ term exhibits fine scale variations (violet dotted lines in the bottom panels of Fig. 6.10), in accordance with the spike features in ω_{ExB}, which cannot be balanced by the smoother pressure gradient profile (green solid). It is the gyroviscous pressure tensor that becomes relevant on scales comparable to the Larmor radius [133] and it will therefore be as-

sumed that fine scale variations in the radial electric field term are compensated by the $\langle(\nabla \cdot \mathbf{\Pi}_\mathrm{i})_x\rangle$-term. This assumption is supported by the observation that the gyroaverage mitigates the $E \times B$-flow connected to fine scale features (see Sec. 6.3.2) and motivates the formal introduction of a corrected electrostatic potential through

$$\nabla_x \langle\overline{\phi}\rangle \equiv \nabla_x \langle\phi\rangle + \langle(\nabla \cdot \mathbf{\Pi}_\mathrm{i})_x\rangle. \tag{6.18}$$

The corrected zonal potential $\langle\overline{\phi}\rangle$ is estimated using the director field under the following assumptions: (i) The director field is assumed to be proportional to the radial gradient of the advecting ZF velocity, i. e., $K_\phi - \langle K_\phi\rangle_x \propto \nabla_x v_\mathrm{ZF}$, which is justified by the director field calibration (Fig. 6.5). (ii) The spike features in the electrostatic potential do hardly contribute to the advection by the $E \times B$-drift and therefore the advecting ZF velocity is assumed to result from the corrected electrostatic potential $v_\mathrm{ZF} \propto \nabla_x \langle\overline{\phi}\rangle/2$. Through radial integration of the director field one then obtains

$$\int K_\phi(x') - \langle K_\phi(x')\rangle_{x'} \, \mathrm{d}x' = \alpha_\mathrm{sim} \nabla_x \langle\overline{\phi}\rangle(x)/2, \tag{6.19}$$

where α_sim is a proportionality constant which is determined by fitting a linear function to Eq. (6.19) with the potential on the right hand side being replaced by the unmodified zonal electrostatic potential $\langle\phi\rangle$. Hence, α_sim serves as a rescaling factor ensuring the corrected and unmodified electrostatic potential being of the same order, i. e., $\langle\overline{\phi}\rangle \sim \langle\phi\rangle$ (compare blue solid and violet dotted line in the bottom left panel of Fig. 6.10). Comparison of the proportionality constants obtained in the director field calibration (Tab. 6.2) and the here obtained $\alpha_\mathrm{sim} = 8.18 \text{ rad} \cdot R_0/v_\mathrm{th,i}$ demonstrates that $\alpha_\mathrm{cal} \approx \alpha_\mathrm{sim}$ as expected.
When applying the above procedure a connection of the corrugations in K_ϕ to 'bump-dip'-like modulations of the estimated zonal flow velocity $v_\mathrm{ZF} \propto \nabla_x \langle\overline{\phi}\rangle/2$ (see blue line in Fig. 6.10) is identified. Summation of the estimated corrected electric field term and the ion pressure term of the radial force balance (orange solid line) eliminates these structures remarkably well, despite the crude approximations made above. This demonstrates that corrugations in K_ϕ are related to flux surface averaged perpendicular pressure corrugations.
Some cautious words are in order regarding the evaluation of the pressure through the gyrocenter distribution function f [see Eq. (6.14)-(6.15)] instead of the formally correct evaluation with the Vlasov particle distribution function F_V [see Eq. (A.6)-(A.7)]. This approach requires the considered length scales to be significantly larger than the Larmor radius; which is also a requirement for validity of the here applied gyrotropic pressure tensor [133]. It is, therefore, justified in the description of the mesoscale corrugations with a spatial scale of $\sim L_x/i_\mathrm{k} \sim 10^1 \ \rho_\mathrm{th,i}$.
A similar overall conclusion can be drawn in the case of $R_0/L_T = 6.9$ (right panels of Fig. 6.10). Since the random phase distribution of the mesoscale ZF component

in this case (see Fig. 6.2) results in a strongly reduced amplitude of the $n_{\mathrm{ZF}} = 1$ component in $\nabla_x \langle \phi \rangle$ when averaging over time, the fitting procedure introduced above is not applicable here. Instead, it is reasonable to set $\alpha_{\mathrm{sim}} = \alpha_{\mathrm{cal}} = 4.8$ (compare Tab. 6.2). This choice again successfully eliminates the corrugations in $\nabla_x \langle \overline{\phi} \rangle$ (orange solid line).
Finally, it is noted that the quantitative agreement of the force balance under utilization of the reasonably rescaled director field and a physically meaningful moment of the distribution function can be considered a validation of the director field method applied to radially varying zonal $E \times B$ flows.

Mesoscale pattern decomposition

The previous section suggests that modified staircase structures can be understood as a superposition of a mesoscale $n_{\mathrm{ZF}} = 1$ component and pressure gradient related ZF corrugations. This section provides a decomposition of the modified staircase structure into the staircase (sc) and corrugation (corr.) component and aims to estimate the shear related to both components of the pattern.
The decomposition $\langle \overline{\phi} \rangle = \langle \overline{\phi} \rangle_{\mathrm{sc}} + \langle \overline{\phi} \rangle_{\mathrm{corr.}}$ is defined by

$$\nabla_x \langle \overline{\phi} \rangle_{\mathrm{corr.}} = -\nabla_x \langle p_{\mathrm{i},\perp} \rangle \tag{6.20}$$

and the identification of $\langle \overline{\phi} \rangle$ with the estimated corrected potential of Eq. (6.19). The shearing rate $\overline{\omega}_{\mathrm{ExB}}$ connected to the so obtained staircase and corrugation component is computed using Eq. (6.5) and is depicted by thin dashed lines in Fig. 6.11. Small scale variations in the pressure gradient (see mid and bottom panels of Fig. 6.10) result in spike structures in $\overline{\omega}_{\mathrm{ExB}}$ after radial derivation and a radial midpoint average is applied (solid lines) to allow for some degree of smoothing. The midpoint average of a quantity G is defined by

$$\langle G \rangle_W(x_i) = \frac{1}{\mathcal{N}} \sum_{j=-W}^{W} \mathcal{W}_j G(x_{i+j}) \tag{6.21}$$

with the normalization $\mathcal{N} = W + 1 + 2\sum_{j=1}^{W} j$ and the weighting factor $\mathcal{W}_j = W + 1 - |j|$. Here, $W = 2$ is chosen as a compromise between the smoothing of small scale variations, while retaining the corrugated structures.
The modified staircase state (left panel) is composed of a conventional staircase like structure (blue profile), i. e., a mesoscale structure in the shearing rate with extended radial intervals exhibiting a characteristic shearing rate and steep flanks at the zero crossings [25], and corrugations in the shearing rate in the vicinity of LORLs (orange profile). Most notably, the characteristic mesoscale shear of $\sim 0.15\ v_{\mathrm{th,i}}/R_0$ discussed in Sec. 6.3.1, here, agrees with the amplitude of both the staircase and the corrugated structures (horizontal grey line in Fig. 6.11). This structure composition and characteristic amplitude is observed over a wide

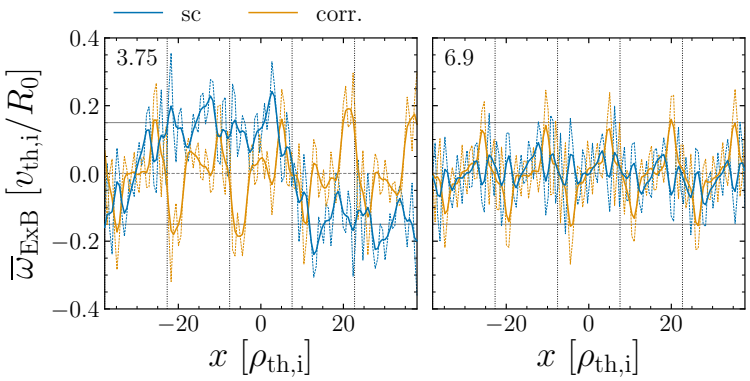

Figure 6.11: Decomposition of the corrected shearing rate $\overline{\omega}_{\mathrm{ExB}}$ into the staircase (blue dashed) and corrugation (orange dashed) part for $R_0/L_T = 3.75$ (left) and $R_0/L_T = 6.9$ (right). Solid lines depict the respective midpoint averaged profiles $\langle\overline{\omega}_{E\times B}\rangle_W$. The typical shearing rate of 0.15 $v_{\mathrm{th,i}}/R_0$ is denoted by horizontal grey lines while vertical dotted lines depict LORLs.

range $R_0/L_T \in [3.5, 3.75, 4.0, 4.5, 5.0]$.
In the strong turbulence case (right panel) the staircase component is absent and the corrugations now appear as symmetric bipolar shear layers centered about LORLs. Hence, a qualitative change from asymmetric corrugations observed close to the threshold (left panel) to symmetric shear layers far away from the threshold (right panel) is found in agreement with the director field profiles shown in Fig. 6.6. This outcome highligths that the shear provided by corrugations and the underlying staircase structures is not merely additive. Rather, the shape of electrostatic potential around rational layers is changed in the presence of a staircase.
Finally, it is stressed that the shearing rate connected to the corrugations discussed here is directly related to a physically meaningful moment of the distribution function rather than to a quantity like the director field that requires a calibration.

6.3.3 Interplay of modified staircase structures, $E\times B$ background shear flows and turbulent heat transport

The previous sections demonstrate the emergence of mesoscale modified staircase structures whose interplay with a constant background $E \times B$ shear is now investigated. Here, the background shear flow is intended to model sheared mean $E\times B$ flows varying on the radial scale of the machine size rather than that of the modified staircase structure. A sufficiently high time and radial resolution, required when applying a background shear [71], has been ensured in a convergence

study. Furthermore, the spatio-temporal organization of turbulent heat transport in the presence of sheared $E \times B$ flows, i. e., both the modified staircase state and background shear, is discussed.

Non-monotonic dependence of the turbulent heat transport on the background shear

Sheared background $E \times B$ flows are considered to have a stabilizing effect on turbulence [29]. By contrast, here, an increase of the background shear γ_E does

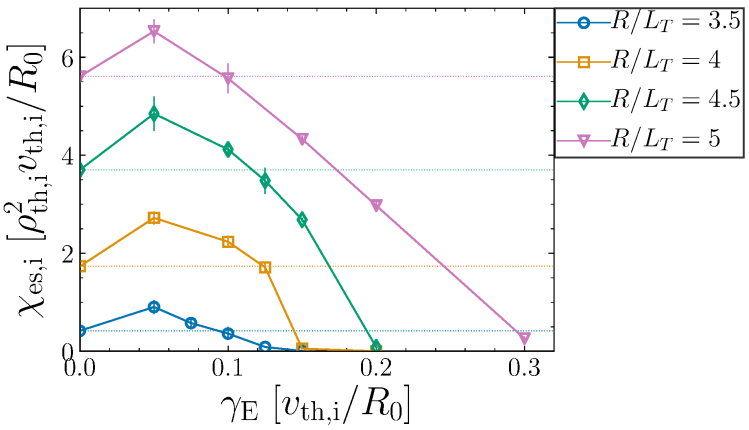

Figure 6.12: Volume and time averaged electrostatic ion heat conductivity $\chi_{\mathrm{es,i}} = Q_{\mathrm{es,i}}/(R_0/L_T)$ against the background $E \times B$ shearing rate γ_E for various values of R_0/L_T. Horizontal dotted lines depict the zero shear transport level.

not necessarily reduce the transport level (see Fig. 6.12). Instead, two regimes with respect to γ_E can be identified:
(I) In the limit of small background shear the dependence of the heat conductivity on the background shear is non-monotonic. After an initial increase with γ_E it eventually decreases and crosses the zero shear transport level (horizontal dotted lines). In this regime a sheared background flow does not cause stabilization with respect to the zero shear limit. Similar results have been obtained recently in a flux driven adiabatic model [134] and is interpreted as resulting from the interplay of staircase structures with a torque induced sheared rotation in the aforementioned reference. Indeed, some aspects of this effect might be present in recent studies in the ASDEX Upgrade experiment, reporting that an increase of the $E \times B$ shear did not result in a confinement improvement [135].
(II) In a subsequent regime the heat conductivity decreases monotonically with γ_E. However, not all R_0/L_T-realization depicted in Fig. 6.12 exhibit this second regime. In the case of $R_0/L_T = 4.0$ rather a sharp drop to zero transport level is found introducing a bivalent behavior of $\chi_{\mathrm{es,i}}(\gamma_\mathrm{E})$. The transport level in the case of $R_0/L_T = 3.5$ is too small to allow for a clear sharp drop.

The critical shearing rate $\gamma_{\mathrm{E}}^{\mathrm{c}} \approx 0.1-0.15\ v_{\mathrm{th,i}}/R_0$ connected to both the transition from regime (I) to (II) as well as the drop in the transport level agrees well with typical shearing rates in the mesoscale ($n_{\mathrm{ZF}} = 1$) ZF component (see Fig. 6.3 and Fig. 6.11) and the ZF corrugations (Fig. 6.11). In agreement with Ref. [134], the above observation is therefore interpreted as a manifestation of an interplay of modified staircase structures with the background shear flow.
This interpretation is supported by an investigation of zonal flow structures analyzed through the director field K_ϕ (orange data in the right panels of Fig. 6.13). In regime (I) of $R_0/L_T = 4.0$ a finite shear of $\gamma_{\mathrm{E}} = 0.1\ v_{\mathrm{th,i}}/R_0$ [panel (b)] results in regions with positive director field developing at the expense of negative plateaus of the modified staircase in the zero shear limit [panel (a)]. Similar to Ref. [134] the imposed background shear does not simply add to the shear connected to the modified staircase structures, i. e., the structure in the right panel of Fig. 6.6 (b) does not result from a shift of the structure displayed in the right panel of (a) by a positive constant. Rather a transformation in the overall structure occurs with the maximum local value of the director field and, hence, the maximum shearing rate, being preserved. The most prominent observation is the occurrence of mesoscale structures with zero crossings in the director field for the $\gamma_{\mathrm{E}} = 0.1\ v_{\mathrm{th,i}}/R_0$ case and their absence in the quenched state at $\gamma_{\mathrm{E}} = 0.2\ v_{\mathrm{th,i}}/R_0$ [panel (c)]. This observation suggests that the reduced shear at zero crossings of the director field allow for instabilities to grow locally [127, 54] leading to the finite turbulent level. In the latter case the level of background shear exceeds typical shearing rates connected to modified staircase structures. As a result no zero crossings in K_ϕ are found and the radially finite positive shear is sufficient to suppress instabilities. Note that in this quenched case K_ϕ does not exhibit ZF corrugations close to LORLs, showing that turbulence has to be active to sustain such structures.
At sufficiently large R_0/L_T zero crossings of the shearing rate are, however, not necessary for a finite turbulent level [see panel (d) in Fig. 6.13]. In the case of $R_0/L_T = 5$ and $\gamma_{\mathrm{E}} = 0.2\ v_{\mathrm{th,i}}/R_0$ which is representative for regime (II) the director field is always larger than zero. Although signatures of ZF corrugations are visible, the shearing rate connected to those structures does not drop to zero.

Spatio-temporal organization of avalanche like transport events in the presence of modified staircase states and background shear flows

Turbulence close to marginal stability is often connected to avalanche like transport [136, 137, 138]. Avalanches are ballistically propagating transport events which organize spatially in the presence of an $E \times B$-staircase [23, 24] as their propagating direction is anti-correlated to the sign of the local $E \times B$ shearing rate [26, 27, 81].
Due to their ballistical propagation, such transport events appear as inclined

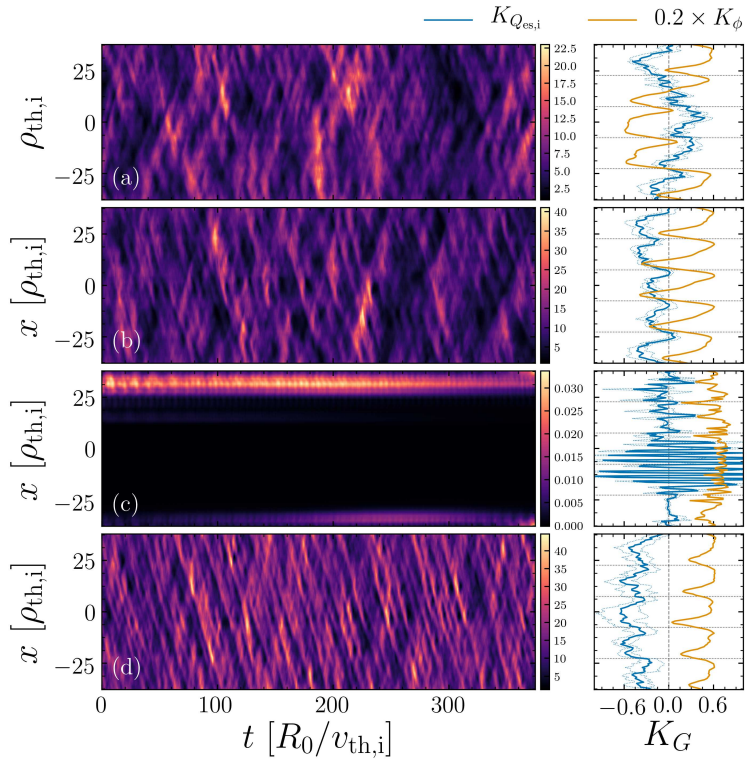

Figure 6.13: Left: Flux-surface averaged electrostatic ion heat flux $Q_{\mathrm{es,i}}$ in the x-t-plane for $R_0/L_T = 4.0$ and $\gamma_{\mathrm{E}} = 0$ (a), $\gamma_{\mathrm{E}} = 0.1\ v_{\mathrm{th,i}}/R_0$ (b) and $\gamma_{\mathrm{E}} = 0.2\ v_{\mathrm{th,i}}/R_0$ (c) and for $R_0/L_T = 5.0$ and $\gamma_{\mathrm{E}} = 0.2\ v_{\mathrm{th,i}}/R_0$ (d). Right: Corresponding temporally averaged radial profiles of the director fields $K_{Q_{\mathrm{es,i}}}$ (blue) and K_ϕ (orange). Horizontal black dotted lines indicate LORLs.

structures in the spatio temporal representation (x-t-plane) of turbulent fields. Treating avalanches as local pattern with the orientation representing the propagation direction and speed, allows for their detection through director field methods. Since heat avalanches are considered here the director field of the flux-surface averaged turbulent ion electrostatic heat flux $K_{Q_{\mathrm{es,i}}}$ is investigated (blue profiles in right panels of Fig. 6.13). Its definition follows Sec. 6.2.2 with $y \to t$ as well as $G = Q_{\mathrm{es,i}}$ and positive (negative) values denote preferential outward (inward) propagation. An error is estimated by the standard deviation of $K_{Q_{\mathrm{es,i}}}$ calculated for six equally long temporal sub intervals from the total time interval (thin blue dotted lines).
Although avalanche like transport events are visible in the spatio temporal evolution of $Q_{\mathrm{es,i}}$ corresponding to a modified staircase state [panel (a) in Fig. 6.13], the spatial scale over which single events correlate appears significantly smaller than the $n_{\mathrm{ZF}} = 1$ mesoscale as usually observed in connection to staircases in local gradient-driven simulations with adiabatic electrons [25, 77].

The propagation pattern especially lacks the clear radial location with respect to the $n_{\mathrm{ZF}} = 1$ mesoscale where avalanches are initiated. More in detail, Refs. [24, 25, 77] find avalanches starting at the zero crossing of the $n_{\mathrm{ZF}} = 1$ structure where the shearing rate changes sign $\omega_{\mathrm{ExB}} > 0 \rightarrow \omega_{\mathrm{ExB}} < 0$ with increasing radial coordinate and a subsequent inward (outward) propagation through regions with positive (negative) $E \times B$ shear. The director field $K_{Q_{\mathrm{es,i}}}$, however, demonstrates that there is an organization of the averaged avalanche propagation direction with respect to the $n_{\mathrm{ZF}} = 1$ mesoscale ZF [see right panel (a)]. The anti-correlation of $K_{Q_{\mathrm{es,i}}}$ and K_ϕ is in agreement with literature and so is the preferential triggering of avalanches close to the zero crossing of the director field satisfying $K_\phi > 0 \rightarrow K_\phi < 0$ with increasing radial coordinate (note that K_ϕ is proportional to the local shearing rate). Therefore, both disparate mesoscales that are characteristic for the modified staircase state are manifest in the spatial organization of avalanches. This outcome confirms that avalanche like transport in connection with modified staircase states share similarities with their adiabatic counterpart.
The finite background shear cases [panel (b) and (d)] both exhibit preferentially inward propagating avalanches in agreement with the director field K_ϕ being positive over almost the entire radial domain. The fact that $K_{Q_{\mathrm{es,i}}}$ approaches zero close to LORLs in case of $R_0/L_T = 4.0$ and $\gamma_{\mathrm{E}} = 0.1\ v_{\mathrm{th,i}}/R_0$ suggests that avalanche like transport dynamics is significantly organized with respect to the ZF corrugations. This claim is supported by the avalanche events visible in panel (b) of Fig. 6.13 being organized on a lengths scale of L_x/i_{k} with the triggering of individual events close to LORLs. In the case of $R_0/L_T = 5.0$ and $\gamma_{\mathrm{E}} = 0.2\ v_{\mathrm{th,i}}/R_0$ [panel (d)], by contrast, the radial structuring of avalanches on corrugation scale is less obvious. Single avalanches rather travel (multiple times) over the entire radial domain, which manifests itself in a clear non-zero negative profile of $K_{Q_{\mathrm{es,i}}}$. Although, the triggering of individual avalanches close to LORLs cannot be identified, an interaction of avalanches with ZF corrugations in this case is nevertheless visible in form of an i_{k}-fold modulation in $K_{Q_{\mathrm{es,i}}}$.
The above observations support the hypothesis that instabilities and the resulting turbulence is influenced by modified staircase in regime (I) but less in regime (II). In order to clarify the role of modified staircase for turbulence generating instabilities a stability analysis of modified staircase equilibria would be necessary, which is beyond the scope of this chapter.

6.4 Conclusion

Microturbulence close to marginality with inclusion of kinetic electrons [1] has been revisited. This chapter focused on the detection of mesoscale sheared zonal

$E \times B$ flow structures and on the comparison of such structures with fine scale features typically dominating the $E \times B$ shearing rate when including electron dynamics [83, 1]. The main results are summarized below.
Mesoscale modes in the zonal potential develop on considerable time scales of the order of $\sim 10^2 - 10^3 \; v_{\mathrm{th,i}}/R_0$. An interplay of those mesocscale modes with lowest order rational layers is observed in the form of a radial lock-in behavior with i_{k}-fold symmetry. In contrast to fine scale features in the $E \times B$ shearing rate whose amplitudes exceed typical growh rates by an order of magnitude, the $E \times B$ shearing rate conntected to the mesoscale modes follows the Waltz rule $\omega_{\mathrm{ExB}} \sim \gamma$ [69, 125] and is therefore physical meaningful.
In this chapter the director field method [108] has been used to directly obtain a measure of the tilting of the eddy structures. It has been shown that the director field can be used to estimate the $E \times B$ shearing rate provided the latter is connected to structures with a sufficient radial extent. The diagnostic shows that small scale $E \times B$ shearing does not result in eddy tilting and, therefore, not in turbulence suppression. This observation is mainly attributed to finite Larmor radius effects that mitigate the ability of fine scale features to efficiently shear turbulent structures. The director field method reveals zonal flow mesoscale pattern formation on two distinct scales; namely (i) mesoscale corrugations in the vicinity of lowest order rational layers and (ii) a mesoscale variation on the length scale of the radial boxsize. The lock-in of mesoscale zonal potential signatures is manifest in a distinct radial orientation of the latter structure. The amplitude of both structures can be related to typical shearing rates of a few $\sim 10^{-1} \; v_{\mathrm{th,i}}/R_0$. Parallel and radial force balance relate the mesoscale corrugations occurring close to lowest order rational layers to perpendicular ion pressure corrugations. A structure decomposition based on the radial force balance demonstrates that the mesoscale pattern in the director field can be understood as being composed of a fully-developed type staircase [25, 77] and pressure related zonal $E \times B$ flow corrugations. The shape of the electrostatic potential around lowest order rational layers is influenced by the presence of a modified staircase, manifesting itself in a radial asymmetry of the zonal flow corrugations.
The combined effect of modified staircase structures and a background $E \times B$ shear flow result in a non-monotonic dependence of the turbulent level on the background $E \times B$ shearing rate. No shear stabilization is observed when the background shearing rate is smaller or comparable to the shearing rate connected to modified staircase structures. Similar observations in connection to the $E \times B$-staircase state have been made within a flux-driven model in Ref. [134]. A director field analysis of the turbulent heat flux demonstrates a spatio-temporal organization of heat avalanches with respect to the modified staircase structure. The averaged propagation direction of avalanches is anticorrelated with the local sign of the $E \times B$ shearing rate [26, 27, 81] and the resulting averaged propagation pattern within the modified staircase is in agreement with heat avalanches in connection to the conventional $E \times B$-staircase state [23, 24].

The implications of this work are now briefly discussed. (i) The longterm dynamics introduced by slowly evolving mesoscale modified staircase states requires long time integration to accurately describe turbulent states close to the threshold. This requirement is computationally highly demanding when treating electrons as a kinetic species. The understanding of turbulence close to the threshold is, however, necessary since future reactors will operate close to marginal stability [115]. (ii) The $E \times B$ shearing rate ω_{ExB}, i. e., the second radial derivative of the electrostatic potential, that is often applied to characterize the shearing action of zonal flows, fails when structures on length scales of the Larmor radius dominate this observable. In this case director field methods provide a more accurate characterization of the shearing action of zonal $E \times B$ flows since they are not biased by finite Larmor radius effects. (iii) Mesoscale $E \times B$ staircase structures do develop in kinetic electron descriptions close to marginality even for CBC parameters. Hence fine scale features do not prevent staircases from developing. (iv) In contrast to the fully and partially developed variants of the $E \times B$ staircase state observed in adiabatic electron models [25], the modified form does not clearly exhibit a structure bifurcation. In particular, it does not allow for the transition of avalanche governed turbulent periods (partially developed staircase) to almost quenched periods (fully developed staircase) when CBC parameters are chosen. This type of turbulence dynamics, also observed in flux-driven near marginal turbulence with adiabatic electrons [24], however, is recovered with the choice of a vanishing electron background temperature gradient. Inclusion of electron dynamics, therefore, bears additional physics that impacts near marginal turbulence and is therefore required to accurately describe such states.

Chapter 7

Transport hysteresis in electromagnetic microturbulence caused by mesoscale zonal flow pattern induced mitigation of high β turbulence runaways

This chapter is based on the publication [139].

7.1 Introduction

An advantageous regime for fusion devices is the operation at high normalized pressure β, where $\beta = n_0 T_0/(B_0^2/2\mu_0)$ compares the thermal plasma pressure to the background magnetic field pressure with n_0, T_0 and B_0 being the equilibrium density, temperature and magnetic field, respectively, and μ_0 is the permeability of free space. A high β is favorable for the fusion power [140, 141] as well as a large non-inductive bootstrap current fraction [6, 7, 8] and constitutes a key ingredient for future steady state tokamak scenarios [116, 117].
With increasing β plasma turbulence responsible for the anomalous particle, heat and momentum transport acquires an electromagnetic character. Perturbed electric current densities then start to couple to perturbations in the magnetic vector potential through Ampère's law. This gives rise to additional plasma dynamics such as shear Alfvén waves and the streaming of particles along perturbed magnetic field lines; —the so-called magnetic flutter.
Several aspects of microturbulence, the mechanism that dominates energy losses from the plasma, are influenced by electromagnetic effects [142]. Beginning with the linear properties, the growth rate of primarily electrostatic microinstabilit-

ies, such as the ion temperature gradient (ITG) driven instability [13, 14, 15], reduces with increasing β due to free energy being diverted into field line bending [20, 21]. Furthermore, additional electromagnetic instabilities like the kinetic ballooning mode (KBM) occur once a threshold in β is exceeded [143, 20, 144]. Proceeding with the nonlinear dynamics, electromagnetic perturbations are able to destroy the intactness of magnetic flux-surfaces resulting in magnetic stochasticity [57, 145]. The streaming along such stochastic magnetic field lines give rise to radial turbulent transport [146, 21, 147, 148]. Finally, zonal flows, i. e., $E \times B$ flows connected with a poloidally and toroidally constant electrostatic potential, are influenced by electromagnetic effects. Most notably, the charge loss associated with magnetic flutter can damp zonal flows [58] and, hence, may impact the nonlinear saturation of electromagnetic (ITG-) mictroturbulence which is mediated by zonal flows [65]. On the other hand, the efficiency of zonal flow mediated nonlinear transfer of free energy to higher radial wave vector modes has been reported to increase with β resulting in the so-called electromagnetic stabilization [65, 66]. And finite β effects also impact zonal flow production through modulational instability [48, 149]. In addition, energetic particle driven modes can add to the zonal flow generation at high β in a reactor relevant burning plasma via force-driven excitation [49, 50].

In view of fusion performance, an important objective is the understanding of the mechanisms determining the maximum achievable β in electromagnetic microturbulence. Extensive gyrokinetic studies [21, 61, 60, 59, 148] revealed a limitation in β caused by the occurrence of turbulence runaways: once a critical β_{c} is exceeded the turbulence does not saturate at reasonable levels anymore but rise to indeterminately values. While Ref. [61] proposes pressure corrugation driven subcritical KBMs being responsible for this phenomenon, Ref. [60] relates it to the depletion of zonal flows through field line decorrelation aided magnetic stochasticity. Dependent on the plasma parameters, this upper β limit can be situated below the KBM threshold and is, therefore, regarded as a new nonlinear critical β [60]. It is also referred to as the nonzonal transition (NZT) in the aforementioned reference.

Ref. [21] indicates the possibility of turbulence to saturate at reasonable levels for values of β exceeding the above discussed threshold, if specific initial conditions are chosen (see also comments in Refs. [150, 59]). In most of those cases, however, the saturation has been of limited duration with turbulence runaways occurring at later simulation times. In Ref. [59] this saturation has then been interpreted as being a transient phenomenon, such that it does not reflect the proper stationary state in the long time limit.

This issue motivates the analysis presented in this chapter, that focuses on the question whether (self-consistent) initial conditions can be found that allow for stationary states above the nonlinear critical β_{c} limit, i. e., above the NZT. Moreover, the recent development in the understanding of mesoscale zonal flow structure formation and the long-term development of such struc-

tures [23, 24, 25, 76, 77, 151, 118] motivates the analysis presented in this paper. Indeed, it is shown that proper stationary states are accessible through the application of mesoscale zonal flow dominated states as initial conditions. Such states develop self-consistently on long time scales of $\sim 10^2 - 10^3\ R_0/v_{\mathrm{th,i}}$ (R_0 is the major radius and $v_{\mathrm{th,i}}$ is the ion thermal velocity) in specific parameter regimes. This finding is gained by means of an extensive (long-term integration) nonlinear gradient-driven gyrokinetic study, complemented by field line tracing methods [57, 59] and a zonal flow energy transfer study. Once this improved β-regime is established, several aspects of it, such as the stability against turbulence runaways, the role of magnetic stochasticity and zonal flow energy transfer processes, are discussed.
The remainder of this chapter is structured as follows: In Sec. 7.2 the governing equations, the gyrokinetic simulation setup, the field line tracing diagnostic and the zonal flow intensity evolution diagnostic are described. The numerical results are presented in Sec. 7.3 including a description of the transport hysteresis phenomenon in Sec. 7.3.1, an investigation of mesoscale zonal flows in Sec. 7.3.2, a numerical convergence study in Sec. 7.3.3, a stability analysis of the improved β-regime in Sec. 7.3.4, a field line tracing analysis in Sec. 7.3.5, a zonal flow intensity transfer study in Sec. 7.3.6 and a confirmation of the transport hysteresis phenomenon using an exact circular concentric geometry model in Sec. 7.3.7. A summary of the main results, a brief discussion and an outlook are presented in Sec. 7.4.

7.2 Numerical experiment and diagnostics

Electromagnetic microturbulence is investigated by means of nonlinear gyrokinetic simulations performed with the fluxtube version of the gyrokinetic solver Gyrokinetic Workshop (GKW) [95]. The set of governing equations solved by GKW is composed of the gyrokinetic equation, the gyrokinetic Poisson equation and the parallel component of the gyrokinetic Ampère's law introduced in Sec. 4.3.1 and 4.3.2, respectively.

7.2.1 Plasma parameters and numerical setup

Plasma parameters

In this chapter CBC parameters (see Sec. 4.4) are chosen and (background) plasma rotation and collisions are neglected. Stationary plasma rotation evolving self-consistently with the turbulence in the form of zonal flows, however, can and will develop. Both a single ion species (deuterium) and electrons are treated as separate kinetic species with the electron to ion mass ratio $m_{\mathrm{e}}/m_{\mathrm{i}} = 2.72 \times 10^{-4}$.

	N_{k_x}	N_{k_θ}	N_s	N_μ	$N_{v_\parallel}$	$k_{x,\max}\rho_{\mathrm{th,i}}$	$k_{\theta,\max}\rho_{\mathrm{th,i}}$	geometry
G_1	83	21	32	9	64	2.8	1.4	$s-\alpha$
G_1-s	83	21	64	9	64	2.8	1.4	$s-\alpha$
G_1-x	165	21	32	9	64	5.6	1.4	$s-\alpha$
G_2	125	21	48	9	64	4.2	1.4	$s-\alpha$
G_3	125	31	48	9	64	4.2	2.1	$s-\alpha$
S_1	43	11	32	9	64	2.8	1.4	$s-\alpha$
L_1	125	31	32	9	64	2.8	1.4	$s-\alpha$
G_1^{circ}	83	21	32	9	64	3.4	1.4	circular

Table 7.1: Summary of the numerical resolution setups applied in this chapter.

Electromagnetic effects are considered by including perturbations in the parallel component of the magnetic vector potential $A_\parallel$, while neglecting magnetic field compression effects. The strength of electromagnetic effects is controlled by the normalized plasma pressure β. The plasma beta enters the parallel component of Ampere's law [95] and is varied in the range $\beta = 0.03 \sim 1.4$ %.
Magnetic equilibria with circular concentric flux-surfaces are considered exclusively in this chapter. For comparability purposes most of the simulations apply a simplified $s-\alpha$ geometry [103] with $\alpha = 0$. This model approximates circular concentric flux-surfaces by retaining only the lowest order terms in an expansion in the inverse aspect ratio $\epsilon = r/R_0$ of the geometry tensors. Note that r is the minor radial coordinate of the circular flux-surfaces. Additional simulations with exact circular concentric flux surfaces [9] are performed as well. The latter geometry model retains all orders of ϵ in the definition of the geometry tensors. The influence of the normalized plasma pressure gradient β' on the the magnetic field equilibrium is not considered in this chapter.

Numerical setup

The different sets of numerical resolution, applied in this chapter, are summarized in Tab. 7.1 listing the number of radial modes N_{k_x}, the number of poloidal modes N_{k_θ}, the number of grid points along the field line N_s, the number of magnetic moment grid points N_μ, the number of parallel velocity grid points $N_{v_\parallel}$, the maximum resolved radial wave vector $k_{x,\max}\rho_{\mathrm{th,i}}$ and the maximum resolved poloidal wave vector $k_{\theta,\max}\rho_{\mathrm{th,i}}$. The poloidal wave vector relates to the y-wave vector through Eq. (4.41). Note that the term 'poloidal' wave vector is historical and kept for consistency with Ref. [95].
The velocity space $(v_\parallel, \mu)$ is always resolved up to $v_{\parallel,\mathrm{max,sp}} = 3.0\ v_{\mathrm{th,sp}}$ and $\mu_{\mathrm{max,sp}} = 4.5\ m_{\mathrm{sp}} v_{\mathrm{th,sp}}^2 / B_0$.

Below, the sets G_1 and G_1^{circ} will be referred to as the standard sets of the respective geometry model. The latter has been shown to produce converged results in the electrostatic limit [1]. Since the rapid parallel motion of electrons along perturbed magnetic field lines may impose more stringent requirements on the spatial resolution [21] additional sets with increased parallel (G_1-s), radial (G_1-x), parallel and radial (G_2) and overall spatial resolution (G_3) are applied.
Finally, numerical (hyper-) dissipation, required for numerical stability, is applied. For a detailed description of the dissipation schemes the reader is referred to appendix B. Note that the $6th$-order zonal flow dissipation scheme introduced in Ref. [25] is applied here, since zonal flow physics, the main essence of this work, has been shown to be sensitive to numerical dissipation in this reference. The dissipation scheme is fixed by the coefficients $D_x = D_y = 0.1$, $D_{v_\parallel} = 0.2$, $D_s = 1.0$ throughout the work (unless stated otherwise).

7.2.2 Field line tracing diagnostic

In order to gain insights into the level of magnetic stochasticity it is necessary to trace the trajectories of perturbed magnetic field lines [57, 145]. Let $\mathbf{x}(\tau)$ represent the field line with τ a scalar parametrizing the field line. Then

$$\frac{\mathrm{d}\mathbf{x}}{\mathrm{d}\tau} = \mathfrak{B}, \tag{7.1}$$

where the total magnetic field $\mathfrak{B} = \mathbf{B} + \delta\mathbf{B}$ is composed of the equilibrium magnetic field $\mathbf{B}$ and the perturbed magnetic field $\delta\mathbf{B} = \nabla \times A_\parallel \mathbf{b} \approx \nabla A_\parallel \times \mathbf{b}$. For the latter approximation it has been used that the equilibrium magnetic field varies on spatial scales larger than the perturbations so that $A_\parallel \nabla \times \mathbf{b}$ can be neglected.
The equations describing the perturbed field line trajectories are obtained by the taking the inner product of Eq. (7.1) with the base vectors ∇s, ∇x and ∇y. In straight field aligned Hamada coordinates $\nabla x \cdot \mathbf{B} = 0$ as well as $\nabla y \cdot \mathbf{B} = 0$ and one finds

$$\frac{\partial y}{\partial s} = \frac{(\nabla y \times \nabla x) \cdot \mathbf{b}}{\nabla s \cdot \mathbf{B}} \frac{\partial A_\parallel}{\partial x} \tag{7.2}$$

$$\frac{\partial x}{\partial s} = -\frac{(\nabla y \times \nabla x) \cdot \mathbf{b}}{\nabla s \cdot \mathbf{B}} \frac{\partial A_\parallel}{\partial y}. \tag{7.3}$$

The factors preceding the spatial derivatives of $A_\parallel$ are directly determined by the chosen geometry and are related to predefined tensors in GKW that can be found in Ref. [95].
In this chapter 3D spatial grid data of $A_\parallel$ is self-consistently obtained through nonlinear simulations and output each transit time $R_0/v_{\text{th,i}}$. An integration algorithm similar to the one described in Ref. [59] is then applied in postprocessing. The following steps are executed per time step:

(i) $A_\parallel$ and the geometric tensors are refined in the s-direction by a factor of two through cubic spline inter- and extrapolation. In addition, $A_\parallel$ is refined in the y-direction through zero padding in the k_y wave vector space to obtain an equal number of x- and y-grid points in real space. (ii) $N_{\mathrm{FL}} = 1024$ field lines are seeded equidistantly in x on the LFS midplane ($s \approx 0$ and mid position on the y-grid). (iii) Eq. (7.2) and Eq. (7.3) are integrated numerically for 100 poloidal turns (unless stated otherwise) and for increasing s using a second order midpoint technique with the refined s-points serving as midpoints. The first order spatial derivatives in x and y on the right hand side (RHS) of the field line equations are approximated by 4−th order central differences. In the evaluation of the RHS the local values of $\partial_x A_\parallel$ and $\partial_y A_\parallel$ at the continuous field line position $[x(s), y(s)]$ are approximated by two dimensional linear interpolation on the x-y-plane. (iv) Periodic boundary conditions are applied in the x- and y-direction, while the shift $\Delta y = -(q_0 \hat{s}_0/\epsilon_0) \times (x - x_0)$ applies in the s-direction at $s = +0.5 \rightarrow -0.5$ as a consequence of the shifted parallel boundary conditions.

7.2.3 Zonal flow intensity evolution diagnostic

A key aspect of this work are zonal flows, which enter the gyrokinetic equation through the $E \times B$ nonlinearity [the $\mathbf{v}_E \cdot \nabla g_{\mathrm{sp}}$ term in Eq. (4.46)]. Zonal flows are $E \times B$ flows connected to the zonal part of the electrostatic potential

$$\langle \phi \rangle = \frac{1}{L_y} \int \mathrm{d}y \int \mathrm{d}s \; \phi \tag{7.4}$$

$$= \sum_{k_{\mathrm{ZF}}} \underbrace{\int \mathrm{d}s \; \hat{\phi}_{\mathbf{k}}(k_{\mathrm{ZF}}, k_y = 0, s)}_{\langle \hat{\phi}_{\mathbf{k}} \rangle} \exp(\mathrm{i} k_{\mathrm{ZF}} x). \tag{7.5}$$

The spectral reprentation Eq. (4.35) has been used to obtain the second expression, which defines the zonal flow wave vector k_{ZF} and the Fourier amplitude of the zonal potential $\langle \hat{\phi}_{\mathbf{k}} \rangle$. In order to obtain a measure of the zonal flow level the zonal flow intensity is defined by

$$\mathcal{E}_Z = k_{\mathrm{ZF}}^2 |\langle \hat{\phi}_{\mathbf{k}} \rangle|^2. \tag{7.6}$$

Strictly speaking $\mathcal{E}_Z$ quantifies the intensity of the radial electric field connected to the zonal potential with wave vector k_{ZF}. In the case of mesoscale zonal structures with $(k_{\mathrm{ZF}} \rho_{\mathrm{th,i}})^2 \ll 1$, investigated exclusively throughout this work, the gyroaverage entering $\mathbf{v}_E$ [Eq. (2.35)] can be neglected. Therefore, the zonal flow velocity is directly proportional to the radial electric field in good approximation. An evolution equation for the zonal flow intensity $\mathcal{E}_Z$ can be derived from the spectral representation of the gyrokinetic Poisson equation [Eq. (B.8)]. The time

derivative of the inverted and flux-surface averaged $k_y = 0$ part of this equation reads

$$\frac{\partial \langle \hat{\phi}_{\mathbf{k}} \rangle}{\partial t} = - \int \mathrm{d}s \, \frac{1}{\mathcal{P}} \sum_{\mathrm{sp}} Z_{\mathrm{sp}} e \frac{2\pi B}{m_{\mathrm{sp}}} \int \mathrm{d}v_{\parallel} \int \mathrm{d}\mu \left[J_0(\lambda_{\mathrm{sp}}) \frac{\partial \hat{g}_{\mathrm{sp},\mathbf{k}}}{\partial t} \right]_{\mathbf{k}=(k_{\mathrm{ZF}},0)}, \quad (7.7)$$

where

$$\mathcal{P} = \sum_{\mathrm{sp}} \frac{n_{0,\mathrm{sp}} Z_{\mathrm{sp}}^2 e^2}{T_{0,\mathrm{sp}}} [\Gamma_0(b_{\mathrm{sp}}) - 1]. \quad (7.8)$$

The time derivative of the perturbed modified distribution function $\partial_t \hat{g}_{\mathrm{sp},\mathbf{k}}$ entering the RHS of Eq. (7.7) is substituted by the right hand side of the gyrokinetic equation (B.8). Finally, Eq. (7.7) is multiplied by $2k_{\mathrm{ZF}}^2 \langle \hat{\phi}_{\mathbf{k}} \rangle^*$, where $\langle \hat{\phi}_{\mathbf{k}} \rangle^*$ denotes the complex conjugate of $\langle \hat{\phi}_{\mathbf{k}} \rangle$, and is recast into the form

$$\begin{aligned} \frac{\partial \mathcal{E}_Z}{\partial t} &= \mathcal{R} + \mathcal{M} + \mathcal{L}_{\parallel,f} + \mathcal{L}_{\parallel,F_M} + \mathcal{L}_{D,f} + \mathcal{L}_{D,F_M} \\ &\quad + \mathcal{L}_{\mathrm{tr}} + \mathcal{L}_{\chi,F_M} + \mathcal{D}. \end{aligned} \quad (7.9)$$

The individual terms on the RHS result from the individual terms of the gyrokinetic equation (B.8): the $E \times B$ nonlinearity $N_E \to \mathcal{R}$, the magnetic flutter nonlinearity $N_{\delta B} \to \mathcal{M}$, parallel streaming $L_{\parallel,f} \to \mathcal{L}_{\parallel,f}$, Landau damping $L_{\parallel,F_{\mathrm{M}}} \to \mathcal{L}_{\parallel,F_M}$, magnetic drift in the perturbed distribution $L_{D,f} \to \mathcal{L}_{D,f}$, magnetic drift in the Maxwellian $L_{D,F_{\mathrm{M}}} \to \mathcal{L}_{D,F_M}$, trapping term $L_{\mathrm{tr}} \to \mathcal{L}_{\mathrm{tr}}$, advection of background gradients by the $E \times B$-drift and magnetic flutter $L_{\chi} \to \mathcal{L}_{\chi,F_M}$, and numerical dissipation $D_{\mathrm{sp}} \to \mathcal{D}$. The contribution from the trapping term ($\mathcal{L}_{\mathrm{tr}}$) and the advection of background gradients by the $E \times B$-drift and magnetic flutter ($\mathcal{L}_{\chi,F_M}$) are mentioned for completeness, but can be shown to vanish. The first two terms on the right hand side of Eq. (7.9) are the only nonlinear terms and are the Reynolds- and Maxwell stress transfer respectively.

7.3 Numerical results

7.3.1 Transport hysteresis with normalized plasma pressure

In this section the transport hysteresis phenomenon is introduced with the turbulent transport level being characterized by the heat conductivity

$$\chi_{j,\mathrm{sp}} = Q_{j,\mathrm{sp}} / n_{0,\mathrm{sp}} T_{0,\mathrm{sp}} L_{T,\mathrm{sp}}^{-1}. \quad (7.10)$$

The volume averaged radial electrostatic ($j = \mathrm{es}$) and electromagnetic ($j = \mathrm{em}$) heat flux is defined by

$$Q_{j,\mathrm{sp}} = \frac{1}{V} \int \mathrm{d}^3 X \int \mathrm{d}^3 v \, \frac{1}{2} m_{\mathrm{sp}} v^2 (\mathbf{v}_j \cdot \nabla x) f_{\mathrm{sp}}, \quad (7.11)$$

where $(1/V)\int \mathrm{d}^3X$ denotes the volume averaging operator,

$$\int \mathrm{d}^3v = \frac{2\pi B}{m_{\mathrm{sp}}} \int \mathrm{d}v_\parallel \int \mathrm{d}\mu, \tag{7.12}$$

$v^2 = v_\parallel^2 + 2\mu B/m_{\mathrm{sp}}$, and $\mathbf{v}_{\mathrm{es}} = \mathbf{v}_E$ [Eq. (3.15)] and $\mathbf{v}_{\mathrm{em}} = \mathbf{v}_{\delta B}$ [Eq. (3.16)] represent the $E \times B$ drift and the parallel motion along perturbed field lines, respectively. The heat flux is always given in terms of $\rho_*^2 n_0 T_0 v_{\mathrm{th,i}}$.
A simplified $s - \alpha$ geometry with $\alpha = 0$ is chosen for comparability reasons throughout section 7.3.1. For a confirmation of the transport hysteresis phenomenon within an exact circular geometry the reader is referred to Sec. 7.3.7. The essence of the transport hysteresis is a multiplicity of the transport level, depending on the initial conditions. Two regimes can be identified in the considered β-range.

In agreement with Refs. [21, 59] the electrostatic ion heat transport decreases

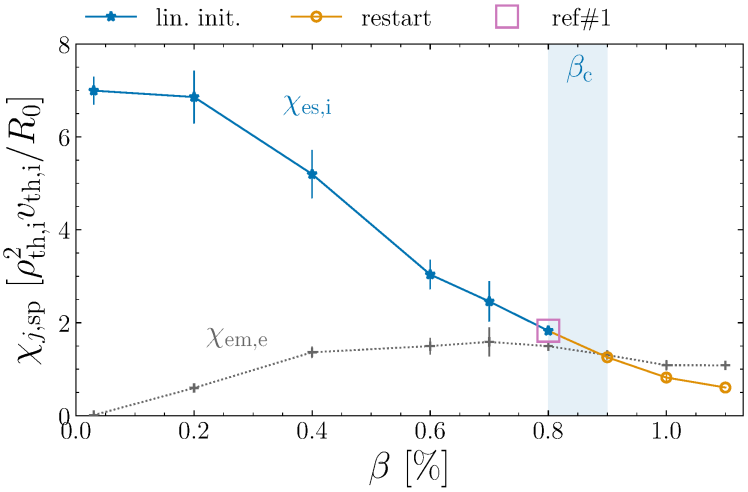

Figure 7.1: Dependence of the time and volume averaged ion electrostatic heat conductivity $\chi_{\mathrm{es,i}}$ (solid lines) and electron electromagnetic flutter heat conductivity $\chi_{\mathrm{em,e}}$ (dotted line) on the plasma β with fixed $R_0/L_T = 6.9$ and $s - \alpha$ geometry. Shown are results with initialization in the linear regime (blue stars) as well as restarted from the late stationary state at $\beta = 0.8$ % (orange circles). The blue shaded region indicates the occurrence of turbulence runaways to extreme levels (see description in the text). The specified statistical errors are determined through six-part time averaging (see appendix C).

and the electromagnetic electron heat transport increases with β (blue data in Fig. 7.1). Above a threshold value of $\beta_{\mathrm{c}} = (0.85 \pm 0.05)$ % (blue shaded area), however, the turbulent fluxes undergo a temporal runaway to extreme values right after the initial linearly growing eigenmodes have saturated nonlinearly. In the case of $\beta = 0.9$ %, for example, initial nonlinear saturation occurs at

$t \approx 20\ R_0/v_{\mathrm{th,i}}$ with $Q_{\mathrm{es,i}} \sim 10^1\ \rho_*^2 n_0 T_0 v_{\mathrm{th,i}}$. In the subsequent runaway $Q_{\mathrm{es,i}}$ increases by several orders of magnitude. This high β runaway has been confirmed by various gyrokinetic codes [152, 21, 61, 148] and is referred to as the nonzonal transition (NZT) in Ref. [60]. The extreme flux levels resulting from this runaway are not included in Fig. 7.1, since for the fixed numerical resolution no physically meaningful solution can be guaranteed in this high amplitude regime. Due to the disruptive nature of this runaway phenomenon, it restricts the accessible regime in terms of plasma parameters β and R_0/L_T. In Ref. [60] it is, therefore, proposed to set a new critical (nonlinear) limit in β.

Significant computational effort has been dedicated to confirm the physical nature of this runaway phenomenon [59]. The threshold $\beta_{\mathrm{c}} = (0.85 \pm 0.05)$ %, obtained with standard parameters G_1 in the present work, agrees well with the aforementioned reference. Furthermore, its value has been reproduced (within the uncertainty given by the scan increment of $\Delta\beta = 0.1$ %) when doubling the resolution in either of the spatial directions. The physics involved in the runaway is, therefore, sufficiently resolved with the standard resolution set G_1.

To proceed, the threshold β_{c} represents an upper limit in β for which proper stationary turbulent states can be obtained, when the simulation is initialized in the linear regime. In the presented simulations this is realized by initializing the turbulent modes ($k_y \neq 0$) of the modified distribution function by $\hat{g}_{\mathbf{k},\mathrm{sp}}(k_x, k_y, s, v_\parallel, \mu) = A \times [\cos(2\pi s) + 1]$ with $A = 10^{-4}$, while the $k_y = 0$ modes are set to zero.

However, states with reasonable turbulence level are reported to be accessible for $\beta > \beta_{\mathrm{c}}$, if modified initial conditions are applied [21, 150] (orange data in Fig. 7.1). Here, the entire 5D distribution function g_{sp} in the end of the $\beta = 0.8$ % case (at $t = 2991.6\ R_0/v_{\mathrm{th,i}}$ of ref#1 in Fig. 7.1) is stored and then loaded as initial condition for all cases of the orange data series. This procedure allows for stationary turbulence up to $\beta \leq 1.1$ %.

While a similar approach has already been applied in Ref. [21] (see also comments in Refs. [150, 59]), some of the simulations in this reference suffered from turbulence runaways after time scales of several $\sim 10^2\ R_0/v_{\mathrm{th,i}}$. Therefore, the saturation of the turbulence to reasonable levels for realizations with $\beta > \beta_{\mathrm{c}}$ has been interpreted as being a transient phenomenon [59], and is assumed not to reflect the proper stationary state in the long time limit. By contrast, all simulations with standard resolution G_1 depicted in Fig. 7.1 ran stable for at least 3000 $R_0/v_{\mathrm{th,i}}$. Cases with increased spatial resolution G_1-x and G_1-s at $\beta = 1.1$ % have been realized through the same restart method as described above. Stationary turbulence during their full duration of 3868 $R_0/v_{\mathrm{th,i}}$ and 1750 $R_0/v_{\mathrm{th,i}}$ respectively is confirmed. In the case of standard resolution G_1 and $\beta = 1.1$ % stationary turbulence up to 7500 $R_0/v_{\mathrm{th,i}}$ has been ensured. The cases with $\beta_{\mathrm{c}} < \beta \leq 1.1$ % are, therefore, suggested to be stable with respect to turbulence runaways being triggered after a sufficiently long time. This regime will be denoted as the *improved β regime* hereafter.

The above discussion demonstrates a path dependence —a *hysteresis* —of the turbulent transport level with respect to the plasma β. Furthermore, it suggests that the choice of proper initial conditions allows for proper stationary states. In this context *proper initial conditions* refers to mesoscale ZF saturated states with amplitudes above a critical ZF level (see Sec. 7.3.4) and *proper stationary states* denotes stationary turbulent states with the absence of turbulence runaways. In the following sections key aspects of this hysteresis behavior are elucidated.

7.3.2 Long-term dynamics caused by mesoscale zonal flow patterns

This section aims for a characterization of the late stationary states that are applied as initial conditions to access the improved β regime. Here, stationary mesoscale zonal flow patterns, developing on long time scales, are shown to play the key role. In this context the term mesoscale refers to zonal flows with a radial scale of the box size $L_x^{s-\alpha} = 91.58\ \rho_{\mathrm{th,i}}$ ($k_{\mathrm{ZF}}\rho_{\mathrm{th,i}} = 0.07$) and $L_x^{\mathrm{circ}} = 76.27\ \rho_{\mathrm{th,i}}$ ($k_{\mathrm{ZF}}\rho_{\mathrm{th,i}} = 0.08$).

Long-term development of mesoscale zonal flow patterns

In order to clarify the difference between the phase just after initial nonlinear saturation and the state in the long-term limit, it is illuminating to study the temporal evolution of observables characterizing the zonal flow as well as the turbulence level. Here, the zonal flow shearing rate

$$\omega_{\mathrm{ExB}} = \frac{1}{B_0}\frac{\partial^2 \langle\phi\rangle_y}{\partial x^2}, \tag{7.13}$$

is considered, where the zonal potential is estimated at the low field side

$$\langle\phi\rangle_y(x) = \frac{1}{L_y}\int \phi(x, y, s \approx 0)\ \mathrm{d}y \tag{7.14}$$

$$= \sum_{k_{\mathrm{ZF}}} \langle\hat{\phi}_{\mathbf{k}}\rangle_y(k_{\mathrm{ZF}}) \times \exp(\mathrm{i}k_{\mathrm{ZF}}x). \tag{7.15}$$

Note hat Eq. (7.15) defines the Fourier amplitude of the estimated zonal potential connected to the wave vector $k_{\mathrm{ZF}} = 2\pi n_{\mathrm{ZF}}/L_x$, with the integer $-(N_x - 1)/2 \leq n_{\mathrm{ZF}} \leq (N_x - 1)/2$. The shearing rate connected to a zonal mode with mode number n_{ZF} is then defined by

$$|\langle\hat{\omega}_{\mathrm{ExB}}\rangle_{n_{\mathrm{ZF}}}| = \frac{2k_{\mathrm{ZF}}^2}{B_0}|\langle\hat{\phi}_{\mathbf{k}}\rangle_y(k_{\mathrm{ZF}})| \tag{7.16}$$

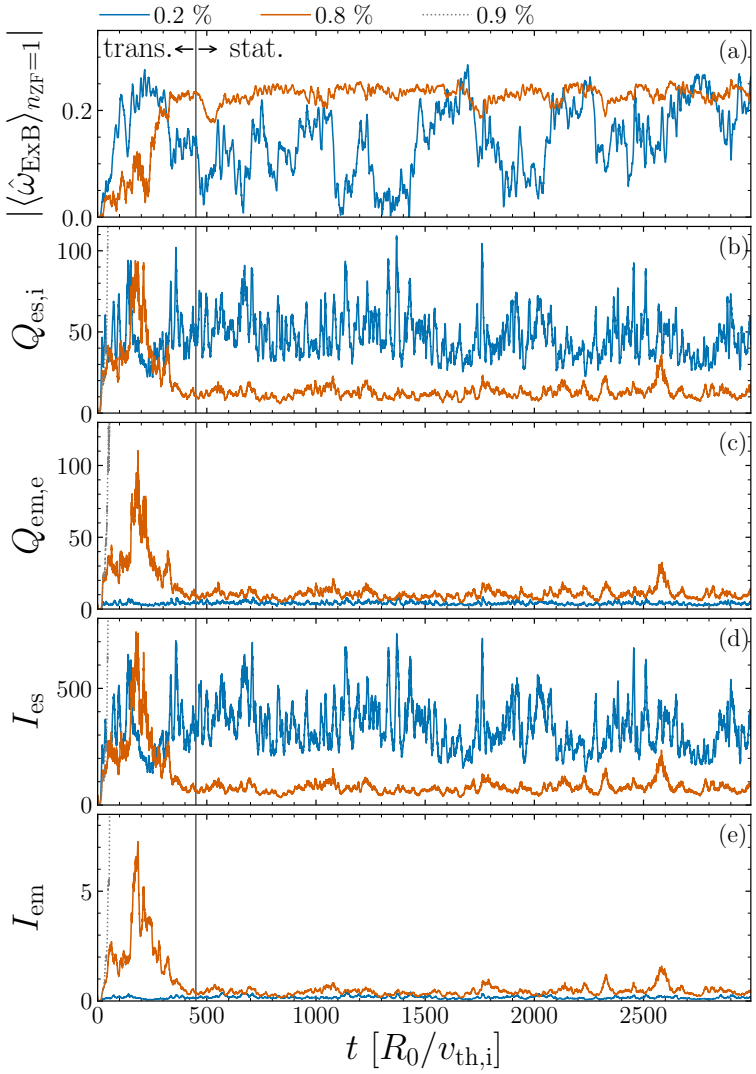

Figure 7.2: Time traces of the mesoscale zonal flow shear $|\langle\hat{\omega}_{\mathrm{ExB}}\rangle_{n_{\mathrm{ZF}}=1}|$ (a), the electrostatic ion heat flux $Q_{\mathrm{es,i}}$ (b), the electromagnetic electron heat flux $Q_{\mathrm{em,e}}$ (c), the electrostatic turbulence intensity I_{es} (d) and the electromagnetic turbulence intensity I_{em} (e) for G_1 resolution, $R_0/L_T = 6.9$ and $\beta = 0.2$ % (blue), $\beta = 0.8$ % (violet) and $\beta = 0.9$ % (gray dotted). The black vertical line roughly marks the transition from the initial transient phase to the final proper stationary state (of the $\beta = 0.8$ % case).

and is always given in terms of $v_{\mathrm{th,i}}/R_0$.
Furthermore, the electrostatic ($j = \mathrm{es}$) and electromagnetic ($j = \mathrm{em}$) turbulence intensities are considered, which are defined by

$$I_j = \sum_{k_y \neq 0} \sum_{k_x} \int \mathrm{d}s\ |\hat{G}_{\mathbf{k},j}|^2 \tag{7.17}$$

where $G_{\mathbf{k},\mathrm{es}} = \hat{\phi}_{\mathbf{k}}$ and $\hat{G}_{\mathbf{k},\mathrm{em}} = \hat{A}_{\parallel,\mathbf{k}}$ represent the Fourier amplitudes of electrostatic and parallel vector potential respectively. Throughout this work the electrostatic and electromagnetic turbulence intensities are given in units of $\rho_*^2 T_0^2/e^2$ and $\rho_*^4 B_0^2 R_0^2$ respectively.
Below, the reference case with $\beta = 0.8$ %, $R_0/L_T = 6.9$ and $s - \alpha$ geometry is focused on (red lines in Fig. 7.2). In the initial phase of this simulation the zonal flow shear carried by the mesoscale zonal mode $|\langle\hat{\omega}_{\mathrm{ExB}}\rangle_{n_{\mathrm{ZF}}=1}|$ develops slowly [see panel (a)]. It requires a time period of $\sim 10^2 - 10^3\ R_0/v_{\mathrm{th,i}}$ until the mesoscale zonal flow reaches saturation, i. e., until it reaches a proper statistically stationary state. Since this time scale is large compared to typical turbulent times scales of a few $\sim 10^1\ R_0/v_{\mathrm{th,i}}$ [see individual turbulent fluctuations in panels (b)-(e)], the slow development of the mescoscale ZF will be referred to as *long-term evolution*. Moreover, since the long-term evolution does not reflect a proper statistically stationary state, the time period bounded by the initial nonlinear saturation of the eigenmodes and the saturation of the mesoscale ZF will be referred to as the *initial transient phase*.
Note that the time scale connected to the ZF long-term development is also large compared to the time scale on which the initially growing linear eigenmodes saturate nonlinearly $\sim 10^1 - 10^2\ R_0/v_{\mathrm{th,i}}$. Since the turbulence runaway at β_{c} typically occurs right after this initial nonlinear saturation process [see gray dotted lines in panels (b)-(c)], it is triggered well *before* the mesoscale ZF has completely evolved. —These two events are, therefore, temporally separated.
The relevance of attaining the proper final stationary state becomes clear from the significant reduction in the turbulence level, when the mesoscale ZF reaches saturation (see Fig. 7.2). The smaller scale ZF modes with $n_{\mathrm{ZF}} > 1$ reach saturation before the mesoscale ZF does, suggesting that it is the mesoscale ZF mode $n_{\mathrm{ZF}} = 1$ that causes the decline in the turbulence level. Note that the reduction pertains to the electrostatic and electromagnetic turbulence intensities in a similar way [panels (d) and (e)]. The same outcome also applies to the ion electrostatic and electron electromagnetic heat flux [panels (b) and (c)]. In terms of the turbulence level, the final mesoscale zonal flow dominated state is, hence, clearly distinct from the initial transient phase. It should be stressed that the above described long-term behavior requires a long time integration of a few $\sim 10^3\ R_0/v_{\mathrm{th,i}}$ in order to resolve the long-term dynamics and to access the proper stationary state. Due to the stringent time step constraint imposed by kinetic electrons an analysis of cases close below β_{c} is, therefore, computationally demanding.
The key role of ZFs for the nonlinear saturation of electromagnetic ITG turbulence has been demonstrated in Refs. [65, 66]. The finding that the slowly evolving mesoscale ZF stabilizes turbulence on long times scales, however, is a new aspect in finite β microturbulence. It represents the key ingredient of the hysteresis phenomenon as will be shown below. At this point it should also be emphasized that the awareness of long-term dynamics and the influence of meso-

scale zonal flow structures on turbulence close to marginality has grown over the recent years [23, 24, 25, 76, 77, 151].
However, not all cases exhibit the same initial long-term evolution as discussed above. For example, in the case of $\beta = 0.2$ % (blue data in Fig. 7.2) a statistically stationary state is established shortly after the linear eigenmodes have saturated. Although the mesoscale ZF shear exhibits long-term dynamics during the statistically stationary state, its amplitude is unsteady and time periods with reduced shearing rate can be observed. The turbulence is found to fluctuate homogeneously and a transition to a low turbulence state is not observed.

Parametric dependence of persistent mesoscale zonal flow patterns

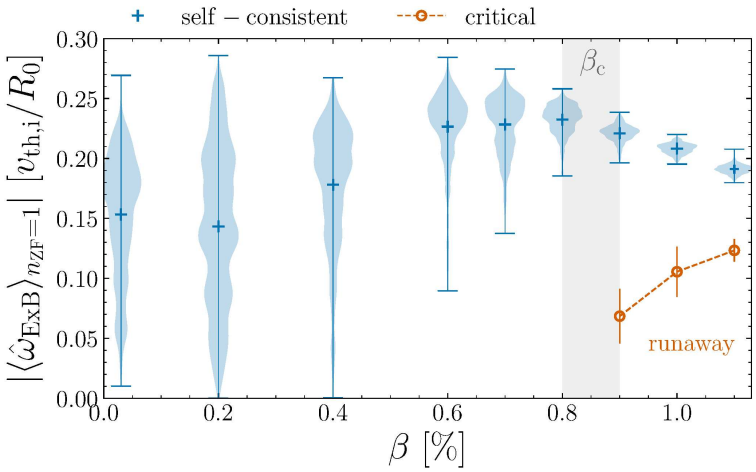

Figure 7.3: Self-consistent mesoscale zonal flow shearing rate $|\langle\hat{\omega}_{\mathrm{ExB}}\rangle_{n_{\mathrm{ZF}}=1}|$ (blue) in the stationary state as function of β for $R_0/L_T = 6.9$, $s-\alpha$ geometry and G_1 resolution. The cases with $\beta \leq 0.8$ % have been initialized in the linear regime, while all cases with $\beta > 0.8$ % have been started from the late mesoscale ZF saturated state of the $\beta = 0.8$ % realization. Shaded regions indicate the temporal distribution during the stationary state, +-symbols the mean value and errorbars the extremal values. Also shown is the critical zonal flow shearing rate $|\langle\hat{\omega}_{\mathrm{ExB}}\rangle_{n_{\mathrm{ZF}}=1}|^{\mathrm{c}}$ (red circles), obtained through the zonal flow scaling scan described in Sec. 7.3.4.

Now that it has been clarified that the state used as initial condition to access the improved β-regime is dominated by persistent mesoscale zonal flows, this section will focus on the parameter dependence of such flows. Fig. 7.3 shows the mesoscale shearing rate $|\langle\hat{\omega}_{\mathrm{ExB}}\rangle_{n_{\mathrm{ZF}}=1}|$ during the stationary state (excluding initial transient phases) for various values of β. Here, the cases with $\beta \leq 0.8$ % have been initialized in the linear regime, while all cases with $\beta > 0.8$ % have been started from the late mesoscale ZF saturated state of the $\beta = 0.8$ %

realization. The characteristics of the mesoscale ZF level undergo a qualitative change with variation of β:
A sufficiently large normalized pressure, i. e., $\beta \gtrsim 0.6$ %, is required for mesoscale ZFs to have a finite (nonzero) amplitude during the entire stationary state. Note that the interval $\beta \approx 0.6 \sim 0.8$ % is also the regime where simulations feature an initial long-term evolution of the mesoscale ZF and a subsequent low turbulence state with a steady saturated ZF amplitude (not shown in Fig. 7.3, but similar to the $\beta = 0.8$ % case in Fig. 7.2). The steady saturated ZF amplitude during the latter phase manifests itself as narrow temporal distributions of $|\langle\hat{\omega}_{\mathrm{ExB}}\rangle_{n_{\mathrm{ZF}}=1}|$ (blue shaded regions in Fig. 7.3). Furthermore, the temporal spread around the most likely amplitude decreases with increasing β, demonstrating an increase in the temporal persistence.
Contrary to this, cases with $\beta \lesssim 0.4$ % exhibit broad distributions of $|\langle\hat{\omega}_{\mathrm{ExB}}\rangle_{n_{\mathrm{ZF}}=1}|$ with variations down to zero zonal flow level. In those cases no initial long-term ZF evolution is observed and transient periods with vanishing mesoscale ZF amplitude exist throughout the entire stationary state (similar to the $\beta = 0.2$ % case in Fig. 7.2).
Against the expectations, the averaged mesoscale ZF shearing rate first increases with β and shows a maximum of a few $\sim 10^{-1}\ v_{\mathrm{th,i}}/R_0$ around $\beta \approx 0.8$ %. For $\beta \gtrsim 0.8$ % it slightly decreases with β. From the decreasing electrostatic and increasing electromagnetic turbulence level in the region $\beta \lesssim 0.8$ % (see $\chi_{\mathrm{es,i}}$ and $\chi_{\mathrm{em,e}}$ in Fig. 7.1) one would at first anticipate a decreasing ZF intensity, since ZFs are known (i) to be driven by the electrostatic Reynolds stress [32] and (ii) to be depleted by electromagnetic flutter [58]. However, it is well established that the proximity of the microturbulence state to marginality is an additional key parameter for the existence of stationary mescoscale ZF pattern [24, 25, 77, 118]. In addition, Refs. [77, 118] report about both a reduction of the averaged mesoscale ZF level and an increase in the temporal variability with increasing distance to marginality.

The hypothesis of the proximity to marginality being partly responsible for the existence of persistent mesoscale ZF pattern is now addressed by two data sets obtained with circular geometry and standard resolution G_1^{circ} (see Tab. 7.1). Fig. 7.4 depicts the dependence of the mesoscale zonal flow shearing rate $|\langle\hat{\omega}_{\mathrm{ExB}}\rangle_{n_{\mathrm{ZF}}=1}|$ on β for two values of R_0/L_T. While the $R_0/L_T = 6.9$ cases exhibit strong turbulence, the $R_0/L_T = 5.5$ cases are closer to marginal stability (compare the heat conductivity in Fig. 7.15). All cases with $R_0/L_T = 6.9$ have been initialized in the linear regime. The cases with $R_0/L_T = 5.5$ and $\beta \leq 1.2$ % have been initialized in the linear regime, while the realization with $\beta = 1.4$ % is started from the late mesoscale ZF saturated state of the $\beta = 1.2$ % case.
In the $R_0/L_T = 6.9$ case (blue), i. e., a realization with high turbulence level, persistent mesoscale ZFs are not observed in the accessible β-range. Instead, highly unsteady mesoscale ZF states are present, as found in the weak electromagnetic limit and for $s - \alpha$ geometry. Contrary to this the $R_0/L_T = 5.5$

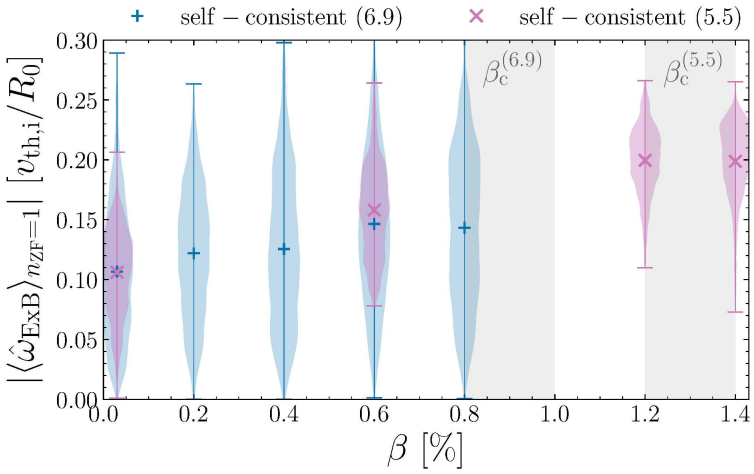

Figure 7.4: Self-consistent mesoscale zonal flow shearing rate $|\langle\hat{\omega}_{\mathrm{ExB}}\rangle_{n_{\mathrm{ZF}}=1}|$ in the stationary state as function of β for circular geometry, G_1^{circ} resolution and $R_0/L_T = 6.9$ (blue, +-symbols) as well as $R_0/L_T = 5.5$ (violet, ×-symbols). All cases with $R_0/L_T = 6.9$ have been initialized in the linear regime. The cases with $R_0/L_T = 5.5$ and $\beta \leq 1.2$ % have been initialized in the linear regime, while the realization with $\beta = 1.4$ % is started from the late mesoscale ZF saturated state of the $\beta = 1.2$ % case. Shaded regions indicate the temporal distribution during the stationary state, +- and ×-symbols the mean value and errorbars the extremal values.

realization (violet), a case with lower turbulence level, exhibit similar mesoscale ZF properties compared to the $s - \alpha$ case: (i) In the electrostatic limit $\beta = 0.03$ % the mesoscale ZF is temporally unsteady with variations down to zero amplitude. (ii) Persistent mesoscale ZFs occur for sufficiently high β with an increase in the averaged ZF amplitude compared to the electrostatic limit. This implies that the proximity to marginality is a key control parameter for persistent mesoscale ZF pattern formation also in electromagnetic turbulence.

7.3.3 Convergence study

Since the long-term evolution of mesoscale zonal flows in electromagnetic microturbulence has been unrecognized before, one might critically question its numerical robustness. This issue is addressed through grid scale and box size convergence tests.

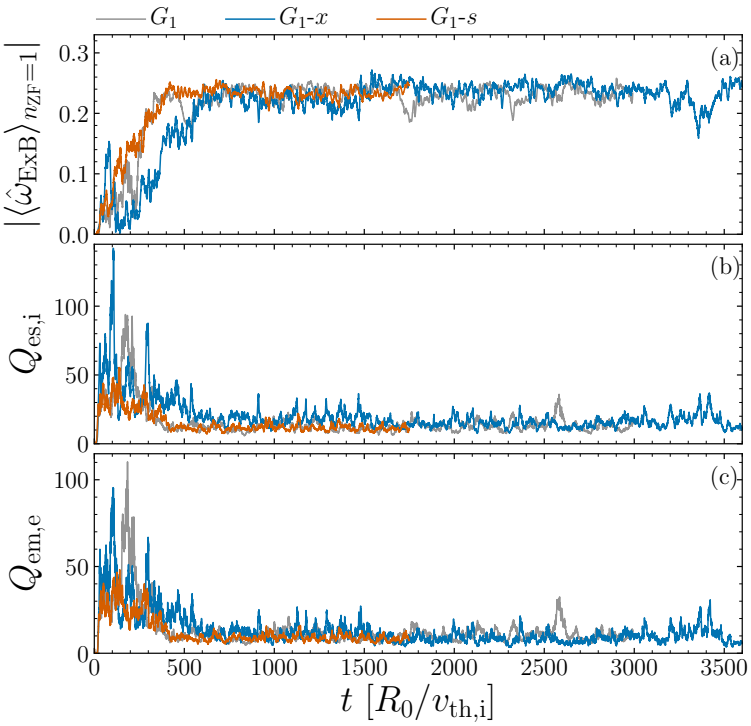

Figure 7.5: Time traces of the mesoscale zonal flow shear $|\langle\hat{\omega}_{\mathrm{ExB}}\rangle_{n_{\mathrm{ZF}}=1}|$ (a), the electrostatic ion heat flux $Q_{\mathrm{es,i}}$ (b) and the electromagnetic electron heat flux $Q_{\mathrm{em,e}}$ (c) for parameters of the reference case ref#1 in Fig. 7.1, i. e., $R_0/L_T = 6.9$, $\beta = 0.8$ % and $s - \alpha$ geometry, and for standard resolution G_1 (gray), double radial resolution G_1-x (blue) and double s-resolution G_1-s (red).

Grid scale convergence

This section focuses on the grid scale convergence through doubling of either the radial or the parallel resolution similar to Ref. [21] (see G_1-x and G_1-s in Fig. 7.5). While the level of the turbulent bursts during the initial transient phase is subject to an unsystematic variation, both the long-term evolution and a similar saturated level of mesoscale ZFs (see left panel of Fig. 7.9) is robustly reproduced independent of the modifications made.
Although the general physics picture is qualitatively converged, a satisfactory judgment of the quantitative convergence is computationally rather prohibitive. Therefore, the numerical error of individual quantities can be large. This applies especially to cases with $\beta \gtrsim 0.8$ %, since (i) the proximity to the NZT and the high value of β renders those points numerically delicate and (ii) the relatively small heat flux results in a large relative error.
For $R_0/L_T = 6.9$, $\beta = 0.8$ % and $s - \alpha$ geometry the doubling of the radial resolution (G_1-x) results in the turbulence to be somewhat more bursty, while the doubling of the parallel resolution (G_1-s) renders it more steady (see Fig. 7.5).

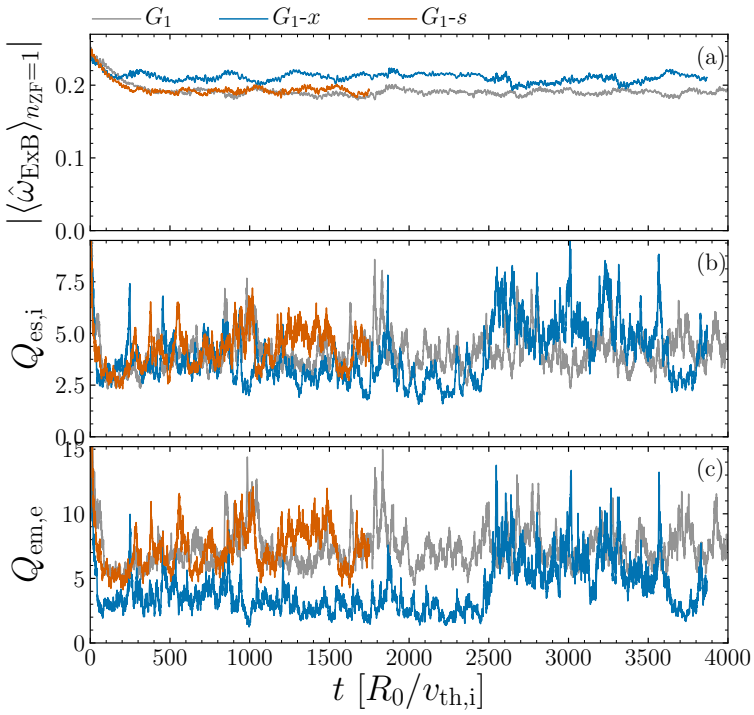

Figure 7.6: Time traces of the mesoscale zonal flow shear $|\langle\hat{\omega}_{\mathrm{ExB}}\rangle_{n_{\mathrm{ZF}}=1}|$ (a), the electrostatic ion heat flux $Q_{\mathrm{es,i}}$ (b) and the electromagnetic electron heat flux $Q_{\mathrm{em,e}}$ (c) for parameters $R_0/L_T = 6.9$, $\beta = 1.1$ %, $s-\alpha$ geometry and for standard resolution G_1 (gray), double radial resolution G_1-x (blue) and double s-resolution G_1-s (red). The simulations have been started using late mesoscale ZF saturated states from realizations with $\beta = 0.8$ % and the respective numerical resolution.

This qualitative trend is confirmed by the ion electrostatic heat flux temporally averaged over the stationary state, for example, which increases by 31 % for double radial resolution and reduces by 8 % for double parallel resolution (cf. Tab. 7.2).
The issue of convergence is also complicated by the occurrence of metastable quasi-stationary states in the case of doubled radial resolution existing for $\sim 10^2-10^3\ R_0/v_{\mathrm{th,i}}$. Note that the existence of metastable states with a relatively long duration is often related to mesoscale ZF structure formation, as reported in adiabatic electron frameworks [24, 25, 77] and in a recent kinetic electron study [118]. The fourth and fifth column of Tab. 7.2 summarize observables that are temporally averaged over the two sub-intervals $\Delta t_1 = [750.0, 1580.2]\ R_0/v_{\mathrm{th,i}}$ and $\Delta t_2 = [1580.2, 3068.8]\ R_0/v_{\mathrm{th,i}}$ that are characteristic for two metastable states. In the former interval the averaged ion electrostatic heat flux, for example, is increased by 48 % compared to the realization with standard resolution, while in the latter by 18 %.
A similar outcome is found in realizations with $R_0/L_T = 6.9$, $\beta = 1.1$ % and

$s - \alpha$ geometry (see Fig. 7.6). The simulations are satisfactory converged with resolution in s. In the case of double radial resolution a transition between metastable quasi-stationary states can be observed. Both metastable states persist for $\sim 10^3\ R_0/v_{\mathrm{th,i}}$. The electromagnetic electron heat flux averaged over the two intervals $\Delta t_1 = [500.0, 2428.6]\ R_0/v_{\mathrm{th,i}}$ and $\Delta t_2 = [2428.6, 3595.7]\ R_0/v_{\mathrm{th,i}}$, for example, differs by 98 % (see Tab. 7.3). While in the former interval its value is reduced by 59 % compared to standard resolution, in the latter interval it is reduced by 18 %. The average over the entire simulation is reduced by 44 % compared to standard resolution.
Based on the discussion above the present work cannot raise the claim of a grid scale convergence within ~ 10 %, as usually specified in the microturbulence context. It highlights that for the plasma parameters and the physical framework chosen, the occurrence of long-term dynamics *requires* a time integration for at least several $\sim 10^3\ R_0/v_{\mathrm{th,i}}$ to be able to properly judge numerical convergence. Simulations with a duration of several $\sim 10^2\ R_0/v_{\mathrm{th,i}}$ are too short to specify the numerical error. In the remainder of this work convergence tests are continually provided that aim for a balance between a proper resolution of the relevant long-term dynamics and computational feasibility.

	$R_0/L_T = 6.9$, $\beta = 0.8$ % and $s - \alpha$ geometry				
	G_1	G_1-x			G_1-s
t_1	400.0	750.0	750.0	1580.2	500.0
t_2	2991.5	3619.5	1580.2	3068.8	1750.1
$\lvert\langle\hat{\omega}_{\mathrm{ExB}}\rangle_{n_{\mathrm{ZF}}=1}\rvert$	0.230 ± 0.006	0.233 ± 0.007	0.223 ± 0.006	0.241 ± 0.004	0.234 ± 0.003
$Q_{\mathrm{es,i}}$	12.58 ± 1.06	16.50 ± 1.59	18.80 ± 1.00	14.85 ± 0.81	11.47 ± 0.45
$Q_{\mathrm{em,e}}$	10.32 ± 1.01	10.03 ± 1.37	11.94 ± 0.77	8.61 ± 0.55	8.81 ± 0.39
I_{es}	73.46 ± 7.47	101.38 ± 11.14	118.29 ± 7.22	89.80 ± 5.93	66.92 ± 3.47
I_{em}	0.44 ± 0.07	0.71 ± 0.10	0.87 ± 0.07	0.62 ± 0.06	0.35 ± 0.03

Table 7.2: Summary of observables temporally averaged over $[t_1, t_2]$ $R_0/v_{\mathrm{th,i}}$ for different sets of numerical resolution and for $R_0/L_T = 6.9$, $\beta = 0.8$ % and $s - \alpha$ geometry. The specified statistical errors are determined through six-part time averaging (see appendix C).

	$R_0/L_T = 6.9$, $\beta = 1.1$ % and $s - \alpha$ geometry				
	G_1	G_1-x			G_1-s
t_1	500.0	500.0	500.0	2428.6	500.0
t_2	7500.0	3868.1	2428.6	3595.7	1750.0
$\lvert\langle\hat{\omega}_{\mathrm{ExB}}\rangle_{n_{\mathrm{ZF}}=1}\rvert$	0.191 ± 0.001	0.210 ± 0.002	0.212 ± 0.003	0.206 ± 0.003	0.192 ± 0.001
$Q_{\mathrm{es,i}}$	4.17 ± 0.09	3.98 ± 0.63	3.25 ± 0.38	5.34 ± 0.18	4.43 ± 0.28
$Q_{\mathrm{em,e}}$	7.47 ± 0.16	4.16 ± 0.91	3.09 ± 0.44	6.12 ± 0.30	7.55 ± 0.53
I_{es}	23.29 ± 0.60	23.14 ± 4.06	18.27 ± 2.41	32.20 ± 1.49	25.83 ± 2.02
I_{em}	0.24 ± 0.01	0.33 ± 0.06	0.25 ± 0.03	0.47 ± 0.04	0.26 ± 0.03

Table 7.3: Summary of observables temporally averaged over $[t_1, t_2]$ $R_0/v_{\mathrm{th,i}}$ for different sets of numerical resolution and for $R_0/L_T = 6.9$, $\beta = 1.1$ % and $s - \alpha$ geometry. The specified statistical errors are determined through six-part time averaging (see appendix C).

Box size convergence

Since zonal flows with a radial scale of the box size are responsible for the reduced turbulence state in the long-term limit, it is justified to critically question the robustness of the presented results with respect to the box size. In this section

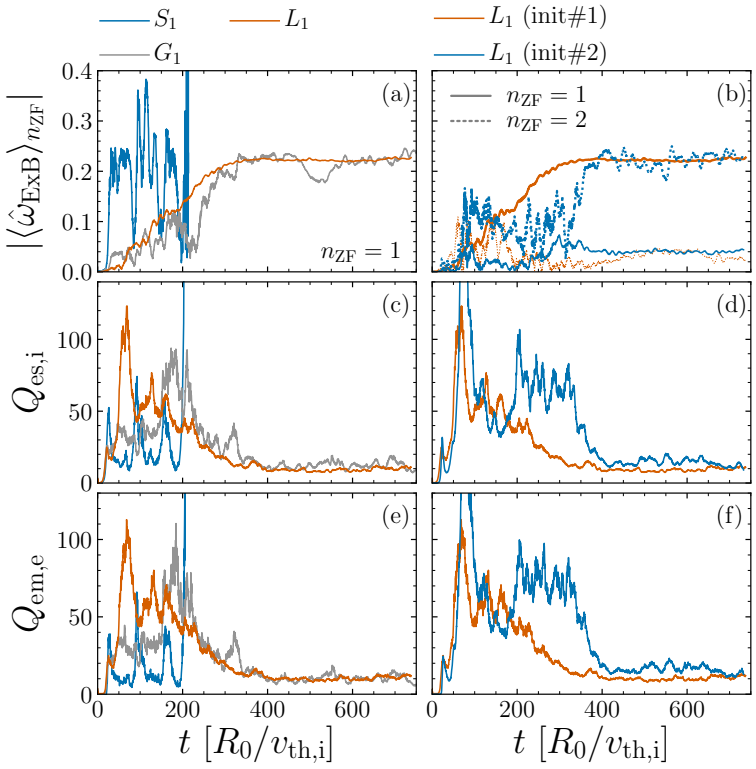

Figure 7.7: Time traces of the $E \times B$ shear $|\langle\hat{\omega}_{\mathrm{ExB}}\rangle_{n_{\mathrm{ZF}}}|$ carried by zonal mode number n_{ZF} [panels (a) and (b)], the electrostatic ion heat flux $Q_{\mathrm{es,i}}$ [panels (c) and (d)], and the electromagnetic electron heat flux $Q_{\mathrm{em,e}}$ [panels (e) and (f)] for parameters of the reference case ref#1 in Fig. 7.1, i. e., $R_0/L_T = 6.9$, $\beta = 0.8$ % and $s - \alpha$ geometry. The left panels compare realizations with standard box size G_1 (gray), half box size S_1 (blue) and 1.5-fold box size L_1 (red). The right panels compare realizations with different initial conditions init#1 (red) and init#2 (blue) for the 1.5-fold box size realization L_1.

the time evolution of $|\langle\hat{\omega}_{\mathrm{ExB}}\rangle_{n_{\mathrm{ZF}}}|$ (for $n_{\mathrm{ZF}} \in [1, 2]$), the ion electrostatic heat flux $Q_{\mathrm{es,i}}$ and the electron electromagnetic heat flux $Q_{\mathrm{em,e}}$ is investigated for $R_0/L_T = 6.9$, $\beta = 0.8$ %, $s-\alpha$ geometry and three realizations with different box size (L_x, L_y): G_1 with the standard box size $(91.58, 89.76)$ $\rho_{\mathrm{th,i}}$, S_1 with half the box size $(45.79, 44.88)$ $\rho_{\mathrm{th,i}}$ and L_1 with 1.5-fold box size $(137.36, 134.64)$ $\rho_{\mathrm{th,i}}$. In the latter case the dissipation coefficient $D_s = 2.0$ had to be adapted to ensure numerical stability.

In addition to the standard initial conditions described in Sec. 7.3.1, here referred to as init#1, simulations with modified initial conditions, referred to as init#2, are considered as well. In the latter case the turbulent modes ($k_y \neq 0$) of the distribution function are initialized by $\hat{g}_{\mathbf{k},\mathrm{sp}}(k_x, k_y, s, v_\parallel, \mu) = A \times [\cos(2\pi s) + 1] \times \exp[-Ck_x^2] \times \exp[-(v_\parallel^2 + 2\mu B)]$, where $C = 5g^{yy}|_{s=0}/18$ with $g^{yy}|_{s=0}$ defined in Sec. 4.2.5 and $A = 10^{-4}$. Analogously to init#1 the $k_y = 0$ mode is set to zero.

Panel (a) of Fig. 7.7 compares the shear carried by the box scale zonal mode $n_{\mathrm{ZF}} = 1$ for S_1, G_1 and L_1 with standard initial conditions init#1. In the latter two cases the box scale zonal flow evolves slowly and converges towards the same saturated $E \times B$ shearing rate. In the half box size case S_1 the box scale zonal mode reaches saturation shortly after the linear eigenmodes have saturated and then fluctuates significantly with time. In general, the box scale zonal flow becomes more steady with increasing box size.

Panel (c) and (e) compare the turbulent fluxes of the same cases shown in panel (b). In the case of G_1 and L_1 the turbulence is reduced by the evolving box scale zonal flow and converges towards a similar level. In the case of S_1 the turbulence is bursty and eventually transitions to a runaway.

This convergence test implies that a minimum box size is required for a proper description of the physics behind the long-term dynamics. Furthermore the box size in the standard case G_1 yields converged results. We would also like to stress that despite the different spatial scale in the G_1 and L_1 case the box scale zonal flow converges towards the same saturated shearing rate of a few $\sim 10^{-1}\ R_0/v_{\mathrm{th,i}}$.

Panel (b) of Fig. 7.7 compares the shearing rate carried by the largest ($n_{\mathrm{ZF}} = 1$, solid lines) and second largest ($n_{\mathrm{ZF}} = 2$, dotted lines) zonal flow mode for two L_1 realizations with different initial conditions. In the case of init#2 (blue) the second largest zonal flow mode dominates over the box scale mode in the quasi-stationary state. The saturated shearing rate of this mode agrees with the box scale zonal flow both in the L_1 and init#1 realization (red) as well as in the G_1 case (gray, left panels). Note that the presented simulations are too short to assess whether a transition to a quasi-stationary state with the dominance of the box scale zonal mode occurs at later times in the init#2 case.

Panel (d) and (f) compare the turbulent fluxes. In both cases a reduction of the turbulence level is observed, when the respective dominant mesoscale zonal flow reaches saturation. In the case of init#2 the turbulence level is somewhat larger than in the case of init#1. This indicates that larger scale zonal flows stabilize turbulence more efficiently.

The above convergence test demonstrates that it is not necessarily the box scale zonal flow that is required for establishing a mesoscale ZF saturated low turbulence state. Rather, the scale of the zonal flow, and therefore the box size, has to be sufficiently large. A zonal flow scale of 68.68 $\rho_{\mathrm{th,i}}$ ($n_{\mathrm{ZF}} = 2$ in the L_1 case)

is sufficient, while $L_{\mathrm{ZF}} = 45.79\ \rho_{\mathrm{th,i}}$ (S_1) is insufficient. Hence, the general physics picture is found to be converged with the box size for standard parameters G_1.

Beside the above discussed grid scale and box size convergence tests, an increase of the numerical dissipation on the zonal flow (slow mesoscale ZF evolution close to marginal can be sensitive to numerical dissipation [25]) and a hydrogen plasma as studied in Refs. [21, 61, 150, 59] instead of the here considered deuterium plasma have been investigated. Both the long-term mesoscale ZF evolution as well as the reduced turbulence state have been confirmed in those tests.

7.3.4 Stability constraints for $\beta > \beta_{\mathrm{c}}$

In this section the role of mesoscale zonal flows for the stability in the improved β-regime, i. e., $\beta > \beta_{\mathrm{c}}$, is investigated. Here, the term *stable* refers to the stability against the triggering of turbulence runaways. The aims of this section are (i) to clarify if mesoscale ZFs are required for the stability and (ii) to assess if the cases with $\beta > \beta_{\mathrm{c}}$ are stable against a turbulence runaway being triggered in the long time limit.
Those issues are addressed through the following stability analysis: The distribution function taken from the late saturated state of cases with $\beta > \beta_{\mathrm{c}}$ is used as initial condition. The so defined initial zonal flow state is manipulated through scaling the $k_y = 0$ box scale ($n_{\mathrm{ZF}} = 1$) mode of the distribution function by a real number $0 \leq S_Z \leq 1$. The turbulent modes ($k_y \neq 0$) are not modified. The response of the system to this scaling of the mesoscale zonal mode is investigated with the focus on the triggering of a runaway.

Since the turbulence runaway is an inherently transient phenomenon, a temporally resolved analysis is necessary. An exemplary case with $\beta = 1.1$ %, $R_0/L_T = 6.9$, $s - \alpha$ geometry and G_1 resolution is concentrated on first (see Fig. 7.8). The initial reduction of the mesoscale ZF results in the turbulence level increasing temporally, as would be expected from the stabilizing effect of the mesoscale ZF. The rate by which the turbulence level increases in time depends on the degree of ZF reduction. Furthermore, after restart all realizations represent environments in which the mesoscale ZF is driven and, hence, grows in time. This temporal growth, however, is slow, as observed earlier in connection to mesoscale ZFs evolution (see Fig. 7.5). The outcome of this experiment in the long-term limit, in turn, depends crucially on the initial ZF reduction:
(i) If the ZF reduction is moderate ($S_Z = 0.7,\ 0.8$) the system relaxes towards the stationary levels of the reference case (gray line and shaded region). During this process the turbulence level can exceed the reference value. (ii) If the reduction is sufficiently large ($S_Z = 0.4,\ 0.6$) the system enters a second transient phase during which the ZF decays and a turbulent runaway occurs —properties of a NZT.

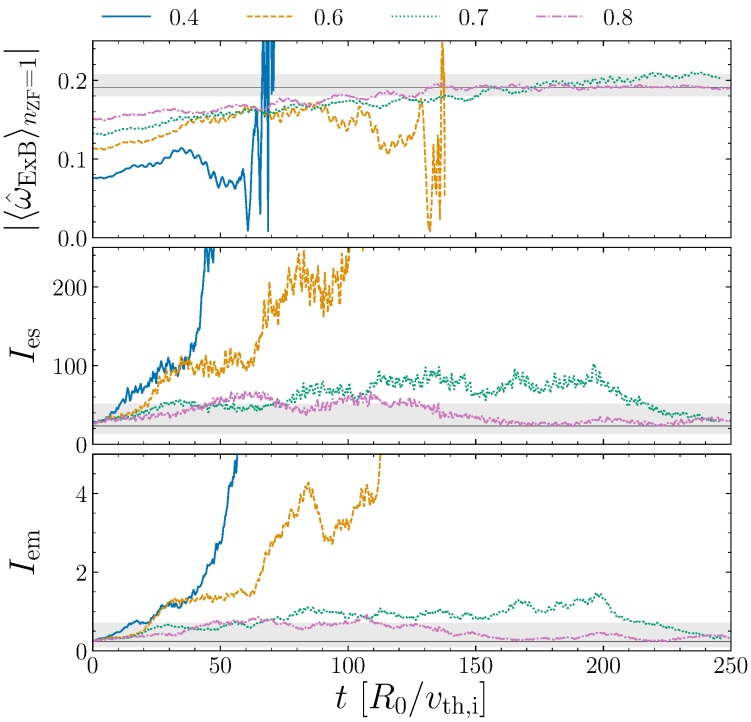

Figure 7.8: Time traces of the mesoscale zonal flow shearing rate $|\langle\hat{\omega}_{\mathrm{ExB}}\rangle_{n_{\mathrm{ZF}}=1}|$ (top), the electrostatic turbulence intensity I_{es} (mid) and the electromagnetic turbulence intensity I_{em} (bottom) for $\beta = 1.1$ %, $R_0/L_T = 6.9$, $s - \alpha$ geometry and G_1 resolution. Shown are four realizations of the zonal flow scaling scan with a scaling factor S_Z of 0.4 (blue, solid), 0.6 (orange, dashed), 0.7 (green, dotted) and 0.8 (violet, dash-dotted). A thin horizontal gray line depicts the respective quantity temporally averaged over the stationary reference case, while the gray shaded region spans the respective extremal values.

In addition to the above mesoscale zonal flow stability study the two second largest zonal modes with $n_{\mathrm{ZF}} = 2$ and $n_{\mathrm{ZF}} = 3$ have been zeroed out individually, while keeping the other zonal modes (including the mesoscale $n_{\mathrm{ZF}} = 1$) unmodified. These modifications did not result in turbulence runaways confirming the importance of the mesoscale ZF for the mitigation of turbulence runaways. It should be noted, however, that the mesoscale ZF level is not the sole parameter controlling the triggering of a turbulence runaway. Despite a similar $|\langle\hat{\omega}_{\mathrm{ExB}}\rangle_{n_{\mathrm{ZF}}=1}|$ at $t \approx 60\ R_0/v_{\mathrm{th,i}}$ the realization with $S_Z = 0.7$ relaxes towards equilibrium, while the one with $S_Z = 0.6$ passes into a runaway (see Fig. 7.8).
In summary, a critical mesoscale ZF level can be found below which turbulence runaways are triggered. Hence, temporally persistent mesoscale ZFs with sufficiently large amplitude are a requirement for the accessibility of the improved β-regime. The time scale connected to both the onset of the runaway phase be-

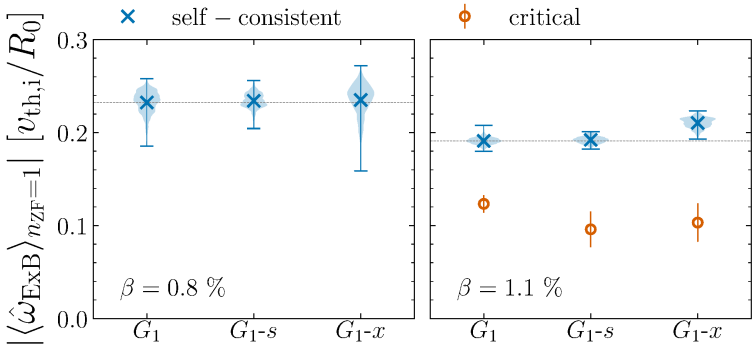

Figure 7.9: Self-consistent mesoscale zonal flow shearing rate $|\langle\hat{\omega}_{\mathrm{ExB}}\rangle_{n_{\mathrm{ZF}}=1}|$ (blue, ×-symbols) during the stationary state for $R_0/L_T = 6.9$, $s-\alpha$ geometry and $\beta = 0.8$ % (left) and $\beta = 1.1$ % (right). Shown are realizations with different numerical resolution (see Tab. 7.1). Shaded regions indicate the temporal distribution, ×-symbols the mean value and errorbars the extremal values. The critical mesoscale zonal flow level in case of $\beta = 1.1$ % is depicted as well (red circles).

low, as well as the relaxation to equilibrium above the threshold increases with proximity to criticality. Furthermore, the clear separation of the self-consistent ZF level (gray line + shaded region) from the threshold in the above considered case demonstrates some degree of *resilience*: Even if the state is perturbed outside the stationary statistics, it relaxes back towards the proper stationary state. The critical mesoscale ZF level is now determined in the entire improved β-regime. The critical curve and its uncertainty are defined by

$$|\langle\hat{\omega}_{\mathrm{ExB}}\rangle_{n_{\mathrm{ZF}}=1}|^{\mathrm{c}} = 0.5 \times (S_Z^- + S_Z^+) \times |\langle\hat{\omega}_{\mathrm{ExB}}\rangle_{n_{\mathrm{ZF}}=1}|^{\mathrm{ref}} \tag{7.18}$$

$$\sigma = 0.5 \times |S_Z^- - S_Z^+| \times |\langle\hat{\omega}_{\mathrm{ExB}}\rangle_{n_{\mathrm{ZF}}=1}|^{\mathrm{ref}}, \tag{7.19}$$

where $S_Z^{-/+}$ denotes the ZF scaling factor just below (−) and above (+) the triggering of a turbulence runaway and $|\langle\hat{\omega}_{\mathrm{ExB}}\rangle_{n_{\mathrm{ZF}}=1}|^{\mathrm{ref}}$ is the reference mesoscale zonal flow shearing rate taken from the last time step of the reference case used as initial condition. Due to its high temporal persistence the self-consistent ZF level is always found to be well separated from the critical curve (see Fig. 7.3). Hence, the states in the improved β-regime are considered stable against a runaway being triggered in the long time limit due to the mesoscale zonal flow falling below the critical level. Since the critical ZF level increases with β, however, it may become harder to access saturated states at higher β.
As discussed in Sec. 7.3.3 the standard resolution G_1 is insufficient to accurately resolve individual observables numerically. It is, therefore, legitimate to critically question the validity of the critical mesoscale zonal flow level obtained with standard resolution in the analysis above. In order to strengthen the soundness

of this outcome, the above stability analysis is repeated at $\beta = 1.1$ % and for double radial (G_1-x) and double parallel (G_1-s) resolution. Both the existence of a critical mesoscale ZF level and its value is confirmed in this convergence test (see right panel of Fig. 7.9). Since the $\beta = 1.1$ % case appears to be most susceptible for the triggering of a runaway, i. e., the distance between the critical curve and the self-consistent level is minimal (see Fig. 7.3), the outcome of this convergence test is assumed to hold equally for $\beta < 1.1$ %.

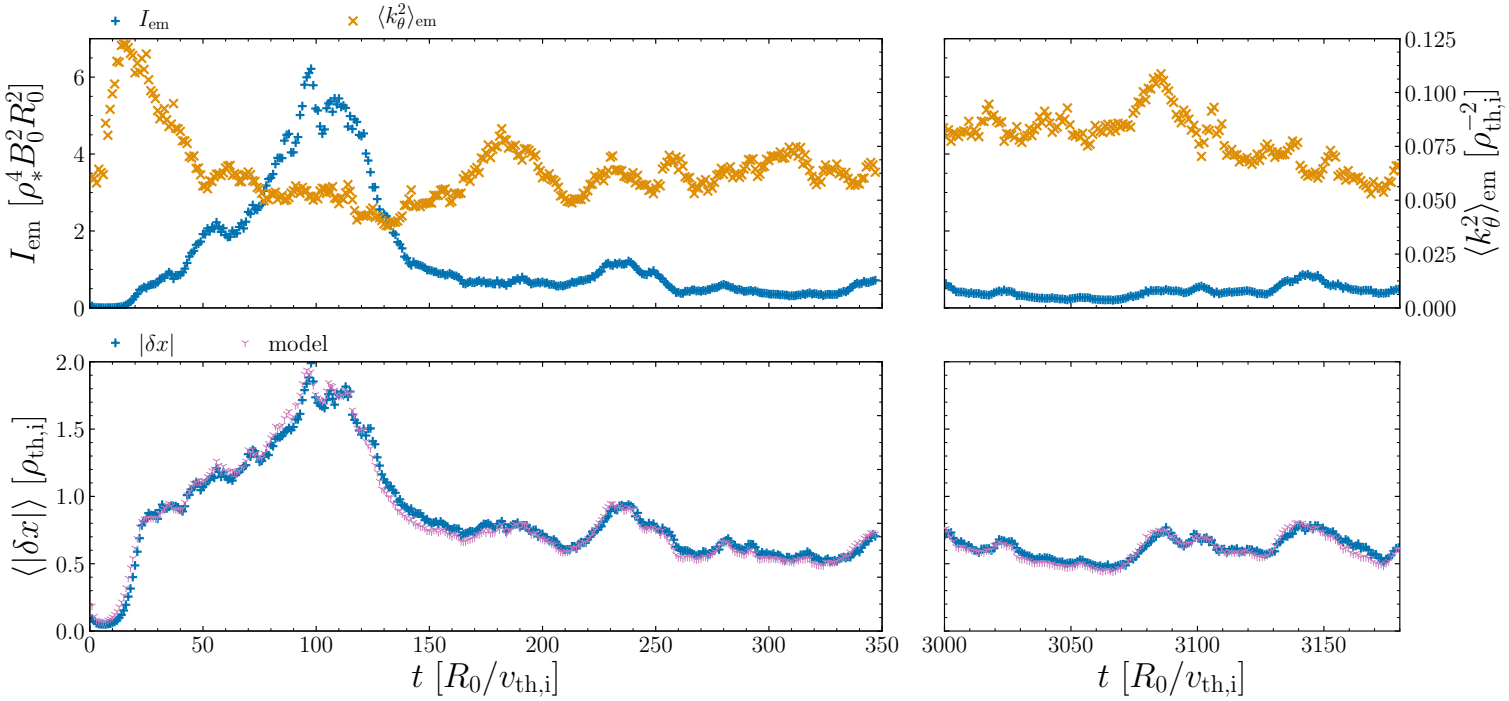

Figure 7.10: Top: Time traces of the electromagnetic turbulence intensity I_{em} (blue +-symbols) and the electromagnetic poloidal wave vector centroid $\langle k_\theta^2 \rangle_{\mathrm{em}}$ (orange ×-symbols, right axis). Bottom: Time traces of the absolute value of the radial full turn displacement $\langle |\delta x| \rangle$ ensemble averaged over poloidal turns and field lines (blue +-symbols) and the model $m \times (\langle k_\theta^2 \rangle_{\mathrm{em}} I_{\mathrm{em}})^{1/2}$ (violet Y-symbols). Shown are cases with $R_0/L_T = 6.9$, $\beta = 0.8$ %, $s - \alpha$ geometry and G_1 resolution during the initial phase (left) and restarted from the late mesoscale ZF dominated state (right).

7.3.5 Investigation of magnetic stochasticity through field line tracing methods

This section investigates magnetic stochasticity. It is motivated by the theory behind the NZT [60], that is based on field line decorrelation aided magnetic stochasticity. In the aforementioned reference field line decorrelation is proposed to result in a sudden increase of electrons shortening out flux-surfaces at β_c and thereby disabling zonal flows [58]. Here, the field line tracing diagnostic (see Sec. 7.2.2) is applied to a second data set for which 3D spatial data of $A_\parallel$ is available each transit time $R_0/v_{\mathrm{th,i}}$, to investigate the influence of the mesoscale zonal flow evolution on magnetic stochasticity.

Influence of mesoscale zonal flow evolution on magnetic stochasticity

An exemplary case with parameters compliant to the reference case $R_0/L_T = 6.9$, $\beta = 0.8$ %, $s - \alpha$ geometry and standard parameters G_1 is concentrated on first (Fig. 7.10). Initial nonlinear saturation occurs at $t \approx 20\ R_0/v_{\mathrm{th,i}}$ and, therefore, the subsequent phase is of interest. The electromagnetic turbulence intensity exhibits a temporal long-term evolution (top left panel), which is correlated with the mesoscale ZF reaching saturation in the interval $t \approx 150 \sim 300\ R_0/v_{\mathrm{th,i}}$ (not shown) as observed earlier.
During both the initial transient and final mesoscale ZF dominated state widespread magnetic stochasticity occurs, as shown by the two Poincaré surface-of-section plots in Fig. 7.11. Here, a Poincaré surface-of-section is constructed by recording the field lines penetration points through the x-y-plane at the low field side for 300 poloidal turns. Individual field lines are colored according to their seeding position (horizontal line) and a mixing of colors, hence, indicates flux-surface breaking or equivalently magnetic stochasticity. While in both cases the perturbed magnetic field is stochastic, in the initial transient phase the level of stochasticity is significantly larger compared to the final mesoscale ZF dominated phase.
This observation is consistent with the temporal evolution of the ensemble averaged radial full turn displacement $\langle|\delta x|\rangle$ (see bottom left panel of Fig. 7.10). Here, angle brackets denote an ensemble average. The full turn displacement of a field line is defined by the radial displacement it exhibits after executing one poloidal turn from HFS to HFS, i. e., $s = -0.5 \rightarrow +0.5$. At a fixed point in time $\langle|\delta x|\rangle$ is defined as the ensemble average over all 1024 seeded field lines and 100 poloidal turns. In the initial transient phase, field lines feature a large radial excursion, while a significant reduction is found when the mesoscale ZF has developed. In addition, a simulation has been restarted from the late saturated state of the reference case (ref#1 in Fig. 7.1) to verify that this low level of mag-

netic stochasticity is expected throughout the entire final stationary mesoscale dominated state (right panels of Fig. 7.10).
To proceed, the physical mechanism behind the reduction in the magnetic stochasticity is further elucidated through a simple model. The analysis be-

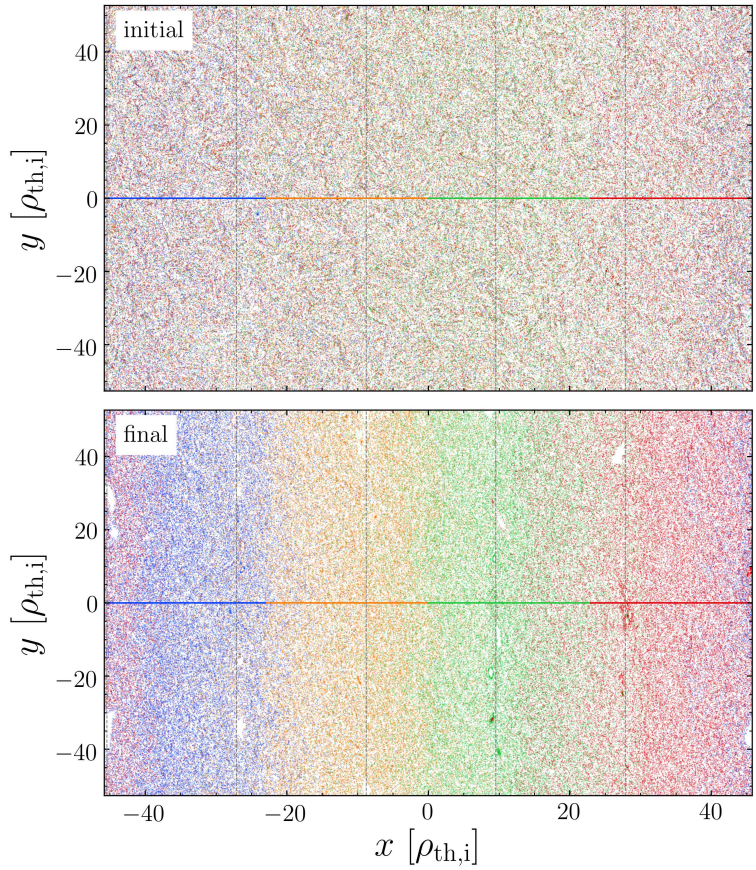

Figure 7.11: Poincaré surface-of-section plots during the initial transient phase at $t = 97\ R_0/v_{\mathrm{th,i}}$ (top) and the final stationary phase at $t = 300\ R_0/v_{\mathrm{th,i}}$ of a case with $R_0/L_T = 6.9$, $\beta = 0.8$ %, $s - \alpha$ geometry and G_1 resolution (cf. left panels of Fig. 7.10).

low concentrates on cases with $\beta < \beta_{\mathrm{c}}$ exclusively. The following assumptions are made: (i) It is assumed that the typical structure of perturbed magnetic field lines does not change substantially with time and β. Variations in the averaged radial displacement are then determined by the electromagnetic field fluctuation level, i. e., the amplitude of the perturbed magnetic field, and not by changes in the structural properties of field lines. (ii) The electromagnetic turbulence

intensity I_{em} together with the squared poloidal wave vector centroid

$$\langle k_\theta^2 \rangle_{\mathrm{em}} = \int \mathrm{d}s \sum_{k_x, k_\theta \neq 0} k_\theta^2 |\hat{A}_{\parallel,\mathbf{k}}(k_x, k_\theta, s)|^2 \Big/ \int \mathrm{d}s \sum_{k_x, k_\theta \neq 0} |\hat{A}_{\parallel,\mathbf{k}}(k_x, k_\theta, s)|^2, \tag{7.20}$$

where the poloidal wave vector is defined through Eq. (4.41), are assumed to provide a reasonable estimate of the radial magnetic field fluctuation level $\delta B_x = \delta \mathbf{B} \cdot \nabla x \propto (\langle k_\theta^2 \rangle_{\mathrm{em}} I_{\mathrm{em}})^{1/2}$. Throughout this work the symbol '$\propto$' means *proportional to*. The radial field line equation [Eq. (7.3)] then motivates the model

$$\langle |\delta x| \rangle = m \times (\langle k_\theta^2 \rangle_{\mathrm{em}} I_{\mathrm{em}})^{1/2}, \tag{7.21}$$

with m an arbitrary constant.
Indeed, the averaged full turn displacement $\langle |\delta x| \rangle$ shows approximately the same linear trend over a wide range of $(\langle k_\theta^2 \rangle_{\mathrm{em}} I_{\mathrm{em}})^{1/2}$ and for various values of β (see bottom panel of Fig. 7.12), supporting the above proposed model. The black dashed line shows a fit of the model Eq. (7.21) with $m = 3.39$ fitted to the data points of the case with $\beta = 0.8$ % and G_1 resolution (blue $\times$-symbols). The large spread in this case is a manifestation of the temporal long-term evolution during the initial transient phase and justifies the application of the model to this stage. This is also confirmed by the respective time traces (see violet 'Y'-symbols in the bottom panels of Fig. 7.10).
Since the spectral centroid $\langle k_\theta^2 \rangle_{\mathrm{em}}$ varies only moderately for $t \gtrsim 50\ R_0/v_{\mathrm{th,i}}$ (see top left panel of Fig. 7.10), the long-term variation of the magnetic turbulence intensity can be identified as dominant reason for the reduction of the averaged radial displacement. This outcome allows for the conclusion that the reduction of the magnetic stochasticity in the final proper stationary state is directly related to the stabilizing effect of the mesoscale ZF on the turbulence level. As the above applied model suggests, this outcome is based on the reduction of the radial excursion amplitude rather than on a change of the overall structural properties of perturbed field lines.

Field line decorrelation

So far, cases below β_{c} have been discussed exclusively, for which field line decorrelation is not expected to be present. The assumption made above, that the typical structure of perturbed magnetic lines does not change with β and time, has been based on this fact. The onset of field line decorrelation around β_{c}, in turn, implicates a sudden change in the structural properties of field lines and a concomitant increase in the radial displacement as discussed below.

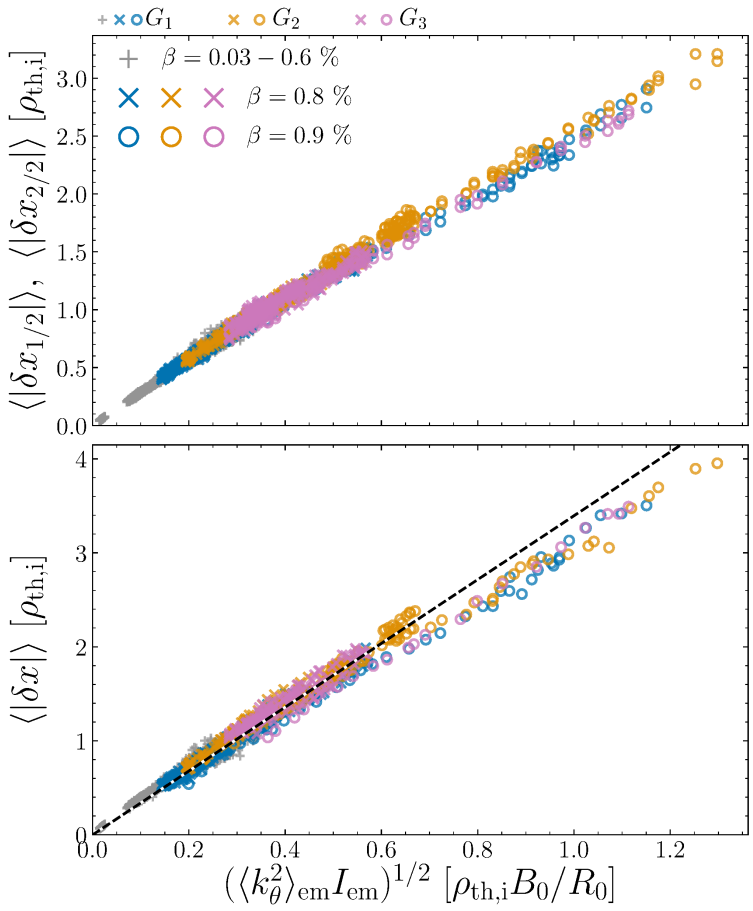

Figure 7.12: Absolute value of the radial displacement perturbed field lines execute during the first- $\langle|\delta x_{1/2}|\rangle$ and second $\langle|\delta x_{2/2}|\rangle$ poloidal half turn (top) and during a complete poloidal turn $\langle|\delta x|\rangle$ (bottom) against $(\langle k_\theta^2\rangle_{\mathrm{em}} I_{\mathrm{em}})^{1/2}$ for $\beta \in [0.03,\ 0.2,\ 0.4,\ 0.6]$ % (+-symbols), $\beta = 0.8$ % (×-symbols) and $\beta = 0.9$ % (circles). Each point depicts the ensemble average of the respective quantity over all 1024 seeded field lines and 100 poloidal turns at a fixed point in time. Shown are results for standard resolution G_1 (gray and blue), simultaneously elevated x- and s-resolution G_2 (orange) and increased overall spatial resolution G_3 (violet). The black dashed line is a fit of the model Eq. (7.21) to the data points with $\beta = 0.8$ % and standard resolution G_1 (blue ×-symbols).

For $\beta < \beta_{\mathrm{c}}$ the total ensemble of perturbed field lines is assumed to be composed of two classes: (i) field lines that preserve flux-surfaces ($\delta x = 0$) and, hence, do not contribute to magnetic stochasticity, and (ii) field lines that break flux-surfaces ($\delta x \neq 0$) and, therefore, contribute to magnetic stochasticity. In the former case the radial displacement of the field line trajectory after the first poloidal half turn $\delta x_{1/2}$ (from $s = -0.5$ to $s = 0$) cancels the displacement of the second half turn $\delta x_{2/2}$ (from $s = 0$ to $s = +0.5$), i. e., $\delta x = \delta x_{1/2} + \delta x_{2/2} = 0$ [60].

Around β_c field lines of the former class are proposed to decorrelate from their original flux-surface, as their half turn displacement becomes comparable to the radial correlation length of the pertubed magnetic field. The trajectory during the second half turn is then statistically independent from the first half turn and the field line does therefore not necessarily return to its original flux-surface. It is then reasonable to assume that $\langle|\delta x|\rangle \propto \langle|\delta x_{1/2}|\rangle$, $\langle|\delta x_{2/2}|\rangle$ for decorrelated field lines. The sudden onset of field line decorrelation around β_c implicates that a larger class of field lines exhibits a finite δx and, hence, a sudden increase in $\langle|\delta x|\rangle$ is expected. Here, the term *sudden* refers to a narrow interval of β around β_c, as the threshold effect described in Ref. [60] suggests.
As indicated by Fig. 7.2 and Fig. 7.12 the magnetic field fluctuation level increases with β. In addition to the linear scaling of $\langle|\delta x|\rangle$ with $(\langle k_\theta^2\rangle_{\mathrm{em}} I_{\mathrm{em}})^{1/2}$, observed below β_c, we expect an additional sudden increase induced by field line decorrelation around $\beta_c = (0.85 \pm 0.05)$ %. In Fig. 7.12 a sudden increase (positive offset) of $\langle|\delta x|\rangle$ with respect to $(\langle k_\theta^2\rangle_{\mathrm{em}} I_{\mathrm{em}})^{1/2}$ is therefore expected when comparing the datasets with $\beta = 0.8$ % (×-symbols) and $\beta = 0.9$ % (circles). Instead, rather a negative offset can be observed. Note that the data for $\beta = 0.9$ % covers the initial phase of the turbulence runaway, i. e., excluding the extreme turbulence levels for which no proper numerical solution can be guaranteed any more. Field line decorrelation should have occurred in this case. Furthermore, the ensemble averaged half turn displacements $\langle|\delta x_{1/2}|\rangle$ and $\langle|\delta x_{2/2}|\rangle$ scale linearly with the magnetic fluctuation level (see top panel of Fig. 7.12). Therefore, the contribution of decorrelated field lines to $\langle|\delta x|\rangle$ is expected to scale linearly with $(\langle k_\theta^2\rangle_{\mathrm{em}} I_{\mathrm{em}})^{1/2}$ as well. Since above β_c a larger number of field lines contributes to $\langle|\delta x|\rangle$ one expects a stronger (linear) scaling of $\langle|\delta x|\rangle$ with $(\langle k_\theta^2\rangle_{\mathrm{em}} I_{\mathrm{em}})^{1/2}$. Although the ensemble averaged full turn displacement $\langle|\delta x|\rangle$ is a linear function of the magnetic field fluctuation level for $\beta = 0.9$ % (circles), the constant of proportionality appears to be somewhat smaller compared to cases with $\beta \leq 0.8$ %.
The findings above are based on turbulence in the initial transient phase, which is observed to be sensitive to variations of the resolution in both the x- and s-direction (see Sec. 7.3.2 and Fig. 7.5). In order to verify numerical convergence, the analysis is repeated for $\beta = 0.8$ % as well as $\beta = 0.9$ % with increased (by a factor of 1.5) resolution in the x- and s-direction (G_2, orange) and in all spatial directions (G_3, violet). Excellent agreement is found, indicating that the observations made above are numerically sound.

Based on the analysis presented in Sec. 7.3.5, we are unable to relate the mitigation of turbulence runaways to a mitigation of the sudden onset of field line decorrelation, as would be expected from previous theories. Yet, a significant reduction of the magnetic stochasticity through the development of mesoscale zonal flows is found, which is likely to contribute to the mitigation of turbulence

runaways.

	$R_0/L_T = 6.9,\ \beta = 0.8\ \%\ (s-\alpha)$						$R_0/L_T = 5.5,\ \beta = 1.2\ \%$ (circ)	
	G_1		G_1-x		G_1-s		G_1^{circ}	
	trans.	stat.	trans.	stat.	trans.	stat.	trans.	stat.
t_1	21.8	400.0	24.5	750.0	21.9	500.0	23.5	360.3
t_2	331.9	2991.6	605.7	3619.6	397.9	1750.1	115.6	1482.9
$\mathcal{R}$	0.149	0.223 ± 0.017	0.169	0.326 ± 0.010	0.199	0.221 ± 0.011	0.214	0.335 ± 0.024
$\mathcal{M}$	-0.148	-0.084 ± 0.011	-0.186	-0.150 ± 0.028	-0.184	-0.073 ± 0.024	-0.255	-0.230 ± 0.035
$\mathcal{L}$	0.032	-0.138 ± 0.012	0.033	-0.174 ± 0.021	0.017	-0.148 ± 0.022	0.115	-0.113 ± 0.044
$\mathcal{L}_{\parallel,f}$	0.264	0.446 ± 0.024	0.152	0.332 ± 0.016	0.202	0.262 ± 0.013	0.138	0.195 ± 0.023
$\mathcal{L}_{D,f}$	-0.209	-0.639 ± 0.039	-0.111	-0.446 ± 0.028	-0.176	-0.392 ± 0.018	-0.022	-0.295 ± 0.049
I_{es}	287.285	73.457 ± 7.475	299.525	101.382 ± 11.139	192.92	66.923 ± 3.467	321.459	112.285 ± 23.935
I_{em}	2.650	0.444 ± 0.071	3.099	0.714 ± 0.098	1.650	0.354 ± 0.028	3.843	1.068 ± 0.341

Table 7.4: Time averaged Reynolds stress transfer $\mathcal{R}$, Maxwell stress transfer $\mathcal{M}$, transfer mediated by linear terms of the gyrokinetic equation $\mathcal{L}$, transfer due to parallel streaming along unperturbed field lines $\mathcal{L}_{\parallel,f}$, transfer due to drift motion $\mathcal{L}_{D,f}$, electrostatic turbulence intensity I_{es} and electromagnetic turbulence intensity I_{em} for $R_0/L_T = 6.9$, $\beta = 0.8\ \%$, $s-\alpha$ geometry and G_1, G_1-x and G_1-s resolution as well as $R_0/L_T = 5.5$, $\beta = 1.2\ \%$, circular geometry and G_1^{circ} resolution. Both the temporal average over the initial transient phase (trans.) and the final stationary mesoscale ZF dominated state (stat.) is given, with the averaging intervals specified by $[t_1, t_2]\ R_0/v_{\mathrm{th,i}}$. The transfer into / out of the mesoscale ZF mode $n_{\mathrm{ZF}} = 1$ is considered only. The specified statistical errors are determined through six-part time averaging (see appendix C).

7.3.6 Zonal flow transfer study

Mesoscale ZFs have been proven crucial for the mitigation of high β turbulence runaways and the accessibility of the improved β-regime. This section focuses on the transfer mechanisms behind the drive and damping of such flows through the use of the zonal flow intensity evolution diagnostic (see Sec. 7.2.3). The transfer into / out of the mesoscale zonal flow mode $n_{\mathrm{ZF}} = 1$ is studied exclusively throughout this section.

Cancellation of the Reynolds- and Maxwell stress close to β_c

The analysis starts with an investigation of the reference case, i. e., $R_0/L_T = 6.9$, $\beta = 0.8$ % and $s - \alpha$ geometry, which features an initial long-term evolution of the mesoscale zonal flow and a late mesoscale zonal flow saturated stationary state (see Sec. 7.3.2). In general, the zonal intensity evolution equation is well satisfied as demonstrated in Fig. 7.13. The initial transient phase ranging

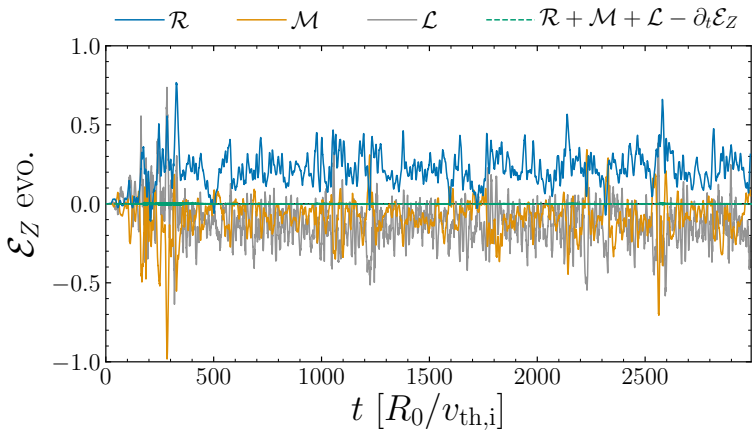

Figure 7.13: Time traces of individual terms of the zonal flow intensity evolution [Eq. (7.9)] for ZF mode number $n_{\mathrm{ZF}} = 1$ and parameters of the reference case ref#1 in Fig. 7.1 with $R_0/L_T = 6.9$, $\beta = 0.8$ %, $s-\alpha$ geometry and G_1 resolution. Shown are the Reynolds stress $\mathcal{R}$ (blue), the Maxwell stress $\mathcal{M}$ (orange), the contribution $\mathcal{L}$ mediated by linear terms of the gyrokinetic equation (gray) and the sum of all terms subtracted by the time derivative of the zonal flow intensity $\mathcal{R}+\mathcal{M}+\mathcal{L}-\partial_t\mathcal{E}_Z$ (green). Solid lines depict a moving box average with window length $\Delta t = 7.5\ R_0/v_{\mathrm{th,i}}$, while dashed lines represent the unmodified time traces.

up to $t \approx 300 \sim 400\ R_0/v_{\mathrm{th,i}}$ is characterized by an increased fluctuation level compared to the final stationary state, which is consistent with the time evolution of the turbulence intensities (see Fig. 7.2). In agreement with the

basic zonal flow paradigm [32] the Reynolds stress drives the mesoscale ZF. The Maxwell stress transfer, in turn, represents a damping mechanism. Similar findings are reported from gyrofluid studies of edge turbulence [153, 45]. Note that $\mathcal{M}$ directly measures the influence of magnetic flutter on the mesoscale zonal flow. The negative Maxwell stress transfer is, therefore, consistent with the residual flow calculations discussed in [60, 58].
The initial transient phase features a comparable amplitude of the Reynolds and Maxwell stress with opposing sign (see also Tab. 7.4), demonstrating a vanishing nonlinear transfer into the mesoscale ZF. In the initial transient phases just below β_c the mesoscale zonal flow is therefore nonlinearly marginal stable. Here, *nonlinearly marginal* refers to the vanishing nonlinear ZF drive. This cancellation might relate to the understanding of the turbulence runaway in terms of a nonzonal transition [60]. It is emphasized, however, that beside the nonlinear transfer terms $\mathcal{R}$ and $\mathcal{M}$, a finite transfer mediated by the linear terms of the gyrokinetic equation $\mathcal{L}$ is possible. Indeed, a positive transfer $\mathcal{L}$ occurs during the initial transient phase (see Tab. 7.4) consistent with the slow ZF evolution in this period. This finding is reproduced by the increased spatial resolution sets G_1-x and G_1-s.
A cancellation of the nonlinear stresses just below β_c is also confirmed for the $R_0/L_T = 6.9$ data set, circular geometry and G_1^circ resolution. The time averaged (over the stationary state) nonlinear transfer terms cancel just below the corresponding critical $\beta_\mathrm{c} = (0.9 \pm 0.1)$ % and, again, a finite positive transfer $\mathcal{L}$ balances the negative nonlinear transfer (see left bottom panel of Fig. 7.14). Mesoscale zonal flows, therefore, appear to be nonlinear marginal stable in the vicinity of turbulence runaways at β_c in general.
It is noted that the temporally averaged Maxwell stress transfer term (orange squares in the left bottom panel of Fig. 7.14) increases continuously in magnitude by approximately $\sim \beta^{2.8}$ (gray dotted line). The mechanism the Maxwell stress is based on, hence, scales continuously with β and eventually results in a cancellation of Maxwell and Reynolds stress. The field line decorrelation theory, by contrast, implies a sharp transition in the Maxwell stress, caused by a sudden increase in the flux-surface breaking field lines. The zonal flow transfer study, hence, supports the outcome of the field line tracing analysis of Sec. 7.3.5 that lacked signatures of a sudden onset of field line decorrelation.

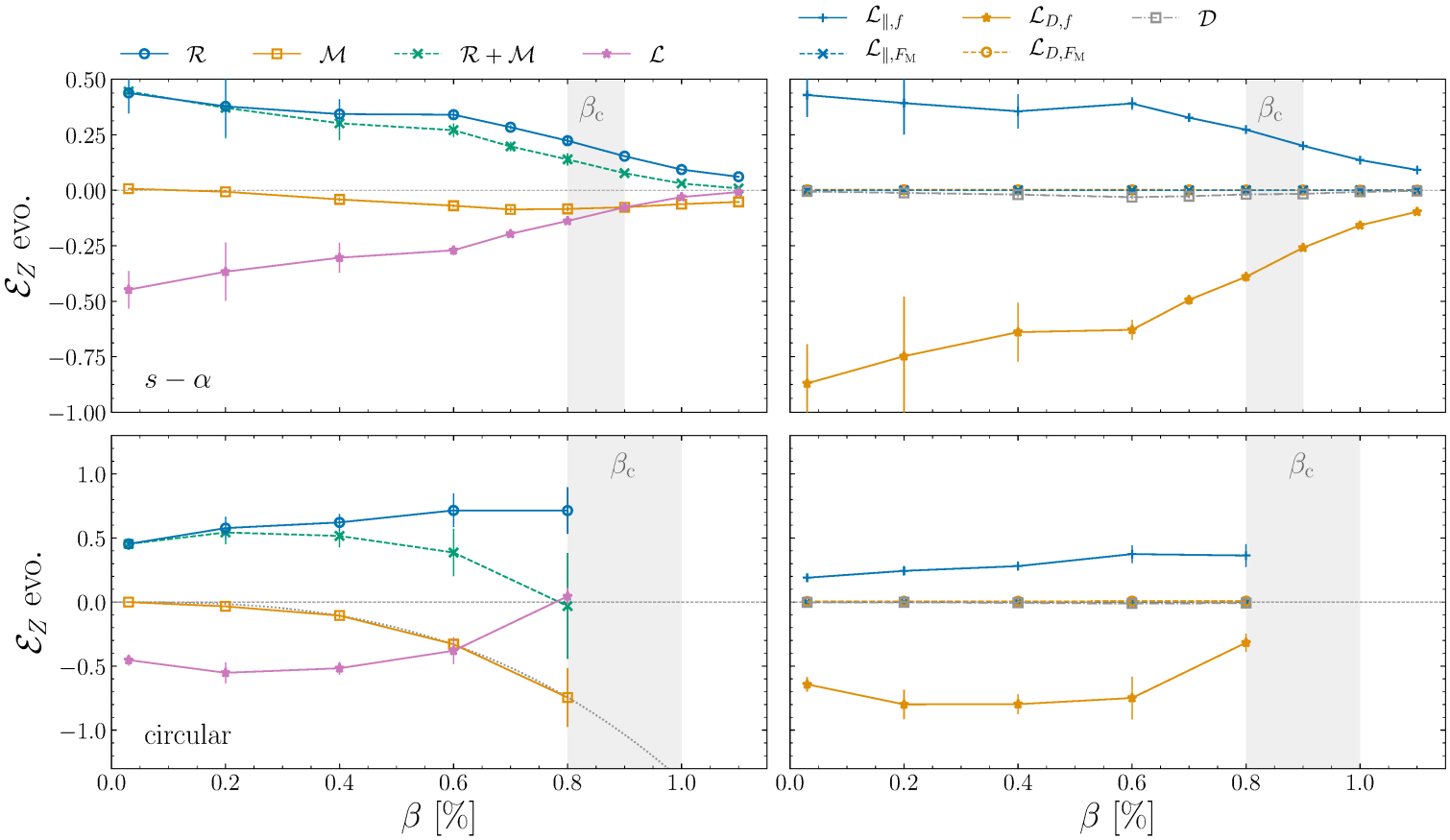

Figure 7.14: Temporally averaged terms of the zonal flow intensity evolution equation [see Eq. (7.9) and discussion below] for zonal flow mode number $n_\mathrm{ZF} = 1$ and against β. Shown are data sets for $R_0/L_T = 6.9$, $s-\alpha$ geometry and G_1 resolution (top) as well as circular geometry and G_1^circ resolution (bottom). The left panels depict the nonlinear transfer terms $\mathcal{R}$ and $\mathcal{M}$ as well as the transfer mediated by linear terms of the gyrokinetic equation $\mathcal{L}$, while the right panels show the individual contributions to $\mathcal{L}$. The time averaged is always performed over the stationary state excluding initial transient phases. The specified statistical errors are determined through six-part time averaging (see appendix C).

Positive feedback mechanism

The above analysis demonstrates that just below β_c the nonlinear generation of mesoscale ZFs is hindered through magnetic flutter induced damping. Cases that feature an initial long-term mesoscale ZF evolution, however, exhibit a transition in the transfer processes when reaching the proper final mesoscale ZF saturated stationary state. This can be readily seen by the time traces of the reference case, i. e., $R_0/L_T = 6.9$, $\beta = 0.8$ %, $s - \alpha$ geometry and G_1, in Fig. 7.13. The averaged Reynolds stress transfer increases by 50 % while the averaged Maxwell stress transfer is reduced by 43 % (cf. Tab. 7.4). As a result the total nonlinear transfer in the final stationary state is positive and, hence, supports the nonlinear sustain of mesoscale ZFs (see also top left panel of Fig. 7.14). This finding is confirmed by the increased spatial resolution sets G_1-x and G_1-s. Since the evolution of the mesoscale ZF directly influences the nonlinear transfer in a favorable way, this process can be regarded as a *positive feedback mechanism*.
The finding that the Maxwell stress transfer decreases when the mesoscale ZF reaches saturation is in agreement with the reduction of electromagnetic turbulence level in the latter phase [see time trace of I_{em} in panel (e) of Fig. 7.2]. As discussed in Sec. 7.3.5 the magnetic stochasticity decreases correspondingly and a reduction of the the magnetic stochasticity induced damping of zonal flows [60, 58] is therefore expected. However, the fact that the Reynolds stress transfer increases although the electrostatic turbulence level is found to decrease similarly to the electromagnetic one [see time trace of I_{es} in panel (d) of Fig. 7.2] is, at first, unexpected and deserves further discussion.
The favorable effect of the mesoscale ZF evolution on the Reynolds stress transfer is interpreted as resulting from the well known modulational instability [33, 34, 35, 46, 36, 37, 40]. This instability is based on the generation of sidebands through the nonlinear coupling of pump drift waves with the zonal flow. The favorable effect of ZFs, hence, is assumed to enter through an increase of the rate by which sidebands are generated. It mirrors the fact that a positive Reynolds stress transfer into the ZF can be caused by the ZF itself through ZF shear induced tilting of turbulent eddies as discussed in Ref. [45].
To proceed, a transition in the total nonlinear transfer due to mesoscale ZF evolution, similar to the above discussed case, can also be found for circular geometry. The exemplary case with $R_0/L_T = 5.5$, $\beta = 1.2$ % and G_1^{circ} resolution lies just below the turbulence runaway at $\beta_c = (1.3 \pm 0.1)$ %. It features an initial long-term mesoscale ZF evolution and a subequent mesoscale zonal flow saturated stationary state. A similar qualitative trend of the Reynolds- and Maxwell stress as well as the turbulence intensities is observed (see Tab. 7.4). Especially, the favorable effect of mesoscale ZFs on the Reynolds stress transfer is reproduced. As a result, the temporally averaged nonlinear transfer changes sign (negative to positive) when the mesoscale ZF has evolved. Again, the

mesoscale ZF is nonlinearly driven in the final stationary state, while a vanishing nonlinear transfer indicates nonlinear marginality in the initial transient phase; —a similar positive feedback process occurs.
Now that the influence of persistent mesoscale ZF evolution on the transfer processes into the $n_{\mathrm{ZF}} = 1$ mode has been studied, the transfer mechanisms in the proper final stationary states for $R_0/L_T = 6.9$ and $s - \alpha$ geometry are investigated (see top left panel of Fig. 7.13). Over the entire β-range considered here the Reynolds stress drives the ZF, while the Maxwell stress acts as a damping mechanism. The favorable positive feedback effect of the mesoscale ZF allows for positive nonlinear transfer $\mathcal{R} + \mathcal{M}$ (green dashed, '+' symbols) up to $\beta = 1.1$ %. The latter observation is interpreted as basis for the accessibility of the improved β regime.

Coupling of the zonal flow to energy and parallel flow sidebands

The remainder of this section concentrates on transfer mechanisms incorporated into $\mathcal{L}$, which act to balance the nonlinear stresses in the stationary state (violet stars in the left panels of Fig. 7.14). Throughout most of the considered β-range $\mathcal{L}$ constitutes a ZF damping mechanism, while it plays a driving role close to β_{c}. In order to identify the transfer mechanisms behind this damping and drive, $\mathcal{L}$ is disaggregated into its individual components (right panels of Fig. 7.14).
In general, numerical dissipation represented by $\mathcal{D}$ plays only a minor role. The dominant damping mechanism is provided by the magnetic drift term $\mathcal{L}_{D,f}$ (see appendix D.1 for more details about this term). In the limit of mesoscale ZFs, i. e., $(k_{\mathrm{ZF}}\rho_{\mathrm{sp}})^2 \lesssim (k_{\mathrm{ZF}}\rho_{\mathrm{th,i}})^2 \ll 1$, this term relates to the coupling of odd parity (in s with respect to $s = 0$) energy sidebands to the zonal potential via geodesic curvature. Here, a sideband is defined by a toroidally symmetric perturbation with poloidal dependency, i. e., a perturbation with $k_y = 0$ that varies along s. $\mathcal{L}_{D,f}$ is the kinetic counterpart of the magneto hydrodynamic geodesic transfer [56, 45]. While in the aforementioned references geodesic transfer has been shown to play a significant role in edge turbulence, the present study confirms its relevance in core turbulence.
The transfer due to parallel streaming along unperturbed field lines $\mathcal{L}_{\parallel,f}$ exhibits a finite contribution as well (see appendix D.2 for more details about this term). Since $\mathcal{L}_{\parallel,f} > 0$ this transfer mechanism acts to increase the zonal potential. It is therefore a zonal flow driving mechanism. In the limit of mesoscale ZFs this term relates to the coupling of the zonal potential to odd parity (in s with respect to $s = 0$) sidebands of the parallel flow. Physically, the divergence of the parallel motion generates a polarization density perturbation, which results in a zonal potential as described by the gyrokinetic Poission equation (4.49). Hence, perpendicular motion in form of a zonal flow arises due to the coupling to parallel

motion.
Note, although $\mathcal{L}_{\parallel,f}$ results from a linear term of the gyrokinetic equation, the zonal potential cannot directly tap energy from the background maxwellian through it. By contrast, the parallel flow sidebands, necessary for $\mathcal{L}_{\parallel,f} \neq 0$, have to be generated nonlinearly by the turbulence. Since both the zonal potential and the parallel flow sidebands are modes with $k_y = 0$, $\mathcal{L}_{\parallel,f}$ describes the coupling of different poloidal modes of axisymmetric perturbations.
To our knowledge, this zonal flow driving mechanism has not been described in literature so far. Note, however, that it plays a non-negligible role here, since the contributions of both the geodesic transfer and the coupling to parallel flow sidebands are of similar magnitude. Furthermore, $\mathcal{L}_{\parallel,f}$ contributes over the entire considered range in β. This mechanism, therefore, occurs both in electrostatic and electromagnetic microturbulence.
While for most values of β considered in this study mesoscale ZFs are damped through geodesic transfer, the coupling to parallel flow sidebands dominate just below β_c. Most notably, the latter transfer mechanism allows for the long-term evolution of mesoscale ZFs just below β_c in the case of $R_0/L_T = 6.9$, $\beta = 0.8$ % and $s - \alpha$ geometry and $R_0/L_T = 5.5$, $\beta = 1.2$ % and circular geometry (cf. Tab. 7.4). This outcome is supported by the elevated spatial resolution sets G_1-x and G_1-s.

7.3.7 Transport hysteresis in circular geometry

The transport hysteresis phenomenon has been introduced in the framework of a simplified $s - \alpha$ geometry with $\alpha = 0$ for comparability with previous studies [60, 59] and one might therefore critically question its broader validity. Especially since turbulent transport levels are known to be sensitive to the geometry model [9].
In order to confirm a more general relevance of the transport hysteresis phenomenon the dependence of the heat conductivity on β is explored for circular geometry and with $R_0/L_T = 6.9$ as well as $R_0/L_T = 5.5$ (see Fig. 7.15). Both R_0/L_T-realizations exhibit turbulence runaways at respective β_c, when initializing the simulation in the linear regime. The corresponding values are indicated by shaded regions and are denoted by $\beta_\mathrm{c}^{(6.9)}$ and $\beta_\mathrm{c}^{(5.5)}$ respectively. Consistent with Ref. [60] the threshold β_c is shifted to larger values for smaller R_0/L_T.
Despite the application of the restart procedure described in Sec. 7.3.1, no stationary state can be achieved for $\beta \gtrsim 1.0$ % in the series with $R_0/L_T = 6.9$. The fact that an improved β-regime cannot be accessed is consistent with the lack of temporally persistent mesoscale ZF states developing in this case: From the statistical analysis of Sec. 7.3.2 a highly unsteady mesoscale ZF can be anticipated for $\beta > \beta_\mathrm{c}^{(6.9)}$ (blue data in Fig. 7.4). It is then reasonable

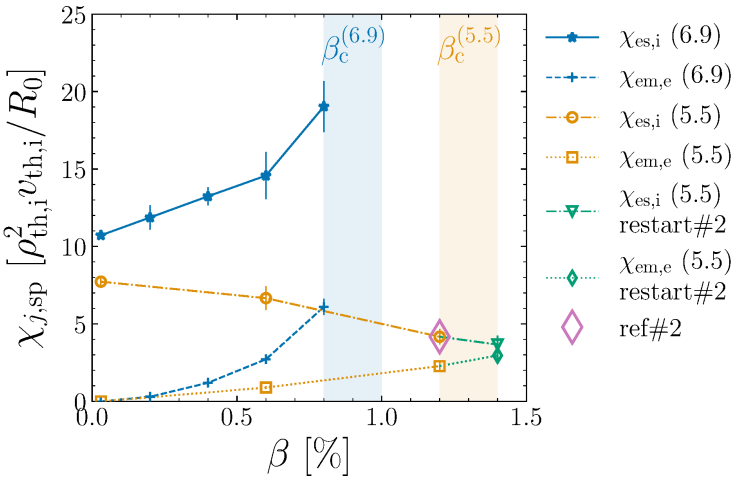

Figure 7.15: Dependence of the time and volume averaged ion electrostatic heat conductivity $\chi_{\mathrm{es,i}}$ and electron electromagnetic flutter heat conductivity $\chi_{\mathrm{em,e}}$ on the plasma β for $R_0/L_T = 6.9$ (blue) and $R_0/L_T = 5.5$ (orange and green), circular geometry and G_1^{circ} resolution. The green data points are obtained by restarting the late mesoscale ZF dominated state at $\beta = 1.2$ % (violet diamond). Shaded regions indicate the occurrence of turbulence runaways to extreme levels (see description in the text).

to assume that time intervals with very small mesoscale ZF amplitude occur regularly during the stationary state such that the condition for the triggering of a runaway $|\langle\hat{\omega}_{\mathrm{ExB}}\rangle_{n_{\mathrm{ZF}}=1}| < |\langle\hat{\omega}_{\mathrm{ExB}}\rangle_{n_{\mathrm{ZF}}=1}|^{\mathrm{c}}$ is satisfied evenually.
In the case of $R_0/L_T = 5.5$, however, stationary states at sufficiently high β feature a steady saturated mesoscale ZF amplitude (violet data in Fig. 7.4). And not surprisingly an improved regime with $\beta > \beta_{\mathrm{c}}^{(5.5)}$ can be accessed when restarting the late mesoscale ZF dominated state of the case with $R_0/L_T = 5.5$ and $\beta = 1.2$ % (ref#2, violet diamond in Fig. 7.15). The so obtained case at $\beta = 1.4$ % exhibits stationary turbulence during the full duration of this simulation of 3060.9 $R_0/v_{\mathrm{th,i}}$. Due to the higher persistence of the mesoscale ZF in this case, the mesoscale shearing rate $|\langle\hat{\omega}_{\mathrm{ExB}}\rangle_{n_{\mathrm{ZF}}=1}|$ can be conjectured to stay above the critical level $|\langle\hat{\omega}_{\mathrm{ExB}}\rangle_{n_{\mathrm{ZF}}=1}|^{\mathrm{c}}$ throughout the entire stationary state.

7.4 Conclusion

This work investigates microturbulence at finite normalized plasma pressure within a local gradient-driven gyrokinetic framework. Aspects of high β turbulence runaways [152, 21, 61, 148] and their mitigation are focused on. The main results are summarized below:

The well known high β turbulence runaway, also referred to as nonzonal transition (NZT) [60], is reproduced in the present work when simulations are initialized in the linear regime. Consistent with literature this threshold, here denoted by β_c, features a runaway to indeterminately turbulence levels just after nonlinear saturation of the initially growing linear eigenmodes.
As main result, however, persistent mesoscale zonal flow patterns are shown to mitigate this turbulence runaway, allowing for the access of an improved regime $\beta > \beta_c$. More in detail, the application of mesoscale zonal flow dominated states, developing naturally just below β_c for certain parameters, as initial conditions for realizations with $\beta > \beta_c$ yields stable stationary turbulent states in the improved regime. Here, the term *stable* refers to the stability against the triggering of turbulence runaways. This dependence of the turbulence level above β_c on the initial conditions, i. e., the history of the system, constitutes a transport hysteresis.
The development of persistent mesoscale zonal flows is parameter dependent and is shown to occur for large β and small R_0/L_T. As a consequence, although realizations with large R_0/L_T exhibit the usual turbulence runway at a respective β_c, they do not necessarily feature an improved β-regime. The hysteresis phenomenon, hence, requires the turbulence to be sufficiently close to marginality, a condition that can be assumed to apply to the experimental conditions. A distinct property of the mesoscale zonal flow pattern is the long time scale of $\sim 10^2 - 10^3\ R_0/v_{\mathrm{th,i}}$ connected to its development. As a result, sufficiently long simulations are required to access the proper stationary mesoscale zonal flow dominated states. Turbulence runaways at β_c, and when initializing the simulation in the linear regime, occur well *before* such zonal flows reach saturation. This temporal separation is at the basis of the hysteresis phenomenon.
When the mesoscale ZF reaches saturation a low turbulence state is induced. A box size scan shows that the radial scale of the ZF flow has to exceed a scale of $46 - 69\ \rho_{\mathrm{th,i}}$ to allow for this long-term transition to a reduced turbulence state. A striking observation is the convergence of the mesoscale ZF amplitude towards the same value of the $E \times B$ shearing rate independent of the radial scale. This ascribes a physical relevance to both the $E \times B$ shearing rate and the corresponding value of a few $\sim 10^{-1}\ R_0/v_{\mathrm{th,i}}$.
The mesoscale zonal flow level is a key quantity for the stability in the improved β-regime. Turbulence runaways can be triggered when the mesoscale ZF falls below a critical level; —a mechanism that potentially sets the upper threshold in β. The depletion of zonal flows due to application of resonant magnetic perturbations [154], for example, could constraint the improved β-regime.
A field line tracing analysis demonstrates that the magnetic stochasticity in the final mesoscale zonal flow dominated states is reduced compared to the initial transient phase in which mesoscale zonal flow still evolve. The reason is a reduction of the radial excursion of perturbed magnetic field lines due to the stabilizing effect of mesoscale zonal flows on the electromagnetic turbulence level. Furthermore, signatures of a sudden onset of field line decorrelation close to β_c,

as anticipated in the decorrelation theory behind the NZT [60], are not observed. A zonal flow transfer analysis reveals a positive feedback effect of mesoscale zonal flows just below β_c: During the evolution of such zonal flows a transition from vanishing to positive nonlinear transfer occurs, allowing for the nonlinear drive of mesoscale zonal flows beyond β_c in the improved β-regime. When the Reynolds stress transfer is balanced by the Maxwell stress, the coupling of the zonal potential to parallel flow sidebands allows for mesoscale zonal flows to be further driven. In the present work such a cancellation occurs just below β_c.
The implications of this study are now discussed:
(i) The main result of this work implies that β_c is not necessarily the upper limit in the normalized plasma pressure for stationary operation in the plasma core, provided persistent mesoscale zonal flow pattern can develop. In tokamak discharges the normalized plasma pressure evolves on time scales of the energy confinement time $\sim 10^0\ s$, which is large compared to the ion transit time $\sim 10^{-5}\ s$. The time scale connected to mesoscale zonal flow evolution of $10^2 - 10^3$ transit times, hence, is significantly smaller than the energy confinement time. Therefore, the zonal flow dominated branch, i. e., the improved β-regime, is assumed to represent the experimentally relevant branch. Note that experimental evidence of persistent mesoscale zonal flow patterns has been reported in JET [78] and Tore Supra [79].
(ii) Evidence is provided that the onset of field line decorrelation, as a threshold phenomenon, is not the reason for the triggering of turbulence runaways. This highlights the need for a more nuanced view of high β turbulence runaways. A link to zonal flow physics as proposed in Refs. [60, 59, 58], such as the cancellation of the Reynolds- and Maxwell stress transfer just below β_c or the correlation of turbulence runaways and the depletion of zonal flows, is nevertheless observed.
(iii) The coupling of the zonal flow to parallel flow sidebands has been demonstrated to be relevant in high β core turbulence, since it directly influence the zonal flow dynamics when the nonlinear Reynolds- and Maxwell stress cancel. A clarification of the physical mechanism behind the ZF drive through this coupling process is a rewarding topic for future work.
(iv) Finally, the present work encourages to look beyond time scales of $10^3\ R_0/v_{\mathrm{th,i}}$ even when dealing with kinetic electrons. Long-term dynamics bears relevant physics that has been shown to allow for the transport hysteresis phenomenon, but also might impact the judgment of numerical convergence.

Chapter 8

Energetics and nonlinear transfer analysis of the self-interaction mechanism in local gyrokinetic fluxtube simulations of ion temperature gradient driven turbulence

8.1 Introduction

The fluxtube approach [104] is widely utilized for the study of plasma microturbulence, such as ion temperature gradient (ITG) driven turbulence [13, 14, 15], in fusion devices due to its advantage in terms of computational costs. Being a local description, the fluxtube requires appropriately modeled boundary conditions, which are periodic transverse to the magnetic field and shifted periodic parallel to it [101]. However, the authors of Ref. [104] pointed at the possibility of artificial correlations introduced by such boundary conditions, when the correlation length of turbulent structures exceeds the size of the fluxtube domain. Due to the high mobility of electrons along the field lines turbulent structures can correlate over multiple poloidal turns, also known as giant tails [19], and, thereby, can introduce correlations through the parallel boundary in a fluxtube. Indeed, local gyrokinetic studies, treating electrons as a kinetic species, report of the self-correlation of such extended modes [64, 155, 148, 156]. For example, Ref. [64] discusses the role of this self-correlation mechanism for the nonlinear saturation of kinetic ballooning mode turbulence in a flat electron temperature gradient setup.

More recently, the self-interaction (SI) mechanism has been shown to be responsible for the generation of fine scale structures in the radial electric field shear [1], also known as the $E \times B$ shearing rate; —structures that are commonly observed to dominate the $E \times B$ shearing rate in gyrokinetic studies including electron dynamics [83, 84, 85, 86].
In principle, a fluxtube can be considered a proper description of an entire flux-surface with a corresponding value of the normalized Larmor radius $\rho_* = \rho_{\mathrm{th,i}}/R_0 \sim (2\pi\epsilon_0/q_0) \times (\rho_{\mathrm{th,i}}/L_y)$ [1, 85] (see Sec. 4.2.5). The self-interaction mechanism, therefore, bears some physical relevance that scales with the domain size L_y as shown in Refs. [1, 85, 84] and is, hence, understood as a finite ρ_* effect. The binormal domain size required for a full flux-surface description compliant to current day tokamaks, however, is one order of magnitude larger than the typical domain size chosen in literature [85]. This constraint alleviates the computational benefits of the fluxtube approach compared to more expensive full surface descriptions.
When correlations over the parallel boundary are eliminated in ITG driven turbulence, turbulent fluxes are reported to increase by up to several ten percent in strong turbulent situations [155, 85], but to be hardly influenced near marginality [85]. In addition, a recent director field analysis of zonal flow pattern formation in ion temperature gradient driven turbulence with inclusion of electron dynamics [118] shows that zonal fine scale features driven by SI hardly contribute to the zonal flow shear induced deformation of turbulent structures. Note that zonal flows usually play a dominant role in the nonlinear saturation of ITG driven turbulence [22, 75, 63, 65, 66].
The aforementioned observations leave the role of self-interaction in ITG driven turbulence unclear and, therefore, motivate the analysis presented in this chapter. Since the self-interaction process is inherently nonlinear, energetics and nonlinear transfer techniques [72, 107, 73, 110, 74, 111, 22, 63, 64, 65, 66, 156, 112] are applied to obtain a direct measure of the influence of self-interaction on the nonlinear saturation physics. CYCLONE base case (CBC) parameters [67] with inclusion of electron dynamics and a standard box size are chosen; —a case which shows clear signatures of self-interaction [1, 85, 118]. This chapter focuses on (i) the direct role of the nonlinear self-interaction process and (ii) the role of self-interaction driven zonal structures for the nonlinear saturation of ion temperature gradient driven turbulence and is structured as follows: In Sec. 8.2 the gyrokinetic simulation setup and the diagnostics are described. In Sec. 8.3 the results are presented, including an energetics description of the generation of twisted modes in Sec. 8.3.1, a nonlinear transfer analysis of the self-interaction mechanism in Sec. 8.3.2, and a study of the role of self-interaction driven zonal modes for the nonlinear transfer of generalized energy in Sec. 8.3.3. Concluding remarks are given in Sec. 8.4.

8.2 Numerical setup and diagnostics

8.2.1 Gyrokinetic simulation setup

In this chapter local nonlinear gradient-driven gyrokinetic simulations are studied. The simulations are performed with the fluxtube version of Gyrokinetic Workshop (GKW) [95] in the δf-approximation. The plasma parameters are compliant to the well known CYCLONE base case [67] (see Sec. 4.4). Background plasma rotation and collisions are not considered. Both a single ion species and electrons are treated as kinetic species with the electron to ion mass ratio $m_\mathrm{e}/m_\mathrm{i} = 2.72 \times 10^{-4}$ of deuterium. A small plasma beta $\beta = 3 \times 10^{-4}$ is chosen to include shear Alfvén wave physics, which allows for a larger time step, while keeping the turbulent dynamics essentially electrostatic. A geometry with exact circular concentric flux surfaces is chosen [9] (see Sec. 4.2.2). The numerical resolution and dissipation scheme is equivalent to the G_1^circ set of Ref. [139] (see also Tab. 7.1) and reader is referred to the aforementioned reference for more details. GKW utilizes straight field-aligned Hamada coordinates (x, y, s) [100], where x is the radial coordinate, y is the binormal coordinate and s is the parallel coordinate (for more details see Refs. [95, 139] and Sec. 4.2). Both the radial and binormal direction are represented by Fourier modes and the parallel extent of the box covers one poloidal turn. For the parameters chosen, the box size is $(L_x,\ L_y) = (76.72,\ 87.67)\ \rho_\mathrm{th,i}$, which represents a size usually chosen in literature. The self-interaction mechanism is expected to be strong for this realization of the box size.

8.2.2 Energetics and nonlinear transfer diagnostic

The Fourier decomposition of the perturbed gyrocenter distribution function f_sp reads

$$f_\mathrm{sp}(x, y, s) = \sum_{k_x} \sum_{k_y} \hat{f}_{\mathrm{sp},\mathbf{k}}(k_x, k_y, s) \exp[\mathrm{i}k_x(x - x_0) + \mathrm{i}k_y(y - y_0)], \tag{8.1}$$

where $x_0 = -L_x/2$ and $y_0 = -L_y/2$ are related to the radial and binormal box size L_x and L_y, respectively. This applies analogously to the perturbed electrostatic potential ϕ and parallel vector potential $A_\parallel$. It is then natural to refer to Fourier modes with wave vector $\mathbf{k} = (k_x,\ k_y)$ as *modes* or *perpendicular modes* in the local description [74, 64, 148]. In this chapter wave vectors are always given in units of $\rho_\mathrm{th,i}^{-1}$, where the ion thermal Larmor radius is defined by $\rho_\mathrm{th,i} = m_\mathrm{i} v_\mathrm{th,i}/(eB_0)$ with the ion thermal velocity $v_\mathrm{th,i} = (2T_\mathrm{0,i}/m_\mathrm{i})^{1/2}$, the elementary charge e and the reference background magnetic field strength B_0.

The generalized energy of a mode with mode label $\mathbf{k} = (k_x,\ k_y)$ is defined by [59, 65, 66]

$$E_{\mathbf{k}} = \frac{1}{2}\mathrm{Re}\sum_{\mathrm{sp}} T_{0,\mathrm{sp}} \int \mathrm{d}s \int \mathrm{d}^3 v\ \frac{\hat{h}^*_{\mathrm{sp},\mathbf{k}}}{F_{\mathrm{M,sp}}} \hat{g}_{\mathrm{sp},\mathbf{k}}, \tag{8.2}$$

with the modified distribution function

$$\hat{g}_{\mathrm{sp},\mathbf{k}} = \hat{f}_{\mathrm{sp},\mathbf{k}} + \frac{Z_{\mathrm{sp}} e}{T_{0,\mathrm{sp}}} v_\parallel \langle \hat{A}_{\parallel,\mathbf{k}} \rangle_{\mathrm{ga,sp}} F_{\mathrm{M,sp}} \tag{8.3}$$

and the nonadiabatic part of the distribution function

$$\hat{h}_{\mathrm{sp},\mathbf{k}} = \hat{f}_{\mathrm{sp},\mathbf{k}} + \frac{Z_{\mathrm{sp}} e}{T_{0,\mathrm{sp}}} \langle \hat{\phi}_{\mathbf{k}} \rangle_{\mathrm{ga,sp}} F_{\mathrm{M,sp}}. \tag{8.4}$$

Several quantities enter the above equations: Z_{sp} is the signed species charge number, $F_{\mathrm{M,sp}}$ is the maxwellian (see Ref. [95] or Sec. 4.3.1 for a definition), $v_\parallel$ is velocity parallel to the ambient magnetic field, $\langle ... \rangle_{\mathrm{ga,sp}}$ denotes the gyro-average and $T_{0,\mathrm{sp}}$ is the species background temperature. The generalized energy is often split into an entropy-like quantity, with a distribution and an electric field contribution, and the magnetic field energy [64, 148]. Related effects like field particle interaction [111] and the resulting transfer of entropy among species [64] are, however, of minor interest in the context of this chapter. The generalized energy $E_{\mathbf{k}}$ in gyrokinetic turbulence, also referred to as the free energy [111, 59, 148, 65, 66] or generalized grand canonical potential [30], is considered to play a similar role compared to the kinetic energy in fluid turbulence [110], as it is conserved by the nonlinearity. In the aforementioned references nonlinear transfer techniques based on the generalized energy have been well established and proven successful for the study of nonlinear processes involved in the saturation of microturbulence. Therefore, working with the generalized energy is well suited for the purpose of this work.

An equation for the evolution of the generalized energy at wave vector $\mathbf{k}$ is obtained by multiplying the gyrokinetic equation, formulated in terms of the Fourier transformed modified distribution function $\hat{g}_{\mathrm{sp},\mathbf{k}}$ (see appendix B), by $T_{0,\mathrm{sp}} \hat{h}^*_{\mathrm{sp},\mathbf{k}} / F_{\mathrm{M,sp}}$, integrating over velocity space as well as the parallel coordinate s and summing over species [99]. It formally reads

$$\frac{\partial E_{\mathbf{k}}}{\partial t} = N_{\mathbf{k}} + Q_{\mathbf{k}} + D_{\mathbf{k}} + T_{\mathbf{k}}, \tag{8.5}$$

with the individual terms on the right-hand side representing the net nonlinear transfer $N_{\mathbf{k}}$, the energy source $Q_{\mathbf{k}}$, energy dissipation $D_{\mathbf{k}}$ and transfer to twisted modes due to parallel streaming $T_{\mathbf{k}}$.

The net nonlinear transfer with respect to mode $\mathbf{k}$ results from the energy transfer within all possible wave vector triplet interactions [112]

$$N_{\mathbf{k}} = \sum_{\mathbf{q}} \sum_{\mathbf{p}} \delta_{\mathbf{k}+\mathbf{q}+\mathbf{p}} S^{\mathbf{k}}_{\mathbf{q},\mathbf{p}} \tag{8.6}$$

satisfying the wave vector matching rule

$$\mathbf{k}+\mathbf{q}+\mathbf{p}=0. \tag{8.7}$$

In Eq. (8.6), $\delta_{\mathbf{k}+\mathbf{q}+\mathbf{p}}$ denotes the Kronecker delta. Energy transfer within triplets is mediated by the $E\times B$- and magnetic flutter nonlinearity and can be formulated in terms of a symmetrized transfer function [22, 112]

$$S^{\mathbf{k}}_{\mathbf{q},\mathbf{p}}=\frac{1}{2}[A^{\mathbf{k}}_{\mathbf{q},\mathbf{p}}+A^{\mathbf{k}}_{\mathbf{p},\mathbf{q}}] \tag{8.8}$$

with the primitive transfer function

$$A^{\mathbf{k}}_{\mathbf{q},\mathbf{p}}=\mathrm{Re}\sum_{\mathrm{sp}}\int \mathrm{d}s\int \mathrm{d}^3v\ \frac{T_{0,\mathrm{sp}}}{F_{\mathrm{M,sp}}}\mathcal{E}^{xy}\times(q_xp_y-q_yp_x)\times\hat{h}_{\mathbf{k}}\hat{\chi}_{\mathrm{sp},\mathbf{q}}\hat{g}_{\mathrm{sp},\mathbf{p}}, \tag{8.9}$$

where $\hat{\chi}_{\mathrm{sp},\mathbf{k}}=\langle\hat{\phi}_{\mathbf{k}}\rangle_{\mathrm{ga,sp}}-v_\parallel\langle\hat{A}_{\parallel,\mathbf{k}}\rangle_{\mathrm{ga,sp}}$, $\mathcal{E}^{xy}=[(\nabla x\times\nabla y)\cdot\mathbf{b}]/B$, $\mathbf{b}$ is the unit vector parallel to the ambient magnetic field and B is the magnitude of the background magnetic field. The symmetrized transfer function measures the gain ($S^{\mathbf{k}}_{\mathbf{q},\mathbf{p}}>0$) or loss ($S^{\mathbf{k}}_{\mathbf{q},\mathbf{p}}<0$) of generalized energy of mode $\mathbf{k}$ due to the nonlinear interaction of the modes $\mathbf{q}$ and $\mathbf{p}$. Within a triplet the energy is nonlinearly conserved as expressed by the detailed triplet energy balance

$$S^{\mathbf{k}}_{\mathbf{q},\mathbf{p}}+S^{\mathbf{p}}_{\mathbf{k},\mathbf{q}}+S^{\mathbf{q}}_{\mathbf{p},\mathbf{k}}=0. \tag{8.10}$$

Furthermore, the symmetrized transfer function satisfies the symmetry property

$$S^{\mathbf{k}}_{\mathbf{q},\mathbf{p}}=S^{\mathbf{k}}_{\mathbf{p},\mathbf{q}}. \tag{8.11}$$

Note that in order to keep the amount of output data within a reasonable level while preserving sufficiently information about the nonlinear dynamics, the nonlinear transfer function $S^{\mathbf{k}}_{\mathbf{q},\mathbf{p}}$ is output every 0.375 $R_0/v_{\mathrm{th,i}}$ only throughout this work.

Energy injection is provided through the advection of the background gradients by the $E\times B$-drift and magnetic flutter and reads

$$\begin{aligned}Q_{\mathbf{k}}=&\mathrm{Re}\sum_{\mathrm{sp}}T_{0,\mathrm{sp}}\int \mathrm{d}s\int \mathrm{d}^3v\ \hat{f}^*_{\mathrm{sp},\mathbf{k}}\mathcal{E}^{xy}\mathrm{i}k_y\hat{\chi}_{\mathrm{sp},\mathbf{k}}\\&\times\left[\frac{1}{L_{n,\mathrm{sp}}}+\left(\frac{m_{\mathrm{sp}}v_\parallel^2/2+\mu B}{T_{0,\mathrm{sp}}}-\frac{3}{2}\right)\frac{1}{L_{T,\mathrm{sp}}}\right],\end{aligned} \tag{8.12}$$

where $1/L_{n,\mathrm{sp}}=-\partial_x\ln(n_{0,\mathrm{sp}})$ and $1/L_{T,\mathrm{sp}}=-\partial_x\ln(T_{0,\mathrm{sp}})$ are the inverse background density and temperature gradient lengths, respectively, and $\mu=m_{\mathrm{sp}}v_\perp^2/(2B)$ is the magnetic moment with $v_\perp$ the velocity perpendicular to the ambient magnetic field and the species mass m_{sp}. $Q_{\mathbf{k}}$ is closely related to the

turbulent gyro-center density and energy fluxes [99, 22, 64].
Energy dissipation $D_{\mathbf{k}} = D_{\parallel,\mathbf{k}} + D_{v_\parallel,\mathbf{k}} + D_{\perp,\mathbf{k}}$ is provided by numerical dissipation in this work. The dissipation scheme applied in GKW is discussed in Ref. [25] and consists of parallel dissipation

$$D_{\parallel,\mathbf{k}} = -\mathrm{Re}\sum_{\mathrm{sp}} T_{0,\mathrm{sp}} \int \mathrm{d}s \int \mathrm{d}^3 v \; \frac{\hat{h}^*_{\mathrm{sp},\mathbf{k}}}{F_{\mathrm{M,sp}}} \times \frac{D_s \Delta s^3}{12} \frac{v_{\parallel,\mathrm{max,sp}}}{\sqrt{3}} \mathbf{b}\cdot\nabla s \frac{\partial^4 \hat{f}_{\mathrm{sp},\mathbf{k}}}{\partial s^4}, \quad (8.13)$$

if $k_y \neq 0$,

$$D_{\parallel,\mathbf{k}} = -\mathrm{Re}\sum_{\mathrm{sp}} T_{0,\mathrm{sp}} \int \mathrm{d}s \int \mathrm{d}^3 v \; \frac{\hat{h}^*_{\mathrm{sp},\mathbf{k}}}{F_{\mathrm{M,sp}}} \times \frac{D_s \Delta s^5}{60} \frac{v_{\parallel,\mathrm{max,sp}}}{\sqrt{3}} \mathbf{b}\cdot\nabla s \frac{\partial^6 \hat{f}_{\mathrm{sp},\mathbf{k}}}{\partial s^6}, \quad (8.14)$$

if $k_y = 0$, parallel velocity space dissipation

$$D_{v_\parallel,\mathbf{k}} = -\mathrm{Re}\sum_{\mathrm{sp}} T_{0,\mathrm{sp}} \int \mathrm{d}s \int \mathrm{d}^3 v \; \frac{\hat{h}^*_{\mathrm{sp},\mathbf{k}}}{F_{\mathrm{M,sp}}} \times \frac{D_{v_\parallel} \Delta {v_\parallel}^3}{12} \frac{\mu_{\mathrm{max,sp}}}{\sqrt{3} m_{\mathrm{sp}}} \mathbf{b}\cdot\nabla B \frac{\partial^4 \hat{f}_{\mathrm{sp},\mathbf{k}}}{\partial {v_\parallel}^4} \quad (8.15)$$

and perpendicular dissipation

$$D_{\perp,\mathbf{k}} = -\mathrm{Re}\sum_{\mathrm{sp}} T_{0,\mathrm{sp}} \int \mathrm{d}s \int \mathrm{d}^3 v \; \frac{\hat{h}^*_{\mathrm{sp},\mathbf{k}}}{F_{\mathrm{M,sp}}} \times \frac{v_{\mathrm{th,i}}}{R_0} \left[D_x \left(\frac{k_x}{k_x^{\mathrm{max}}} \right)^4 - D_y \left(\frac{k_y}{k_y^{\mathrm{max}}} \right)^4 \right] \hat{f}_{\mathrm{sp},\mathbf{k}}. \quad (8.16)$$

Here, D_s, $D_{v_\parallel}$, D_x and D_y are dimensionless dissipation coefficients, $v_{\parallel,\mathrm{max,sp}}$ and $\mu_{\mathrm{max,sp}}$ is the maximum resolved parallel velocity and magnetic moment respectively, k_x^{max} as well as k_y^{max} is the maximum resolved radial and binormal wave vector respectively, and R_0 is the major radius of the magnetic axis.
The transfer to twisted modes results from parallel streaming along unperturbed field lines and can be recast into the form

$$T_{\mathbf{k}} = -\mathrm{Re}\sum_{\mathrm{sp}} T_{0,\mathrm{sp}} \int \mathrm{d}s \int \mathrm{d}^3 v \; v_\parallel \mathbf{b}\cdot\nabla s \times \frac{\partial}{\partial s} \left[\hat{f}^*_{\mathrm{sp},\mathbf{k}} \left(\frac{\hat{f}_{\mathrm{sp},\mathbf{k}}}{2F_{\mathrm{M,sp}}} + \frac{Z_{\mathrm{sp}} e}{T_{0,\mathrm{sp}}} \langle \hat{\phi}_{\mathbf{k}} \rangle_{\mathrm{ga,sp}} \right) \right]. \quad (8.17)$$

A finite $T_{\mathbf{k}}$ is the consequence of the shifted parallel boundary conditions [64]. This term is further discussed in Sec. 8.3.1.
The individual terms of the energy balance equation (8.5) are given in units of $\rho_{\mathrm{th,i}}^2 T_0 n_0 v_{\mathrm{th,i}} / R_0^3$ throughout this chapter. For the nominal parameters the energy balance Eq. (8.5) is well satisfied as shown exemplary for the modes $\mathbf{k} = (0,\ 0.22)$ and $\mathbf{k} = (1.28,\ 0.22)$ in Fig. 8.1 and Fig. 8.2 respectively. In both cases the sum $\partial_t E_{\mathbf{k}} - Q_{\mathbf{k}} - D_{\mathbf{k}} - T_{\mathbf{k}}$ (gray line) agrees well with the net nonlinear transfer $N_{\mathbf{k}}$ (violet dots).

8.2.3 Radial electric field intensity diagnostic

The radial electric field intensity connected to the zonal potential is defined by

$$\mathcal{E}_Z = k_{\mathrm{ZF}}^2 |\langle\hat{\phi}_{\mathbf{k}}\rangle|^2, \tag{8.18}$$

where the zonal potential reads

$$\langle\phi\rangle(x) = \frac{1}{L_y}\int \mathrm{d}y \int \mathrm{d}s\ \phi(x,y,s) \tag{8.19}$$

$$= \sum_{k_{\mathrm{ZF}}} \langle\hat{\phi}_{\mathbf{k}}\rangle(k_{\mathrm{ZF}}) \times \exp[\mathrm{i}k_{\mathrm{ZF}}\cdot(x-x_0)], \tag{8.20}$$

which defines the Fourier amplitude of the zonal potential $\langle\hat{\phi}_{\mathbf{k}}\rangle$ and the zonal wave vector k_{ZF}. Throughout this work $\mathcal{E}_Z$ is given in terms of $T_0^2/(e^2R_0^2)$.
The evolution equation of the radial electric field intensity $\mathcal{E}_Z$ follows from the time derivative of the inverted and flux-surface averaged $k_y = 0$ part of gyrokinetic Poisson equation

$$\frac{\partial\langle\hat{\phi}_{\mathbf{k}}\rangle}{\partial t} = -\int \mathrm{d}s\ \frac{1}{\mathcal{P}}\sum_{\mathrm{sp}} Z_{\mathrm{sp}} e \frac{2\pi B}{m_{\mathrm{sp}}} \int \mathrm{d}v_\parallel \int \mathrm{d}\mu\ \left[J_0(\lambda_{\mathrm{sp}})\frac{\partial\hat{g}_{\mathrm{sp},\mathbf{k}}}{\partial t}\right]_{\mathbf{k}=(k_{\mathrm{ZF}},0)}, \tag{8.21}$$

where

$$\mathcal{P} = \sum_{\mathrm{sp}} \frac{n_{0,\mathrm{sp}} Z_{\mathrm{sp}}^2 e^2}{T_{0,\mathrm{sp}}}[\Gamma_0(b_{\mathrm{sp}}) - 1]. \tag{8.22}$$

J_0 (Γ_0) is the zeroth order (modified) Bessel function of the first kind. The arguments are defined by $\lambda_{\mathrm{sp}}^2 = -\rho_{\mathrm{sp}}^2\nabla_\perp^2$ and $b_{\mathrm{sp}} = -0.5\times[m_{\mathrm{sp}}v_{\mathrm{th,sp}}/(Z_{\mathrm{sp}}eB)]^2\nabla_\perp^2$, with the species thermal velocity $v_{\mathrm{th,sp}} = (2T_{0,\mathrm{sp}}/m_{\mathrm{sp}})^{1/2}$ and the species Larmor radius radius $\rho_{\mathrm{sp}} = \sqrt{2m_{\mathrm{sp}}\mu/B}/(e|Z_{\mathrm{sp}}|)$. Note that $\nabla_\perp$ denotes the component of the gradient perpendicular to the equilibrium magnetic field.
As described in Ref. [139] the time derivative of the perturbed modified distribution function $\partial_t\hat{g}_{\mathrm{sp},\mathbf{k}}$ entering the right-hand side of Eq. (8.21) is substituted by the individual terms on the right-hand side of the gyrokinetic equation. Finally, Eq. (8.21) is multiplied by $2k_{\mathrm{ZF}}^2\langle\hat{\phi}_{\mathbf{k}}\rangle^*$, where $\langle\hat{\phi}_{\mathbf{k}}\rangle^*$ denotes the complex conjugate of $\langle\hat{\phi}_{\mathbf{k}}\rangle$, and is formally recast into the form

$$\frac{\partial\mathcal{E}_Z}{\partial t} = \mathcal{R} + \mathcal{M} + \mathcal{L}, \tag{8.23}$$

where $\mathcal{R}$ originates from the $E\times B$-noninearity and is denoted by the Reynolds stress, $\mathcal{M}$ results from the magnetic flutter nonlinearity and is referred to as Maxwell stress, and $\mathcal{L}$ combines all linear terms of the gyrokinetic equation (for more details see Sec. 7.2.3). The individual terms on the RHS of Eq. (8.23) are given in units of $v_{\mathrm{th,i}}T_0^2/(e^2R_0^3)$ in this chapter. Note that $\mathcal{E}_Z$ is a positive definit

quantity that provides information about the intensity (amplitude) of the zonal potential $\langle\hat{\phi}_{\mathbf{k}}\rangle$ of the mode $\mathbf{k} = (k_{\mathrm{ZF}},\ 0)$. A positive (negative) sign of the RHS terms of Eq. (8.23), hence, corresponds to the increase (decrease) of the modes intensity.
The self-interaction mechanism is a nonlinear effect that enters the evolution of the radial electric field intensity through $\mathcal{R}$ and $\mathcal{M}$. The contribution of individual non-zonal ($k_y \neq 0$) modes to the Reynolds stress can be isolated by exploiting the hermitian symmetry of the spectrum. A k_{ZF}-k'_y-spectrum of the nonlinear stresses, i. e., $\mathcal{R}(k_{\mathrm{ZF}}, k'_y)$ and $\mathcal{M}(k_{\mathrm{ZF}}, k'_y)$, is obtained by substituting

$$\left[J_0(\lambda_{\mathrm{sp}})\frac{\partial \hat{g}_{\mathrm{sp},\mathbf{k}}}{\partial t}\right]_{\mathbf{k}=(k_{\mathrm{ZF}},0)} = -2k'_y k_{\mathrm{ZF}} \mathcal{E}^{xy} J_0(\lambda_{\mathrm{sp}}) \times \sum_{k'_x} \hat{\chi}_{\mathrm{sp},\mathbf{k}'} \hat{g}^*_{\mathrm{sp},\mathbf{k}'-\mathbf{k}_Z} \tag{8.24}$$

into Eq. (8.21), where $\mathbf{k}_Z = (k_{\mathrm{ZF}}, 0)$. Note that $\mathbf{k}'$ and $\mathbf{k}$ distinguish between the nonlinearly interacting non-zonal modes (with prime) and the generated zonal mode (without prime). At fixed k'_y the nonlinear interaction of modes with radial wave vectors separated by the zonal wave vector k_{ZF}, i. e., k'_x and $k'_x - k_{\mathrm{ZF}}$, contribute to the nonlinear evolution of $\mathcal{E}_Z$ at k_{ZF} only. This requirement is equivalent to the wave vector matching rule [Eq. (8.7)] introduced in Sec. 8.2.2 and represents the interaction of a turbulent mode and a sideband mode. Note that the Reynolds stress $\mathcal{R}$ relates to the electrostatic potential part of $\hat{\chi}_{\mathrm{sp},\mathbf{k}'}$ (see Sec. 8.2.2 for a definition of this quantity) and is considered exclusively throughout this chapter. Due to the small β chosen in this chapter, the Maxwell stress $\mathcal{M}$ related to the parallel vector potential part of $\hat{\chi}_{\mathrm{sp},\mathbf{k}'}$ is negligible.

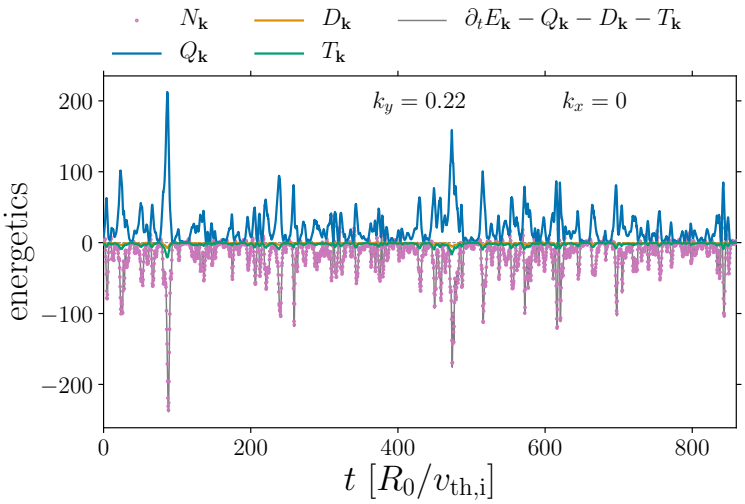

Figure 8.1: Time trace of individual terms of the energy balance Eq. (8.5) for the maximum transport driving mode $\mathbf{k} = (0,\ 0.22)$ and nominal parameters.

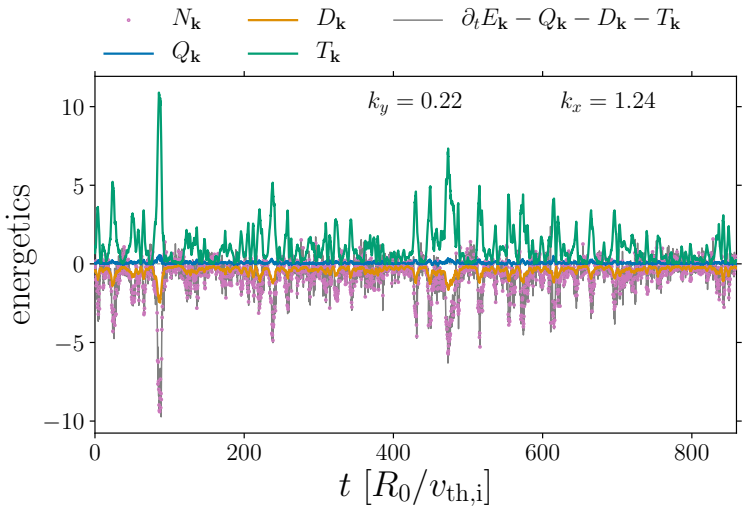

Figure 8.2: Time trace of individual terms of the energy balance Eq. (8.5) for the first order connection of the maximum transport driving mode $\mathbf{k} = (1.24,\ 0.22)$ and nominal parameters.

8.3 Numerical results

8.3.1 Definition of the extended mode and generation of twisted modes

This section aims for an energetics description of the excitation of twisted modes, which represents the basis for the nonlinear self-interaction mechanism.
Passing electron dynamics can result in extended modes with a parallel correlation length of multiple poloidal turns [19, 83, 85]. In the present local fluxtube description the parallel extent of the simulation domain, however, is limited to one poloidal turn $s \in [-0.5,\ 0.5]$. As a result, at the parallel boundaries $s = \pm 0.5$, an extended mode is therefore mapped back into the simulation domain according to shifted periodic parallel boundary conditions $\hat{f}_{\mathbf{k}}(k_x,\ k_y,\ s = \pm 0.5) = \hat{f}_{\mathbf{k}}(k_x \pm \Delta k_x,\ k_y,\ s = \mp 0.5)$, with the radial wave vector shift [1]

$$\Delta k_x = k_y \frac{q_0 \hat{s}_0}{\epsilon_0} \tag{8.25}$$

accounting for the twist of the mode due to the sheared background magnetic field. As a consequence of the extended mode structure, a *central (perpendicular) mode* $\mathbf{k}_0 = (k_x,\ k_y)$ may correlate with its *twisted (perpendicular) modes* $\mathbf{k}_{\pm n} = (k_x \pm n \cdot \Delta k_x,\ k_y)$, where the order n specifies the number of poloidal turns the extended mode is correlated over. Below, the modes $\mathbf{k}_{\pm n}$ will also be referred to as $\pm n$-th order connection of the central mode $\mathbf{k}_0$. Note that in the

$(k_x,\ k_y)$	$N_{\mathbf{k}}$	$N_{\mathbf{k}}^{\mathrm{SI}}$	$Q_{\mathbf{k}}$	$D_{\mathbf{k}}$	$T_{\mathbf{k}}$	$E_{\mathbf{k}}$
$(0,\ 0.22)$	-17.790	-0.144	21.042	-0.925	-2.347	34.337
$(+1.24,\ 0.22)$	-0.758	-0.113	0.052	-0.430	1.136	1.125
$(-1.24,\ 0.22)$	-0.682	-0.1	0.045	-0.418	1.050	1.068
$(+2.47,\ 0.22)$	0.136	-0.016	0.002	-0.203	0.062	0.281
$(-2.47,\ 0.22)$	0.153	-0.017	0.001	-0.203	0.059	0.280
$\sum$	-18.940	-0.388	21.142	-2.179	-0.039	37.091

Table 8.1: Individual terms of the energy balance Eq. (8.5) temporally averaged over the stationary state, for various perpendicular modes $(k_x,\ k_y)$ of the same extended mode with central mode $\mathbf{k}_0 = (0,\ 0.22)$ and for nominal parameters. The last row specifies the sum over the individual perpendicular modes of the extended mode.

local description the *extended mode* is defined as the complete set composed of the central (perpendicular) mode $\mathbf{k}_0$ and its twisted (perpendicular) modes $\mathbf{k}_{\pm n}$. The term $T_{\mathbf{k}}$ of the energy balance Eq. (8.5) describes the conservative transfer of generalized energy from the central mode $\mathbf{k}_0$ to the parallel connected modes $\mathbf{k}_{\pm n}$ within an extended mode and is further elucidated through solving the s-integral in Eq. (8.17) explicitly

$$T'_{\mathbf{k}} = -\mathrm{Re}\sum_{\mathrm{sp}} T_{0,\mathrm{sp}} \int \mathrm{d}^3v\ v_\parallel \mathbf{b}\cdot\nabla s \times \left[\hat{f}^*_{\mathrm{sp},\mathbf{k}}\left(\frac{\hat{f}_{\mathrm{sp},\mathbf{k}}}{2F_{\mathrm{M,sp}}} + \frac{Z_{\mathrm{sp}}e}{T_{0,\mathrm{sp}}}\langle\hat{\phi}_{\mathbf{k}}\rangle_{\mathrm{ga,sp}}\right)\right]_{s=-0.5}^{s=+0.5}. \tag{8.26}$$

Note that $\int \mathrm{d}s$ and $\mathbf{b}\cdot\nabla s \mathrm{d}^2v = 2\pi B\mathbf{b}\cdot\nabla s \mathrm{d}\mu\mathrm{d}v_\parallel$ commute, since $B\mathbf{b}\cdot\nabla s$ is constant with respect to s. Due to the shifted parallel boundary conditions, the evaluation of the integrand of $T'_{\mathbf{k}_0}$ at the upper boundary $s = +0.5$ agrees with the evaluation of $T'_{\mathbf{k}_{+1}}$ at the lower boundary $s = -0.5$ (and analogously for $T'_{\mathbf{k}_0}$ at $s = -0.5$ and $T'_{\mathbf{k}_{-1}}$ at $s = +0.5$). The net energy transfer $T_{\mathbf{k}_0}$ with respect to mode $\mathbf{k}_0$ is, hence, compensated by $T'_{\mathbf{k}_{\pm1}}$. The above calculation highlights that a central mode $\mathbf{k}_0$ and its twisted modes $\mathbf{k}_{\pm n}$ are directly correlated as a consequence of the spreading of energy along the field line.
Fig. 8.3 demonstrates the generation of twisted modes through the transfer of energy out of modes with $k_x \approx 0$ ($T_{\mathbf{k}} < 0$) into modes with radial wave vector $k_x \approx \pm n\cdot\Delta k_x$ ($T_{\mathbf{k}} > 0$) for the nominal parameters. In the considered ITG turbulence the spectrum of the turbulent electrostatic heat flux $Q_{\mathrm{es},\mathbf{k}} = Q_{\mathrm{es,i},\mathbf{k}} + Q_{\mathrm{es,e},\mathbf{k}}$ (and also the energy source $Q_{\mathbf{k}}$), where

$$Q_{\mathrm{es,sp},\mathbf{k}} = 2k_y\mathcal{E}^{xy}\int \mathrm{d}^3v\ \frac{m_{\mathrm{sp}}v^2}{2}\mathrm{Im}[\langle\hat{\phi}_{\mathbf{k}}\rangle^*_{\mathrm{ga,sp}}\hat{f}_{\mathrm{sp},\mathbf{k}}] \tag{8.27}$$

and Im[G] denotes the imaginary part of the complex quantity G, has its maximum at $\mathbf{k} = (0,\ 0.22)$ in agreement with previous studies [22, 65]. This mode

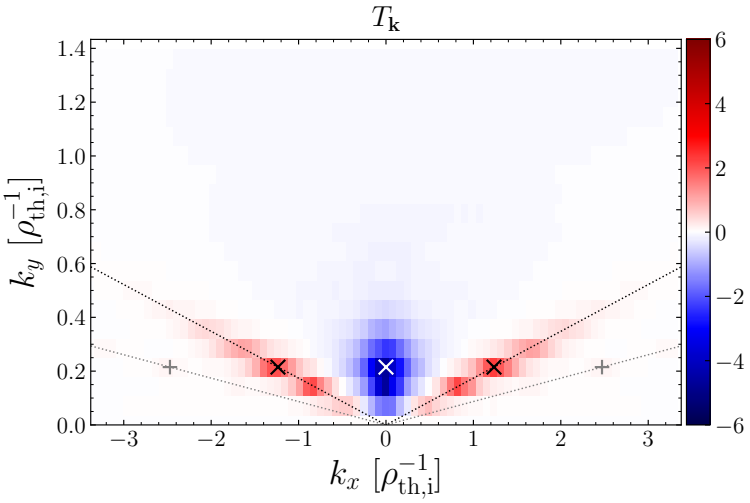

Figure 8.3: Transfer to twisted modes $T_\mathbf{k}$ against k_x and k_y averaged over the stationary state and for nominal parameters. The white ×-symbol depicts the maximum transport driving mode $\mathbf{k} = (0,\ 0.22)$, black ×-symbols and gray +-symbols its first and second order connections over the parallel boundary. Black and gray dotted lines depict $k_x = \pm n \cdot \Delta k_x$ [Eq. (8.25)] with $n = 1$ and $n = 2$ respectively.

(white ×-symbol in Fig. 8.3) transfers $T_\mathbf{k}(0,\ 0.22) = -2.35$ to its twisted modes. The first order connections (black ×-symbols) receive $T_\mathbf{k}(1.24,\ 0.22) = 1.14$ and $T_\mathbf{k}(-1.24,\ 0.22) = 1.05$ and the second order connections (gray +-symbols) receive $T_\mathbf{k}(2.47,\ 0.22) = 0.06$ and $T_\mathbf{k}(-2.47,\ 0.22) = 0.06$. In agreement with Ref. [84] first order connections are dominant. Despite being much smaller, correlations to second order connections, however, do exist, demonstrating that extended ITG driven modes indeed correlate over multiple poloidal turns.
In the case of the maximum transport driving mode $\mathbf{k} = (0,\ 0.22)$ the energy injection is provided by the energy source $Q_\mathbf{k}$ (see Fig. 8.1 and Tab. 8.1), as expected for an unstable ITG driven mode [74, 22, 63]. The energy source is mainly balanced by a negative net nonlinear transfer $N_\mathbf{k}$. However, since the transfer $T_\mathbf{k}$ has a magnitude of roughly 11 % of the energy source $Q_\mathbf{k}$, the transfer to parallel connected modes represents a non-negligible contribution to the energy balance. Energy dissipation balances roughly 4 % of the energy injection.
The first order twisted modes $\mathbf{k}_{\pm 1} = (\pm 1.28,\ 0.22)$, in turn, are dominantly driven through $T_\mathbf{k}$ (see Fig. 8.2 and Tab. 8.1). As part of the perpendicular wave vector spectrum in the local approach, twisted modes are, therefore, directly excited by unstable ITG modes through the spreading of energy within an extended mode. Both the nonlinear transfer $N_\mathbf{k}$ and energy dissipation $D_\mathbf{k}$ contribute similarly to

the energy balance.
From a global point of view the central unstable ITG driven mode $\mathbf{k}_0 = (0,\ 0.22)$ and its twisted modes $\mathbf{k}_{\pm 1} = (\pm 1.24,\ 0.22)$ as well as $\mathbf{k}_{\pm 2} = (\pm 2.47,\ 0.22)$ represent one extended mode. The nonlinear transfer and dissipation of free energy connected to the twisted modes, therefore, directly add to the saturation of the central unstable ITG driven mode. This is outlined in the last row of Tab. 8.1, which summarizes terms of the energy balance summed over the individual modes of the same extended mode. While twisted modes constitute only a small contribution to the drive $Q_{\mathbf{k}}$ of the entire extended mode (< 1 %), they make up 58 % of the energy dissipation. The nonlinear transfer summed over the twisted modes represent 6 % of the total net nonlinear transfer with respect to the extended mode. The nonlinear saturation of the extended mode, hence, is mostly determined by nonlinear processes involving the central mode.

8.3.2 Nonlinear self-interaction

Having established the energetics behind the twisted mode generation in Sec. 8.3.1, now the nonlinear self-interaction is focused on. First, this section introduces the wave vector triplets connected to the nonlinear self-interaction. Then, the SI mediated energy transfer is compared to the total net nonlinear energy transfer to obtain a measure of the direct influence of the self-interaction on the nonlinear saturation processes in ITG driven turbulence.

Self-interaction triplets

As discussed in Sec. 8.3.1 a central unstable ITG mode with a wave vector $\mathbf{k}_0 = (k_x,\ k_y)$ correlates with the twisted modes $\mathbf{k}^a_{\pm n} = (-k_x \mp n \cdot \Delta k_x,\ -k_y)$ and $\mathbf{k}^b_{\pm n} = (k_x \pm n \cdot \Delta k_x,\ k_y)$. Note that the reality of physical quantities such as the distribution function f requires $\hat{f}_{\mathbf{k}} = \hat{f}^*_{-\mathbf{k}}$. A perturbation of the central unstable ITG driven mode $\hat{f}_{\mathbf{k}_0}$, therefore, determines the mirror mode $\hat{f}_{-\mathbf{k}_0} = \hat{f}^*_{\mathbf{k}_0}$ entirely. Any wave vector combination of $\pm\mathbf{k}_0$ with $(\pm n \cdot \Delta k_x,\ 0)$, where n being an integer, labels a valid mode within the same extended mode.
Although, $\pm\mathbf{k}_0$ and its twisted modes $\mathbf{k}^{a/b}_{\pm n}$ are parts of the same extended mode structure, in the local approach they are treated as independent modes. This pertains especially to the evaluation of the $E \times B$-nonlinearity, which allows for their nonlinear interaction —referred to as self-interaction [1].
Any combination of two modes out of the set $[\pm\mathbf{k}_0;\ \mathbf{k}^{a/b}_{\pm n}]$ forms a valid nonlinear self-interaction triplet defined by the matching rule Eq. (8.7). Since the central ITG unstable mode $\mathbf{k}_0$ usually has the largest amplitude (see last column of Tab. 8.1), self-interaction triplets including $\mathbf{k}_0$ are particularly strong and will be

explicitly defined below.
The central unstable ITG mode and its twisted modes form triplets with two classes of modes $\mathbf{k}^a_{\mathrm{SI},\pm n} = (\pm n \cdot \Delta k_x,\ 0)$ and $\mathbf{k}^b_{\mathrm{SI},\pm n} = (-2k_x \mp n \cdot \Delta k_x, -2k_y)$ according to the wave vector matching rule Eq. (8.7):

$$\mathbf{k}_0 + \mathbf{k}^a_{\pm n} + \mathbf{k}^a_{\mathrm{SI},\pm n} = 0 \tag{8.28}$$

$$\mathbf{k}_0 + \mathbf{k}^b_{\pm n} + \mathbf{k}^b_{\mathrm{SI},\pm n} = 0 \tag{8.29}$$

The modes $\mathbf{k}^a_{\mathrm{SI},\pm n}$ and $\mathbf{k}^b_{\mathrm{SI},\pm n}$ will also be denoted by matching modes throughout this work. The tripplet Eq. (8.28) describes the interaction with a toroidally symmetric $k_y = 0$ (sometimes referred to as zonal) mode as already discussed in Refs. [64, 1]. Note that the resulting zonal matching mode $\mathbf{k}^a_{\mathrm{SI},\pm n}$ is independent of the radial wave vector k_x of the central mode. At fixed k_y all unstable ITG driven modes, i. e., independent of k_x, drive the same zonal modes with zonal wave vector $\mathbf{k}_Z = (\pm n \cdot \Delta k_x,\ 0)$. Hereafter, such modes will be referred to as self-interaction driven zonal modes.
Exploiting the symmetry properties of the symmetrized nonlinear transfer function [Eq. (8.8)] allows for the quantification of the detailed triplet energy balance [Eq. (8.10)] through the graph of $S^{\mathbf{k}}_{\mathbf{q},\mathbf{p}}$ as function of $\mathbf{k}$ at fixed $\mathbf{q}$ [see Fig. 8.4 for $\mathbf{q} = (0,\ 0.22)$]. The triplets connected to the nonlinear

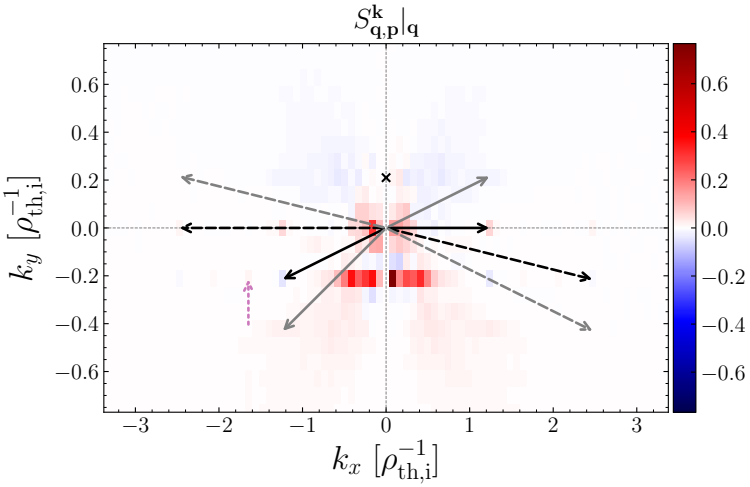

Figure 8.4: Symmetrized nonlinear transfer function $S^{\mathbf{k}}_{\mathbf{q},\mathbf{p}}|_{\mathbf{k}}$ with fixed $\mathbf{q} = (0,\ 0.22)$ (black $\times$-symbol) and as function of $\mathbf{k}$. Arrows indicate the triplets $\mathbf{k}_0 + \mathbf{k}^a_{+1} + \mathbf{k}^a_{\mathrm{SI},+1} = 0$ (black solid), $\mathbf{k}_0 + \mathbf{k}^b_{-1} + \mathbf{k}^b_{\mathrm{SI},-1} = 0$ (gray solid), $\mathbf{k}_0 + \mathbf{k}^a_{+2} + \mathbf{k}^a_{\mathrm{SI},+2} = 0$ (black dashed) and $\mathbf{k}_0 + \mathbf{k}^b_{-2} + \mathbf{k}^b_{\mathrm{SI},-2} = 0$ (gray dashed) connected to the self-interaction of the central mode $\mathbf{k}_0 = (0,\ 0.22) \leftrightarrow \mathbf{q}$. The violet dotted arrow indicates the sideband mode $\mathbf{k}_S = (-1.67, -0.22) \leftrightarrow \mathbf{k}$ generated through the nonlinear interaction of the central unstable ITG mode $\mathbf{k}_0 \leftrightarrow \mathbf{q}$ with the zonal mode $\mathbf{k}_Z = (1.67,\ 0) \leftrightarrow \mathbf{p}$ (see also the discussion in Sec. 8.3.3).

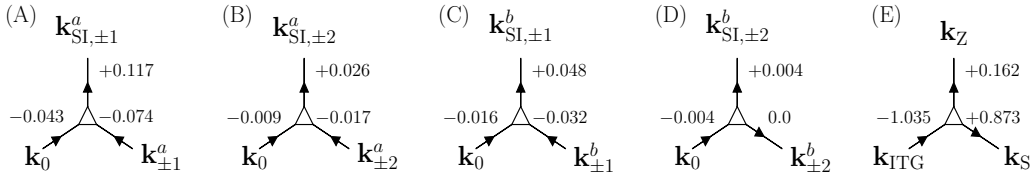

Figure 8.5: (A)-(E): Detailed energy balance of triplets connected to the nonlinear self-interaction mechanism of a central unstable ITG mode $\mathbf{k}_0 = (0,\ 0.22)$ with (A) $\mathbf{k}^a_{\pm1} = (\mp1.24,\ -0.22)$ as well as $\mathbf{k}^a_{\mathrm{SI},\pm1} = (\pm1.24,\ 0)$, (B) $\mathbf{k}^a_{\pm2} = (\mp2.47,\ -0.22)$ as well as $\mathbf{k}^a_{\mathrm{SI},\pm2} = (\pm2.47,\ 0)$, (C) $\mathbf{k}^b_{\pm1} = (\pm1.24,\ 0.22)$ as well as $\mathbf{k}^b_{\mathrm{SI},\pm2} = (\mp1.28,\ 0.43)$ and (D) $\mathbf{k}^b_{\pm2} = (\pm2.47,\ 0.22)$ as well as $\mathbf{k}^b_{\mathrm{SI},\pm2} = (\mp2.47,\ 0.43)$. The numbers specify values of the symmetrized transfer function $S^{\mathbf{k}}_{\mathbf{q},\mathbf{p}}$ with $\mathbf{k}$ given by the wave vector the respective arrow is pointing to/away from. The sign and direction of the arrow indicate, if energy is removed from (negative) or injected into (positive) the mode through the nonlinear interaction with the remaining two modes. (E): Detailed energy balance for a triplet of the unstable ITG mode $\mathbf{k}_{\mathrm{ITG}} = (0,\ 0.22)$ with a zonal mode $\mathbf{k}_Z = (\pm0.08, 0)$ and the sidebands $\mathbf{k}_S = (\mp0.08, -0.22)$.

self-interaction involving the central mode $\mathbf{k}_0 = (0,\ 0.22) \leftrightarrow \mathbf{q}$ [Eq. (8.28) and (8.29)] are indicated by black and gray arrows respectively.[1] Solid arrows depict first order ($n = 1$) self-interaction triplets, while dashed arrows correspond to second order ($n = 2$) self-interactions. Note that for visibility reasons only one of the two (sign-) combinations per triplet is depicted. The self-interaction triplets stand out due to the relatively small contributions of $S^{\mathbf{k}}_{\mathbf{q},\mathbf{p}}$ for modes $\mathbf{k}$ in the vicinity of such triplets. It is also evident that the self-interaction with first order twisted modes dominate over interactions with higher order (here second order) twisted modes.

In addition, a schematic summary of the detailed energy balance of the self-interaction triplets (summed over both signs) is depicted in Fig. 8.5. Energy is removed from the central ITG unstable mode $\mathbf{k}_0 = (0,\ 0.22)$ by all possible triplet interactions. Also from the respective twisted modes $\mathbf{k}^{a/b}_{\pm\mathrm{n}}$ energy is removed. The self-interaction mechanism, hence, directly adds to the nonlinear saturation of the extended mode. Since the nonlinear transfer is conservative, the matching modes, in turn, $\mathbf{k}^{a/b}_{\mathrm{SI},\pm n}$ gain energy. This finding is consistent with the drive of zonal structures through self-interaction [64, 1], which is represented by panels (A) and (B) in Fig. 8.5. It is emphasized that in the cases (A), (B) and (C) roughly two thirds of the energy gain is provided by the twisted mode.

[1] Here, the notation $'\mathbf{k}_0 \leftrightarrow \mathbf{q}'$ means that the mode $\mathbf{q}$ in the symmetrized transfer function is substituted by $\mathbf{k}_0$ and is applied analogously to $\mathbf{q}$ and $\mathbf{k}$.

Furthermore, the self-interaction drive of zonal structures [panels (A) and (B)] represents the dominant triplet interaction.

Self-interaction mediated nonlinear transfer of generalized energy

The nonlinear dynamics of a mode $\mathbf{k}$ is determined by the sum of all nonlinear triplet interactions satisfying the matching condition [112], as expressed through the net nonlinear transfer $N_{\mathbf{k}}$ [Eq. (8.6)]. Insight into the contribution of individual triplet interactions to the net nonlinear transfer with respect to the mode $\mathbf{k}$ is obtained by the graph of $S^{\mathbf{k}}_{\mathbf{q},\mathbf{p}}$ as function of $\mathbf{q}$ at fixed $\mathbf{k}$ [see Fig. 8.6 for $\mathbf{k} = (0,\ 0.22)$].
The contribution of the above discussed self-interaction triplets to the net nonlinear transfer is negligibly small (see black and gray arrows). Instead, dominant

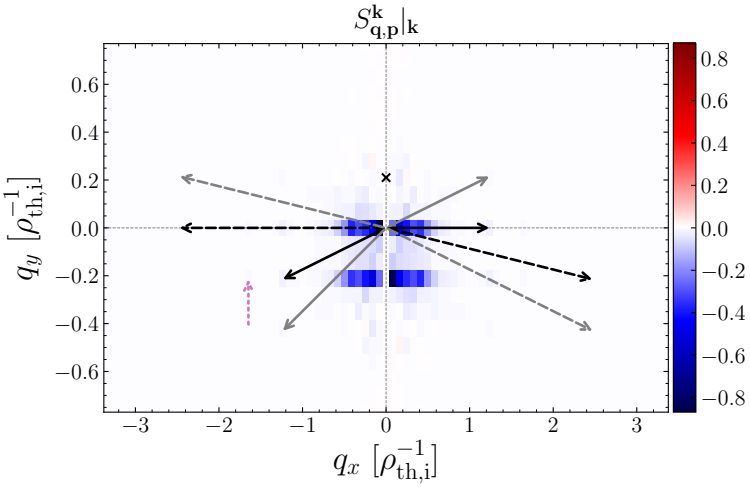

Figure 8.6: Symmetrized nonlinear transfer function $S^{\mathbf{k}}_{\mathbf{q},\mathbf{p}}|_{\mathbf{k}}$ with fixed $\mathbf{k} = (0,\ 0.22)$ (black $\times$-symbol) and as function of $\mathbf{q}$ and averaged over the stationary state for nominal parameters. Black and gray arrows depict the same self-interaction triplets as described in the caption of Fig. 8.4 with $\mathbf{k}_0 \leftrightarrow \mathbf{k}$. Analogously, the violet dotted arrow indicates the sideband mode $\mathbf{k}_S \leftrightarrow \mathbf{q}$ generated through the nonlinear interaction of the unstable ITG mode $\mathbf{k}_0 \leftrightarrow \mathbf{k}$ with the zonal mode $\mathbf{k}_Z \leftrightarrow \mathbf{p}$.

band structures at $q_y = 0$ and $q_y = -0.22$ and $|q_x| < 1.0$ occur, demonstrating a significant anisotropic nonlinear transfer of generalized energy. The connected triplets represent nonlinear interactions of the considered ITG mode with zonal flows, which are known to dominate the nonlinear saturation of ITG driven turbulence [22, 63, 66]. This process is characterized by the transfer of free energy to larger radial wave vector regions (at fixed k_y) through zonal flow shearing [22],

thereby allowing for the effective transfer to stable Eigenmodes [74, 63, 65].
The self-interaction mediated nonlinear transfer with respect to mode $\mathbf{k}$ can be formally defined by

$$N_{\mathbf{k}}^{\mathrm{SI}} = \sum_{\mathbf{q}\in\Omega_{\mathrm{SI}}} S^{\mathbf{k}}_{\mathbf{q},-\mathbf{k}-\mathbf{q}}, \tag{8.30}$$

where Ω_{SI} denotes the subset of modes (wave vectors) related to any valid self-interaction triplet. For example in the case of $\mathbf{k} \leftrightarrow \mathbf{k}_0$, $\mathbf{q}$ runs both over the twisted modes and the matching modes of the individual self-interaction triplets defined in Eq. (8.28) and Eq. (8.29). In the case of the maximum transport driving mode $\mathbf{k} = (0,\ 0.22)$ one finds $N_{\mathbf{k}}^{\mathrm{SI}}/N_{\mathbf{k}} = 0.81\ \%$. The direct contribution of the self-interaction to the nonlinear saturation of the maximum transport driving mode, hence, is negligible.
As discussed in Sec. 8.3.1 the central unstable ITG driven mode and its twisted modes represent the same extended mode. A proper evaluation of the role of self-interaction, hence, requires the inclusion of the twisted modes into the nonlinear transfer considerations. Fig. 8.7 and Fig. 8.8 depict $S^{\mathbf{k}}_{\mathbf{q},\mathbf{p}}$ as function of $\mathbf{q}$ at fixed first order $\mathbf{k} = (-1.24,\ -0.22)$ and second order $\mathbf{k} = (-2.47,\ -0.22)$ twisted mode, respectively, along with the self-interaction triplets (black solid and gray dashed arrows) involving the central unstable ITG mode $\mathbf{k}_0 = (0,\ \pm 0.22)$ only.
Clearly, self-interaction mediated nonlinear transfer constitutes a non-negligible

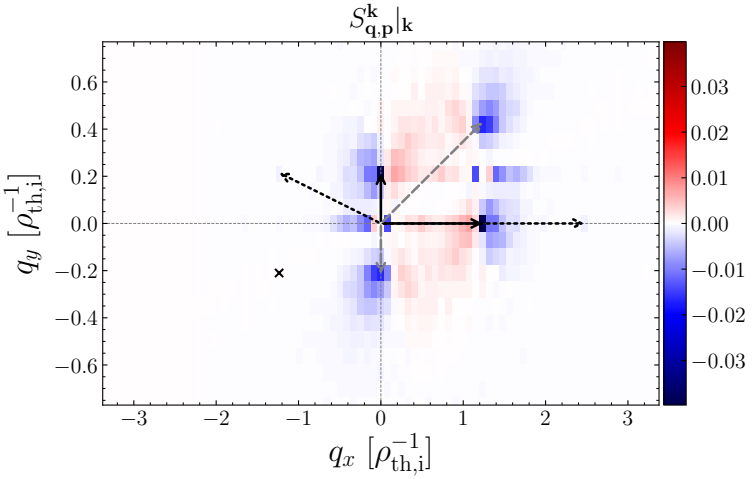

Figure 8.7: Symmetrized nonlinear transfer function $S^{\mathbf{k}}_{\mathbf{q},\mathbf{p}}|_{\mathbf{k}}$ with fixed $\mathbf{k} = (-1.24,\ -0.22)$ (black $\times$-symbol) and as function of $\mathbf{q}$ and averaged over the stationary state for nominal parameters. Black solid and gray dashed arrows depict the self-interaction triplets involving the central mode $\mathbf{k}_0 + \mathbf{k}^a_{+1} + \mathbf{k}^a_{\mathrm{SI},+1} = 0$ [$\mathbf{k}_0 = (0,\ 0.22)$, $\mathbf{k}^a_{+1} \leftrightarrow \mathbf{k}$] and $\mathbf{k}_0 + \mathbf{k}^b_{+1} + \mathbf{k}^b_{\mathrm{SI},+1} = 0$ [$\mathbf{k}_0 = (0,\ -0.22)$, $\mathbf{k}^b_{+1} \leftrightarrow \mathbf{k}$], respectively. Black dotted arrows indicate a triplet involving two twisted modes $\mathbf{k}^a_{+1} + \mathbf{k}^b_{-1} + \mathbf{k}^a_{\mathrm{SI},+2} = 0$, with $\mathbf{k}^a_{+1} \leftrightarrow \mathbf{k}$ and $\mathbf{k}^b_{-1},\ \mathbf{k}^a_{\mathrm{SI},+2} \leftrightarrow \mathbf{q},\ \mathbf{p}$.

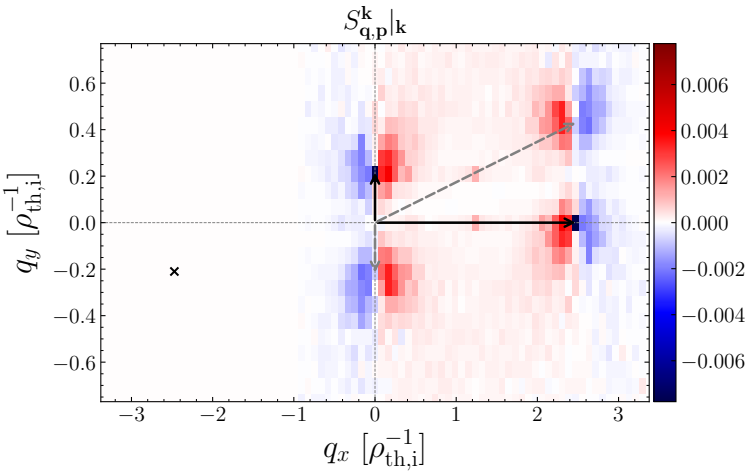

Figure 8.8: Symmetrized nonlinear transfer function $S^{\mathbf{k}}_{\mathbf{q},\mathbf{p}}|_{\mathbf{k}}$ with fixed $\mathbf{k} = (-2.47,\ -0.22)$ (black $\times$-symbol) and as function of $\mathbf{q}$ and averaged over the stationary state for nominal parameters. Black and gray arrows depict the self-interaction triplets $\mathbf{k}_0 + \mathbf{k}^a_{+2} + \mathbf{k}^a_{\mathrm{SI},+2} = 0$ $[\mathbf{k}_0 = (0,\ 0.22),\ \mathbf{k}^a_{+2} \leftrightarrow \mathbf{k}]$ and $\mathbf{k}_0 + \mathbf{k}^b_{+2} + \mathbf{k}^b_{\mathrm{SI},+2} = 0$ $[\mathbf{k}_0 = (0,\ -0.22),\ \mathbf{k}^b_{+2} \leftrightarrow \mathbf{k}]$, respectively.

contribution to the net nonlinear transfer of the twisted modes. Especially, the excitation of zonal modes through the self-interaction with the central mode (black solid arrows) exhibits a strong contribution. In the case of first order twisted mode (Fig. 8.7) the SI mediated nonlinear transfer $N^{\mathrm{SI}}_{\mathbf{k}}$ represents roughly 15 % of the net nonlinear transfer $N_{\mathbf{k}}$ (see Tab. 8.1). Note that in determining $N^{\mathrm{SI}}_{\mathbf{k}}$ all possible self-interaction triplets have been considered, i. e., not only the self-interaction of the considered twisted mode with the central mode $\pm\mathbf{k}_0$. The self-interaction of different order twisted modes within the same extended mode is included as well. The contribution of such triplets (see black dotted arrows in Fig. 8.7 for one exemplary triplet), however, is small.
The relevance of self-interaction for the nonlinear saturation of the global extended mode can be quantified by summing both $N_{\mathbf{k}}$ and $N^{\mathrm{SI}}_{\mathbf{k}}$ over all perpendicular modes within the extended mode structure, i. e., $\mathbf{k}$ running over the central mode and all order twisted modes (see penultimate row of Tab. 8.1). In this case self-interaction mediated nonlinear transfer constitutes approximately 2 % of the total net nonlinear transfer. Even when considering the entire extended mode, the influence of nonlinear self-interaction on the nonlinear saturation is found to be relatively small.

$(k_x,\ k_y)$	$N_{\mathbf{k}}$	$N_{\mathbf{k}}^{\mathrm{SI}}$	$\eta_{\mathbf{k}}^{\mathrm{SI}}$ [%]	$N_{\mathbf{k}}^{Z}$	$N_{\mathbf{k}}^{Z,\mathrm{SI}}$	$Q_{\mathbf{k}}$	$D_{\mathbf{k}}$	$T_{\mathbf{k}}$	$Q_{\mathrm{es},\mathbf{k}}$	n_{triplet}	$n_{\mathrm{triplet}}^{\mathrm{SI}}$
(0, 0.07)	+0.157	+0.051	32.69	−1.364	−0.018	3.820	−3.959	−0.014	1.110	42006	816
(0, 0.14)	−10.861	−0.174	1.60	−6.099	−0.117	13.895	−2.859	−0.012	4.026	21315	216
(0, 0.22)	−18.940	−0.388	2.05	−10.464	−0.227	21.142	−2.179	−0.389	6.137	12340	60
(0, 0.29)	−12.036	−0.194	1.62	−6.008	−0.159	13.726	−1.676	−0.040	3.963	10905	60
(0, 0.36)	−5.853	−0.057	0.97	−2.533	−0.091	6.765	−0.792	−0.109	1.964	7158	20
(0, 0.43)	−2.243	−0.031	1.38	−1.084	−0.050	2.930	−0.623	−0.060	0.842	6609	20
(0, 0.5)	−0.559	−0.001	0.21	−0.358	−0.027	1.180	−0.579	−0.056	0.339	6080	20
(0.08, 0.22)	−14.614	−0.302	2.07	−7.427	−0.172	16.442	−1.991	−0.148	4.757	12302	60
(0.16, 0.22)	−8.384	−0.159	1.89	−2.604	−0.129	10.009	−1.669	0.092	2.860	12264	64
(0.25, 0.22)	−3.484	−0.043	1.23	+0.587	−0.066	4.897	−1.358	−0.032	1.395	12226	64
(0.33, 0.22)	−0.752	−0.008	1.05	+1.808	−0.046	2.219	−1.441	−0.027	0.628	13782	84
(0.41, 0.22)	+0.158	+0.003	1.07	+2.360	−0.043	1.268	−1.365	−0.064	0.358	13782	84

Table 8.2: Total net nonlinear transfer $N_{\mathbf{k}}$, self-interaction mediated nonlinear transfer $N_{\mathbf{k}}^{\mathrm{SI}}$, the fraction $\eta_{\mathbf{k}}^{\mathrm{SI}} = N_{\mathbf{k}}^{\mathrm{SI}}/N_{\mathbf{k}}$, zonal flow mediated nonlinear transfer $N_{\mathbf{k}}^{Z}$, self-interaction driven zonal flow mediated transfer $N_{\mathbf{k}}^{Z,\mathrm{SI}}$, energy source $Q_{\mathbf{k}}$, energy dissipation $D_{\mathbf{k}}$, transfer to twisted modes $T_{\mathbf{k}}$ and electrostatic heat flux $Q_{\mathrm{es},\mathbf{k}}$ summed over the extended mode with central mode $\mathbf{k}_0$ specified by $(k_x,\ k_y)$. Also given is the total number of possible nonlinear triplet interactions n_{triplet} the extended mode can participate in and the contained subset of self-interaction triplets $n_{\mathrm{triplet}}^{\mathrm{SI}}$.

The analysis presented above concentrates on the extended mode with the maximum transport driving mode $\mathbf{k} = (0,\ 0.22)$ being the central mode exclusively. In order to generalize the above finding a comparison of the total net nonlinear transfer and the self-interaction mediated transfer, summed over the entire extended mode, is repeated for two subset of central modes (see Tab. 8.2): (i) The binormal wave vector k_y is varied at fixed radial wave vector $k_x = 0$. (ii) The radial wave vector k_x is varied at fixed binormal wave vector $k_y = 0.22$. These subsets cover the region in the perpendicular wave vector space that contributes most to the turbulent heat flux (see tenth column of Tab. 8.2). In general, the magnitude of the net nonlinear transfer $N_{\mathbf{k}}$ is largest for the maximum transport driving mode and decreases with both de- and increasing binormal wave vector k_y and with increasing radial wave vector k_x. This behavior follows closely, and thereby balances, the spectral dependency of the positive energy source $Q_{\mathbf{k}}$. As two exceptions, the modes $\mathbf{k} = (0,\ 0.07)$ and $\mathbf{k} = (0.41,\ 0.22)$ exhibit a positive nonlinear transfer that balances the negative dissipation dominated sum $Q_{\mathbf{k}} + D_{\mathbf{k}} + T_{\mathbf{k}}$. In most of the cases, i. e., excluding the two exceptions above, the self-interaction mediated nonlinear transfer $N^{\mathrm{SI}}_{\mathbf{k}}$ is negative and, hence, contributes to the nonlinear saturation of the respective extended mode. In agreement with the analysis above $N^{\mathrm{SI}}_{\mathbf{k}}/N_{\mathbf{k}} \approx 1 \sim 2$ % mostly, confirming that the influence of self-interaction, indeed, is relatively small for a larger class of extended modes.

The mode with the smallest binormal wave vector $\mathbf{k} = (0,\ 0.07)$ represents an exception, since the self-interaction mechanism appears to be strong ($N^{\mathrm{SI}}_{\mathbf{k}}/N_{\mathbf{k}} \approx 33$ %) and, therefore, deserves further discussion. For this purpose individual quantities summarized in Tab. 8.2 are broken down into the contributions of individual modes within the extended mode (see Fig. 8.9). The small positive net nonlinear transfer $N_{\mathbf{k}}$ given in Tab. 8.2 result from the balance of a strong negative nonlinear transfer out of the central mode as well as the first order twisted modes ($|n| \leq 1$) and a strong cumulative positive nonlinear excitation of higher order twisted modes ($|n| \geq 2$). Furthermore, the self-interaction mediated nonlinear transfer $N^{\mathrm{SI}}_{\mathbf{k}}$ is negligible except for $|n| \leq 1$. In these cases, the first order self-interaction triplets which involve a zonal mode [Eq. (8.28) with $n = 1$] constitute a nonlinear transfer of $+0.066$ ($N^{\mathrm{SI}}_{\mathbf{k}=(-0.41,\ -0.07)} = 0.054$; $n = +1$), -0.143 ($N^{\mathrm{SI}}_{\mathbf{k}=(0,\ 0.07)} = -0.184$; $n = 0$) and $+0.099$ ($N^{\mathrm{SI}}_{\mathbf{k}=(+0.41,\ -0.07)} = 0.071$; $n = -1$). As given in parentheses, the SI-mediated transfer summed over all possible self-interaction triads is comparable to the transfer connected to the first order SI-triplet involving zonal modes only. Hence, $N^{\mathrm{SI}}_{\mathbf{k}}$ shown in the top panel of Fig. 8.9 is dominated by this coupling process. This is also confirmed by the graph of $S^{\mathbf{k}}_{\mathbf{q},\mathbf{p}}$ at fixed $\mathbf{k} = (-0.41,\ -0.07)$ (see Fig. 8.10). The SI-triplet involving a zonal mode (black arrows) clearly dominates.

Having $k_x = \pm 0.41$, the first order twisted modes $n = \pm 1$ lie within a radial wave vector range where zonal flow shearing has a large influence on the

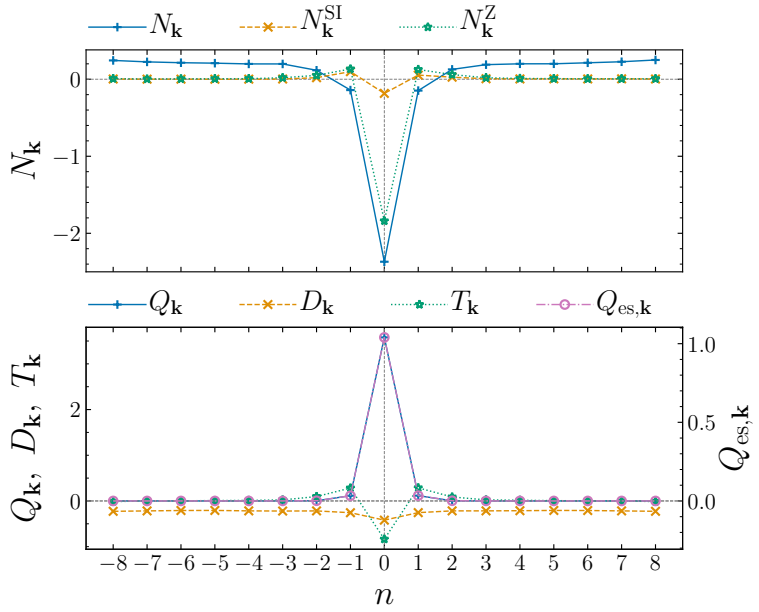

Figure 8.9: Several energetics terms (see caption of Tab. 8.2 for more details) as function of the order n of individual perpendicular modes of the same extended mode. The central mode ($n = 0$) is $\mathbf{k}_0 = (0,\ 0.07)$.

nonlinear transfer of energy (see discussion in Sec. 8.3.3). In addition, as shown in Figs. 8.5, 8.7 and 8.8, self-interaction usually removes energy from the twisted modes, while here the first order twisted modes are clearly driven as demonstrated by the postivie $N^{\mathrm{SI}}_{\mathbf{k}}$ for $n = \pm 1$ in the top panel of Fig. 8.9. Hence, the negative SI mediated transfer out of the central mode ($n = 0$) and the positive SI mediated transfer into the first order twisted modes ($n = \pm 1$) is interpreted as a zonal flow shearing process. Within a shearing process most of the energy is typically transferred from the central mode to the twisted modes [22, 66], also referred to as sidebands. As a result, the nonlinear transfer balances when summing over $n = -1,\ 0,\ +1$. The large fraction $N^{\mathrm{SI}}_{\mathbf{k}}/N_{\mathbf{k}} \approx 33\ \%$ is, therefore, flawed in the case of $\mathbf{k} = (0,\ 0.07)$ and instead the self-interaction is found not to play a significant role.

At least three arguments can be invoked to explain the general outcome of this section that self-interaction plays only a minor role in the considered ITG driven turbulence: (i) Self-interaction triplets represent only a small (discrete) subset of possible triad interactions. For example, the extended mode with central mode $\mathbf{k}_0 = (0,\ 0.22)$ is susceptible to a total number of 12340 nonlinear triplet interactions representable by the numerical grid. Only 60 of which are related to self-interaction. This pertains to a larger class of extended modes as summarized in the last two columns of Tab. 8.2. (ii) Based on amplitude arguments only a

small fraction of self-interaction triplets exhibit a significant contribution to the net nonlinear transfer; —that are self-interactions involving the central mode and lower order twisted modes. Self-interaction processes involving the central mode and higher order twisted modes (see Fig. 8.4 and discussion) or twisted modes only (see Fig. 8.7 and discussion), in turn, are in general relatively weak. This is interpreted to result from the small amplitudes of twisted modes compared to the central mode (see last row of Tab. 8.1). (iii) Free energy transfer mediated by zonal flows is the preferred transfer channel in ITG driven turbulence (see Fig. 8.4 and Sec. 8.3.3). Nonlinear transfer due to interactions with (mesoscale) ZFs typically dominates over the transfer related to self-interaction.

8.3.3 Role of self-interaction driven zonal structures for the nonlinear transfer of generalized energy

One consequence of the self-interaction mechanism is the generation of zonal structures [64, 1] (see also Sec. 8.3.2). Being manifest as fine scale structures in the radial electric field shear [83, 1, 84], such zonal structures may contribute to the zonal flow mediated saturation of ITG driven turbulence [22, 63, 65, 66]. This section aims for a clarification of the role of self-interaction driven zonal structures for the nonlinear transfer of generalized energy.
The zonal flow enters the gyrokinetic equation (and the energy balance) through the $E \times B$-nonlinearity in form of the $E \times B$-drift

$$\mathbf{v}_{\mathrm{ZF}} = \frac{\nabla x \times \mathbf{b}}{B} \frac{\partial \langle\langle \phi \rangle\rangle_{\mathrm{ga,sp}}}{\partial x} \tag{8.31}$$

connected to the zonal part of the radial electric field $\langle E_x \rangle = -\partial_x \langle \phi \rangle$. In Sec. 8.3.3 the role of self-interaction for the generation of structures in the zonal part of the radial electric field is discussed through the application of the zonal electric field intensity diagnostic (see Sec. 8.2.3). Then, the zonal flow mediated nonlinear transfer of generalized energy is discussed in Sec. 8.3.3.

Self-interaction drive of zonal structures in the radial electric field

In this section the radial electric field intensity diagnostic (see Sec. 8.2.3) is utilized to study the generation of zonal structures in the radial electric field. The SI mechanism acts through the nonlinearity which is composed of the electrostatic Reynolds stress transfer $\mathcal{R}$ ($E \times B$ nonlinearity) and the electromagnetic Maxwell stress transfer $\mathcal{M}$ (magnetic flutter nonlinearity). The latter arises due to perturbations in the parallel vector potential $A_\parallel$ being present at finite values of the normalized plasma pressure and can be neglected for the small plasma β chosen in this chapter.
Clear signatures of the self-interaction drive can be identified in the spectrum

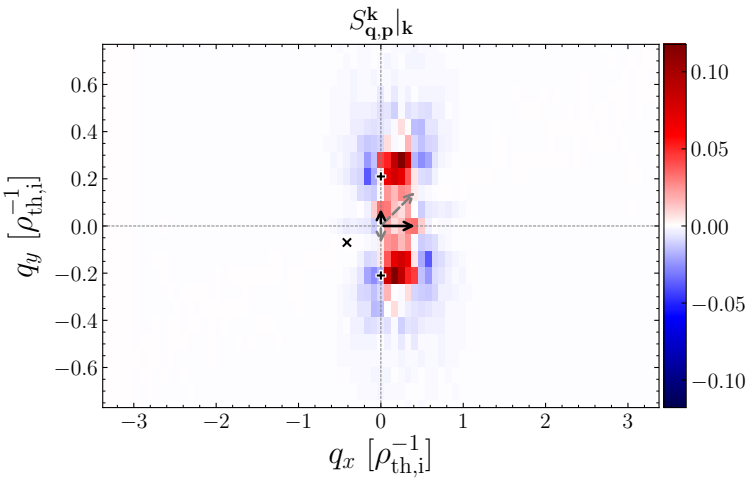

Figure 8.10: Symmetrized nonlinear transfer function $S^{\mathbf{k}}_{\mathbf{q},\mathbf{p}}|_{\mathbf{k}}$ with fixed $\mathbf{k} = (-0.41,\ -0.07)$ (black $\times$-symbol) as function of $\mathbf{q}$ and averaged over the stationary state for nominal parameters. Black and gray arrows depict first order self-interaction triplets with the central mode $\mathbf{k}_0 = (0,\ \pm 0.07)$.

$\mathcal{R}(k_{\mathrm{ZF}}, k'_y)$ (see Fig. 8.11): Discrete positive peaks occur at wave vector combinations that are susceptible to self-interaction (black symbols highlight mode combinations involving different order connections), as they satisfy the matching condition

$$k^{\mathrm{si}}_{\mathrm{ZF}} = n \cdot \Delta k_x(k'^{,\mathrm{match}}_y). \tag{8.32}$$

The above expression in combination with Eq. (8.25) defines the SI-driven zonal modes $k^{\mathrm{si}}_{\mathrm{ZF}}$ and the corresponding matching modes k^{match}_y.

For certain $k^{\mathrm{si}}_{\mathrm{ZF}}$ the Reynolds stress resulting from the self-interaction with higher order connections ($n \geq 2$) can dominate the drive. Consider, for example, the zonal mode with wave vector $k^{\mathrm{si}}_{\mathrm{ZF}} = 2.47$ (fourth vertical stripe viewed from left in Fig. 8.11). It is driven by the self-interaction of $k'_y = 0.07$ with its $6th$-order connection (diamond), $k'_y = 0.14$ with its $3th$-order connection (circle), $k'_y = 0.22$ with its second order connection ($\times$ symbol) and $k'_y = 0.43$ with its first order connection (+ symbol). The Reynolds stress connected to the penultimate self-interaction process (second order, $\times$ symbol) exceeds the stress due to the last self-interaction (first order, + symbol).

The cumulative effect of self-interactions of different order may explain the composition of the spectrum of the $E \times B$ shearing rate

$$|\langle\hat{\omega}_{\mathrm{ExB}}\rangle_{k_{\mathrm{ZF}}}| = \frac{2k^2_{\mathrm{ZF}}}{B_0}|\langle\hat{\phi}_{\mathbf{k}}\rangle(k_{\mathrm{ZF}})|, \tag{8.33}$$

shown in Fig. 8.12. The shear carried by the zonal modes with $k^{\mathrm{si}}_{\mathrm{ZF}} = 1.65$ and $k^{\mathrm{si}}_{\mathrm{ZF}} = 2.47$, which are subject to multiple self-interactions of different order, is relatively stronger than the shear in the adjacent modes $k^{\mathrm{si}}_{\mathrm{ZF}} = 1.24$ and $k^{\mathrm{si}}_{\mathrm{ZF}} = 2.24$.

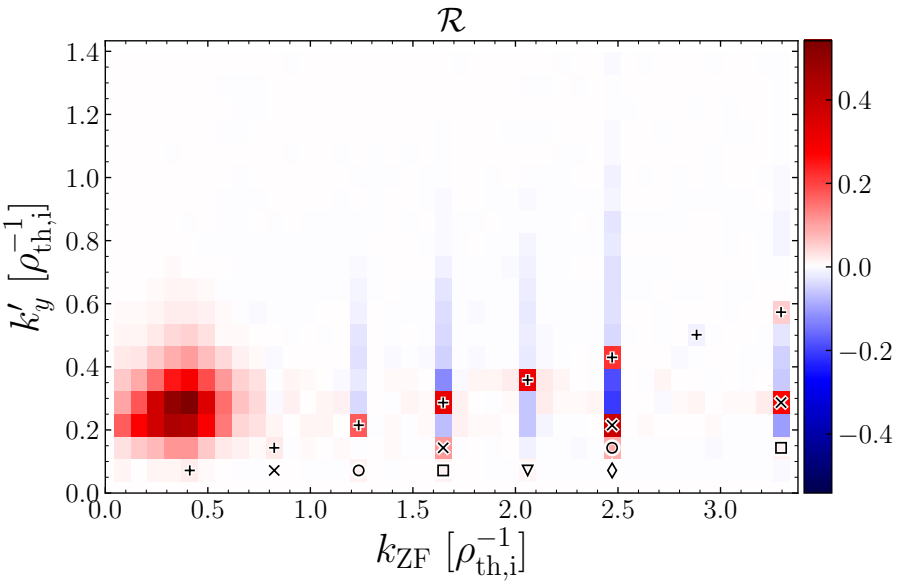

Figure 8.11: Reynolds stress $\mathcal{R}$ as function of k_{ZF} and k_y' temporally averaged over the stationary state and for nominal parameters. Black symbols highlight mode combinations that are susceptible to self-interaction involving first- (+), second- (×), third- (circles), fourth- (squares), fifth- (triangles) and sixth- (diamonds) order connections.

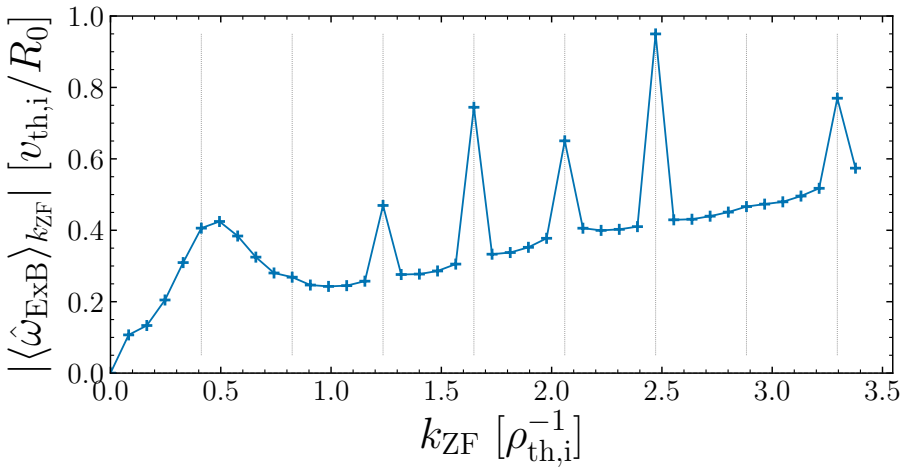

Figure 8.12: Time averaged $E \times B$ shearing rate $|\langle\hat{\omega}_{\mathrm{ExB}}\rangle_{k_{\mathrm{ZF}}}|$ as function of the zonal flow wave vector k_{ZF}. Vertical dotted lines depict self-interaction driven zonal modes $k_{\mathrm{ZF}}^{\mathrm{si}}$.

While the drive through SI dominates the radial electric field excitation at relatively small scales, the spectral contributions to the Reynolds stress that are not susceptible to self-interaction, i. e., $k_{\mathrm{ZF}} \neq n \cdot \Delta k_x(k_y')$, peaks in the interval $0 < k_{\mathrm{ZF}} \lesssim 0.75$ and $0 < k_y \lesssim 0.75$ (see Fig. 8.11). Furthermore, in contrast to the SI mediated Reynolds stress having a discrete spectrum, the Reynolds stress that is not related to SI exhibits a continuous spectrum. Both observations highlight the difference of the underlying physical mechanisms, which will be further elaborated on below through an energetics consideration.
Note that the nonlinear energy transfer within triplets involving zonal modes differ between SI and non-SI driven zonal modes as shown in Fig. 8.4 and panels (A) and (E) of Fig. 8.5. For example, in the case of the box scale zonal mode $\mathbf{k}_Z = (-0.08,\ 0)$ the sideband $\mathbf{k}_S = (0.08,\ -0.22)$, necessary to couple the zonal mode to the maximum transport driving mode $\mathbf{k}_{\mathrm{ITG}} = (0,\ 0.22)$ through $\mathbf{k}_{\mathrm{ITG}} + \mathbf{k}_Z + \mathbf{k}_S = 0$, is nonlinearly excited by the interaction of $\mathbf{k}_{\mathrm{ITG}}$ and $\mathbf{k}_Z$, i. e., $S^{\mathbf{k}_S}_{\mathbf{k}_Z,\mathbf{k}_{\mathrm{ITG}}} > 0$. Physically, the nonlinear generation of the sideband mode reflects the shearing of the turbulent mode by the zonal flow [72, 73] and is at the basis of the modulational instability [33, 34, 35, 46, 36, 37, 40].
In the case of the SI-driven zonal mode $\mathbf{k}_Z = (-1.24,\ 0)$ the twisted mode $\mathbf{k}_T = (-1.24,\ -0.22)$ plays the role of the sideband mode in the nonlinear coupling process $\mathbf{k}_{\mathrm{ITG}} + \mathbf{k}_Z + \mathbf{k}_T = 0$. However, energy is removed nonlinearly from the twisted mode, i. e., $S^{\mathbf{k}_T}_{\mathbf{k}_Z,\mathbf{k}_{\mathrm{ITG}}} < 0$, within this triple. A nonlinear generation of the sideband, i. e., the zonal flow shearing process, does, therefore, not occur. The difference between the zonal mode generation through SI and non-SI, hence, is based on a difference in the sideband generation: In the case of SI, sidebands result from the twisted mode generation through parallel streaming, while in the case of non-SI it is a consequence of the shearing of turbulent modes by the zonal flow.
To proceed, the net Reynolds stress $\mathcal{R}_{\mathrm{tot}}(k_{\mathrm{ZF}}) = \sum_{k_y'} \mathcal{R}(k_{\mathrm{ZF}}, k_y')$ with respect to the zonal mode k_{ZF} is split into contributions from modes contributing to the SI $\mathcal{R}_{\mathrm{SI}}(k^{\mathrm{si}}_{\mathrm{ZF}}) = \sum_{k_y',\mathrm{match}} \mathcal{R}(k^{\mathrm{si}}_{\mathrm{ZF}},\ k_y'^{,\mathrm{match}})$ and the residual $\mathcal{R}_{\mathrm{res}} = \mathcal{R}_{\mathrm{tot}} - \mathcal{R}_{\mathrm{SI}}$. Note that at fixed $k^{\mathrm{si}}_{\mathrm{ZF}}$ multiple matching modes are possible due to the self-interaction with higher order connections as discussed above. The decomposition of $\mathcal{R}$ allows for the evaluation of the relative importance of the SI for the drive of zonal structures in the radial electric field.
SI is found to dominate the electric field generation for $k_{\mathrm{ZF}} \geq 0.82$ (see Fig. 8.13). Although the zonal mode with $k_{\mathrm{ZF}} = 0.41$ is susceptible to SI, the Reynolds stress not related to SI significantly exceeds the SI drive. Hence, SI plays only a negligible role for the generation of zonal modes with $k_{\mathrm{ZF}} < 0.82$ for the nominal parameters. This finding may be interpreted as follows:
(i) The zonal mode $k_{\mathrm{ZF}} = 0.41$ is subject to one self-interaction only, namely the interaction of $\mathbf{k} = (0,\ 0.07)$ with its first order twisted mode (see Fig. 8.11). Hence, it does not benefit from multiple self-interactions of higher order connec-

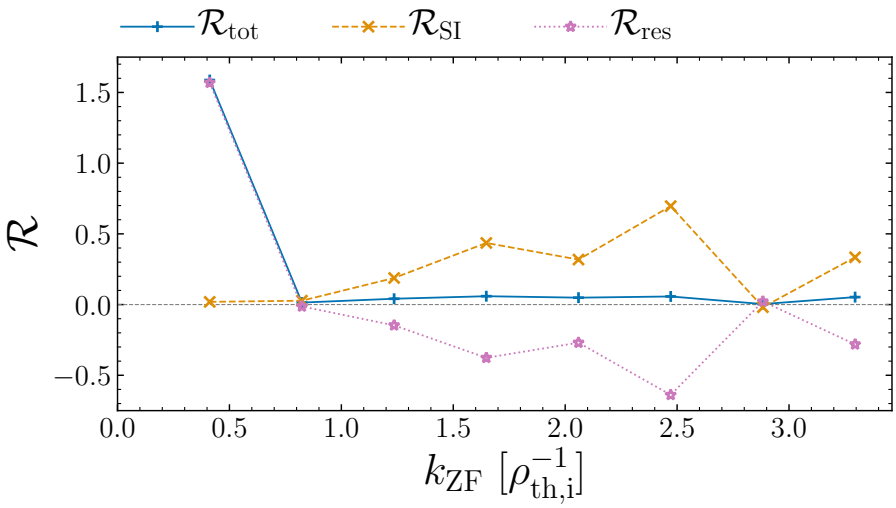

Figure 8.13: Total (k_y' summed) Reynolds stress $\mathcal{R}_{\mathrm{tot}}$ (blue +-symbols), Reynolds stress due to self-interaction $\mathcal{R}_{\mathrm{SI}}$ (orange ×-symbols) as well as the residual $\mathcal{R}_{\mathrm{res}}$ (violet stars) as function of k_{ZF} temporally averaged over the stationary state and for nominal parameters.

tions.
(ii) Motivated by its definition [Eq. (8.24)], the Reynolds stress transfer may be roughly approximated (neglecting gyro-average effects) by $\mathcal{R} \sim k_{\mathrm{ZF}} k_y' \hat{\phi}_{\mathbf{k}_S} \hat{\phi}^*_{\mathbf{k}_0} \sim k_{\mathrm{ZF}} k_y' C |\hat{\phi}_{\mathbf{k}_0}|^2$, where $\hat{\phi}_{\mathbf{k}_S}$ is the potential perturbation of the sideband $\mathbf{k}_S = (k_{\mathrm{ZF}}, k_y')$, $\hat{\phi}_{\mathbf{k}_0}$ denotes the potential perturbation of the central mode $\mathbf{k}_0 = (0,\ k_y')$ and C is a coefficient describing the correlation between the central mode and the twisted mode. Note that the expression after the second $' \sim\ '$ symbol relates to the self-interaction, since $\hat{\phi}_{\mathbf{k}_S}$ is taken to be a twisted mode of the central mode $\hat{\phi}_{\mathbf{k}_0}$. The small self-interaction drive at $k_{\mathrm{ZF}} = 0.41$ may then relate to the dependence of $\mathcal{R}$ on k_y' and k_{ZF}, both being minimal. In addition, the spectrum of $\int \mathrm{d}s \sum_{k_x} |\hat{\phi}_{\mathbf{k}}(k_x, k_y', s)|^2$ peaks at $k_y' = 0.22$ (not shown) and is found to decay for smaller k_y'. In summary, the generation of zonal structures by self-interaction, hence, can be assumed to be small in case of the smallest k_y'.

Zonal flow mediated nonlinear transfer of generalized energy

This section investigates the zonal flow mediated nonlinear transfer of generalized energy. It aims to clarify whether SI-driven zonal structures contribute to the zonal flow mediated transfer and, thereby, add to the nonlinear saturation of ITG driven turbulence.
The nonlinear interaction of a mode $\mathbf{k} = (k_x,\ k_y)$ with a zonal mode $\mathbf{k}_Z = (k_{\mathrm{ZF}},\ 0)$ involves the coupling to a sideband $\mathbf{k}_S = (-k_x - k_{\mathrm{ZF}},\ -k_y)$ consistent with the

wave vector matching rule $\mathbf{k} + \mathbf{k}_Z + \mathbf{k}_S = 0$. The net nonlinear transfer with respect to the mode $\mathbf{k}$ due to the coupling to a zonal mode then reads [see Eq. (8.6)]

$$N_{\mathbf{k}}^{\mathbf{k}_Z} = S_{\mathbf{k}_Z,\mathbf{k}_S}^{\mathbf{k}} + S_{\mathbf{k}_S,\mathbf{k}_Z}^{\mathbf{k}}. \tag{8.34}$$

In the case of the maximum transport driving mode $\mathbf{k} = (0, 0.22)$ the first term on the right-hand side of the expression above represents the horizontal band with $q_y = 0$ in Fig. 8.6, while the second term corresponds to the band with $q_y = -0.22$.

Consistent with previous studies [22, 65, 66] nonlinear couplings with the zonal mode predominantly extract energy from the maximum transport driving mode (see Fig. 8.14). Here, the net nonlinear transfer due to zonal couplings

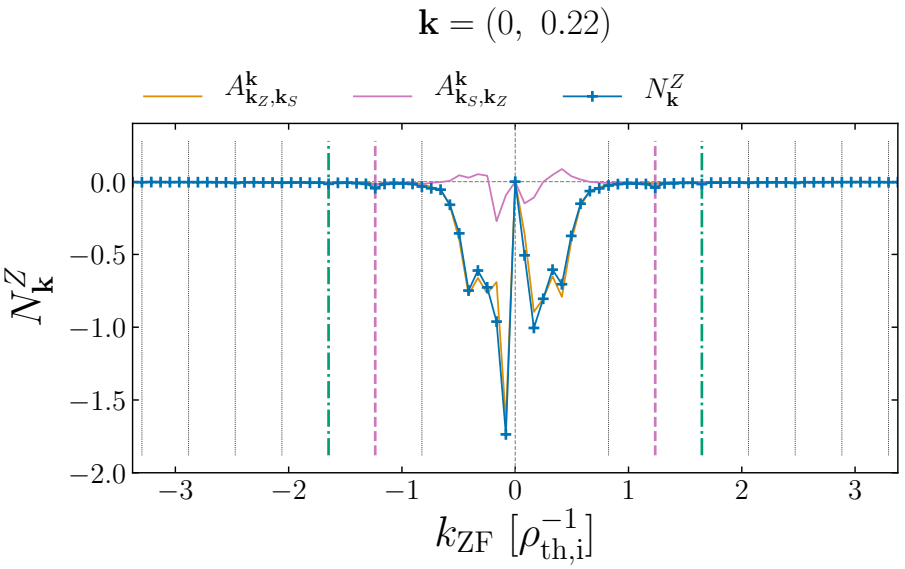

Figure 8.14: Zonal mode mediated nonlinear transfer $N_{\mathbf{k}}^{\mathrm{Z}}$ [Eq. (8.34)] with respect to the maximum transport driving mode $\mathbf{k} = (0,\ 0.22)$ due to the coupling with a zonal mode $\mathbf{k}_Z = (k_{\mathrm{ZF}},\ 0)$ temporally averaged over the stationary state for nominal parameters. Also shown is the decomposition into zonal flow mediated $A^{\mathbf{k}}_{\mathbf{k}_Z,\mathbf{k}_S}$ (orange solid) and sideband flow mediated $A^{\mathbf{k}}_{\mathbf{k}_S,\mathbf{k}_Z}$ (violet solid) transfer defined by Eq. (8.36). Vertical black dotted lines indicate zonal modes that are driven by SI, the violet dashed lines depict zonal modes that are driven by the first order self-interaction of $\mathbf{k}$ and the green dashed dotted lines specify SI driven zonal modes that are not susceptible to the self-interaction of $\mathbf{k}$.

$$N_{\mathbf{k}}^{Z} = \sum_{k_{\mathrm{ZF}}} N_{\mathbf{k}}^{\mathbf{k}_Z} \tag{8.35}$$

represents 60 % of the total nonlinear transfer $N_{\mathbf{k}}$ and, hence, contributes significantly to the saturation of the considered ITG driven turbulence [22, 63, 65].

90 % of the zonal mode mediated transfer occurs within a radial wave vector range $k_{\mathrm{ZF}} \in [-0.58,\ 0.58]$. This region corresponds to intermediate to mesoscale zonal modes. As discussed in Sec. 8.3.3, the SI drive of zonal structures is negligible in this wave vector regime.
Strictly speaking zonal flow mediated transfer constitutes only a part of $N_{\mathbf{k}}^{\mathbf{k}_Z}$ defined in Eq. (8.35). Expressing $N_{\mathbf{k}}^{\mathbf{k}_Z}$ through the primitive nonlinear transfer function [Eq. (8.9)]

$$N_{\mathbf{k}}^{\mathbf{k}_Z} = A_{\mathbf{k}_Z,\mathbf{k}_S}^{\mathbf{k}} + A_{\mathbf{k}_S,\mathbf{k}_Z}^{\mathbf{k}}, \tag{8.36}$$

allows for the splitting into zonal flow mediated transfer $A_{\mathbf{k}_Z,\mathbf{k}_S}^{\mathbf{k}}$ and sideband flow mediated transfer $A_{\mathbf{k}_S,\mathbf{k}_Z}^{\mathbf{k}}$. In the former case the zonal part of the modified potential $\hat{\chi}_{\mathrm{sp},\mathbf{k}_Z}$ determines the advecting $E\times B$-drift, while in the latter case it is the sideband mode $\hat{\chi}_{\mathrm{sp},\mathbf{k}_S}$. Fig. 8.14 shows that the zonal flow mediated transfer (orange) causes most of the zonal mode mediated transfer (blue, +-symbols), justifying the terminology *zonal flow mediated* transfer here.
To proceed, the nonlinear transfer mediated by zonal modes that are dominantly driven by SI (vertical black dotted lines, violet dashed lines and green dashed dotted lines in Fig. 8.14)

$$N_{\mathbf{k}}^{Z,\mathrm{SI}} = \sum_{|k_{\mathrm{ZF}}^{\mathrm{si}}|\geq 0.82} N_{\mathbf{k}}^{\mathbf{k}_Z} \tag{8.37}$$

contributes only 2 % to the total transfer due to zonal couplings $N_{\mathbf{k}}^{Z}$. The maximum contribution within this subset is provided by the zonal mode $\mathbf{k}_Z = (\pm 1.24,\ 0)$ and relates to the drive of this zonal mode due to the self-interaction with the considered maximum transport driving mode $\mathbf{k} = (0,\ 0.22)$. As discussed in Sec. 8.3.3 the underlying nonlinear transfer mechanism does not reflect a zonal flow shearing process. Hence, in this case the nonlinear transfer cannot be interpreted as being zonal flow mediated.
Now, the SI driven zonal mode with $\mathbf{k}_Z = (\pm 1.67,\ 0)$ is considered more in detail (green dashed dotted line in Fig. 8.14). It is driven through the self-interaction of modes with $k_y \in [0.07,\ 0.14,\ 0.29]$ (see Fig. 8.11), explicitly excluding $k_y = 0.22$. Since this SI driven zonal mode exhibits a significant contribution to the $E\times B$ shearing rate (see Fig. 8.12), this specific example allows to study the zonal flow mediated nonlinear transfer with respect to the fixed mode $\mathbf{k} = (0,\ 0.22)$, while making sure that the nonlinear transfer is not biased by any self-interaction process (as encountered in the previous paragraph). In this case the generation of sidebands $\mathbf{k}_S = (\mp 1.67,\ -0.22)$ through zonal flow shearing $S_{\mathbf{k}_{\mathrm{ITG}},\mathbf{k}_Z}^{\mathbf{k}_S} > 0$ occurs to some extent (see violet dotted arrow in Fig. 8.4). Its contribution to the total zonal flow mediated nonlinear transfer $N_{\mathbf{k}}^{Z}$, however, is negligible (see green dashed dotted lines in Fig. 8.14).
Tab. 8.2 summarizes $N_{\mathbf{k}}^{Z}$ [Eq. 8.35] and $N_{\mathbf{k}}^{Z,\mathrm{SI}}$ [Eq. (8.37)] for the two subsets of extended modes, already discussed in Sec. 8.3.2. The SI-driven zonal mode related nonlinear transfer is always negative and, therefore, adds to the nonlinear saturation of the extended modes. In most of the cases $|N_{\mathbf{k}}^{Z,\mathrm{SI}}|$ is small compared

to the zonal flow mediated transfer $|N_{\mathbf{k}}^{Z}|$, generalizing the above finding to a larger class of modes.
The analysis presented in this section demonstrates that the role of self-interaction driven zonal structures for the zonal flow mediated transfer of generalized energy is negligible. This finding supports our recent result that SI driven zonal fine scale structures do hardly contribute to the zonal flow mediated deformation of turbulent structures [118] and question their importance for the nonlinear saturation physics of ITG driven turbulence.

8.4 Conclusion

This chapter investigates the self-interaction mechanism in gyrokinetic ion temperature gradient driven turbulence by means of an energetics and nonlinear transfer analysis. As an exemplary case CYCLONE base case (CBC) parameters [67] are chosen; —parameters for which clear signatures of self-interaction have been reported of in Refs. [1, 85, 118].
First, the self-interaction mechanism, that is, the nonlinear interaction of an elongated (parallel to the magnetic field) mode with itself [104, 64, 1, 85], is found to have only a small direct influence, of the order of a few percent, on the nonlinear saturation processes. Here, the term *direct* refers to the contribution of the nonlinear self-interaction of a mode to the total net nonlinear transfer of generalized energy out of / into the mode. Although individual self-interaction processes exhibit finite or even dominant contributions to the net nonlinear transfer of free energy out of / into individual perpendicular modes, the small number of self-interaction triplets compared to the total number of possible nonlinear triplet interactions of an extended mode renders self-interaction processes insignificant. The direct influence of self-interaction, however, may increase for magnetic geometries with smaller magnetic shear, since the reduced twist of modes then results in an increase of the relative number of self-interaction triplets.
Second, the contribution of self-interaction driven zonal structures, commonly observed in form of dominant radial fine scale structures in the zonal part of the radial electric field shear [83, 1, 84, 85, 86], to the zonal flow mediated nonlinear transfer of generalized energy is small (of the order of a few percent). Here, *fine scale* refers to wave lengths comparable to the ion thermal Larmor radius. This finding corroborates our recent director field analysis [118], which demonstrates that the self-interaction driven radial fine scale features do hardly contribute to the zonal flow shear induced deformation of turbulent eddies. Although zonal flow mediated transfer is a preferred saturation process in ITG driven turbulence [74, 22, 65], also in the present study, most of the transfer is caused by mesoscale zonal flows, i. e., zonal flows with wave lengths significantly larger than the ion

thermal Larmor radius. The self-interaction drive is shown to be negligible in the case of mesoscale flows.
The overall outcome of this chapter suggests that the self-interaction mechanism hardly influences the turbulence (-zonal flow) dynamics in ITG driven turbulence with CBC parameters. Since the self-interaction mechanism can be assumed to scale with the turbulence level [1] and since zonal flow dynamics typically dominates close to marginal stability [67, 25, 118], the findings of this chapter are expected to apply also to experimentally more relevant cases close to marginality. Indeed, our recent director field study [118] mainly investigated cases close to marginality. Whether the self-interaction mechanism plays some role in parameter regimes with increased mode extent along the field line (e. g., electromagnetic ITG turbulence [149]) is unclear and needs further studies.
The results presented in this chapter suggest that self-interaction is not responsible for the variation of several ten percent in the turbulent fluxes when eliminating correlations over the parallel boundary as found in Ref. [85] for the same strong turbulence CBC parameter setup investigated in the present chapter. Other mechanisms have to be active which allow for correlations to influence the turbulence dynamics in this case. In strong turbulence correlations may propagate nonlinearily, for example; —a hypothesis that is left for future work.

Chapter 9

Stability analysis of toroidally symmetric secondary modified staircase equilibria

9.1 Introduction

As demonstrated in chapters 6 and 7, close to marginality microturbulence typically self-organizes through the generation of quasi-stationary secondary zonal flow patterns [23, 24, 25]. Here, the term *secondary* refers to perturbations that are generated nonlinearly by the turbulence, with the latter being driven by primary instabilities such as the ITG driven instability. These zonal structures (zonal flow but also zonal perturbations in the density or temperature), in turn, may modify the primary instabilities driven by the background density and temperature gradients, or may even drive instabilities. The idea of this dynamical hierarchy is embodied in the tertiary instability formalism [54] and instabilities being driven by secondary zonal structures are referred to as *tertiary instabilities*.[1] In the aforementioned reference tertiary instabilities are considered to determine the nonlinear critical temperature gradient for turbulence generation.
This chapter investigates (tertiary) instabilities in the presence of modified staircase patterns; —structures that develop close to marginality with inclusion of electron dynamics (see chapter 6). The presented study represents a modification of previous (adiabatic electron) studies [54, 127], in that, (i) it considers electron dynamics and (ii) it considers zonal patterns, featuring structures that

[1]Note that although tertiary instabilities are driven by secondary structures such as zonal flows, the background temperature and density gradients may add to the tertiary instability drive. For example, the tertiary instabilities discussed in Ref. [54] explicitly require a finite temperature gradient beside the zonal flow. Consequently the growth rate of the tertiary instabilities found in the aforementioned reference increase with increasing background temperature gradient.

are directly related to electron dynamics. The following questions will be addressed:

- How do instabilities in the presence of secondary modified staircase states compare to primary instabilities?
- What is the role of patterns with disparate spatial scales connected to a modified staircase state [i. e., (i) the basic zonal flow mode on the scale of the radial box size, (ii) the corrugations close to LORLs and (iii) the fine scale features driven by self-interaction]?
- What is the influence of the electron drive, i. e., the perturbations in the electron distribution function f_{e} and the inverse electron background temperature gradient length $R_0/L_{T,\mathrm{e}}$, on tertiary instabilities?

To address these questions secondary modified staircase equilibria are extracted from nonlinear gyrokinetic simulations. The stability properties are then studied by prescribing those equilibria (i. e., setting them constant in time) in separate simulations and by determining the dominantly growing Eigenmodes through forward time integration. Several properties of those Eigenmodes such as the growth rates, the mode structure and the influence of amplitude variations of the secondary modified staircase equilibria are investigated. In general, modified staircase structures and electron dynamics are found to have a significant influence on the stability properties close to marginality.

9.2 Numerical experiment

9.2.1 Gyrokinetic simulation setup

The gyrokinetic simulation setup applied in this chapter is equivalent to the G_1^{circ} set introduced in chapter 7 (see also Tab. 7.1). For more details the reader is referred to the aforementioned chapter.

9.2.2 Definition of toroidally symmetric secondary equilibria and measurement of the growth rate

In this chapter toroidally symmetric secondary equilibria refer to the stationary $k_y = 0$ component of both the perturbed distribution function f_{sp} and the electrostatic potential ϕ that develop self-consistently in a nonlinear turbulent state. Therefore, secondary equilibria contain gradients of the plasma rotation (ZFs and parallel rotation) as well as gradients in the perturbed plasma pressure, both capable to add to the free energy budget provided by the constant inverse

background gradient lengths R_0/L_n and R_0/L_T. Note that, below, the so defined toroidal equilibria are sometimes referred to as ZF equilibria.
The self-consistent equilibria are extracted from the saturated simulations by averaging the $k_y = 0$ part of the perturbed distribution function over a time interval of $\Delta t = 750\ R_0/v_{\mathrm{th,i}}$. Influences of turbulent fluctuations occurring on time scales of a few $10^1\ R_0/v_{\mathrm{th,i}}$ are successfully averaged out for this choice of averaging interval. In separate simulations the so obtained averaged toroidal equilibria are then set persistent in time, while the response of the turbulent ($k_y \neq 0$) modes of f and ϕ is solved for through forward time integration.
In general, the toroidal equilibria are functions of the two spatial coordinates x and s and, hence, the Eigenmodes have the form

$$G(x, y, s, t) = \hat{G}(x, s, [v_\parallel, \mu], t) \exp(\mathrm{i}k_y y) + c.c. \tag{9.1}$$

with

$$\hat{G}(x, s, [v_\parallel, \mu], t) = \hat{G}_A(x, [v_\parallel, \mu], s) \exp(\sigma t) \tag{9.2}$$

and $G \in [\delta f, \phi]$. In the above expressions $\hat{G}_A \in \mathbb{C}$ and $\sigma = \gamma - i\omega$ with $\gamma, \omega \in \mathbb{R}$ being the linear growth rate and frequency respectively. Furthermore, the notation $[v_\parallel, \mu]$ denotes the velocity space dependence of the Eigenmodes, if $G = \delta f$. The large number of degrees of freedom introduced by the four dimensional space $(x, s, v_\parallel, \mu)$ results in a vast amount of possible Eigenmodes whose detailed decomposition requires an Eigenvalue solver approach [74]. The forward time integration applied in this chapter allows for a discussion of the dominantly growing mode only.
In order to allow for the coupling of modes with $k_y \neq 0$ to the prescribed secondary equilibrium, the $E \times B$-nonlinearity is kept while integrating forward in time. Rescaling the amplitudes of the turbulent modes to a small level of $\mathcal{O}(\varepsilon)$ with $\varepsilon \sim 10^{-10}$ makes the coupling among turbulent $k_y \neq 0$ modes negligible and forces the state to the linear regime. More in detail, with the decomposition of a quantity G into its turbulent $k_y \neq 0$ part $\tilde{G}$ and its toroidally symmetric $k_y = 0$ part $\langle G \rangle$, i. e.,

$$G = \langle G \rangle + \tilde{G} \tag{9.3}$$

and the ordering

$$\langle G \rangle \sim \mathcal{O}(1) \tag{9.4}$$

$$\tilde{G} \sim \mathcal{O}(\varepsilon) \tag{9.5}$$

the $E \times B$-nonlinearity can be linearized

$$\mathbf{v}_E \cdot \nabla g_{\mathrm{sp}} \approx \rho_*^2 \mathcal{E}^{xy} \left(\frac{\partial \widetilde{\langle \phi \rangle_{\mathrm{ga,sp}}}}{\partial y} \frac{\partial \langle g_{\mathrm{sp}} \rangle}{\partial x} - \frac{\partial \tilde{g}_{\mathrm{sp}}}{\partial y} \frac{\partial \langle \langle \phi \rangle_{\mathrm{ga,sp}} \rangle}{\partial x} \right). \tag{9.6}$$

In the above expression $\langle ... \rangle_{\mathrm{ga,sp}}$ denotes a gyro-average and $\mathcal{E}^{xy} = [(\nabla x \times \nabla y) \cdot \mathbf{b}]/B$. The secondary equilibrium enters both terms within parenthesis on the

right-hand side (RHS) of the above expression: (i) The first term includes the radial derivative of the distribution function $\partial_x \langle g_{\mathrm{sp}} \rangle$. (ii) The second term introduces the radial derivative of the zonal electrostatic potential $\partial_x \langle \langle \phi \rangle_{\mathrm{ga,sp}} \rangle$. Hence, both gradients in the moments of the perturbed distribution like density, bulk velocity and kinetic energy etc. as well as the $E \times B$-drift (including the zonal flow) connected to the toroidal equilibrium can influence the stability behavior.
The rescaling of turbulent modes is applied after each integration time step and for each k_y mode individually. This allows for an accurate determination of the saturated growth rate γ and mode structure $|\hat{G}_A(x,s)|$ of the dominantly growing Eigenmode for each k_y-mode.
Individual cases exhibit a time dependent growth rate: (i) In some cases the growth rate oscillates around a well defined mean value with the mean value being of the order of typical growth rates

$$\gamma_{\mathrm{typical}} = 10^{-1}\ v_{\mathrm{th,i}}/R_0. \tag{9.7}$$

(ii) Close to the instability threshold, i. e., for small growth rates, extremely long time traces are necessary for the dominant Eigenmode to reach saturation in the sense that oscillations around the saturated growth rate are negligible. In order to save computational resources those cases are not run until saturation, but a statistical approach is applied instead. In all cases the temporally averaged growth rate $\langle \gamma \rangle_t$ is determined and its quality is quantified by its error (see appendix C for a definition of the statistical error). Furthermore, the degree of oscillations around the averaged growth rate is quantified by the temporal standard deviation over the interval Δt

$$\mathrm{std}(\gamma) = \sqrt{\frac{1}{N_t} \sum_{i=1}^{N_t} [\langle \gamma \rangle_t - \gamma(t_i)]^2}, \tag{9.8}$$

where N_t denotes the number of time samples in the interval Δt and t_i represents the time of the i-th sample. Only proper growing cases are selected by discarding realizations for which either the error of the mean value is larger than 10 % of the order of typical growth rates $\gamma_{\mathrm{typical}}$ [Eq. (9.7)] or the temporal standard deviation exceeds typical growth rates.

9.3 Numerical results

9.3.1 Characterization of a toroidally symmetric secondary modified staircase equilibrium

Before the stability properties of secondary equilibria are studied, here, a characterization of one of such equilibria is presented. Radial profiles of the primitive

zonal flow velocity

$$v_{\mathrm{ZF}} = \frac{1}{B_0}\frac{\partial\langle\phi\rangle}{\partial x}, \tag{9.9}$$

the estimated ZF velocity deduced from the director field

$$\overline{v_{\mathrm{ZF}}} = \alpha \int \mathrm{d}x'\ K_\phi(x'), \tag{9.10}$$

with α a proportionality constant (see chapter 6), the director field K_ϕ, the primitive shearing rate ω_{ExB} and the perturbed electron density and energy gradient lengths are depicted in Fig. 9.1 for an exemplary case with $R_0/L_T = 3.75$. The

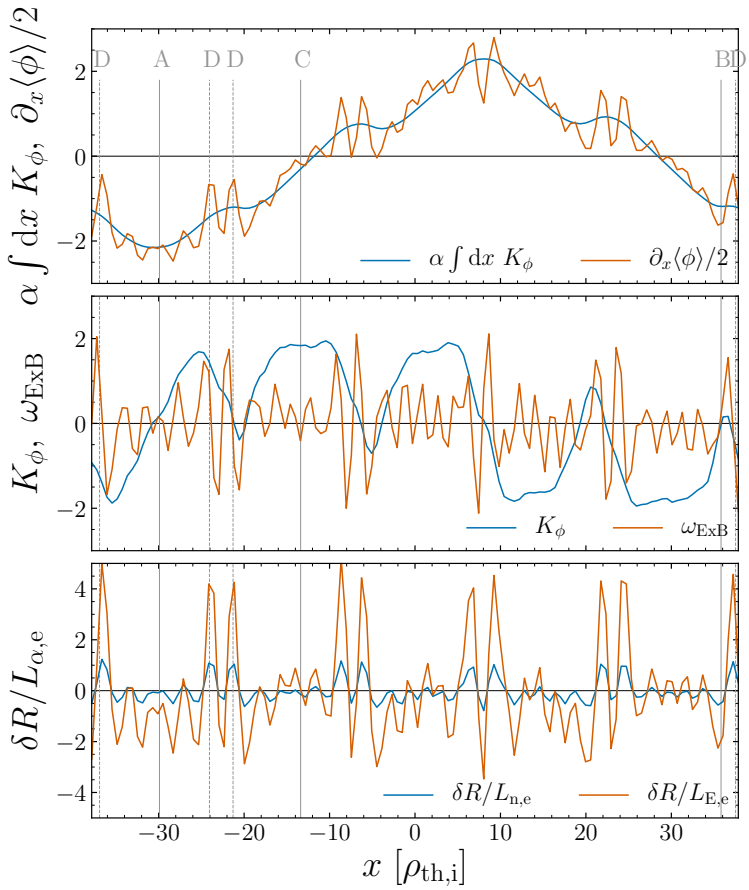

Figure 9.1: Radial profiles of several characteristic quantities connected to a secondary equilibrium extracted from a nonlinear simulation with $R_0/L_T = 3.75$ and CBC parameters. Vertical lines indicate mode centers of mode Type A, B, C and D (see Fig. 9.4).

perturbed gradient lengths are defined by

$$\delta R/L_{G,\mathrm{e}} = -\frac{R_0}{G_{0,\mathrm{e}}}\frac{\partial \delta G_{\mathrm{e}}}{\partial x} \tag{9.11}$$

with

$$\delta G_{\mathrm{e}} = \frac{2\pi B}{m_{\mathrm{e}}} \int \mathrm{d}v_{\parallel} \int \mathrm{d}\mu \; \alpha_{G,\mathrm{e}} \delta f_{\mathrm{e}} \tag{9.12}$$

and

$$\alpha_{G,\mathrm{e}} = \begin{cases} 1, & \text{if } G_{\mathrm{e}} \equiv n_{\mathrm{e}} \\ m_{\mathrm{e}} v_{\parallel}^2/2 + \mu B, & \text{if } G_{\mathrm{e}} \equiv E_{\mathrm{e}} \end{cases}, \tag{9.13}$$

As discussed in chapter 6 the secondary modified staircase equilibrium features pattern formation on three distinct scales: (i) The estimated zonal flow velocity exhibits a structure on the scale of the box size (see top panel of Fig. 9.1). In this chapter the zero crossings of this structure are referred to as *main zero crossings*.[2] (ii) On the scale of LORLS the director field features cut-ins (see mid panel of Fig. 9.1). These cut-ins constitute radial locations with reduced zonal flow shear. (iii) Fine scale structures on scales of a few $\rho_{\mathrm{th,i}}$ occur in the profiles of the primitive zonal flow velocity and the perturbed electron inverse gradient lengths. The following sections discuss the role of each pattern for the stability close to marginality.

9.3.2 Comparison of primary instabilities and instabilities in the presence of secondary equilibria

First, the stability properties of self-consistent toroidally symmetric equilibria (ZF) are compared to unmodified states driven by background gradients only (w/o ZF). This comparison is undertaken for a representative case with $R_0/L_T = 3.75$ by means of dominant growth rate spectra $\gamma(k_\theta)$ (see Fig. 9.2), where the 'poloidal' wave vector is defined by

$$k_\theta = k_y / \sqrt{g^{yy}(s=0)} \tag{9.14}$$

and $\sqrt{g^{yy} g^{\zeta\zeta}(s=0)}$ is the y-y-component of the metric tensor evaluated at the LFS.

The toroidal equilibrium allows for a finite growth rate (blue circles) with the maximum growth rate (maximized over the k_θ-spectrum), however, being significantly reduced compared to the maximum primary growth rate (black stars). Especially the dominant primary ITG mode residing at $k_\theta \rho_{\mathrm{th,i}} \approx 0.4 \sim 0.5$ is subject to a strong stabilization which is interpreted to be related to the stabilizing effect of sheared ZFs on the ITG instability [127].

A striking feature is the occurrence of unstable modes at poloidal wave vectors

[2] This nomenclature is adopted both in the case of the zonal flow velocity ($\sim \alpha \int \mathrm{d}x \; K_\phi$) as well as the shearing rate ($\sim K_\phi$). Note, however, that the respective main zero crossings are shifted by $L_x/4$ due to the different order of the radial derivative (see $\alpha \int \mathrm{d}x \; K_\phi$ in the top panel and K_ϕ in the mid panel of Fig. 9.1).

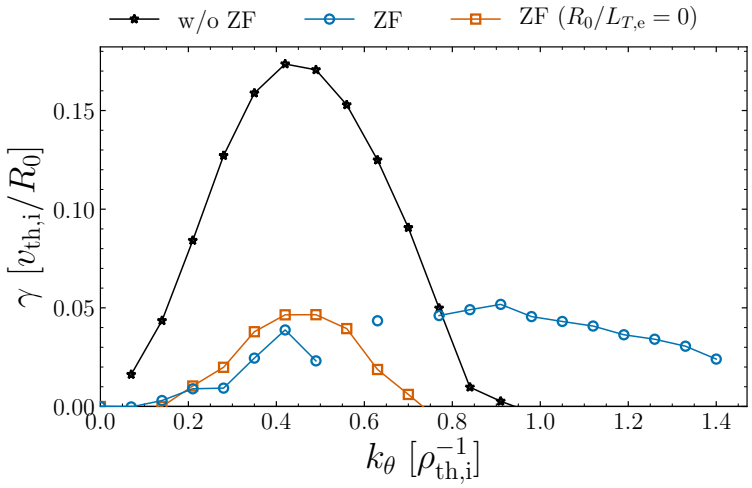

Figure 9.2: Growth rate γ against the poloidal wave vector k_θ for $R_0/L_T = 3.75$. Shown are primary instabilities driven by background gradients only (black stars), modified instabilities in the presence of a toroidally symmetric secondary equilibrium (blue circles) and the latter with the modification $R_0/L_{T,e} = 0$ (red squares).

satisfying $k_\theta \rho_{th,i} \gtrsim 1$. Those modes are absent from the primary instability spectrum and, therefore, can be identified as tertiary modes directly driven by the toroidal symmetric secondary equilibrium.
The fact that the tertiary modes observed here are driven unstable in a wave vector regime in which the TEM dominates the primary spectrum (although the primary TEM instability being unstable at larger R_0/L_T for CBC parameters as shown in Fig. 2.4 for example) and in which finite Larmor radius effects suppress the primary ITG mode suggests that the underlying physics is carried by electrons. In order to test this hypothesis a similar stability study is carried out, i. e., prescribing the same ZF equilibrium, with the temperature gradient drive of electron modes being reduced by zeroing out the electron background temperature gradient ($R_0/L_{T,e} = 0$). This modification removes the tertiary modes in the high k_θ regime from the spectrum (red squares) strengthening the conjecture of electron physics being responsible for the tertiary modes.
Not only does the choice of zero $R_0/L_{T,e}$ remove the electron modes, it also modifies the modes properties in the interval with $k_\theta \rho_{th,i} < 1$. A slight increase in the growth rate is observed, demonstrating that a finite electron temperature gradient can act stabilizing. Note, however, that while the prescribed toroidal equilibria are self-consistently obtained for CBC parameters, i. e., $R_0/L_{T,i} = R_0/L_{T,e}$, the self-consistent equilibrium for the pure ITG case ($R_0/L_{T,e} = 0$) might differ as well as the linear response to it.

Second, the dependence of the above discussed instability in the ITG wave

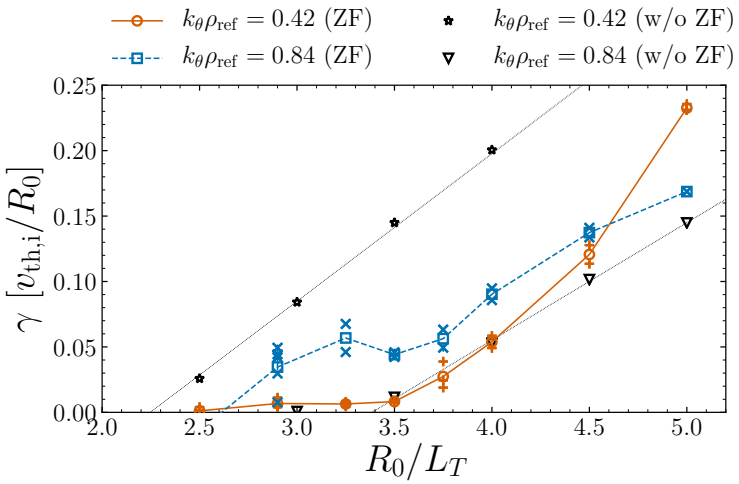

Figure 9.3: Growth rate γ against the background inverse temperature gradient length R_0/L_T for the two modes $k_\theta\rho_{\mathrm{th,i}} = 0.42$ and $k_\theta\rho_{\mathrm{th,i}} = 0.84$. Blue $\times$- and red $+$-symbols represent results obtained from different toroidal equilibria at the same R_0/L_T. Blue squares and red circles depict the ensemble average of different realizations at fixed R_0/L_T. The growth rate obtained in the presence of background gradients only, i. e., in the absence of toroidal equilibria, is shown by black stars and triangles with black dotted lines representing linear fits.

vector regime and the tertiary electron mode with the main control parameter R_0/L_T is investigated. Since kinetic electrons render the numerical calculations computationally demanding, not the full k_θ-spectrum is considered but individual modes are concentrated on only. Both instability regimes are accounted for by considering two modes with $k_\theta\rho_{\mathrm{th,i}} = 0.42$ and $k_\theta\rho_{\mathrm{th,i}} = 0.84$. Those modes dominate the respective stability balloons for $R/L_T = 3.75$ in the full-k_θ study (see Fig. 9.2). At fixed R_0/L_T the growth rate is obtained for an ensemble of toroidal symmetric equilibria taken from disjunct time intervals of the respective nonlinear simulation.
Several observations can be made: (i) The growth rate of the mode $k_\theta\rho_{\mathrm{th,i}} = 0.84$ in the presence of toroidal equilibria (blue $\times$-symbols and squares) always exceeds the growth rate of the primary instability (black triangles). Secondary toroidal equilibria, hence, contribute to the instability drive in this wave vector regime. In the interval $2.9 \lesssim R_0/L_T \lesssim 3.5$ the growth rate of this mode is approximately constant and instability occurs although the mode is stable in the presence of background gradients only. For $R_0/L_T \gtrsim 3.5$ the growth rate shows a similar increase compared with the primary instability with a positive offset. (ii) In the presence of secondary equilibria the growth rate of the mode $k_\theta\rho_{\mathrm{th,i}} = 0.42$ (red $+$-symbols and circles) is always smaller compared to the primary growth rate (black stars). The smooth transition from a vanishing to a finite growth rate is

similar to the dependence of the heat flux on R_0/L_T (see Fig. 6.4 of chapter 6). To summarize, the above outcome shows that modified staircase states significantly influence the stability properties close to marginality. Both a stabilization in the regime $k_\theta \rho_{\mathrm{th,i}} \lesssim 1$ and a destabilization in the regime $k_\theta \rho_{\mathrm{th,i}} \gtrsim 1$ is observed.

9.3.3 Mode structure in the presence of secondary equilibria

In contrast to the homogeneous background gradients driving the primary instabilities, the toroidally symmetric equilibria are radially structured. A radially

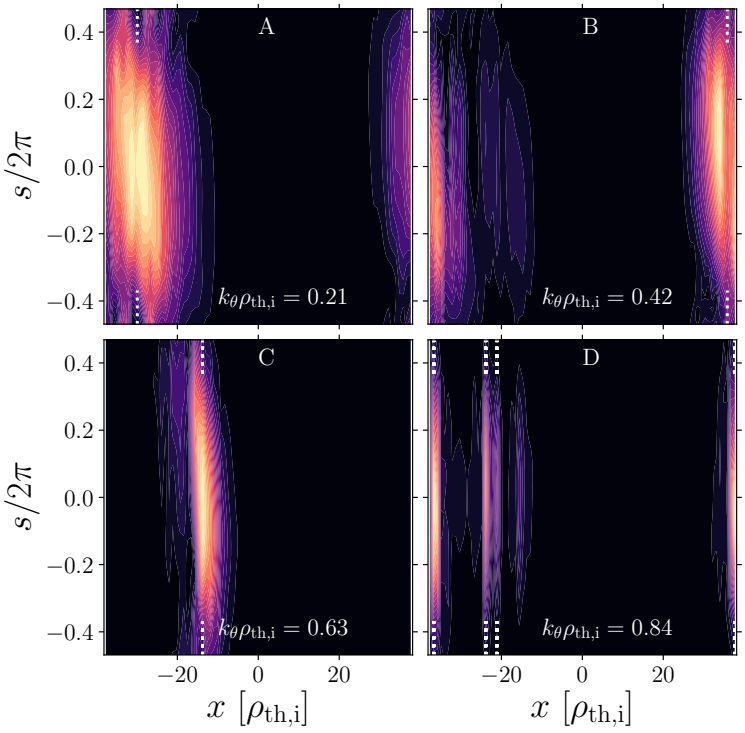

Figure 9.4: Mode structure $|\hat{\phi}_A|$ normalized to the maximum value as function of x and s for $k_\theta \rho_{\mathrm{th,i}} = 0.21$ (top left, A), $k_\theta \rho_{\mathrm{th,i}} = 0.42$ (top right, B), $k_\theta \rho_{\mathrm{th,i}} = 0.63$ (bottom left, C) and $k_\theta \rho_{\mathrm{th,i}} = 0.84$ (bottom right, D) and for $R_0/L_T = 3.75$. Vertical lines indicate mode centers with respect to the radial direction. The color range scales as $[0,\ 1] \rightarrow [\mathrm{black},\ \mathrm{yellow}]$.

dependent equilibrium is known to result in a radial localization of the mode structure [54, 127]. In this section the mode localization with respect to the secondary toroidal symmetric equilibria is studied.
Here, the mode structure of an Eigenmode with wave vector k_θ is defined by $|\hat{\phi}_A(x, s)|$ [see Eq. (9.2) for a definition of this quantity]. Fig. 9.4 depicts the

mode structure of the four modes $k_\theta \rho_{\mathrm{th,i}} = 0.21$ (top left, A), $k_\theta \rho_{\mathrm{th,i}} = 0.42$ (top right, B), $k_\theta \rho_{\mathrm{th,i}} = 0.63$ (bottom left, C) as well as $k_\theta \rho_{\mathrm{th,i}} = 0.84$ (bottom right, D) and for $R_0/L_T = 3.75$. In the cases A, B, and C a radial mode center is determined by fitting a gaussian to the radial profile $\langle |\hat{\phi}_A(x,s)| \rangle_s$, where $\langle ... \rangle_s$ denotes a spatial average with respect to s. In case D the mode structure exhibits radial fine scale features and the radial mode centers are defined by the local maxima connected to the spikes in the above defined radial profile. The radial mode centers are depicted by vertical white dotted lines in Fig. 9.4 and by vertical gray solid and dashed lines in Fig. 9.1 and are labeled accordingly. Four distinct modes can be distinguished when considering the modes orientation with respect to the underlying secondary equilibrium:

(A) For $k_\theta \rho_{\mathrm{th,i}} = 0.21$ the mode is broadly (i. e., having a width of several $\rho_{\mathrm{th,i}}$) centered at the zero crossing of the structure in K_ϕ varying on the scale of the box size, where $K_\phi < 0 \rightarrow K_\phi > 0$ with increasing radial coordinate. This location corresponding to the negative maximum of the box scale variation in the estimated zonal flow velocity $\overline{v}_{\mathrm{ZF}}$ (see blue profile in the top panel of Fig. 9.1) and is a location of zero $E \times B$ shear.

(B) For $k_\theta \rho_{\mathrm{th,i}} = 0.42$ the mode is broadly centered at the cut-ins in K_ϕ with a mirror symmetry with respect to the same main zero crossing of K_ϕ mentioned under type (A).

(C) For $k_\theta \rho_{\mathrm{th,i}} = 0.63$ the mode is localized to the radial position where K_ϕ exhibits a plateau like maximum. At this radial position the estimated ZF velocity amplitude $\overline{v}_{\mathrm{ZF}}$ connected to the box size variation crosses zero (see blue profile in the top panel of Fig. 9.1).

(D) For $k_\theta \rho_{\mathrm{th,i}} = 0.84$ the mode exhibit multiple sharply localized fine scale features being correlated with spike features in the perturbed electron gradient lengths.

The localization of the mode type A close to the main zero crossing of the director field K_ϕ is in agreement with the localization of instabilities at positions with zero zonal flow shear as reported of in the adiabatic electron studies of Refs. [54, 127]. However, the additional orientations of Eigenmodes B, C and D demonstrate a degree of delocalization with respect to the zonal flow equilibrium, which is likely to be related to electron physics.

This conjecture is now further tested through setting the electron background temperature gradient to zero $R_0/L_{T,\mathrm{e}} = 0$, while retaining the same secondary equilibrium as shown in Fig. 9.1. Fig. 9.5 depicts the corresponding mode structure of the four modes $k_\theta \rho_{\mathrm{th,i}} = 0.21$ (top left), $k_\theta \rho_{\mathrm{th,i}} = 0.42$ (top right), $k_\theta \rho_{\mathrm{th,i}} = 0.63$ (bottom left) as well as $k_\theta \rho_{\mathrm{th,i}} = 0.84$ (bottom right) and for $R_0/L_T = 3.75$. All of the cases shown are of mode type A, corroborating the

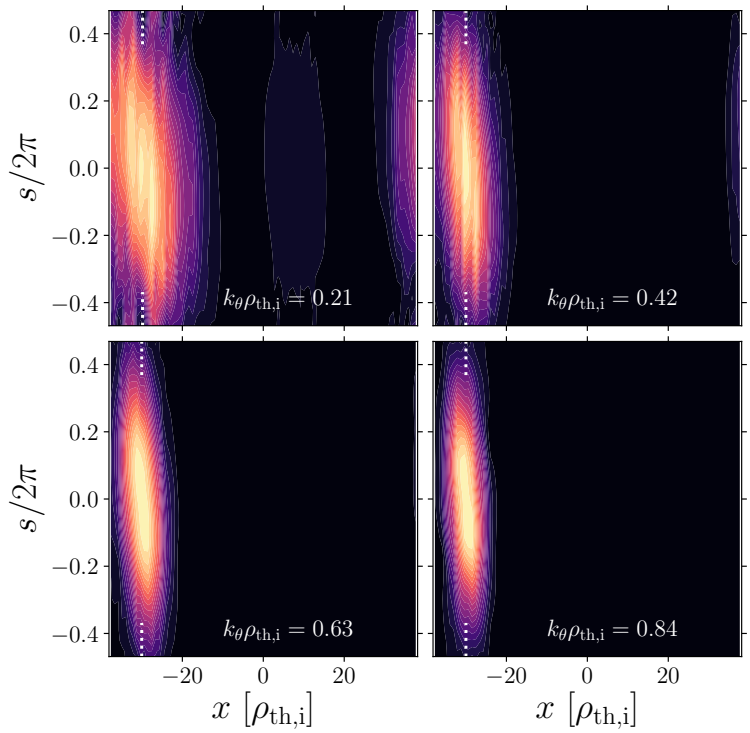

Figure 9.5: Mode structure $|\hat{\phi}_A|$ normalized to the maximum value as function of x and s for $k_\theta\rho_{\mathrm{th,i}} = 0.21$ (top left), $k_\theta\rho_{\mathrm{th,i}} = 0.42$ (top right), $k_\theta\rho_{\mathrm{th,i}} = 0.63$ (bottom left) and $k_\theta\rho_{\mathrm{th,i}} = 0.84$ (bottom right) and for $R_0/L_T = 3.75$ as well as $R/L_{T\mathrm{e}} = 0$. Vertical lines indicate mode centers with respect to the radial direction. The color range scales as $[0,\ 1] \rightarrow$ [black, yellow].

above hypothesis.
To summarize, electron dynamics allows for various Eigenmodes to grow in the presence of modified staircase structures, which are absent with reduced electron drive. The localization of those Eigenmodes at specific structures connected to the modified staircase state shows that structure formation on disparate scales directly influences the stability properties.

9.3.4 Tertiary instability analysis

This section considers the parametric dependence of the instabilities discussed in the previous sections on amplitude variation of the ZF equilibria. Since the extracted equilibria represent the averaged ZF state, the amplitude variations can be interpreted as possible realizations due to temporal fluctuations around the mean value. Again, the two modes with $k_\theta\rho_{\mathrm{th,i}} = 0.42$ and $k_\theta\rho_{\mathrm{th,i}} = 0.84$ are concentrated on exclusively.

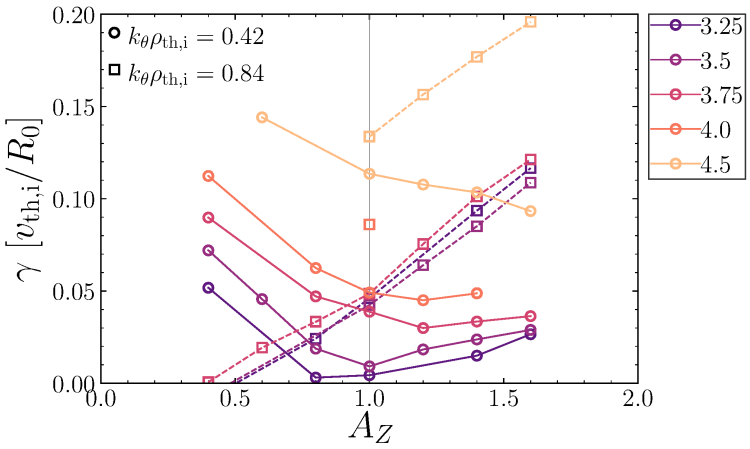

Figure 9.6: Growth rate γ against the amplitude scaling factor A_Z used for scaling of the full toroidally symmetric equilibrium. Shown is the data of the $k_\theta\rho_{\mathrm{th,i}} = 0.42$ mode (solid lines + circles) and of the $k_\theta\rho_{\mathrm{th,i}} = 0.84$ mode (dashed lines + squares) and for $R_0/L_T \in [3.25, 3.5, 3.75, 4.0, 4.5]$.

Variation of the full equilibrium

The full toroidally symmetric equilibrium consisting of both the distribution f_{sp} as well as the potential ϕ is scaled by a real factor A_Z resulting in a variation of both the perturbed moments as well as the zonal $E\times B$-flow. Fig. 9.6 shows the growth rate γ as function of the scaling factor A_Z for secondary equilibria extracted from simulations with various values of R_0/L_T. The following observations can be made:
(i) In the case of $k_\theta\rho_{\mathrm{th,i}} = 0.42$ (circles, solid lines) the growth rate increases with decreasing A_Z for $A_Z \lesssim 1$, demonstrating a stabilizing effect of the zonal flow equilibria in this amplitude regime. For inverse background temperature gradient lengths of $R_0/L_T \lesssim 4.0$ the growth rate exhibits a minimum at $A_Z \approx 1$ and increases slightly with increasing scaling factor. This suggests that tertiary instabilities are driven by the secondary equilibrium for amplitudes larger than the self-consistent value. The self-consistent amplitude ($A_Z = 1$) minimizes the instability drive and, hence, represents the optimal zonal flow state. For $R_0/L_T = 4.5$ the growth rate decreases monotonically with increasing A_Z in general. This suggests that the instability drive by the secondary equilibrium is less important further away from marginality.
(ii) In the case of $k_\theta\rho_{\mathrm{th,i}} = 0.84$ (squares, dashed lines) the growth rate increases with A_Z in general. This confirms that the fine scale modes are directly driven by the secondary equilibrium. For inverse background temperature gradient lengths of $R_0/L_T \lesssim 3.75$ the growth rate is independent of R_0/L_T, in agreement with the outcome shown in Fig. 9.3.

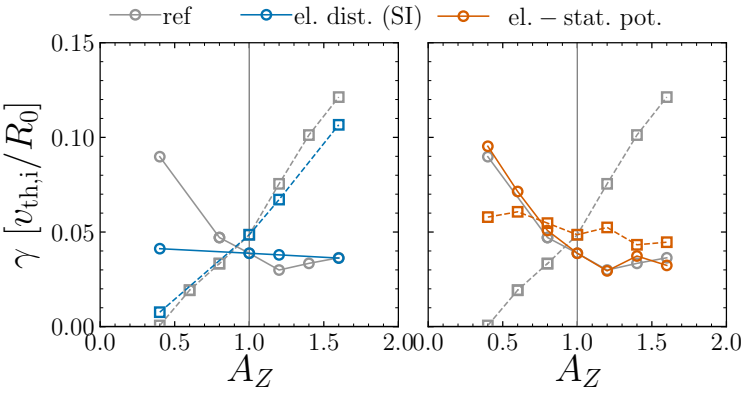

Figure 9.7: Growth rate γ against the amplitude scaling factor A_Z for scaling of the SI-driven radial modes in the electron distribution function (left panels) and the full electrostatic potential (right panels). $R_0/L_T = 3.75$ always and gray data depicts the reference case with variation of the full equilibrium. Solid lines with circles correspond to $k_\theta \rho_{\mathrm{th,i}} = 0.42$, while dashed lines with squares correspond to $k_\theta \rho_{\mathrm{th,i}} = 0.84$.

Variation of the electron distribution function or the electrostatic potential

This section investigates the role of zonal fine scale features in the electron distribution function and the zonal flow in general for the instabilities drive. The former is realized by scaling the self-interaction driven modes [see Eq. (8.32) of chapter 8 for a definition of those modes] of the electron distribution function f_{e} by a real factor A_Z, while keeping the remainder of the secondary equilibrium fixed. The latter is achieved by scaling the electrostatic potential part of the secondary equilibrium only, while holding the distribution part fixed. Since the potential is coupled to the distribution function via the gyrokinetic Poisson equation the resulting states have to be valued artificial.
The left panel of Fig. 9.7 compares the growth rate of the full equilibrium scaling scan (gray) with the electron distribution scaling scan (blue) for a toroidal equilibrium with $R_0/L_T = 3.75$. While the growth rate of the mode with $k_\theta \rho_{\mathrm{th,i}} = 0.42$ is hardly affected by the amplitude scaling, the fine scale modes having $k_\theta \rho_{\mathrm{th,i}} = 0.84$ scale with A_Z similarly to the full equilibrium scan. This experiment demonstrates that the fine scale modes in the large wave vector regime are, indeed, driven by the electron distribution part of the secondary equilibrium and are hereafter referred to as *tertiary electron modes*.
The right panel of Fig. 9.7 compares the growth rate of the full equilibrium scan (gray) with the zonal flow scaling scan (red) for the same equilibrium as discussed above. Here, the growth rate of the mode $k_\theta \rho_{\mathrm{th,i}} = 0.42$ (red circles and solid line) closely tracks the outcome of the full equilibrium scan, suggesting that it

is the zonal flow that determines the instability in this case. By contrast, the tertiary electron mode with $k_\theta \rho_{\mathrm{th,i}} = 0.84$ (red squares and dashed line) varies only moderately with the scaling factor.
In summary, this section confirms that the fine scale modes in the wave vector regime $k_\theta \rho_{\mathrm{th,i}} \gtrsim 1$ are driven by fine scale structures in the electron distribution. Also in the $k_\theta \rho_{\mathrm{th,i}} \lesssim 1$ regime the modes are driven by the secondary equilibrium, when the amplitude of the latter exceeds the self-consistent amplitude.

9.4 Conclusion

This chapter investigated instabilities in the presence of toroidally symmetric secondary modified staircase equilibria that have been directly extracted from the nonlinear gyrokinetic turbulence simulations presented in chapter 6. The focus has been on the role of electron dynamics as well as on the influence of patterns on disparate scales connected with modified staircase structure.
In general, modified staircase structures and electron dynamics influence the stability behavior close to marginal stability significantly:

- The growth rate of Eigenmodes with poloidal wave vectors k_θ in the regime in which the primary ITG instability dominates is significantly reduced compared to the primary growth rate. Here the term *primary* refers to instabilities driven by background gradients only. The zonal flow part of the modified staircase structure is responsible for the stabilization.

- In the wave vector region $k_\theta \rho_{\mathrm{th,i}} \gtrsim 1$ where the primary ITG is stabilized due to finite Larmor radius effects, in turn, secondary staircase equilibria are found to drive instabilities. Several tests demonstrate that these tertiary instabilities are driven by fine scale features in the electron distribution and are, therefore, referred to as *tertiary electron modes*.

- An investigation of the mode structures shows that in the presence of modified staircase structures Eigenmodes are radially localized. The localization can be related to patterns on disparate scales connected to the modified staircase structure and four distinct modes are discernible: (i) In the small wave vector regime $k_\theta \rho_{\mathrm{th,i}} \lesssim 1$ modes are typically broad with respect to the radial direction (i. e., the radial width is of the order of several $\rho_{\mathrm{th,i}}$). Those modes are centered at distinct radial locations with respect to mesoscale structures in the zonal flow, i. e., either at the zero crossing or the maximum of the zonal flow mode varying on the radial box size or at the corrugations at lowest order resonant layers (also referred to as *cut-ins* in chap. 6). The latter structure is a direct consequence of electron dynamics. (ii) In the wave vector regime $k_\theta \rho_{\mathrm{th,i}} \gtrsim 1$ the Eigenmodes are sharply

localized to maxima of fine scale features in the inverse perturbed electron gradient lengths. Such fine scale features are driven by self-interaction and, again, are a direct consequence of electron dynamics.

- A reduction of the electron drive (i. e. setting $R_0/L_{T,\mathrm{e}} = 0$) removes three of the observed modes, i. e., (i) the tertiary electron modes, (ii) the modes localized to the 'cut-ins' in the director field and (iii) the modes localized to the zero crossing of the structure in the zonal flow velocity that varies on the scale of the box size. Only the mode that is localized to the main zero crossing of the director field (zonal flow shearing rate) remains.

Given that zonal flow patterns typically occur in microturbulence close to marginal stability [67, 23, 25] (and chapter 6), the outcome of this chapter suggests that the inclusion of electron dynamics may be required for a proper description of near marginal microturbulence as it modifies various aspects of instabilities in the presence of such patterns.

Since the high k_θ fine scale tertiary electron modes become unstable just above

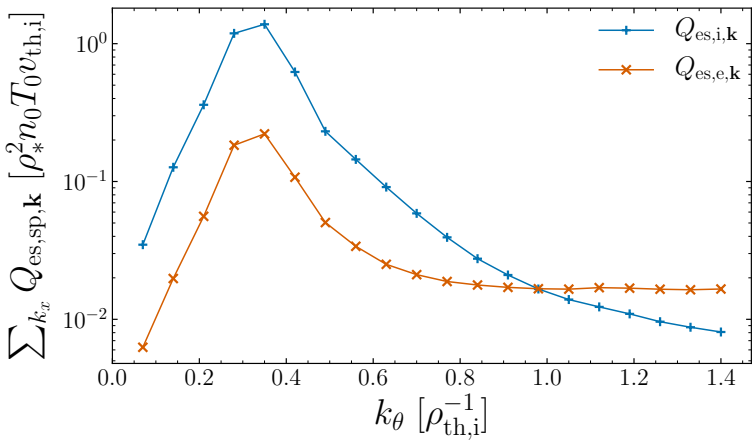

Figure 9.8: Temporally averaged electrostatic heat flux spectra $\sum_{k_x} Q_{\mathrm{es,sp,k}}$ [see Eq. (8.27) for a definition] as function of the poloidal wave vector k_θ and for $R_0/L_{T,\mathrm{i}} = R_0/L_{T,\mathrm{e}} = 3.75$ and CBC parameters.

the primary instability threshold and since those modes are rather unaffected by zonal flows, one might speculate that they cause the smooth transition to turbulence in the case of CBC parameters with kinetic electrons (see the flux-gradient relation in Fig. 6.4). Although signatures of those modes are visible in the spectrum of the electron electrostatic heat flux (see Fig. 9.8), both the electron and the ion heat flux are dominated by contributions from low k_θ modes. The tertiary instabilities of type B and C (see Sec. 9.3.3), hence, may be responsible for the smooth transition, which is further supported by the smooth transition in the corresponding growth rate as shown in Fig. 9.3.

The occurrence of tertiary instabilities localized to the 'cut-ins' at lowest order resonant layers (type B) may also explain the finite turbulence level despite the application of a background $E \times B$ shear as found in Sec. 6.3.3 of chapter 6. Such modes, growing locally, could be responsible for the triggering of avalanches, which are then able to travel through regions with finite $E \times B$ shear [26, 27] thereby maintaining turbulent transport.
Finally, the change of tertiary modes in the case of $R_0/L_{T,\mathrm{e}} = 0$ may relate to the difference in the near marginal turbulence dynamics among cases with equal ion- and electron background temperature gradient ($R_0/L_{T,\mathrm{i}} = R_0/L_{T,\mathrm{e}}$) compared to cases with $R/L_{T\mathrm{e}} = 0$ as observed in Sec. 6.3.1 of chapter 6. The clarification of this hypothesis is a rewarding topic for future work.

Chapter 10

Conclusion

The interplay of microturbulence and zonal flow pattern has been investigated in this thesis within a gyrokinetic framework. The focus has been on the influence of electron dynamics and electromagnetic effects. This chapter summarizes the main results and provides a short discussion and outlook.

10.1 Summary of the main results

Chapter 6: *Analysis of zonal flow pattern formation and the modification of staircase states by electron dynamics in gyrokinetic near marginal turbulence*

- Fine scale structures in the $E \times B$ shearing rate, that typically dominate this quantity when including electron dynamics [83, 1], do hardly contribute to the zonal flow. The $E \times B$ shearing rate is therefore unable to diagnose zonal flow structure formation in this case. Other diagnostics, such as the director field techniques applied in this thesis, may be chosen instead.

- Self-interaction driven fine scale features in the $E \times B$ shearing rate do not prevent staircase pattern form developing as anticipated in Ref. [1]. A director field analysis shows that mesoscale staircase structures do develop close to marginality for Cyclone base case parameters with inclusion of electron dynamics.

- The conventional staircase pattern (here *conventional staircase pattern* refers to structures observed in adiabatic electron studies [25]) is modified by electron dynamics: (i) A radial lock-in of the staircase pattern correlated with lowest order resonant layers occurs. (ii) Additional zonal flow corrugations at lowest order rational layers do develop.

- Long-term dynamics associated with mesoscale staircase structure formation highlights the need for sufficiently long simulation time traces. This requirement renders gyrokinetic studies of near marginal microturbulence with inclusion of electron dynamics computationally demanding.

Chapter 7: *Transport hysteresis in electromagnetic microturbulence caused by mesoscale zonal flow pattern induced mitigation of high β turbulence runaways*

- Temporally persistent mesoscale zonal flow patterns do develop also in electromagnetic near marginal microturbulence. The averaged amplitude and the temporal persistence of mesoscale zonal flows increases for moderate normalized plasma pressure β (i. e.,$\beta \lesssim 1$ %) compared to the electrostatic limit ($\beta \to 0$).

- Mesoscale zonal flow dominated states feature an enhanced stability against the triggering of turbulence runaways. The application of such states as initial conditions in gyrokinetic simulations mitigate turbulence runaways, which occur above a critical plasma beta β_{c} when small amplitude noise is chosen as initial condition. Hence, mesoscale zonal flow pattern formation allows for the access of an improved regime with $\beta > \beta_{\mathrm{c}}$ and introduces a transport hysteresis.

- Beside the Reynolds stress, mesoscale zonal flows are driven by the coupling to parallel flow sidebands;—a zonal flow driving mechanism that has not been identified so far (to the best knowledge of the author). This mechanism may be of greater relevance for microturbulence (i) since it is of the order of the Reynolds stress and (ii) since it is active in the electrostatic limit as well as in electromagnetic turbulence. It plays a significant role for the zonal flow dynamics at high β in particular, when the driving Reynolds stress is canceled by the damping Maxwell stress just below β_c.

- Provided persistent mesoscale zonal flow pattern do develop, a positive feedback effect occurs just below β_c, i. e., during the evolution of such flows the net nonlinear transfer $\mathcal{R} + \mathcal{M}$ changes sign (from negative to positive). As a result, mesoscale zonal flows are nonlinearly sustained beyond β_c; —a mechanism that is interpreted to allow for the access of the improved regime $\beta > \beta_c$.

Chapter 8: *Energetics and nonlinear transfer analysis of the self-interaction mechanism in local gyrokinetic fluxtube simulations of ion temperature gradient driven turbulence*

- Within a proper nonlinear energy transfer analysis the self-interaction mechanism [1] is demonstrated to have a negligible effect on the nonlinear

saturation of ion temperature gradient driven turbulence and for Cyclone base case parameters.

- The contribution of self-interaction driven zonal fine scale features to the zonal flow mediated nonlinear transfer of energy is shown to be negligible. This supports the finding of the director field analysis presented in chapter 6 that fine scale features in the $E \times B$ shearing rate do hardly contribute to shear deformation of turbulent structures.

Chapter 9: *Stability analysis of toroidally symmetric secondary modified staircase equilibria.*

- Electron dynamics introduce unstable Eigenmodes in the presence of modified staircase states that are absent both in the primary instability spectrum (here *primary instability* refers to instabilities in the presence of background gradients only) and when the electron background temperature gradient $R_0/L_{T,\mathrm{e}}$ is set to zero.

- Disparate scales connected to the modified staircase state are found to drive tertiary instabilities: (i) Self-interaction driven fine scale features in the perturbed electron distribution function drive tertiary electron modes with a radial fine scale mode structure. These modes occur in a poloidal wave vector regime $k_\theta \rho_{\mathrm{th,i}} \gtrsim 1$ in which the trapped electron mode dominates the primary instability spectrum. (ii) In the wave vector regime $k_\theta \rho_{\mathrm{th,i}} \lesssim 1$ Eigenmodes are found that grow locally at corrugations close to lowest order resonant layers. Both modes are absent when the electron temperature gradient drive is reduced.

10.2 Discussion and Outlook

This section discusses the implications of this thesis and motivates future research.

- This thesis suggests that mesoscale zonal flow pattern formation may be ubiquitous in near marginal ion temperature gradient driven turbulence, as it persists with inclusion of electron dynamics and electromagnetic effects. Since future fusion reactors will operate close to marginality[1], mesoscale zonal flow pattern formation and associated turbulent dynamics is likely to influence core energy confinement in a fusion reactor. In addition, a typical value of the $E \times B$-shearing rate has been demonstrated to constraint the saturation of the mesoscale zonal flow amplitude, rather than the zonal flow

[1] Predictive modeling of ITER scenarios [114, 115] suggest that microturbulence will be close to marginality and that zonal flow activity plays a major role.

velocity or the electrostatic potential amplitude (see Fig. 7.7 of chapter 7). An explanation for this observation has not been attempted and is left as a rewarding task for future work. Furthermore, since energetic particles influence the zonal flow dynamics through force-driven excitation [49, 50], with regard to burning fusion plasmas, the influence of energetic particles on mesoscale zonal flow pattern formation close to marginality may be investigated in future work.

- The finding that electron dynamics and instabilities (i. e. instabilities in the presence of zonal flow structures that require an electron temperature gradient drive) may be relevant in mesoscale zonal flow pattern dominated near marginal (primary) ITG driven turbulence has been gained within a gradient-driven gyrokinetic approach. An investigation of this outcome within a more realistic flux-driven study[2] is highly desirable, especially since flux-driven studies robustly report of zonal flow structure formation [26, 23, 157, 76, 158] while mostly being based on the adiabatic electron approximation.

- The interplay of mesoscale zonal flow patterns with a large scale background flow needs further study both in terms of simulation technique and physical interpretation. The wave vector re-mapping method, applied in this thesis, is known to introduce fictitious nonlinear interactions[3] and more advanced approaches as introduced in Ref. [159], for example, may be used in future. Future work may address the questions: Does the typical shearing rate connected to mesoscale zonal flow structures play a role for the plateau behavior of the heat flux as function of the background shearing rate, as found in Sec. 6.3.3 of chapter 6? What is the role of zero crossings in the radial profile of the total $E \times B$ shearing rate (background shear flow + self-consistent mesoscale structures) for turbulence generating instabilities and turbulent transport?

- Electromagnetic turbulence favors mesoscale zonal flow pattern development (at moderate β and sufficiently close to marginality) in that the temporal persistence and the (temporally averaged) amplitude of such patterns increase with β. Steady state tokamak scenarios require high β [116, 117], suggesting that mesoscale zonal flow pattern formation may play a role in

[2] In a flux-driven approach energy and particles are injected in and removed from the simulation domain through (spatially localized) sources and sinks, respectively. The radial profiles of temperature and density adjust self-consistently as a balance of source, turbulent transport and sink and, hence, flux-driven simulations properly account for mean profile dynamics.

[3] The re-mapping method causes fictitious nonlinear interactions, when the interacting modes are non-zonal modes, while interactions including a zonal mode are unaffected [159]. Since the cases of interest are dominated by mesoscale zonal flow patterns the error introduced by fictitious nonlinear interactions may be small.

such scenarios. The above finding raises the questions: Is the favorable effect of finite β on mesoscale zonal flow pattern formation a consequence of the turbulence approaching marginality with increasing β?[4] Or is this outcome related to the direct influence of electromagnetic effects on zonal flow generation [149] and saturation mechanisms?

- The dependence of transport caused by ion temperature gradient driven microturbulence on β has been subject of various studies. In Refs. [21, 150, 65, 66] the turbulence level has been reported to decrease with β, also referred to electromagnetic stabilization, while Ref. [156] reports of the persistence of ion temperature gradient driven turbulence with β when including the Shafranov shift. This thesis reports of another aspect of the β-dependence: The functional relation of the microturbulence level on β is found to depend on the proximity to marginality, i. e., close to marginality the turbulence level decrease with β, while far away from it increases with β (see Fig. 7.15). Aspects of this scaling dependence may apply to the experimental studies [160, 161, 162, 163, 164] that find discrepant trends of the energy confinement with β. Since temporal persistent mesoscale zonal flow pattern formation is found to occur close to marginality but is absent far away from it (see Fig. 7.4 of chapter 7), the above outcome raise the question: Is the dependence of the turbulence level on β related to (persistent) mesoscale zonal flow pattern formation?

- The electromagnetic transport hysteresis has been described within a gradient-driven approach with β being a constant background parameter. In flux-driven descriptions, which allow for the temporal evolution of the pressure profile (and therefore β), this phenomenon may introduce (theoretically) unexplored dynamical effects.[5] Several questions could be addressed in flux-driven studies: Can the mesoscale zonal flow pattern develop fast enough to mitigate turbulence runaways? How does this depend on the heating rate? If the system enters the mesoscale zonal flow dominated branch, what happens at the threshold of the kinetic ballooning mode?

- The analysis presented in chapter 7 suggests that the sudden onset of field line decorrelation is not responsible for high β turbulence runaways. Although the cancellation of Reynolds- and Maxwell stress close below β_c (see Fig. 7.14 of chapter 7) indicates that turbulence runaways are, indeed, related to the depletion of zonal flows by magnetic flutter, the present work

[4] The growth rate of the ITG driven instability decreases with β [20, 21].

[5] For example, aspects of the electromagnetic transport hysteresis described in this thesis may apply to the observation of so-called "grassy" ELMs in DIII-D [82], i. e., a transport bifurcation correlated with the emergence of staircase structures in the pedestal top of a high-confinement shot. This connection, however, needs further studies due to the different plasma parameters in the edge compared to the typical core parameters chosen in this thesis.

is unable to provide a consistent alternative explanation. Furthermore, the role of the transfer mechanisms based on the coupling of zonal flows to pressure and energy sidebands for the zonal flow dynamics close to β_c is left unclear. Hence, a consistent description of high β turbulence runaways remains elusive and is a rewarding subject for future research.

- In this thesis the Shafranov shift, the pressure gradient correction of the drift and parallel magnetic perturbations have been neglected. All those effects may influence microturbulence at sufficiently high β [156, 165]. An investigation of the electromagnetic transport hysteresis phenomenon with inclusion of such effects may be addressed in future work.

Appendix A

Parallel and radial force balances in the presence of a strong and curved ambient magnetic field

Here, parallel electron and radial ion force balance that are used in Sec. 6.3.2 are discussed. Starting point is the momentum density evolution equation following from taking moments of the Vlasov equation [166, 133, 167]

$$\frac{\partial m_{\mathrm{sp}} n_{\mathrm{sp}} \mathbf{u}_{\mathrm{sp}}}{\partial t} + \nabla \cdot (m_{\mathrm{sp}} n_{\mathrm{sp}} \mathbf{u}_{\mathrm{sp}} \mathbf{u}_{\mathrm{sp}}) + \nabla \cdot \mathbf{P}_{\mathrm{sp}} - q_{\mathrm{sp}} n_{\mathrm{sp}} (\mathbf{E} + \mathbf{u}_{\mathrm{sp}} \times \mathbf{B}) = 0, \tag{A.1}$$

where the index sp denotes the species. The stress tensor

$$\mathbf{P}_{\mathrm{sp}} = m_{\mathrm{sp}} \int (\mathbf{v} - \mathbf{u}_{\mathrm{sp}})(\mathbf{v} - \mathbf{u}_{\mathrm{sp}}) F_{V,\mathrm{sp}} \mathrm{d}^3 v, \tag{A.2}$$

the bulk velocity

$$\mathbf{u}_{\mathrm{sp}} = \frac{1}{n_{\mathrm{sp}}} \int \mathbf{v} F_{V,\mathrm{sp}} \mathrm{d}^3 v \tag{A.3}$$

and the density

$$n_{\mathrm{sp}} = \int F_{V,\mathrm{sp}} \mathrm{d}^3 v \tag{A.4}$$

enter Eq. (A.1), where $F_{V,\mathrm{sp}}$ is the Vlasov particle distribution function, m_{sp} is the species mass and $\mathbf{v}$ is the velocity space coordinate. In a strong ambient magnetic field the pressure tensor can be written as [168, 133]

$$\mathbf{P}_{\mathrm{sp}} = p_{\perp,\mathrm{sp}} \mathbb{1} + (p_{\parallel,\mathrm{sp}} - p_{\perp,\mathrm{sp}}) \mathbf{bb} + \mathbf{\Pi}, \tag{A.5}$$

with the first two terms on the right hand side constitute the gyrotropic pressure tensor $\mathbf{P}^g_{\mathrm{sp}}$, and the last term, the gyroviscous stress tensor $\mathbf{\Pi}$, including finite

Larmor radius effects.
The parallel and perpendicular pressure can be obtained from the pressure tensor by double contraction and read [133]

$$p_{\parallel,\mathrm{sp}} = m_{\mathrm{sp}} \int (v_\parallel - u_\parallel)^2 F_{V,\mathrm{sp}} \mathrm{d}^3 v \tag{A.6}$$

$$p_{\perp,\mathrm{sp}} = \frac{m_{\mathrm{sp}}}{2} \int |\mathbf{v}_\perp - \mathbf{u}_\perp|^2 F_{V,\mathrm{sp}} \mathrm{d}^3 v, \tag{A.7}$$

with $v_\parallel$ and $\mathbf{v}_\perp$ being the velocity coordinates parallel and perpendicular to the magnetic field and $u_\parallel$ and $\mathbf{u}_\perp$ the respective bulk velocity components. It is the divergence of the pressure tensor

$$\nabla \cdot \mathbf{P}_{\mathrm{sp}} = \nabla p_\perp + (p_\parallel - p_\perp)[\mathbf{b}(\nabla \cdot \mathbf{b}) + (\mathbf{b} \cdot \nabla)\mathbf{b}] \tag{A.8}$$

$$+ \mathbf{b}(\mathbf{b} \cdot \nabla)(p_\parallel - p_\perp) + \nabla \cdot \mathbf{\Pi} \tag{A.9}$$

that enters the momentum equation. The terms within the squared brackets describe magnetic curvature effects.
The δf-approximation applied in this work splits the distribution function into a background Maxwellian and a perturbed distribution $F = F_{\mathrm{M}} + f$ with $F_{\mathrm{M}} \sim \mathcal{O}(1)$ and $f \sim \mathcal{O}(\rho_*)$. Only the perturbed distribution f is evolved in the δf-approximation and the pressure entering the force balance equations below is formulated in terms of this latter distribution. The usual ordering $\mathbf{u}_{\mathrm{sp}}, \phi, n_{\mathrm{sp}} \sim \mathcal{O}(\rho_*)$ and $n_{0,\mathrm{sp}}, \mathbf{B} \sim \mathcal{O}(1)$ is adopted, where $n_{0,\mathrm{sp}}$ is the species background density, i. e., the zeroth order moment over F_{M}. The equations below will be formulated in first order of ρ_* and therefore the second term of Eq. A.1 as well as the bulk velocity $\mathbf{u}_{\mathrm{sp}}$ contributions in Eq. A.2 are neglected.
The parallel electron force balance is obtained by the inner product of Eq. (A.1) with the unit vector tangential to the ambient magnetic field $\mathbf{b}$ together with $q_{\mathrm{e}} = -e$. Its dimensionless and first order in ρ_* form reads

$$0 = \nabla_\parallel \phi - [\mathcal{K}_\parallel(p_{\parallel,\mathrm{e}}, p_{\perp,\mathrm{e}}) + \nabla_\parallel p_{\parallel,\mathrm{e}}], \tag{A.10}$$

with normalization in units of $\rho_{\mathrm{th,i}} n_0 T_0 / R_0^2$. The divergence of the gyroviscous pressure tensor has been neglected due to the small electron Larmor radius. Furthermore, the parallel gradient is

$$\nabla_\parallel = \mathbf{b} \cdot \nabla = \frac{\mathbf{B} \cdot \nabla s}{B} \frac{\partial}{\partial s} \tag{A.11}$$

as well as

$$\mathcal{K}_\parallel(p_{\parallel,\mathrm{e}}, p_{\perp,\mathrm{e}}) = (p_{\parallel,\mathrm{e}} - p_{\perp,\mathrm{e}})(\nabla \cdot \mathbf{b}) \tag{A.12}$$

$$= -(p_{\parallel,\mathrm{e}} - p_{\perp,\mathrm{e}}) \frac{\mathbf{B} \cdot \nabla B}{B^2}, \tag{A.13}$$

which defines the curvature term. Curvature effects enter the lowest order electron parallel force balance since the scales connected to both the ambient magnetic field and the variation of perturbed quantities parallel to the magnetic field are of the machine size $\sim R_0$. The parallel force balance is well satisfied for the

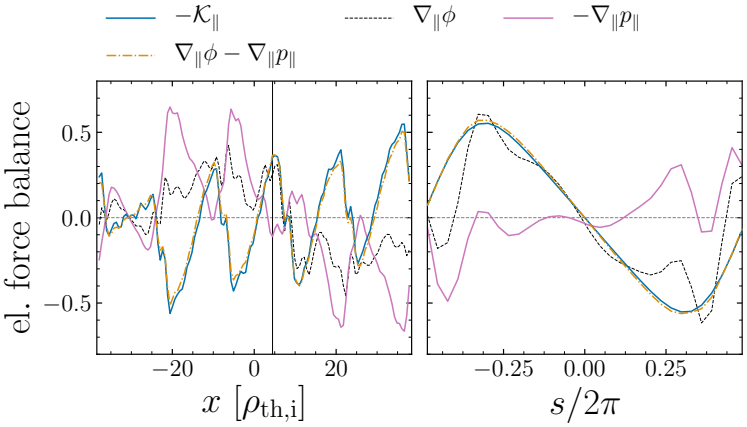

Figure A.1: Temporally averaged terms of the parallel electron force balance for a modified staircase state with $R_0/L_T = 3.75$. Shown are radial profiles averaged over a poloidal half turn $s \in [-0.5, 0]$ (left) and s-profiles (right) for the radial location indicated by the vertical line in the left panel.

modified staircase state (Fig. A.1). Note that parallel and perpendicular electron pressure are evaluated through the gyro-center distribution function f_{sp} according to Eq. (6.14).
The radial ion force balance is obtained by the inner product of the momentum equation [Eq. (A.1)] with the radial unit vector $\hat{\mathbf{e}}_r$ as well as $q_{\mathrm{i}} = +e$. Its dimensionless and first order in ρ_* form reads

$$0 = \nabla_x\phi + [\nabla_x p_{\perp,\mathrm{i}} + (\nabla\cdot\mathbf{\Pi}_{\mathrm{i}})_x] - 2(\mathbf{u}_{\mathrm{i}}\times\mathbf{B})_x, \tag{A.14}$$

with normalizations in units of n_0T_0/R_0. The normalized radial coordinate $x = r/\rho_{\mathrm{th,i}}$ and the notation $\nabla_x = \partial_x$ have been introduced. The radial curvature term $\rho_*\mathcal{K}_r(p_{\parallel,\mathrm{i}}, p_{\perp,\mathrm{i}}) = \rho_*(p_{\parallel,\mathrm{i}} - p_{\perp,\mathrm{i}})\hat{\mathbf{e}}_r(\mathbf{b}\cdot\nabla)\mathbf{b}$ is of higher order in ρ_*. The factor ρ_* results from the ambient magnetic field varying on the machine size $\sim R_0$, while the radial variation of the perturbed quantities is of the size of the Larmor radius $\sim \rho_{\mathrm{th,i}}$. In the local limit $\rho_* \to 0$ the curvature term is negligible.

Appendix B

Governing equations in the spectral representation

B.1 Gyrokinetic equation

In the representation Eq. (4.56) the gyrokinetic equation (4.46) reads

$$\begin{aligned}
\frac{\partial \hat{g}_{\mathrm{sp},\mathbf{k}}}{\partial t} = & \underbrace{-v_\parallel \mathbf{b}\cdot\nabla \hat{f}_{\mathrm{sp},\mathbf{k}}}_{L_{\parallel,f}} \underbrace{-\frac{\mathrm{i}}{Z_{\mathrm{sp}}e}\left[\frac{m_{\mathrm{sp}}v_\parallel^2}{B}+\mu\right]\frac{\mathbf{B}\times\nabla B}{B^2}\cdot\nabla x^\alpha k_\alpha \hat{f}_{\mathrm{sp},\mathbf{k}}}_{L_{D,f}} \\
& \underbrace{-\frac{Z_{\mathrm{sp}}eF_{\mathrm{M,sp}}}{T_{0,\mathrm{sp}}}v_\parallel \mathbf{b}\cdot\nabla\langle\hat{\phi}_{\mathbf{k}}\rangle_{\mathrm{ga,sp}}}_{L_{\parallel,F_{\mathrm{M}}}} \\
& \underbrace{+\frac{\mu\mathbf{b}\cdot\nabla B}{m_{\mathrm{sp}}}\frac{\partial \hat{f}_{\mathrm{sp},\mathbf{k}}}{\partial v_\parallel}}_{L_{\mathrm{tr}}} \underbrace{+\frac{\nabla x\times\nabla y}{B}\cdot\mathbf{b}\sum_{\mathbf{k}'}\sum_{\mathbf{k}''}\delta_{\mathbf{k}'+\mathbf{k}'',\mathbf{k}}(k_y''k_x'-k_x''k_y')\langle\hat{\phi}_{\mathbf{k}'}\rangle_{\mathrm{ga,sp}}\hat{g}_{\mathrm{sp},\mathbf{k}''}}_{N_E} \\
& \underbrace{-\frac{\nabla x\times\nabla y}{B}\cdot\mathbf{b}\sum_{\mathbf{k}'}\sum_{\mathbf{k}''}\delta_{\mathbf{k}'+\mathbf{k}'',\mathbf{k}}(k_y''k_x'-k_x''k_y')v_\parallel\langle\hat{A}_{\parallel\mathbf{k}'}\rangle_{\mathrm{ga,sp}}\hat{g}_{\mathrm{sp},\mathbf{k}''}}_{N_{\delta B}} \\
& \underbrace{-\frac{\mathrm{i}F_{\mathrm{M,sp}}}{T_{0,\mathrm{sp}}}\left[\frac{m_{\mathrm{sp}}v_\parallel}{B}+\mu\right]\frac{\mathbf{B}\times\nabla B}{B^2}\cdot\nabla x^\alpha k_\alpha\langle\hat{\phi}_{\mathbf{k}}\rangle_{\mathrm{ga,sp}}}_{L_{D,F_{\mathrm{M}}}} \\
& \underbrace{+\mathrm{i}k_y\frac{\nabla y\times\nabla x}{B}\cdot\mathbf{b}\hat{\chi}_{\mathrm{sp}}\times\left[\frac{1}{L_{n,\mathrm{sp}}}+\left(\frac{m_{\mathrm{sp}}v_\parallel^2/2+\mu B}{T_{0,\mathrm{sp}}}-\frac{3}{2}\right)\frac{1}{L_{T,\mathrm{sp}}}\right]F_{\mathrm{M,sp}}}_{L_{\chi,F_{\mathrm{M}}}} \\
& + D_{\mathrm{sp}}, \qquad \text{(B.1)}
\end{aligned}$$

where $\nabla x^\alpha k_\alpha = \nabla x k_x + \nabla y k_y$, $\sum_{\mathbf{k}'} = \sum_{k'_x} \sum_{k'_y}$ (and analogously for $\sum_{\mathbf{k}''}$) and $\hat{\chi}_{\mathrm{sp}} = \langle \hat{\phi}_{\mathbf{k}} \rangle_{\mathrm{ga,sp}} - v_\parallel \langle \hat{A}_{\parallel,\mathbf{k}} \rangle_{\mathrm{ga,sp}}$. Furthermore, $\delta_{\mathbf{k}'+\mathbf{k}'',\mathbf{k}} = 1$, if $k'_x + k''_x = k_x$ and $k'_y + k''_y = k_y$, $\delta_{\mathbf{k}'+\mathbf{k}'',\mathbf{k}} = 0$ otherwise. The numerical dissipation scheme is defined by $D_{\mathrm{sp}} = D_{s,\mathrm{sp}} + D_{v_\parallel,\mathrm{sp}} + D_{\perp,\mathrm{sp}}$ with

$$D_{s,\mathrm{sp}} = -\frac{D_s (\Delta s)^3}{12} \frac{v_{\parallel,\mathrm{max,sp}}}{\sqrt{3}} \mathbf{b} \cdot \nabla s \frac{\partial^4 \hat{f}_{\mathrm{sp},\mathbf{k}}}{\partial s^4}, \tag{B.2}$$

$$\tag{B.3}$$

if $k_y \neq 0$, and

$$D_{s,\mathrm{sp}} = -\frac{D_s (\Delta s)^5}{60} \frac{v_{\parallel,\mathrm{max,sp}}}{\sqrt{3}} \mathbf{b} \cdot \nabla s \frac{\partial^6 \hat{f}_{\mathrm{sp},\mathbf{k}}}{\partial s^6}, \tag{B.4}$$

$$\tag{B.5}$$

if $k_y = 0$ ($6th$-order zonal flow scheme), and

$$D_{v_\parallel,\mathrm{sp}} = -\frac{D_{v_\parallel} (\Delta v_\parallel)^3}{12} \frac{\mu_{\mathrm{max,sp}}}{\sqrt{3} m_{\mathrm{sp}}} \mathbf{b} \cdot \nabla B \frac{\partial^4 \hat{f}_{\mathrm{sp},\mathbf{k}}}{\partial {v_\parallel}^4} \tag{B.6}$$

and

$$D_{\perp,\mathrm{sp}} = -\frac{v_{\mathrm{th,i}}}{R_0} \left[D_x \left(\frac{k_x}{k_{x,\max}} \right)^4 + D_y \left(\frac{k_y}{k_{y,\max}} \right)^4 \right] \hat{f}_{\mathrm{sp},\mathbf{k}}. \tag{B.7}$$

The maximum resolved radial wave vector is $k_{x,\max} = [(N_{k_x} - 1)/2] \cdot k_{x,\min}$, with $k_{x,\min}$ defined in Eq. (4.42). The parallel dissipation and the parallel velocity dissipation include the grid spacing $\Delta s = 1/N_s$ and $\Delta v_\parallel = 2 v_{\parallel,\mathrm{max,sp}}/N_{v_\parallel}$, where N_s and $N_{v_\parallel}$ specify the number of grid points in the s- and $v_\parallel$ direction and $v_{\parallel,\mathrm{max,sp}}$ and $\mu_{\mathrm{max,sp}}$ denote the maximum resolved parallel velocity and magnetic moment respectively.

B.2 Field equations

In the representation Eq. (4.56) the gyrokinetic Poisson equation equation (4.49) reads

$$\sum_{\mathrm{sp}} Z_{\mathrm{sp}} e \left[\frac{2\pi B}{m_{\mathrm{sp}}} \int \mathrm{d}v_\parallel \int \mathrm{d}\mu \; J_0(\lambda_{\mathrm{sp},\mathbf{k}}) \hat{g}_{\mathrm{sp},\mathbf{k}} + \frac{Z_{\mathrm{sp}} e n_{0,\mathrm{sp}}}{T_{0,\mathrm{sp}}} [\Gamma_0(b_{\mathrm{sp},\mathbf{k}}) - 1] \hat{\phi}_{\mathbf{k}} \right] = 0, \tag{B.8}$$

with $\lambda^2_{\mathrm{sp},\mathbf{k}} = \rho^2_{\mathrm{sp}} k^2_\perp$ and $b_{\mathrm{sp},\mathbf{k}} = 0.5 \times [m_{\mathrm{sp}} v_{\mathrm{th,sp}}/(Z_{\mathrm{sp}} e B)]^2 k^2_\perp$. The perpendicular wave vector is defined by $k^2_\perp = g^{x^\alpha x^\beta} k_\alpha k_\beta$ (Einstein sum convention is applied),

where $g^{x^\alpha x^\beta} = \nabla x^\alpha \cdot \nabla x^\beta$ is the metric tensor and $x^\alpha, x^\beta \in [x, y]$.
Similarly, the Fourier space representation of the parallel component of the gyrokinetic Ampère's law [Eq. (4.50)] reads

$$\left[k_\perp^2 + \mu_0 \sum_{\mathrm{sp}} Z_{\mathrm{sp}}^2 e^2 \frac{n_{0,\mathrm{sp}}}{m_{\mathrm{sp}}} \Gamma_0(b_{\mathrm{sp},\mathbf{k}})\right] \hat{A}_{\parallel,\mathbf{k}} =$$
$$\mu_0 \sum_{\mathrm{sp}} Z_{\mathrm{sp}} e \frac{2\pi B}{m_{\mathrm{sp}}} \int \mathrm{d}v_\parallel \int \mathrm{d}\mu \; v_\parallel J_0(\lambda_{\mathrm{sp},\mathbf{k}}) \hat{g}_{\mathrm{sp},\mathbf{k}}. \tag{B.9}$$

Appendix C

Statistical error estimate

Throughout this work the quality of time averages is specified by a statistical error determined through six-part time averaging. More in detail, the statistical error of the time average of a quantity G is defined by

$$\sigma = \sqrt{\frac{1}{N_{\text{sub}}} \sum_{i=1}^{N_{\text{sub}}} \Big(\langle G \rangle_{\Delta T} - \langle G \rangle_{\Delta T_i} \Big)^2}, \tag{C.1}$$

where the averaging time interval ΔT is divided into $N_{\text{sub}} = 6$ subintervals of same length ΔT_i and $\langle G \rangle_{\Delta T}$ as well as $\langle G \rangle_{\Delta T_i}$ denote the time averages over the entire interval and the i-th subinterval respectively.

Appendix D

Zonal flow transfer mechanisms $\mathcal{L}_{D,f}$ and $\mathcal{L}_{\parallel,f}$

This section provides details about the two transfer terms $\mathcal{L}_{D,f}$ and $\mathcal{L}_{\parallel,f}$ of the zonal flow intensity evolution equation [Eq. (8.23)] that dominate the transfer $\mathcal{L}$ in this work (see Fig. 7.14). To this end, a sideband is defined as an axisymmetric ($k_y = 0$) perturbation in the perturbed distribution function f_{sp} that varies poloidally (along s). Furthermore, zonal potential perturbations with a wavelength of the box size are considered exclusively. In this case $(k_{\mathrm{ZF}}\rho_{\mathrm{sp}})^2 \lesssim (k_{\mathrm{ZF}}\rho_{\mathrm{th,i}})^2 \ll 1$ and, hence, $J_0(k_{\mathrm{ZF}}\rho_{\mathrm{sp}}) = 1 + \mathcal{O}(k_{\mathrm{ZF}}^2\rho_{\mathrm{sp}}^2) \approx 1$.

D.1 Transfer due to coupling to energy sidebands

Using the spectral representation of the gyrokinetic equation (B.8) the term $\mathcal{L}_{D,f}$ reads

$$\mathcal{L}_{D,f} \approx 2\mathrm{i}k_{\mathrm{ZF}}^3\langle\hat{\phi}_{\mathbf{k}}\rangle^* \int \mathrm{d}s\ \frac{\mathcal{D}^x}{\mathcal{P}} \times \sum_{\mathrm{sp}} \left[2\hat{E}_{\parallel,\mathrm{sp},\mathbf{k}} + \hat{E}_{\perp,\mathrm{sp},\mathbf{k}}\right]_{\mathbf{k}=(k_{\mathrm{ZF}},0)}, \tag{D.1}$$

where $\mathcal{D}^x = (\mathbf{B} \times \nabla B) \cdot \nabla x / B^3$ is the geodesic part of the magnetic drift tensor and

$$\hat{E}_{\parallel,\mathrm{sp},\mathbf{k}} = \frac{2\pi B}{m_{\mathrm{sp}}} \int \mathrm{d}v_\parallel \int \mathrm{d}\mu\ \frac{1}{2} m_{\mathrm{sp}} v_\parallel^2 \hat{f}_{\mathrm{sp},\mathbf{k}} \tag{D.2}$$

$$\hat{E}_{\perp,\mathrm{sp},\mathbf{k}} = \frac{2\pi B}{m_{\mathrm{sp}}} \int \mathrm{d}v_\parallel \int \mathrm{d}\mu\ \mu B \hat{f}_{\mathrm{sp},\mathbf{k}} \tag{D.3}$$

defines the perturbed parallel and perpendicular energy respectively. In the considered magnetic geometry $\mathcal{P}$ has even parity in s (with respect to $s = 0$), while $\mathcal{D}^x$ has odd parity. Therefore, the occurrence of odd parity sidebands of the perturbed energies is a necessary condition for a finite $\mathcal{L}_{D,f}$.

D.2 Transfer due to coupling to parallel flow sidebands

Using the spectral representation of the gyrokinetic equation (B.8) the term $\mathcal{L}_{\parallel,f}$ reads

$$\mathcal{L}_{\parallel,f} \approx 2k_{\mathrm{ZF}}^2 \langle \hat{\phi}_{\mathbf{k}} \rangle^* \int \mathrm{d}s \; \frac{B\mathcal{F}}{\mathcal{P}} \frac{\partial}{\partial s} \left[\frac{1}{B} \sum_{\mathrm{sp}} Z_{\mathrm{sp}} e \hat{u}_{\parallel,\mathrm{sp},\mathbf{k}} \right]_{\mathbf{k}=(k_{\mathrm{ZF}},0)}, \tag{D.4}$$

where $\mathcal{F} = \mathbf{B} \cdot \nabla s / B$ and

$$\hat{u}_{\parallel,\mathrm{sp},\mathbf{k}} = \frac{2\pi B}{m_{\mathrm{sp}}} \int \mathrm{d}v_{\parallel} \int \mathrm{d}\mu \; v_{\parallel} \hat{f}_{\mathrm{sp},\mathbf{k}} \tag{D.5}$$

defines the parallel flow. Here, $B\mathcal{F}$ is constant with respect to s (flux function) and B^{-1} has even parity with respect to the low field side midplane ($s = 0$). The occurrence of odd parity sidebands of the parallel flow $\hat{u}_{\parallel,\mathrm{sp},\mathbf{k}}$ is, therefore, a necessary condition for a finite $\mathcal{L}_{\parallel,f}$.

Appendix E

ASDEX Upgrade and ITER reference parameters

This section summarizes reference parameters and typical plasma parameters for a deuterium plasma based on the technical details of the ASDEX Upgrade [169] and the ITER [170] tokamaks.

	ASDEX Upgrade	ITER
R_0 [m]	1.6	6.2
B_0 [T]	3.9	5.3
n_0 [m^{-3}]	2×10^{20}	1×10^{20}
T_0 [K]	100×10^6	150×10^6
$v_{\mathrm{th,i}}$ [m/s]	0.91×10^6	1.11×10^6
$v_{\mathrm{th,e}}$ [m/s]	55.06×10^6	67.32×10^6
ρ_{i} [mm]	4.87	4.38
ρ_{e} [mm]	0.08	0.07
$\omega_{\mathrm{c,i}}$ [s^{-1}]	1.87×10^8	2.49×10^8
$\omega_{\mathrm{c,e}}$ [s^{-1}]	6.86×10^{11}	9.15×10^{11}
ρ_*	3.04×10^{-3}	7.21×10^{-4}
β [%]	4.56	1.92

Table E.1: Technical details of the ASDEX Upgrade [169] and the ITER [170] tokamak and typcial plasma parameters assuming a deuterium plasma.

Bibliography

[1] A. Weikl, A. G. Peeters, F. Rath, F. Seiferling, R. Buchholz, S. R. Grosshauser and D. Strintzi, *The occurrence of staircases in itg turbulence with kinetic electrons and the zonal flow drive through self-interaction*, Physics of Plasmas **25**, 072305 (2018).

[2] International Atomic Energy Agency, *Evaluated nuclear data file*, https://www-nds.iaea.org/exfor/endf.htm, accessed: 13.07.2022.

[3] J. Wesson, *Tokamaks*, Oxford University Press, Oxford (2011).

[4] D. D. Clayton, *Principles of Stellar Evolution and Nucleosynthesis*, University of Chicago Press, Chicago (1983).

[5] U. Stroth, *Plasmaphysik*, Viewg+Teubner, Wiesbaden (2011).

[6] R. J. Bickerton, J. W. Connor and J. B. Taylor, *Diffusion driven plasma currents and bootstrap tokamak*, Nature Physical Science **229**, 110–112 (1971).

[7] A. Galeev, *Diffusion-electrical phenomena in a plasma confined in a tokamak machine*, Sov. Phys. JETP **32**, 752 (1971).

[8] A. G. Peeters, *The bootstrap current and its consequences*, Plasma Physics and Controlled Fusion **42**, B231 (2000).

[9] X. Lapillonne, S. Brunner, T. Dannert, S. Jolliet, A. Marinoni, L. Villard, T. Görler, F. Jenko and F. Merz, *Clarifications to the limitations of the $s-\alpha$ equilibrium model for gyrokinetic computations of turbulence*, Physics of Plasmas **16**, 032308 (2009).

[10] A. J. Brizard and T. S. Hahm, *Foundations of nonlinear gyrokinetic theory*, Rev. Mod. Phys. **79**, 421 (2007).

[11] X. Garbet, Y. Idomura, L. Villard and T. Watanabe, *Gyrokinetic simulations of turbulent transport*, Nuclear Fusion **50**, 043002 (2010).

[12] W. Horton, *Drift waves and transport*, Rev. Mod. Phys. **71**, 735 (1999).

[13] L. Rudakov and R. Sagdeev, *On the instability of a nonuniform rarefied plasma in a strong magnetic field*, Dokl. Akad. Nauk. SSSR **138**, 581 (1961).

[14] B. Coppi, M. N. Rosenbluth and R. Z. Sagdeev, *Instabilities due to temperature gradients in complex magnetic field configurations*, The Physics of Fluids **10**, 582 (1967).

[15] S. C. Cowley, R. M. Kulsrud and R. Sudan, *Considerations of ion-temperature-gradient-driven turbulence*, Physics of Fluids B: Plasma Physics **3**, 2767 (1991).

[16] F. Casson, *Turbulent transport in rotating tokamak plasmas*, Ph.D. thesis, University of Warwick (2011).

[17] T. Dannert, *Gyrokinetische Simulation von Plasmaturbulenz mit gefangenen Teilchen und Elektromagnetischen Effekten*, Ph.D. thesis, Technische Universtät München (2005).

[18] M. Beer, *Gyrofluid models of turbulent transport in tokamaks*, Ph.D. thesis, Princeton University (1994).

[19] K. Hallatschek and W. Dorland, *Giant electron tails and passing electron pinch effects in tokamak-core turbulence*, Phys. Rev. Lett. **95**, 055002 (2005).

[20] J. Y. Kim, W. Horton and J. Q. Dong, *Electromagnetic effect on the toroidal ion temperature gradient mode*, Physics of Fluids B: Plasma Physics **5**, 4030 (1993).

[21] M. J. Pueschel, M. Kammerer and F. Jenko, *Gyrokinetic turbulence simulations at high plasma beta*, Physics of Plasmas **15**, 102310 (2008).

[22] M. Nakata, T.-H. Watanabe and H. Sugama, *Nonlinear entropy transfer via zonal flows in gyrokinetic plasma turbulence*, Physics of Plasmas **19**, 022303 (2012).

[23] G. Dif-Pradalier, P. H. Diamond, V. Grandgirard, Y. Sarazin, J. Abiteboul, X. Garbet, P. Ghendrih, A. Strugarek, S. Ku and C. S. Chang, *On the validity of the local diffusive paradigm in turbulent plasma transport*, Phys. Rev. E **82**, 025401 (2010).

[24] F. Rath, A. G. Peeters, R. Buchholz, S. R. Grosshauser, P. Migliano, A. Weikl and D. Strintzi, *Comparison of gradient and flux driven gyrokinetic turbulent transport*, Physics of Plasmas **23**, 052309 (2016).

[25] A. G. Peeters, F. Rath, R. Buchholz, Y. Camenen, J. Candy, F. J. Casson, S. R. Grosshauser, W. A. Hornsby, D. Strintzi and A. Weikl, *Gradient-driven flux-tube simulations of ion temperature gradient turbulence close to the non-linear threshold*, Physics of Plasmas **23**, 082517 (2016).

[26] Y. Idomura, H. Urano, N. Aiba and S. Tokuda, *Study of ion turbulent transport and profile formations using global gyrokinetic full- f vlasov simulation*, Nuclear Fusion **49**, 065029 (2009).

[27] B. F. McMillan, S. Jolliet, T. M. Tran, L. Villard, A. Bottino and P. Angelino, *Avalanchelike bursts in global gyrokinetic simulations*, Physics of Plasmas **16**, 022310 (2009).

[28] P. H. Diamond, S.-I. Itoh, K. Itoh and T. S. Hahm, *Zonal flows in plasma—a review*, Plasma Physics and Controlled Fusion **47**, R35 (2005).

[29] H. Biglari, P. H. Diamond and P. W. Terry, *Influence of sheared poloidal rotation on edge turbulence*, Physics of Fluids B: Plasma Physics **2**, 1 (1990).

[30] K. Hallatschek, *Turbulent saturation of tokamak-core zonal flows*, Phys. Rev. Lett. **93**, 065001 (2004).

[31] K. Itoh and S.-I. Itoh, *The role of the electric field in confinement*, Plasma Physics and Controlled Fusion **38**, 1 (1996).

[32] P. H. Diamond and Y. Kim, *Theory of mean poloidal flow generation by turbulence*, Physics of Fluids B: Plasma Physics **3**, 1626 (1991).

[33] P. N. Guzdar, *Shear-flow generation by drift/rossby waves*, Physics of Plasmas **2**, 4174 (1995).

[34] L. Chen, Z. Lin and R. White, *Excitation of zonal flow by drift waves in toroidal plasmas*, Physics of Plasmas **7**, 3129 (2000).

[35] M. A. Malkov, P. H. Diamond and M. N. Rosenbluth, *On the nature of bursting in transport and turbulence in drift wave–zonal flow systems*, Physics of Plasmas **8**, 5073 (2001).

[36] C. N. Lashmore-Davies, D. R. McCarthy and A. Thyagaraja, *The nonlinear dynamics of the modulational instability of drift waves and the associated zonal flows*, Physics of Plasmas **8**, 5121 (2001).

[37] G. Manfredi, C. M. Roach and R. O. Dendy, *Zonal flow and streamer generation in drift turbulence*, Plasma Physics and Controlled Fusion **43**, 825 (2001).

[38] W. Dorland, F. Jenko, M. Kotschenreuther and B. N. Rogers, *Electron temperature gradient turbulence*, Phys. Rev. Lett. **85**, 5579 (2000).

[39] F. Jenko, *Streamer saturation: a dynamical systems approach*, Physics Letters A **351**, 417 (2006).

[40] D. Strintzi and F. Jenko, *On the relation between secondary and modulational instabilities*, Physics of Plasmas **14**, 042305 (2007).

[41] G. Plunk, *Gyrokinetic secondary instability theory for electron and ion temperature gradient driven turbulence*, Physics of Plasmas **14**, 112308 (2007).

[42] A. Hasegawa and K. Mima, *Pseudo-three-dimensional turbulence in magnetized nonuniform plasma*, The Physics of Fluids **21**, 87 (1978).

[43] J. A. Krommes and C.-B. Kim, *Interactions of disparate scales in drift-wave turbulence*, Phys. Rev. E **62**, 8508 (2000).

[44] D. H. E. Dubin, J. A. Krommes, C. Oberman and W. W. Lee, *Nonlinear gyrokinetic equations*, The Physics of Fluids **26**, 3524 (1983).

[45] B. D. Scott, *Energetics of the interaction between electromagnetic ExB turbulence and zonal flows*, New Journal of Physics **7**, 92 (2005).

[46] P. N. Guzdar, R. G. Kleva and L. Chen, *Shear flow generation by drift waves revisited*, Physics of Plasmas **8**, 459 (2001).

[47] A. I. Smolyakov, P. H. Diamond and M. V. Medvedev, *Role of ion diamagnetic effects in the generation of large scale flows in toroidal ion temperature gradient mode turbulence*, Physics of Plasmas **7**, 3987 (2000).

[48] J. Anderson, H. Nordman, R. Singh and R. Singh, *Secondary instability of electromagnetic ion-temperature-gradient modes for zonal flow generation*, Physics of Plasmas **18**, 072306 (2011).

[49] F. Zonca, L. Chen, S. Briguglio, G. Fogaccia, A. V. Milovanov, Z. Qiu, G. Vlad and X. Wang, *Energetic particles and multi-scale dynamics in fusion plasmas*, Plasma Physics and Controlled Fusion **57**, 014024 (2014).

[50] Z. Qiu, L. Chen and F. Zonca, *Effects of energetic particles on zonal flow generation by toroidal Alfvén eigenmode*, Physics of Plasmas **23**, 090702 (2016).

[51] F. L. Hinton and M. N. Rosenbluth, *Dynamics of axisymmetric and poloidal flows in tokamaks*, Plasma Physics and Controlled Fusion **41**, A653 (1999).

[52] Z. Lin, T. S. Hahm, W. W. Lee, W. M. Tang and P. H. Diamond, *Effects of collisional zonal flow damping on turbulent transport*, Phys. Rev. Lett. **83**, 3645 (1999).

[53] Y. Xiao, P. J. Catto and K. Molvig, *Collisional damping for ion temperature gradient mode driven zonal flow*, Physics of Plasmas **14**, 032302 (2007).

[54] B. N. Rogers, W. Dorland and M. Kotschenreuther, *Generation and stability of zonal flows in ion-temperature-gradient mode turbulence*, Phys. Rev. Lett. **85**, 5336 (2000).

[55] F. Seiferling, A. G. Peeters, R. Buchholz, S. R. Grosshauser, F. Rath and A. Weikl, *Damping of zonal modes through turbulent momentum transport*, Physics of Plasmas **25**, 022505 (2018).

[56] B. Scott, *The geodesic transfer effect on zonal flows in tokamak edge turbulence*, Physics Letters A **320**, 53 (2003).

[57] W. M. Nevins, E. Wang and J. Candy, *Magnetic stochasticity in gyrokinetic simulations of plasma microturbulence*, Phys. Rev. Lett. **106**, 065003 (2011).

[58] P. W. Terry, M. J. Pueschel, D. Carmody and W. M. Nevins, *The effect of magnetic flutter on residual flow*, Physics of Plasmas **20**, 112502 (2013).

[59] M. J. Pueschel, D. R. Hatch, T. Görler, W. M. Nevins, F. Jenko, P. W. Terry and D. Told, *Properties of high-β microturbulence and the non-zonal transition*, Physics of Plasmas **20**, 102301 (2013).

[60] M. J. Pueschel, P. W. Terry, F. Jenko, D. R. Hatch, W. M. Nevins, T. Görler and D. Told, *Extreme heat fluxes in gyrokinetic simulations: A new critical β*, Phys. Rev. Lett. **110**, 155005 (2013).

[61] R. E. Waltz, *Nonlinear subcritical magnetohydrodynamic beta limit*, Physics of Plasmas **17**, 072501 (2010).

[62] W. A. Cooper, *Ballooning instabilities in tokamaks with sheared toroidal flows*, Plasma Physics and Controlled Fusion **30**, 1805 (1988).

[63] K. D. Makwana, P. W. Terry, M. J. Pueschel and D. R. Hatch, *Subdominant modes in zonal-flow-regulated turbulence*, Phys. Rev. Lett. **112**, 095002 (2014).

[64] S. Maeyama, A. Ishizawa, T.-H. Watanabe, M. Nakata, N. Miyato, M. Yagi and Y. Idomura, *Comparison between kinetic-ballooning-mode-driven turbulence and ion-temperature-gradient-driven turbulence*, Physics of Plasmas **21**, 052301 (2014).

[65] G. G. Whelan, M. J. Pueschel and P. W. Terry, *Nonlinear electromagnetic stabilization of plasma microturbulence*, Phys. Rev. Lett. **120**, 175002 (2018).

[66] G. G. Whelan, M. J. Pueschel, P. W. Terry, J. Citrin, I. J. McKinney, W. Guttenfelder and H. Doerk, *Saturation and nonlinear electromagnetic stabilization of itg turbulence*, Physics of Plasmas **26**, 082302 (2019).

[67] A. M. Dimits, G. Bateman, M. A. Beer, B. I. Cohen, W. Dorland, G. W. Hammett, C. Kim, J. E. Kinsey, M. Kotschenreuther, A. H. Kritz, L. L. Lao, J. Mandrekas, W. M. Nevins, S. E. Parker, A. J. Redd, D. E. Shumaker, R. Sydora and J. Weiland, *Comparisons and physics basis of tokamak transport models and turbulence simulations*, Physics of Plasmas **7**, 969 (2000).

[68] K. H. Burrell, *Effects of $E \times B$ velocity shear and magnetic shear on turbulence and transport in magnetic confinement devices*, Physics of Plasmas **4**, 1499 (1997).

[69] R. E. Waltz, G. D. Kerbel and J. Milovich, *Toroidal gyro-landau fluid model turbulence simulations in a nonlinear ballooning mode representation with radial modes*, Physics of Plasmas **1**, 2229 (1994).

[70] J. E. Kinsey, R. E. Waltz and J. Candy, *Nonlinear gyrokinetic turbulence simulations of $E \times B$ shear quenching of transport*, Physics of Plasmas **12**, 062302 (2005).

[71] F. J. Casson, A. G. Peeters, Y. Camenen, W. A. Hornsby, A. P. Snodin, D. Strintzi and G. Szepesi, *Anomalous parallel momentum transport due to $E \times B$ flow shear in a tokamak plasma*, Physics of Plasmas **16**, 092303 (2009).

[72] C. Holland, P. Diamond, S. Champeaux, E. Kim, O. Gurcan, M. Rosenbluth, G. Tynan, N. Crocker, W. Nevins and J. Candy, *Investigations of the role of nonlinear couplings in structure formation and transport regulation: experiment, simulation, and theory*, Nuclear Fusion **43**, 761 (2003).

[73] C. Holland, G. R. Tynan, R. J. Fonck, G. R. McKee, J. Candy and R. E. Waltz, *Zonal-flow-driven nonlinear energy transfer in experiment and simulation*, Physics of Plasmas **14**, 056112 (2007).

[74] D. R. Hatch, P. W. Terry, F. Jenko, F. Merz and W. M. Nevins, *Saturation of gyrokinetic turbulence through damped eigenmodes*, Phys. Rev. Lett. **106**, 115003 (2011).

[75] K. D. Makwana, P. W. Terry and J.-H. Kim, *Role of stable modes in zonal flow regulated turbulence*, Physics of Plasmas **19**, 062310 (2012).

[76] G. Dif-Pradalier, G. Hornung, X. Garbet, P. Ghendrih, V. Grandgirard, G. Latu and Y. Sarazin, *The $E\times B$ staircase of magnetised plasmas*, Nuclear Fusion **57**, 066026 (2017).

[77] A. Weikl, A. G. Peeters, F. Rath, S. R. Grosshauser, R. Buchholz, W. A. Hornsby, F. Seiferling and D. Strintzi, *Ion temperature gradient turbulence close to the finite heat flux threshold*, Physics of Plasmas **24**, 102317 (2017).

[78] J. C. Hillesheim, E. Delabie, H. Meyer, C. F. Maggi, L. Meneses, E. Poli and J. Contributors, *Stationary zonal flows during the formation of the edge transport barrier in the jet tokamak*, Phys. Rev. Lett. **116**, 065002 (2016).

[79] G. Hornung, G. Dif-Pradalier, F. Clairet, Y. Sarazin, R. Sabot, P. Hennequin and G. Verdoolaege, *$E \times B$ staircases and barrier permeability in magnetised plasmas*, Nuclear Fusion **57**, 014006 (2016).

[80] W. Liu, Y. Chen, R. Ke, G. McKee, Z. Yan, K. Fang, Z. Yang, Z. Gao, Y. Tan and G. R. Tynan, *Evidence of $E \times B$ staircase in HL-2A L-mode tokamak discharges*, Physics of Plasmas **28**, 012512 (2021).

[81] M. J. Choi, H. Jhang, J.-M. Kwon, J. Chung, M. Woo, L. Qi, S. Ko, T.-S. Hahm, H. K. Park, H.-S. Kim, J. Kang, J. Lee, M. Kim and G. S. Y. and, *Experimental observation of the non-diffusive avalanche-like electron heat transport events and their dynamical interaction with the shear flow structure*, Nuclear Fusion **59**, 086027 (2019).

[82] A. Ashourvan, R. Nazikian, E. Belli, J. Candy, D. Eldon, B. A. Grierson, W. Guttenfelder, S. R. Haskey, C. Lasnier, G. R. McKee and C. C. Petty, *Formation of a high pressure staircase pedestal with suppressed edge localized modes in the DIII-D tokamak*, Phys. Rev. Lett. **123**, 115001 (2019).

[83] J. Dominski, S. Brunner, T. Görler, F. Jenko, D. Told and L. Villard, *How non-adiabatic passing electron layers of linear microinstabilities affect turbulent transport*, Physics of Plasmas **22**, 062303 (2015).

[84] A. C. J., S. Brunner, B. McMillan, J. Ball, J. Dominski and G. Merlo, *How eigenmode self-interaction affects zonal flows and convergence of tokamak core turbulence with toroidal system size*, Journal of Plasma Physics **86**, 905860504 (2020).

[85] J. Ball, S. Brunner and A. C.J., *Eliminating turbulent self-interaction through the parallel boundary condition in local gyrokinetic simulations*, Journal of Plasma Physics **86**, 905860207 (2020).

[86] A. C. J., S. Brunner and J. Ball, *Effect of collisions on non-adiabatic electron dynamics in ITG-driven microturbulence*, Physics of Plasmas **28**, 092303 (2021).

[87] E. A. Frieman and L. Chen, *Nonlinear gyrokinetic equations for low-frequency electromagnetic waves in general plasma equilibria*, The Physics of Fluids **25**, 502 (1982).

[88] W. W. Lee, *Gyrokinetic approach in particle simulation*, The Physics of Fluids **26**, 556 (1983).

[89] J. A. Krommes, *Nonlinear gyrokinetics: a powerful tool for the description of microturbulence in magnetized plasmas*, Physica Scripta **T142**, 014035 (2010).

[90] J. A. Krommes, *The Gyrokinetic Description of Microturbulence in Magnetized Plasmas*, Annual Review of Fluid Mechanics **44**, 175 (2012).

[91] E. Lifshitz and L. Pitaevskii, *Physical Kinetics*, Taylor & Francis, New York (1995).

[92] J. R. Cary, *Lie transform perturbation theory for Hamiltonian systems*, Physics Reports **79**, 129 (1981).

[93] J. R. Cary and R. G. Littlejohn, *Noncanonical Hamiltonian mechanics and its application to magnetic field line flow*, Annals of Physics **151**, 1 (1983).

[94] R. G. Littlejohn, *A guiding center Hamiltonian: A new approach*, Journal of Mathematical Physics **20**, 2445 (1979).

[95] A. Peeters, Y. Camenen, F. Casson, W. Hornsby, A. Snodin, D. Strintzi and G. Szepesi, *The nonlinear gyro-kinetic flux tube code GKW*, Computer Physics Communications **180**, 2650 (2009).

[96] G. Szepesi, *Derivation of the fully electro-magnetic, non-linear, gyrokinetic vlasov-maxwell equations in a rotating frame of reference for GKW with lie transform perturbation method* (2012), part of the GKW documentation.

[97] R. Goldston and P. Rutherford, *Introduction to Plasma Physics*, Butterworth Heinemann, Oxford (2008).

[98] A. Peeters, Y. Camenen, F. Casson, W. Hornsby, P. Manas, A. Snodin, D. Strintzi and G. Szepesi, *GKW how and why* (2014), gKW documentation.

[99] J. Candy, R. E. Waltz, S. E. Parker and Y. Chen, *Relevance of the parallel nonlinearity in gyrokinetic simulations of tokamak plasmas*, Physics of Plasmas **13**, 074501 (2006).

[100] S. Hamada, Kakuyugo Kenkyu **1**, 542 (1958).

[101] B. Scott, *Global consistency for thin flux tube treatments of toroidal geometry*, Physics of Plasmas **5**, 2334 (1998).

[102] H. Lütjens, A. Bondeson and O. Sauter, *The CHEASE code for toroidal MHD equilibria*, Computer physics communications **97**, 219 (1996).

[103] J. W. Connor, R. J. Hastie and J. B. Taylor, *Shear, periodicity, and plasma ballooning modes*, Phys. Rev. Lett. **40**, 396 (1978).

[104] M. A. Beer, S. C. Cowley and G. W. Hammett, *Field-aligned coordinates for nonlinear simulations of tokamak turbulence*, Physics of Plasmas **2**, 2687 (1995).

[105] C. Angioni and A. G. Peeters, *Gyrokinetic calculations of diffusive and convective transport of α particles with a slowing-down distribution function*, Physics of Plasmas **15**, 052307 (2008).

[106] E. A. Belli and J. Candy, *An eulerian method for the solution of the multi-species drift-kinetic equation*, Plasma Physics and Controlled Fusion **51**, 075018 (2009).

[107] J. Candy and R. E. Waltz, *Velocity-space resolution, entropy production, and upwind dissipation in eulerian gyrokinetic simulations*, Physics of Plasmas **13**, 032310 (2006).

[108] D. A. Egolf, I. V. Melnikov and E. Bodenschatz, *Importance of local pattern properties in spiral defect chaos*, Phys. Rev. Lett. **80**, 3228 (1998).

[109] GKW Team, *gkw*, https://bitbucket.org/gkw/gkw/src/develop/, accessed: 20.07.2022.

[110] A. A. Schekochihin, S. C. Cowley, W. Dorland, G. W. Hammett, G. G. Howes, E. Quataert and T. Tatsuno, *ASTROPHYSICAL GYROKINETICS: KINETIC AND FLUID TURBULENT CASCADES IN MAGNETIZED WEAKLY COLLISIONAL PLASMAS*, The Astrophysical Journal Supplement Series **182**, 310 (2009).

[111] A. Bañón Navarro, P. Morel, M. Albrecht-Marc, D. Carati, F. Merz, T. Görler and F. Jenko, *Free energy balance in gyrokinetic turbulence*, Physics of Plasmas **18**, 092303 (2011).

[112] S. Maeyama, M. Sasaki, K. Fujii, T. Kobayashi, R. O. Dendy, Y. Kawachi, H. Arakawa and S. Inagaki, *On the triad transfer analysis of plasma turbulence: symmetrization, coarse graining, and directional representation*, New Journal of Physics **23**, 043049 (2021).

[113] C. Greenfield, J. DeBoo, T. Osborne, F. Perkins, M. Rosenbluth and D. Boucher, *Enhanced fusion performance due to plasma shape modification of simulated ITER discharges in DIII-D*, Nuclear Fusion **37**, 1215 (1997).

[114] J. Kinsey, G. Staebler, J. Candy, R. Waltz and R. Budny, *ITER predictions using the GYRO verified and experimentally validated trapped gyro-landau fluid transport model*, Nuclear Fusion **51**, 083001 (2011).

[115] J. Candy, *TGLF recalibration for ITER standard case parameters FY2015: Theory and simulation performance target final report (GA-A–28239). United states* (2015).

[116] Y. Kamada, K. Ushigusa, O. Naito, Y. Neyatani, T. Ozeki, K. Tobita, S. Ishida, R. Yoshino, M. Kikuchi, M. Mori and H. Ninomiya, *Non-inductively current driven H mode with high beta$_n$ and high beta$_p$ values in JT-60u*, Nuclear Fusion **34**, 1605 (1994).

[117] C. Gormezano, A. Sips, T. Luce, S. Ide, A. Becoulet, X. Litaudon, A. Isayama, J. Hobirk, M. Wade, T. Oikawa, R. Prater, A. Zvonkov, B. Lloyd, T. Suzuki, E. Barbato, P. Bonoli, C. Phillips, V. Vdovin, E. Joffrin, T. Casper, J. Ferron, D. Mazon, D. Moreau, R. Bundy, C. Kessel, A. Fukuyama, N. Hayashi, F. Imbeaux, M. Murakami, A. Polevoi and H. S. John, *Chapter 6: Steady state operation*, Nuclear Fusion **47**, S285 (2007).

[118] F. Rath, A. G. Peeters and A. Weikl, *Analysis of zonal flow pattern formation and the modification of staircase states by electron dynamics in gyrokinetic near marginal turbulence*, Physics of Plasmas **28**, 072305 (2021).

[119] Z. Lin, T. S. Hahm, W. Lee, W. M. Tang and R. B. White, *Turbulent transport reduction by zonal flows: Massively parallel simulations*, Science **281**, 1835 (1998).

[120] R. E. Waltz and C. Holland, *Numerical experiments on the drift wave–zonal flow paradigm for nonlinear saturation*, Physics of Plasmas **15**, 122503 (2008).

[121] T. S. Hahm and K. H. Burrell, *Flow shear induced fluctuation suppression in finite aspect ratio shaped tokamak plasma*, Physics of Plasmas **2**, 1648 (1995).

[122] M. W. Shafer, R. J. Fonck, G. R. McKee, C. Holland, A. E. White and D. J. Schlossberg, *2d properties of core turbulence on DIII-D and comparison to gyrokinetic simulations*, Physics of Plasmas **19**, 032504 (2012).

[123] M. F. J. Fox, F. van Wyk, A. R. Field, Y. c Ghim, F. I. Parra and A. A. S. and, *Symmetry breaking in MAST plasma turbulence due to toroidal flow shear*, Plasma Physics and Controlled Fusion **59**, 034002 (2017).

[124] J. Pinzón, T. Happel, P. Hennequin, C. Angioni, T. Estrada, A. Lebschy and U. S. and, *Experimental investigation of the tilt angle of turbulent structures in the core of fusion plasmas*, Nuclear Fusion **59**, 074002 (2019).

[125] R. E. Waltz, R. L. Dewar and X. Garbet, *Theory and simulation of rotational shear stabilization of turbulence*, Physics of Plasmas **5**, 1784 (1998).

[126] Y. Idomura, *Saturation mechanism of decaying ion temperature gradient driven turbulence with kinetic electrons*, Plasma and Fusion Research **11**, 2403006 (2016).

[127] B. F. McMillan, P. Hill, A. Bottino, S. Jolliet, T. Vernay and L. Villard, *Interaction of large scale flow structures with gyrokinetic turbulence*, Physics of Plasmas **18**, 112503 (2011).

[128] P. Migliano, R. Buchholz, S. Grosshauser, W. Hornsby, A. Peeters and O. Stauffert, *Turbulence spreading in gyro-kinetic theory*, Nuclear Fusion **56**, 014002 (2016).

[129] R. E. Waltz, M. E. Austin, K. H. Burrell and J. Candy, *Gyrokinetic simulations of off-axis minimum-q profile corrugations*, Physics of Plasmas **13**, 052301 (2006).

[130] A. Dimits, B. Cohen, W. Nevins and D. Shumaker, *Parameter dependences of ion thermal transport due to toroidal ITG turbulence*, Nuclear Fusion **41**, 1725 (2001).

[131] O. Yamagishi, *Non-isomorphic radial wavenumber dependencies of residual zonal flows in ion and electron larmor radius scales, and effects of initial parallel flow and electromagnetic potentials in a circular tokamak*, Plasma Physics and Controlled Fusion **60**, 045009 (2018).

[132] J. Candy, *Beta scaling of transport in microturbulence simulations*, Physics of Plasmas **12**, 072307 (2005).

[133] P. Hunana, A. Tenerani, G. P. Zank, E. Khomenko, M. L. Goldstein, G. M. Webb, P. S. Cally, M. Collados, M. Velli and L. Adhikari, *An introductory guide to fluid models with anisotropic temperatures Part 1 – CGL description and collisionless fluid hierarchy* (2019), arXiv:1901.09354v2.

[134] F. Seiferling, A. G. Peeters, S. R. Grosshauser, F. Rath and A. Weikl, *The interplay of an external torque and $E \times B$ structure formation in tokamak plasmas*, Physics of Plasmas **26**, 102306 (2019).

[135] M. Reisner, E. Fable, J. Stober, A. Bock, A. B. Navarro, A. D. Siena, R. Fischer, V. Bobkov and R. M. and, *Increased core ion temperatures in high-beta advanced scenarios in ASDEX upgrade*, Nuclear Fusion **60**, 082005 (2020).

[136] P. H. Diamond and T. S. Hahm, *On the dynamics of turbulent transport near marginal stability*, Physics of Plasmas **2**, 3640 (1995).

[137] X. Garbet and R. E. Waltz, *Heat flux driven ion turbulence*, Physics of Plasmas **5**, 2836 (1998).

[138] P. A. Politzer, *Observation of avalanchelike phenomena in a magnetically confined plasma*, Phys. Rev. Lett. **84**, 1192 (2000).

[139] F. Rath and A. G. Peeters, *Transport hysteresis in electromagnetic microturbulence caused by mesoscale zonal flow pattern-induced mitigation of high β turbulence runaways*, Physics of Plasmas **29**, 042305 (2022).

[140] J. R. McNally, *The ignition parameter $Tn\tau$ and the energy multiplication factor k for fusioning plasmas*, Nuclear Fusion **17**, 1273 (1977).

[141] E. J. Strait, *Stability of high beta tokamak plasmas*, Physics of Plasmas **1**, 1415 (1994).

[142] P. Terry, D. Carmody, H. Doerk, W. Guttenfelder, D. Hatch, C. Hegna, A. Ishizawa, F. Jenko, W. Nevins, I. Predebon, M. Pueschel, J. Sarff and G. Whelan, *Overview of gyrokinetic studies of finite-β microturbulence*, Nuclear Fusion **55**, 104011 (2015).

[143] W. Tang, J. Connor and R. Hastie, *Kinetic-ballooning-mode theory in general geometry*, Nuclear Fusion **20**, 1439 (1980).

[144] A. Hirose, L. Zhang and M. Elia, *Higher order collisionless ballooning mode in tokamaks*, Phys. Rev. Lett. **72**, 3993 (1994).

[145] E. Wang, W. M. Nevins, J. Candy, D. Hatch, P. Terry and W. Guttenfelder, *Electron heat transport from stochastic fields in gyrokinetic simulations*, Physics of Plasmas **18**, 056111 (2011).

[146] A. B. Rechester and M. N. Rosenbluth, *Electron heat transport in a tokamak with destroyed magnetic surfaces*, Phys. Rev. Lett. **40**, 38 (1978).

[147] W. Guttenfelder, J. Candy, S. M. Kaye, W. M. Nevins, E. Wang, R. E. Bell, G. W. Hammett, B. P. LeBlanc, D. R. Mikkelsen and H. Yuh, *Electromagnetic transport from microtearing mode turbulence*, Phys. Rev. Lett. **106**, 155004 (2011).

[148] A. Ishizawa, S. Maeyama, T.-H. Watanabe, H. Sugama and N. Nakajima, *Electromagnetic gyrokinetic simulation of turbulence in torus plasmas*, Journal of Plasma Physics **81**, 435810203 (2015).

[149] M. J. Pueschel, T. Görler, F. Jenko, D. R. Hatch and A. J. Cianciara, *On secondary and tertiary instability in electromagnetic plasma microturbulence*, Physics of Plasmas **20**, 102308 (2013).

[150] M. J. Pueschel and F. Jenko, *Transport properties of finite-β microturbulence*, Physics of Plasmas **17**, 062307 (2010).

[151] G. Colyer, A. Schekochihin, F. Parra, C. Roach, M. Barnes, Y. Ghim and W. Dorland, *Collisionality scaling of the electron heat flux in etg turbulence*, Plasma Physics and Controlled Fusion **59**, 055002 (2017).

[152] J. Candy and R. Waltz, *An eulerian gyrokinetic-maxwell solver*, Journal of Computational Physics **186**, 545 (2003).

[153] V. Naulin, A. Kendl, O. E. Garcia, A. H. Nielsen and J. J. Rasmussen, *Shear flow generation and energetics in electromagnetic turbulence*, Physics of Plasmas **12**, 052515 (2005).

[154] Z. Williams, M. Pueschel, P. Terry, T. Nishizawa, D. Kriete, M. Nornberg, J. Sarff, G. McKee, D. Orlov and S. Nogami, *Impact of resonant magnetic perturbations on zonal flows and microturbulence*, Nuclear Fusion **60**, 096004 (2020).

[155] T.-H. Watanabe, H. Sugama, A. Ishizawa and M. Nunami, *Flux tube train model for local turbulence simulation of toroidal plasmas*, Physics of Plasmas **22**, 022507 (2015).

[156] A. Ishizawa, D. Urano, Y. Nakamura, S. Maeyama and T.-H. Watanabe, *Persistence of ion temperature gradient turbulent transport at finite normalized pressure*, Phys. Rev. Lett. **123**, 025003 (2019).

[157] Y. Idomura, *Full-f gyrokinetic simulation over a confinement time*, Physics of Plasmas **21**, 022517 (2014).

[158] W. Wang, Y. Kishimoto, K. Imadera, H. Liu, J. Li, M. Yagi and Z. Wang, *Statistical study for ITG turbulent transport in flux-driven tokamak plasmas based on global gyro-kinetic simulation*, Nuclear Fusion **60**, 066010 (2020).

[159] B. F. McMillan, J. Ball and S. Brunner, *Simulating background shear flow in local gyrokinetic simulations*, Plasma Physics and Controlled Fusion **61**, 055006 (2019).

[160] H. Urano, T. Takizuka, H. Takenaga, N. Oyama, Y. Miura and Y. Kamada, *Confinement degradation with beta for elmy h-mode plasmas in jt-60u tokamak*, Nuclear Fusion **46**, 781 (2006).

[161] L. Vermare, F. Ryter, C. Angioni, A. Peeters, J. Stober, R. Bilato, L. Horton, B. Kurzan, C. Maggi, H. Meister, J. Schirmer, G. Tardini and the ASDEX Upgrade Team, *Study of the β dependence of confinement and heat transport in ASDEX upgrade*, Nuclear Fusion **47**, 490 (2007).

[162] C. C. Petty, *Sizing up plasmas using dimensionless parameters*, Physics of Plasmas **15**, 080501 (2008).

[163] D. C. McDonald, L. Laborde, J. C. DeBoo, F. Ryter, M. Brix, C. D. Challis, P. de Vries, C. Giroud, J. Hobirk, D. Howell, E. Joffrin, T. C. Luce, J. Mailloux, V. Pericoli-Ridolfini, A. C. C. Sips and K. T. and, *JET confinement studies and their scaling to high β, ITER scenarios*, Plasma Physics and Controlled Fusion **50**, 124013 (2008).

[164] C. Challis, J. Garcia, M. Beurskens, P. Buratti, E. Delabie, P. Drewelow, L. Frassinetti, C. Giroud, N. Hawkes, J. Hobirk, E. Joffrin, D. Keeling, D. King, C. Maggi, J. Mailloux, C. Marchetto, D. McDonald, I. Nunes, G. Pucella, S. Saarelma and J. S. and, *Improved confinement in JET high β plasmas with an ITER-like wall*, Nuclear Fusion **55**, 053031 (2015).

[165] N. Joiner, A. Hirose and W. Dorland, *Parallel magnetic field perturbations in gyrokinetic simulations*, Physics of Plasmas **17**, 072104 (2010).

[166] F. L. Hinton and R. D. Hazeltine, *Theory of plasma transport in toroidal confinement systems*, Rev. Mod. Phys. **48**, 239 (1976).

[167] P. Hunana, A. Tenerani, G. P. Zank, E. Khomenko, M. L. Goldstein, G. M. Webb, P. S. Cally, M. Collados, M. Velli, L. Adhikari and et al., *An introductory guide to fluid models with anisotropic temperatures. Part 1. CGL description and collisionless fluid hierarchy*, Journal of Plasma Physics **85**, 205850602 (2019).

[168] F. G. Chew, M. L. Goldberger and F. E. Low, *The Boltzmann equation and the one-fluid hydromagnetic equations in the absence of particle collisions*, Proc. R. Soc. **112**, A236 (1956).

[169] Max-Planck-Institut für Plasmaphysik, *Einführung*, https://www.ipp.mpg.de/10268/einfuehrung, accessed: 20.06.2022.

[170] Iter Organization, *The iter tokamak*, https://www.iter.org/mach, accessed: 20.06.2022.

List of Publications

A complete list of works published in peer reviewed journals with contributions of the author is given below.

- F. Rath, A. G. Peeters, R. Buchholz, S. R. Grosshauser, P. Migliano, A. Weikl, and D. Strintzi, *Comparison of gradient and flux driven gyro-kinetic turbulent transport*, Phys. Plasmas **23**, 052309 (2016)
- A. G. Peeters, F. Rath, R. Buchholz, Y. Camenen, J. Candy, F. J. Casson, S. R. Grosshauser, W. A. Hornsby, D. Strintzi, and A. Weikl, *Gradient-driven flux-tube simulations of ion temperature gradient turbulence close to the non-linear threshold*, Phys. Plasmas **23**, 082517 (2016)
- A. Weikl, A. G. Peeters, F. Rath, S. R. Grosshauser, R. Buchholz, W. A. Hornsby, F. Seiferling, and D. Strintzi, *Ion temperature gradient turbulence close to the finite heat flux threshold*, Phys. Plasmas **24**, 102317 (2017)
- A. Weikl, A. G. Peeters, F. Rath, F. Seiferling, R. Buchholz, S. R. Grosshauser, and D. Strintzi, *The occurrence of staircases in ITG turbulence with kinetic electrons and the zonal flow drive through self-interaction*, Phys. Plasmas **25**, 072305 (2018)
- F. Seiferling, A. G. Peeters, R. Buchholz, S. R. Grosshauser, F. Rath, and A. Weikl, *Damping of zonal modes through turbulent momentum transport*, Phys. Plasmas **25**, 022505 (2018)
- F. Rath, A. G. Peeters, R. Buchholz, S. R. Grosshauser, F. Seiferling, and A. Weikl, *On the tertiary instability formalism of zonal flows in magnetized plasmas*, Phys. Plasmas **25**, 052102 (2018)
- F. Seiferling, A. G. Peeters, S. R. Grosshauser, F. Rath, and A. Weikl, *The interplay of an external torque and $E\times B$ structure formation in tokamak plasmas*, Phys. Plasmas **26**, 102306 (2019)
- B. N. Schobert, A. G. Peeters, and F. Rath, *The Impact of Accretion Heating and Thermal Conduction on the Dead Zone of Protoplanetary Disks*, ApJ **881**, 56 (2019)

- F. Rath, A. G. Peeters, R. Buchholz, S. R. Grosshauser, F. Seiferling, and A. Weikl, *Retraction: "On the tertiary instability formalism of zonal flows in magnetized plasmas" [Phys. Plasmas 25, 052102 (2018)]*, Phys. Plasmas **27**, 069901 (2020)

- F. Rath, A. G. Peeters, and A. Weikl, *Analysis of zonal flow pattern formation and the modification of staircase states by electron dynamics in gyrokinetic near marginal turbulence*, Phys. Plasmas **28**, 072305 (2021)

- F. Rath, and A. G. Peeters, *Transport hysteresis in electromagnetic microturbulence caused by mesoscale zonal flow pattern-induced mitigation of high β turbulence runaways*, Phys. Plasma **29**, 042305 (2022)

Eidesstattliche Erklärung

Hiermit versichere ich an Eides statt, dass ich die vorliegende Arbeit selbstständig verfasst habe und keine anderen als die von mir angegebenen Quellen und Hilfsmittel verwendet habe.

Weiterhin erkläre ich, dass ich die Hilfe von gewerblichen Promotionsberatern bzw. -vermittlern oder ähnlichen Dienstleistern weder bisher in Anspruch genommen habe, noch künftig in Anspruch nehmen werde.

Zusätzlich erkläre ich hiermit, dass ich keinerlei frühere Promotionsversuche unternommen habe.

Bayreuth, den _____

_____

Florian Rath